



**Design of a Mechatronic Measurement  
System for Surface Fatigue of Dental  
Composites**

**by**

**Simon Ignace Marandu**

**Thesis submitted in fulfillment of the requirements  
for the Degree of Doctor of Philosophy**

**School of Mechanical and Systems Engineering  
Newcastle University, United Kingdom**

**August 2014**

### **Dedication**

This thesis is dedicated to the loving memory of my beloved father, the late Ignatius J. Marandu, who died on the 29<sup>th</sup> June 2013.

Fond memories of your words of inspiration and encouragement in pursuit of excellence still linger on.

May Your Soul Rest In Peace

## ABSTRACT

This thesis focuses on the design and development of a rolling-ball mechatronic system for on-line testing and measurement of surface contact fatigue of dental composites, and is based on a technique initially developed at the Newcastle Dental School. The mechatronic system synergistically combines the mechanical/electronic hardware with a low-cost embedded digital signal controller (DSC microcontroller) hardware and software to monitor and measure in real-time surface wear due to contact fatigue.

ISO/TS 14569-2:2001 standard specification for testing of dental materials was used for selecting appropriate test variables. The mechatronic system attempts to simulate the human oral environment with temperature and moisture being controlled. A closed-loop PI control algorithm combining both optical encoder pulse timing and counting methods is used to drive a dc brushless motor at speeds of 240 and 2040 rpm. A small (2mm diameter) ruby ball is mounted in a V-grooved mandrel which over time creates a circular orbital wear path in the dental composite material. One algorithm has been designed to acquire and process the on-line measurement of wear using a linear voltage differential transformer (LVDT), with another monitoring the fatigue cycling process. A graphical user interface (GUI) has also been designed and implemented on a laptop which is connected to the rig embedded controller.

A kinematic model of the rolling ball constrained in a V-groove has been developed along with a finite element analysis of the surface deformation. This has been augmented by a comprehensive test programme, in dry, moisturized and elevated temperature (i.e. 37°C), using Synergy D6 specimens. Using ANOVA test, 70% reproducibility of fatigue track measurements was attained. A comparison of LVDT transducer and profilometer measurements indicated 5% consistence with each other. The insight gained from the testing programme sets a basis for an extensive programme to qualify and validate the measurement system basing on ISO/TS 14569-2:2001 specifications.

**KEY WORDS:** Design, Mechatronic, Embedded System, Digital Signal Controller, PI Control, LVDT, GUI, Surface Contact Fatigue, Dental Composites.

## ACKNOWLEDGEMENTS

Firstly, I would like to thank my supervisors, Dr R. Bicker and Dr M. German for their support, encouragement and guidance in this research. In a special way, I am extending sincere gratitude to Dr R. Bicker for his profound patience and mentorship through my studies; in particular, for impacting on me the know-how of electronics, embedded systems designing and programming. His desire to develop an intelligent mechatronic rolling-ball fatigue measurement system offered me with unique insights to the research.

I am truly grateful to the Tanzania government and the University of Dar es salaam for the financial and material support throughout my PhD studies. I promise to use the acquired knowledge initiating and advancing mechatronic know-how at the university and across the education institutions in the country.

Sincere and heartfelt thanks to my wife, Edna and daughters, Catherine and Theresa for their love, courage and persistent endurance throughout my four years of studies. Their moral support was so precious in the challenging moments. I simply could not have completed my studies without them.

I owe deepest gratitude to my parents who have supported me materially and then morally throughout the study years and in life generally. Their endeavour sparked my interests to excel in studies even at the most challenging times. In a special way, I acknowledge the inspirational and moral support to continue studying; received from my deceased father, Ignatius, even at his very critical illness. May he Rest in Peace.

Lastly, I would like to thank my colleagues PhD research students, Paramin, Ahmad, Imam, Erwin, Jaya and Steven with whom I shared joys and challenges during my studies. Thank you for extending support in many ways. I wish you all everything, I would wish myself.

## TABLE OF CONTENTS

|  |     |
|--|-----|
| Dedication .....   | ii  |
| ABSTRACT .....   | iii |
| ACKNOWLEDGEMENTS .....   | iv  |
| LIST OF FIGURES .....  | x   |
| LIST OF TABLES .....   | xiv |
| CHAPTER 1 INTRODUCTION .....   | 1   |
| 1.2 Aim and Objectives .....   | 3   |
| 1.3 Research Hypothesis .....  | 3   |
| 1.4 Significance of the Research .....   | 4   |
| 1.5 Overview of the Research .....   | 4   |
| CHAPTER 2 LITERATURE REVIEW .....  | 6   |
| 2.1 Human Dental Structure .....   | 6   |
| 2.2 Dental Composites .....  | 8   |
| 2.3 Physical and Mechanical Properties of Dental Composites .....                                  | 11  |
| 2.4 Tribological Wear Behaviour of Dental Composites .....   | 14  |
| 2.5 Dental Composite Wear Testing Methods .....  | 16  |
| 2.5.1 In-vivo testing .....  | 16  |
| 2.5.2 In-vitro testing .....   | 17  |
| 2.5.3 In-situ testing .....  | 20  |
| 2.6 Overview of Dental Composite Surface Contact Fatigue .....                                     | 21  |
| 2.7 Spherical Rolling Contact Application in Materials Characterization .....                      | 25  |
| 2.8 Use of Spherical Contact Rolling in Dental Composite Testing .....                             | 29  |
| 2.9 Use of Finite Element Analysis to Predict Failures of Dental Composites .....                  | 34  |
| 2.10 Summary .....   | 40  |
| CHAPTER 3 EXPERIMENTAL VALIDATION OF LVDT SENSOR AND<br>MODELLING OF ROLLING BALL KINEMATICS ..... | 43  |
| 3.1 Prototype Rig Set Up .....   | 43  |
| 3.2 Surface Fatigue Actuation and Data Acquisition .....   | 45  |
| 3.3 Calibration of the Measurement System .....  | 46  |
| 3.4 Dental Specimen Preparation and Testing .....  | 47  |
| 3.5 Kinematic Modelling of the Beating Effect .....  | 48  |
| 3.6 Preliminary Surface Contact Fatigue Results and Discussion .....                               | 57  |
| 3.7 Summary .....  | 60  |

|  |     |
|--|-----|
| CHAPTER 4 ROLLING BALL FINITE ELEMENT ANALYSIS .....                           | 61  |
| 4.1 Basis of Surface Contact Fatigue Modelling.....                            | 61  |
| 4.2 Ruby Ball and Dental Composite Analytical Modelling.....                   | 63  |
| 4.3 Finite Element Analysis (FEA) .....  | 71  |
| 4.3.1 Modelling and meshing.....   | 71  |
| 4.3.2 Boundary and loading conditions.....                                     | 74  |
| 4.3.3 Convergence test .....   | 76  |
| 4.4 FEA results .....  | 76  |
| 4.5 Fatigue Life Prediction Based on FEA Analysis.....                         | 83  |
| 4.6 Summary .....  | 88  |
| CHAPTER 5 DESIGN OF THE MECHATRONIC MEASUREMENT SYSTEM .....                   | 89  |
| 5.1 Mechatronic Design Specifications.....                                     | 89  |
| 5.1.1 Design synthesis and trade-off analysis .....                            | 93  |
| 5.2 Mechatronic Hardware Design.....   | 94  |
| 5.2.1 Working principle and frame design.....                                  | 94  |
| 5.2.2 Contact fatigue actuator drive .....                                     | 97  |
| 5.2.3 Contact force loading and sensing module .....                           | 102 |
| 5.2.4 Precision linear sliding bearing.....                                    | 102 |
| 5.2.5 LVDT wear transducer.....  | 103 |
| 5.2.6 LVDT Hybrid Simulator and Demodulator .....                              | 103 |
| 5.2.7 Specimen carriage .....  | 103 |
| 5.2.8 Heating System .....   | 104 |
| 5.2.9 Lubricating system.....  | 106 |
| 5.2.10 Vibration Isolator .....  | 107 |
| 5.3 Modelling, engineering drawings and prototype manufacturing .....          | 108 |
| 5.4 Summary .....  | 110 |
| CHAPTER 6 DESIGN OF THE EMBEDDED CONTROL AND DATA<br>ACQUISITION SYSTEMS ..... | 111 |
| 6.1 Embedded System Specific Requirements.....                                 | 111 |
| 6.2 DsPICDEMTM 80-Pin Starter Development Board.....                           | 114 |
| 6.3 Embedded Hardware Design.....  | 115 |
| 6.3.1 BLDC motor drive and control interface .....                             | 118 |
| 6.3.2 BLDC motor speed and position control .....                              | 121 |
| 6.3.3 Updating speed and position .....  | 125 |

|   |   |            |
|---|---|------------|
| 6.4   | LVDT Wear Transducer Interface.....                                       | 129        |
| 6.5   | Lubricating Pump Driver Interface .....                                   | 132        |
| 6.6   | Heating Circuit Interface .....   | 133        |
| 6.7   | RS 232 Serial Communication Port .....                                    | 135        |
| 6.8   | Embedded Software Design .....  | 137        |
| 6.8.1   | Embedded real time program.....   | 137        |
| 6.8.2   | Program and interrupt routines configurations .....                       | 138        |
| 6.8.3   | Configuring PWM port .....  | 140        |
| 6.8.4   | Configuring Timers.....   | 141        |
| 6.8.5   | Configuring ADC sampling, online and offline data processing.....         | 141        |
| 6.8.7   | Serial Communication Interface .....                                      | 146        |
| 6.8.8   | Program modules and data storages.....                                    | 147        |
| 6.8.9   | Embedded software integration.....  | 148        |
| 6.9   | Summary .....   | 149        |
| <b>CHAPTER 7 MECHATRONIC ROLLING BALL DEVICE SET-UP, OPERATION AND EXPERIMENTAL RESULTS .....</b> |   | <b>150</b> |
| 7.1   | Mechatronic System Set-up.....  | 150        |
| 7.2   | System Operation Procedures .....   | 153        |
| 7.3   | Sensor Calibration .....  | 155        |
| 7.3.1   | LVDT transducer calibration .....   | 155        |
| 7.3.2   | Accelerometer calibration .....   | 156        |
| 7.3.3   | Temperature calibration .....   | 158        |
| 7.4   | LVDT Transducer Signal Processing.....                                    | 158        |
| 7.5   | Experimental Set-up .....   | 159        |
| 7.5.1   | Design of Experiments (DoE) .....   | 159        |
| 7.5.2   | Selection of compressive load.....  | 160        |
| 7.5.3   | Materials preparation and method.....                                     | 161        |
| 7.6   | Experimental Results: Time-domain Analysis.....                           | 163        |
| 7.6.1   | LVDT transducer measurements validation.....                              | 163        |
| 7.6.2   | Category A: Effects of testing condition on surface contact fatigue ..... | 165        |
| 7.6.3   | Category B: Effects of loading on surface contact fatigue .....           | 170        |
| 7.6.4   | Peak, RMS, Crest Factor and Kurtosis surface fatigue indicators .....     | 171        |
| 7.7   | Experimental Results: Frequency-domain Analysis .....                     | 176        |
| 7.7.1   | Low speed-LVDT frequency domain analysis .....                            | 176        |

|             |   |     |
|-------------|---|-----|
| 7.7.2       | Running-speed accelerometer frequency domain analysis .....       | 179 |
| 7.8         | Summary .....   | 182 |
| CHAPTER 8   | DISCUSSION .....  | 183 |
| 8.1         | Rolling Ball Kinematic Modelling and LVDT Sensor Validation.....  | 183 |
| 8.2         | FEA of Surface Contact Fatigue and Fatigue Life Prediction.....   | 185 |
| 8.3         | Designing the Mechatronic System Hardware .....                   | 187 |
| 8.4         | Designing the Embedded System Hardware and Software.....          | 189 |
| 8.5         | Testing and Evaluation of the Mechatronic Measurement System..... | 191 |
| 8.6         | Summary .....   | 196 |
| CHAPTER 9   | CONCLUSION AND FUTURE WORK.....                                   | 197 |
| 9.1         | Conclusions .....   | 197 |
| 9.2         | Summary of Achievements .....                                     | 198 |
| 9.3         | Recommendations for Future Work .....                             | 199 |
| 9.4         | Publications .....  | 202 |
| REFERENCES  | .....   | 203 |
| APPENDICES  | .....   | 213 |
| Appendix 1: | Rolling ball Kinematic Modelling Matlab Codes .....               | 213 |
| A1.1        | Time-domain to frequency-domain (FFT) codes.....                  | 213 |
| A1.2        | Beating phenomenon modelling codes .....                          | 213 |
| A1.3        | 3D plotting to depict surface fatigue wear codes.....             | 213 |
| A1.4        | 3D Waterfalls plotting to depict surface fatigue trends .....     | 215 |
| Appendix 2: | Embodiment Design Evaluation and Estimation.....                  | 216 |
| A2.1        | BLDC Servomotor torques estimation.....                           | 216 |
| A2.2        | Linear bearing estimation.....                                    | 218 |
| A2.3        | LVDT's sensor specifications.....                                 | 220 |
| A2.4        | Heating wattage estimation .....                                  | 221 |
| Appendix 3: | Mechatronic Rolling-ball Device Hardware Documents .....          | 223 |
| A3.1        | Assembled layout of the mechatronic rolling-ball device .....     | 223 |
| A3.2        | Part list of the mechatronic rolling-ball device .....            | 223 |
| A3.3        | BLDC motor control and driver circuit schematic.....              | 225 |
| A3.4        | Peristaltic pump driver circuit schematic .....                   | 226 |
| A3.5        | Solid state relay (SSR) for powering the heater.....              | 226 |
| Appendix 4: | Supplementary Embedded Hardware and Software Documents.....       | 227 |
| A4.1        | Configuration set-up of CCS_PCD/MPLAB IDE C-Programming .....     | 227 |



|             |   |     |
|-------------|---|-----|
| A4.2        | Interrupt Service Routine for speed control Flowchart.....          | 227 |
| A4.3        | Overall Embedded System Program Flowchart (attached A3 sheet).....  | 227 |
| Appendix 5: | Synergy D6 Martens Hardness Tests Results for Dental Specimens ...  | 228 |
| A5.1        | Synergy D6 Packable Composite.....                                  | 228 |
| A5.2        | Synergy D6 Flowable Composite .....                                 | 229 |
| Appendix 6: | Encoder, LVDT and Accelerometer Signal Measurements .....           | 230 |
| A6.1        | Extract table showing online cycle counting method .....            | 230 |
| A6.2        | LabVIEW codes for PI speed data acquisition and GUI display .....   | 234 |
| A6.3        | LabVIEW code for Accelerometer data acquisition and GUI display.... | 234 |
| A6.4        | Accelerometer FFT plot for the axial horizontal (X-axis) _ .....    | 235 |
| A6.5        | Accelerometer FFT plot for the radial vertical (Y-axis) _ .....     | 235 |
| Appendix 7: | Supplementary Frequency Domain Results for Synergy D6 Flow .....    | 235 |
| A7.1        | 2D plots for Synergy D6 flow dry testing at 20°C .....              | 235 |
| A7.2        | 2D plots for Synergy D6 flow lubricated testing at 20°C .....       | 235 |
| A7.3        | 2D plots for Synergy D6 flow lubricated testing at 37°C .....       | 235 |

## LIST OF FIGURES

|             |  |    |
|-------------|--|----|
| Figure 1-1  | Oral interactions and wear mechanisms.....                               | 1  |
| Figure 2-1  | Natural tooth structures .....   | 7  |
| Figure 2-2  | Illustration of the dental structure layout. ....                        | 7  |
| Figure 2-3  | Applications and appearances of amalgam and composite restorations ..... | 8  |
| Figure 2-4  | Filler particles in different dental composites.....                     | 10 |
| Figure 2-5  | Bilinear properties of polymer-based dental composites.....              | 12 |
| Figure 2-6  | Illustration of tooth occlusal contact and contact free areas .....      | 15 |
| Figure 2-7  | Traditional dental material testing methods.....                         | 17 |
| Figure 2-8  | Schematic of the tooth brushing machine .....                            | 18 |
| Figure 2-9  | Two-body and three-body dental wear simulator configurations .....       | 19 |
| Figure 2-10 | Configurations of the Chewing robot. ....                                | 20 |
| Figure 2-11 | Illustration of pitting and spalling phenomena.....                      | 21 |
| Figure 2-12 | Stages of fatigue growth in structured polymeric composites .....        | 22 |
| Figure 2-13 | Characteristic curves of polymeric composites failure .....              | 23 |
| Figure 2-14 | Factors governing spherical rolling contact on materials.....            | 26 |
| Figure 2-15 | Fatigue test of a polymeric material .....                               | 26 |
| Figure 2-16 | Steel ball rolling on a polymer plate .....                              | 27 |
| Figure 2-17 | Factors influencing distortion mechanism in polymeric materials.....     | 28 |
| Figure 2-18 | SEM images illustrating wear characteristics of polymeric material....   | 28 |
| Figure 2-19 | Rolling-ball devices for dental composites fatigue. ....                 | 30 |
| Figure 2-20 | Fatigue track depth for the 57 vol% with silanated glass filler .....    | 31 |
| Figure 2-21 | Revised rolling-ball device for measuring contact fatigue .....          | 32 |
| Figure 2-22 | Fatigue track depth against load cycles .....                            | 33 |
| Figure 2-23 | Schematic of the spherical indentation model.....                        | 36 |
| Figure 2-24 | Simulated intraoral resurfacing process .....                            | 38 |
| Figure 2-25 | Methods for establishing crack propagation direction .....               | 39 |
| Figure 3-1  | Photo image of the revised prototype rig .....                           | 43 |
| Figure 3-2  | Prototype rig set up and instruction flow. ....                          | 44 |
| Figure 3-3  | Illustrations of the rolling ball prototype rig .....                    | 45 |
| Figure 3-4  | LabVIEW VI for acquiring measurement data .....                          | 46 |
| Figure 3-5  | SM1 LVDT calibration graph in the range of $\pm 10\mu\text{m}$ . ....    | 47 |
| Figure 3-6  | LVDT time domain signal depicting the beating phenomenon. ....           | 49 |
| Figure 3-7  | LVDT frequency domain plot depicting the signal's components .....       | 50 |

|             |  |     |
|-------------|--|-----|
| Figure 3-8  | Kinematics of mandrel, ruby ball and dental specimen .....                 | 51  |
| Figure 3-9  | Mandrel and ruby ball contact kinematics during rolling .....              | 52  |
| Figure 3-10 | Relationship of mandrel, ball and specimen three point-contact. ....       | 53  |
| Figure 3-11 | Influence of mandrel groove angle on mandrel-ball orbit speeds ratio. 55   |     |
| Figure 3-12 | Schematic illustration of specimen misalignment (exaggerated).....         | 55  |
| Figure 3-13 | Schematic illustration of mandrel misalignment (exaggerated).....          | 56  |
| Figure 3-14 | Combined effect of mandrel and specimen misalignment with $\alpha=125^0$   | 57  |
| Figure 3-15 | Fatigue wear data recorded using LVDT measurement transducer .....         | 58  |
| Figure 4-1  | Illustration of cyclic rolling and induced elasto-plastic deformation..... | 62  |
| Figure 4-2  | Symmetry contact nomenclature of rolling ball and dental composite ...     | 63  |
| Figure 4-4  | Contact stress distribution on the uniformly loaded half-space. ....       | 69  |
| Figure 4-5  | Displacement versus load relationship for the dental composite .....       | 70  |
| Figure 4-6  | Ruby ball and dental composite contact nomenclature.....                   | 71  |
| Figure 4-7  | Schematic of the FEA Set-Up.....   | 72  |
| Figure 4-8  | Half 3D FE model of the rolling ball and planar dental composite .....     | 73  |
| Figure 4-9  | Contact loading boundary conditions .....                                  | 74  |
| Figure 4-10 | Static loading von Mises stress contour plot .....                         | 77  |
| Figure 4-11 | Stress distributions along the contact region in static loading .....      | 78  |
| Figure 4-12 | Distribution of stress contour in x-axis direction .....                   | 79  |
| Figure 4-13 | Distribution of stress contour in z-axis direction .....                   | 80  |
| Figure 4-14 | Distribution of stress contour in y-axis direction .....                   | 81  |
| Figure 4-15 | Distribution of von Mises stress contour plot .....                        | 81  |
| Figure 4-16 | Stress distributions along the contact region in cyclic loading .....      | 82  |
| Figure 4-17 | Conceptual differences between LCF and HCF.....                            | 84  |
| Figure 4-18 | Modified Goodman diagram showing limit and range of stresses .....         | 85  |
| Figure 4-19 | Nomenclature of fluctuating stress parameters in fatigue loading .....     | 86  |
| Figure 5-1  | Systematic design approach method].....                                    | 90  |
| Figure 5-2  | Design synthesis and optimization process flow .....                       | 91  |
| Figure 5-3  | Mechatronic system design optimisation flow.....                           | 93  |
| Figure 5-4  | Schematic of the cyclic rolling ball surface fatigue process .....         | 94  |
| Figure 5-5  | Interaction of different parts' models of the rolling ball device.....     | 97  |
| Figure 5-6  | Illustration of the synchronous toothed belt drive system .....            | 100 |
| Figure 5-7  | BLDC servo actuator trapezoidal speed profile .....                        | 100 |
| Figure 5-8  | BLDC servo actuator torque profile.....                                    | 101 |

|             |  |     |
|-------------|--|-----|
| Figure 5-9  | EC-max 30 (model 272766) brushless dc servo motor.....                       | 102 |
| Figure 5-10 | Schematic of precision linear bearing .....                                  | 102 |
| Figure 5-11 | Versatile specimen carriages .....   | 104 |
| Figure 5-12 | PMMA mould plate for dental specimen .....                                   | 104 |
| Figure 5-13 | Self-adhesive silicone heating mat .....                                     | 106 |
| Figure 5-14 | Peristaltic pump .....   | 107 |
| Figure 5-15 | Male Radiaflex vibration mounts .....  | 108 |
| Figure 5-16 | Pictorial representation of the mechatronic rolling ball device.....         | 109 |
| Figure 6-1  | DsPICDEM <sup>TM</sup> 80-pin starter development board. ....                | 115 |
| Figure 6-2  | Embedded hardware layout using dsPIC33FJ256GP710A device .....               | 117 |
| Figure 6-3  | EVAL 6235N 3-phase BLDC motor evaluation board.....                          | 119 |
| Figure 6-4  | EVAL6235N low pass-filters for the reference voltage .....                   | 120 |
| Figure 6-5  | Encoder HEDL 5540 functional characteristics .....                           | 120 |
| Figure 6-6  | Encoder interface schematic.....   | 121 |
| Figure 6-7  | Encoder timing schematic .....   | 121 |
| Figure 6-8  | Schematic illustration of main actuator closed loop control system.....      | 122 |
| Figure 6-9  | Schematic illustration of the M/T speed measurement method.....              | 124 |
| Figure 6-10 | Speed fluctuation for pulse timing and pulse counting methods.....           | 125 |
| Figure 6-11 | PI Controller loop ultimate gains for the 2040 rpm .....                     | 129 |
| Figure 6-12 | Block diagram of the hybrid oscillator.....                                  | 130 |
| Figure 6-13 | Schematic of the hybrid demodulator circuit .....                            | 130 |
| Figure 6-14 | Circuit schematic for the 5 V <sub>DC</sub> output and 5 kHz frequency ..... | 131 |
| Figure 6-15 | Layout of the surface fatigue data processing.....                           | 131 |
| Figure 6-16 | L293D dual motor driver board for driving the peristaltic pump.....          | 132 |
| Figure 6-17 | Pump brushed DC motor control algorithm .....                                | 133 |
| Figure 6-18 | Heating system accessories connection layout.....                            | 134 |
| Figure 6-19 | Temperature sampling algorithm flowchart .....                               | 135 |
| Figure 6-20 | dsPIC33FJ256GP710A DSC UART serial port.....                                 | 136 |
| Figure 6-21 | RS 232 Communication sub routine .....                                       | 136 |
| Figure 6-22 | Schematic of embedded software functional relationship.....                  | 137 |
| Figure 6-23 | Combined pulse timing and counting algorithm flowchart.....                  | 139 |
| Figure 6-24 | Sensors ADC sampling algorithm.....  | 143 |
| Figure 6-25 | Block diagram of the LVDT online and offline features extraction ...         | 144 |
| Figure 6-26 | Schematics of GUI program and device interface.....                          | 146 |

|                |   |     |
|----------------|---|-----|
| Figure 6-27    | LabVIEW and DSC serial communication algorithm flowchart .....          | 146 |
| Figure 6-28    | Schematic of VISA Event serial data communication .....                 | 147 |
| Figure 6-29    | Schematics of GUI program and device interface.....                     | 148 |
| Figure 7-1     | Interaction and layout of mechatronic sub-systems .....                 | 151 |
| Figure 7-2     | BLDC motor for the actuator speed profile curve .....                   | 152 |
| Figure 7-3     | Sequence of operations of the mechatronic measurement system.....       | 154 |
| Figure 7-4     | Re-calibrated SM1 LVDT transducer and hybrid modules plot. ....         | 156 |
| Figure 7-5     | Accelerometer mounted on the specimen carriage .....                    | 156 |
| Figure 7-6     | Accelerometer time history .....  | 157 |
| Figure 7-7     | Contact load versus load cycles to failure from experimental data ..... | 161 |
| Figure 7-8     | Pre and post test appearances of Synergy D6 dental composite .....      | 163 |
| Figure 7-9     | Mitutoyo surface profilometer suite.....                                | 164 |
| Figure 7-10    | Schematic illustrations of the profilometer measuring method.....       | 165 |
| Figure 7-11    | Effects of testing conditions on the surface contact fatigue.....       | 167 |
| Figure 7-12    | Illustration of the overlapping curing method .....                     | 167 |
| Figure 7-13    | Effects of contact load on surface fatigue .....                        | 170 |
| Figure 7-14    | Peak amplitude as function of load cycles .....                         | 172 |
| Figure 7-15    | Root mean square (RMS) as function of load cycles .....                 | 173 |
| Figure 7-16    | Crest factor as function of load cycles .....                           | 173 |
| Figure 7-17    | Kurtosis as function of load cycles.....                                | 174 |
| Figure 7-18    | LVDT transducer raw digitized data .....                                | 175 |
| Figure 7-19    | LVDT transducer moving average filter data.....                         | 175 |
| Figure 7-20    | Frequency domain plot at 0 load cycles .....                            | 177 |
| Figure 7-21    | Frequency domain plot at end of 600,000 load cycles .....               | 178 |
| Figure 7-22    | Frequency domain plot at end of 1,000,000 load cycles .....             | 178 |
| Figure 7-23(a) | Waterfall plots for Synergy D6 flow dry testing at 20°C.....            | 180 |
| Figure 7-23(b) | Waterfall plots for Synergy D6 flow lubricated testing at 20°C .....    | 180 |
| Figure 7-23(c) | Waterfall plots for Synergy D6 flow lubricated testing at 37°C .....    | 180 |
| Figure 8-1     | New mechatronic surface fatigue measurement system .....                | 190 |

## LIST OF TABLES

|           |   |     |
|-----------|---|-----|
| Table 2-1 | Current Unfilled polymers and composites.....                             | 11  |
| Table 2-2 | Mechanical and physical properties of dental materials .....              | 12  |
| Table 2-3 | Physical and mechanical properties of dental composites .....             | 14  |
| Table 4-1 | List of used mechanical properties of ruby ball and dental composite..... | 64  |
| Table 4-2 | Static contact deformation parameters and stress for a load of 2.5N.....  | 68  |
| Table 5-2 | DMA for evaluating the mechatronic device frame .....                     | 95  |
| Table 5-4 | Decision matrix table (DMA) for selecting optimum DC servo motor ....     | 99  |
| Table 5-5 | Decision matrix table (DMA) for evaluating heating system .....           | 105 |
| Table 6-1 | Semiconductor technologies evaluation matrix .....                        | 113 |
| Table 6-2 | Summary of the key dsPIC33FJ256GP710A specifications.....                 | 114 |
| Table 6-3 | Ziegler-Nichols method mathematical expressions .....                     | 129 |
| Table 7-2 | Summarized layout of experiments and test variables.....                  | 160 |
| Table 7-3 | Description of the dental composite materials used in the test .....      | 162 |
| Table 7-5 | Synergy D6 Universal reproducibility indicators by ANOVA analysis .       | 168 |

## CHAPTER 1 INTRODUCTION

Tribological interactions during chewing, working, relaxing, and sleeping subject both natural and artificial (false) teeth in the oral cavity to complicated wear processes involving abrasion, adhesion, attrition, corrosion, fretting and fatigue [Mair,1996; Zhou and Zheng, 2008]. Figure 1-1 illustrates the complexity of the oral interactions, effects and related wear outcomes. Of these, surface contact fatigue and its causal mechanisms are still not fully understood and research is ongoing to establish their contribution to the overall dental structure's failure. Intrinsic difficulties in evaluating *in-vivo* surface contact fatigue have motivated this study to investigate the development of an *in-vitro* method to measure online surface contact fatigue of dental composites. The focus on dental composites is due to the fact that they are now commonly used materials in dental restoration and failure patterns are often too elusive to allow conclusions to be drawn from one dimension of application characteristics in the oral cavity.

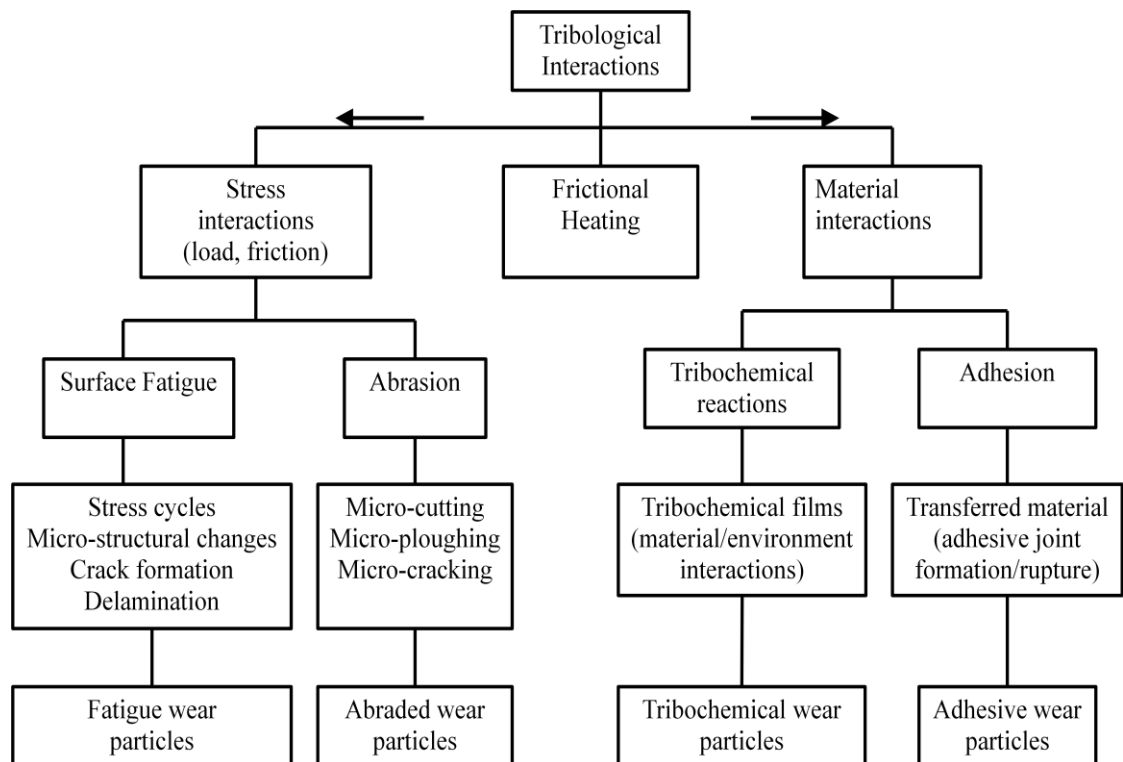


**Figure 1-1** Oral interactions and wear mechanisms [Czichos, 1986]

It is important to isolate dental wear mechanisms in order to measure the contribution of each in a controlled manner. Although extensive studies have been conducted to

establish wear in dental composites using *in-vivo* and *in-vitro* methods, earlier focus tended to be on the characteristics of abrasive, adhesive, compression and flexural failure, including the development of devices to simulate wear and failure arising from these mechanisms [De Gee and Pallav, 1994; Mair, 1994; Condon and Ferracane, 1996, and Mehl et al, 1997; Heintze et al, 2005; Lambretch et al, 2007; De Souza et al; 2012]. On the other hand, it has been established that frequent and intermittent contact of antagonist teeth may prompt the development of surface and subsurface micro-cracks which eventually lead to surface contact fatigue [McCabe et al, 1997; 2000; Baran et al, 2001; De Souza, 2012]. The limitations of *in-vivo* simulation technology have necessitated the development of cost effective, adaptable and user-friendly intelligent devices to monitor and measure the surface contact fatigue of dental composites *in-vitro*.

Alternatively, finite element analysis (FEA) has been developed in the past few decades as a very strong tool for the analysis of complex engineering and structural interactions in order to characterize the nature and mechanisms of deformation, including induced stresses and strains. Advances in the development of powerful and efficient computer technology and the implementation of finite element method (FEM) in user-friendly Windows-based programs have facilitated the realization of the FEA approach. In other words, FEA is a numerical procedure for analyzing structures and continua. Problems analyzed using FEA are usually too complicated to analyze satisfactorily using the classical analytical method. FEA subdivides the mathematical model into disjoint components of simple geometry called finite elements [Cooks et al, 1988]. The response of each element is expressed in terms of a finite number of degrees of freedom characterized as the value of an unknown function or functions at a set of nodal points.

A key component of the surface contact fatigue modelling of dental composites is an understanding of the stresses encountered during service when two-body or three-body interaction causes failure on the surface of the dental restorations [Sadeghipour et al, 1994]. Therefore FEA is used to study and characterize the distribution of stresses around the cyclic contact loading so as to establish the characteristics of stresses due to deformation and associated failures. Using FEA, it is possible to establish the stresses accumulated in each load cycle and the overall damage occurring inside the dental composites, and consequently it is possible to optimise the actual conditions of the rolling-ball experiments.



## 1.2 Aim and Objectives

The aim of this research is to develop a real-time mechatronic rolling-ball device for testing surface contact fatigue of dental composites. Ultimately, a device suitable for more accurately testing dental composites will be manufactured and commissioned. The research aim will be achieved through the following specific objectives:

- (i) To review previous relevant research work on the human dental structure, dental composites and their physical and mechanical properties, methods and devices for testing dental composites, theories and principles of fatigue mechanisms in dental composites, and the modelling and analysis of surface contact fatigue so as to create a sound basis for the research.
- (ii) To use kinematic modelling to assess the influence of constrained rolling ball and surface variables on the experimental results by considering the misalignment of rotational and fixed axes of the rolling-ball device, including any effect of ball slip.
- (iii) To optimise the design and develop a mechatronic solution and software system for the rolling-ball device to meet the specifications and requirements for real-time testing of surface contact fatigue in dental composites.
- (iv) To design a condition-monitoring system for the testing environment, this includes temperature, lubrication and vibration monitoring in order to meet the ISO/TS 14569-2:2001 specifications for the testing of dental materials.
- (v) To undertake a comprehensive testing programme using the rolling-ball device and compare the experimental results with finite element analysis (FEA) prediction models of dental composites with regards to the dental composites' surface wear specifications.

## 1.3 Research Hypothesis

The *in-vitro* measurement of surface contact fatigue in dental composites is important in order to obtain realistic data concerning the surface wear resistance of the specific formulations of dental restorations. This could be achieved by developing a mechatronic testing device simulating the oral environment and having the necessary human-machine interface to facilitate the real-time monitoring and measuring process. Thus, the hypothesis asserts “*It is feasible to develop an intelligent mechatronic rolling-ball device to measure real-time surface contact fatigue in dental composites*” In the context

of this research, intelligence means ability to automatically acquire and process online surface fatigue measurements including displaying and storing on a graphical user interface (GUI).

#### **1.4 Significance of the Research**

The outcome of the research will be a convenient and affordable technology for testing surface contact fatigue (wear resistance) in formulated dental composites based on ISO/TS 14569-2:2001. Ultimately, the longevity of dental restorations will be improved and reduced restoration costs to patients. On the other hand, people with dental composite restorations may be protected from health disorders such as digestive problems, lack of fibre nutrients and vitamins; resulting from swallowing improperly chewed food due to worn out restorations and incorrect masticating forces and cycles. Equally importantly, there will be gain in terms of environmental protection and the reduction of carbon emissions by savings in the energy and materials used in manufacturing dental restorations.

#### **1.5 Overview of the Research**

Chapter 2 focuses on previous and recent research on dental structures and synthetic dental materials, with a focus on dental composites, methods and tests currently in use to evaluate their properties and wear. Theories of fatigue mechanism and its influence on dental composite failure are then reviewed, and the application of the rolling-ball technique to measure the surface contact fatigue of structured materials, including dental composites is discussed. The application of finite element analysis (FEA) models to predict and analyze the failure properties of materials is also included. The chapter concludes by providing a summary of the research reviewed.

The kinematic modelling of the rolling-ball geometry taking into account the parameters which influence the rolling-ball motion is explained in Chapter 3. The influence of speed, rotational axis alignment/and dental specimen misalignment on the accuracy of measurements and any effects of rolling-ball slips are presented and subsequently applied in improving the new design. Chapter 4 concentrates on FEA of the deformation mechanisms and prediction models on the fatigue life of dental composites under cyclic-rolling using ANSYS software. The models were used to simulate pre-loading

and post-loading on the deformation of dental specimens with relation to the surface contact fatigue of dental composites.

Chapters 5 and 6 discuss the re-design and development of the mechatronic rolling-ball device. This includes the development of the mechatronic hardware and software systems to enable real-time testing and data acquisition from the sensor modules. Details of the re-designed systems and parts are elaborated precisely. The design of temperature and lubrication modules to simulate the human oral cavity is also detailed. The development and integration of the embedded and GUI software are described in Chapter 6.

Chapter 7 presents set-up and operation of the mechatronic rolling ball device. It also includes a comprehensive testing programme to qualify and validate the system performance, including quantitative analysis of the experimental results and comparison of the predicted and actual fatigue life of the dental composites. Chapter 8 evaluates and discusses qualitatively the performance of the mechatronic rolling-ball devices as a new technology for measuring the surface contact fatigue of dental composites. Chapter 9 provides the conclusions of the study and offers recommendations for future work based on the current research findings.

## CHAPTER 2 LITERATURE REVIEW

This review gives an overview of the human dental structure and synthetic dental materials, with an emphasis on dental composites and their properties followed by insight into suitable methods for testing them. Details of fatigue failure mechanisms and their manifestation in dental composites are discussed. Previous research on the application of rolling-ball devices to investigate the wear properties of materials, and in particular dental composites, are discussed. There is also a section detailing the use of finite element analysis (FEA) to predict and validate the fatigue wear of materials using different techniques. Finally, a summary of the literature review is given.

### 2.1 Human Dental Structure

Natural teeth (enamel and dentin) and most restorative materials are essentially layered structures. The natural tooth shown on Figure 2-1 has a unique layered structure composing mainly of three parts: enamel, the dentine-enamel junction and dentine and pulp. Each of the parts is anisotropic [Berkovitz et al, 1977]. The enamel part of natural teeth is the hardest known tissue in the human body and contains 92-96% inorganic substances, 1-2% organic materials and 3-4% water by weight [Gwinnet, 1992]. The natural dental structure comprises initially twenty (20) deciduous teeth in babies, which are replaced by thirty-two permanent teeth during childhood [Lewis and Dwyer-Joyce, 2005]. The teeth are arranged in two opposing arches in the mouth to facilitate shearing (incisor teeth), holding prey (canine teeth) and chewing (molar teeth). A quadrant of human tooth orientation is shown in Figure 2-2.

Unavoidably, pathological factors, traumas and tooth lesions cause partial or complete tooth loss. Restorations, including dental filling materials are used to fill and repair tooth lesions such as caries and cavities and/or fully replacing a tooth loss. Restorations are also used for cosmetic purposes such as reconstruction of anterior teeth and correction of stains and erosions. Therefore, materials for restoring tooth loss or fill lesions on a natural tooth structure have been in constant development for over 200 years [Upadlhyay et al, 2006, Bharti et al, 2010]. Nevertheless, dental composites for restoring tooth loss or filling lesions on a natural tooth structure were introduced in early 1960s as an alternative to amalgam restorations [Bowen and Rodriguez, 1962].

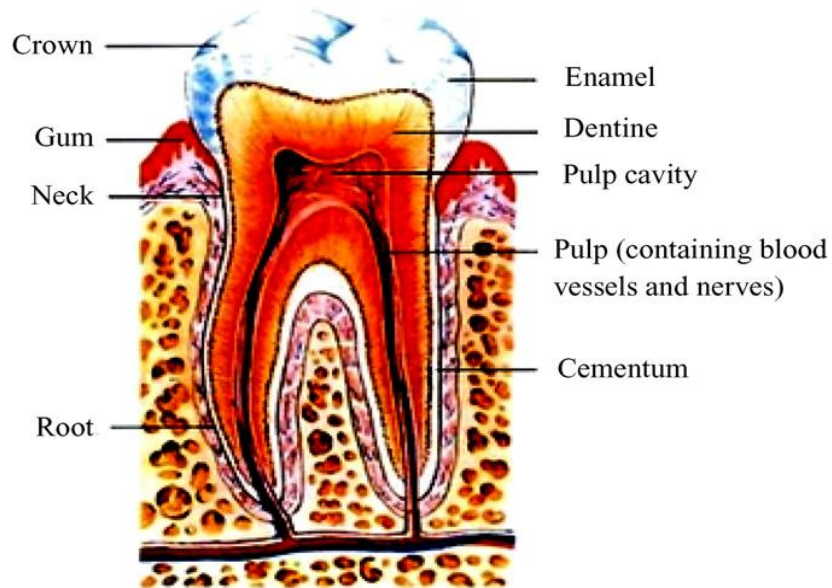


**Figure 2-1** Natural tooth structures [Zhou and Zheng, 2008].

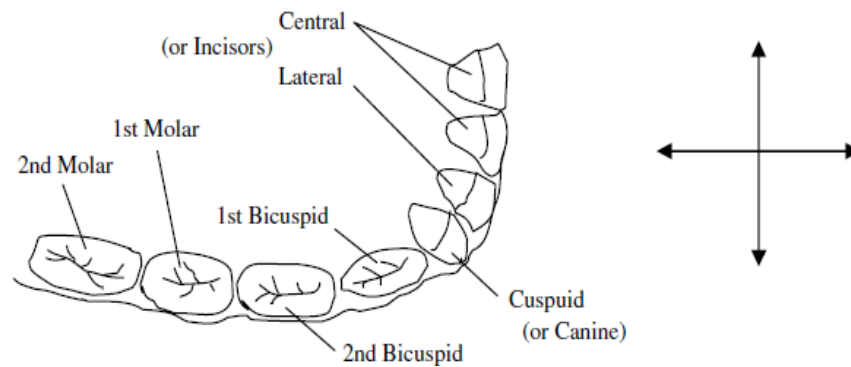


**Figure 2-2** Illustration of the dental structure layout [Lewis and Dwyer-Joyce 2005].

Dental restorations are broadly grouped into two classes:

- (a) Indirect restorations involving outside preparation of the restorations (i.e. inlays, onlays, crowns, veneers and bridges) in the laboratory.
- (b) Direct restorations in which the restorative material is applied *in-situ* into the tooth cavity. Materials used for direct restorations include amalgam, glass ionomers and dental composites.

Figure 2-3(a) shows direct molar restorations using polymer composites (white fillings), with appearances matching those of the natural teeth. Figure 2-3 (b) shows a comparison of amalgam and dental composite fillings in different oral applications in

order to appreciate their aesthetical appearances [[www.crossbankdental.co.uk](http://www.crossbankdental.co.uk)-accessed on 12<sup>th</sup> March, 2014]. The amalgam fillings can be easily detected by their colour whereas it is not easy to distinguish the natural teeth from the dental composite fillings. Although dental composites are now the most favoured dental restorative materials, still there is a limited application of metallic alloys (i.e. amalgam) and pure ceramics. The choice of dental restorative materials depends on factors such as biocompatibility, corrosion behaviour, and mechanical properties including strength and wear resistance, cost, availability and user preferences, the latter being mostly aesthetic [Zhou and Zheng, 2008].



(a) Dental composite restoration of the molars



(b) Aesthetical comparison of dental composite and amalgam restorations

**Figure 2-3** Applications and appearances of amalgam and composite restorations

## 2.2 Dental Composites

Dental composites refer to a mixture of two or more classes of materials in paste. They are complex, tooth-coloured filling materials composed of synthetic polymers, particulate ceramic reinforcing fillers, and molecules which produce the cross-linked polymer matrix from the dimethacrylate resin monomers and silane coupling agents which bond the reinforcing fillers to the polymer matrix [Ferracane, 1995]. The most

commonly used resin monomers are bisPhenol A-glycidyl methacrylate (BIS-GMA), urethane dimethacrylate (UDMA), and triethylene glycol dimethacrylate (TEGDMA). In order to facilitate polymerization, initiators sensitive to visible light are used.

Nowadays, dental composites are widely used as alternative to amalgam and ceramic restorations due to their good physical, mechanical, bio-compatibility and aesthetic properties [Chimello et al, 2001]. This has led to the progressive development and availability since their appearance in the mid-1960s of many brands in the market with different formulations, processing methods, and physical and mechanical properties [Randall and Wilson, 1999]. The composition of dental composites is critical for the best performance and longevity of the dentition. The first resin-based restoratives were mainly unfilled resins (called polymers) and their use was confined to dental adhesives and direct restorative materials in anterior teeth, due to their material properties being inadequate for other purposes [Nicholson, 2000; Lewis and Dwyer-Joyce, 2005]. However, significant improvements in dental composite formulation have extended their application to posterior teeth. Currently, dental composites have a variety of fillers, such as fused silica, quartz and radiopaque silicate particles based on the oxides of barium, strontium, zinc, aluminium and zirconium [McCabe and Walls, 2008].

The fillers improve the properties of dental composites such as strength, hardness and wear resistance. They also reduce polymerization shrinkage and thermal expansion, provide radiopacity, and enhance aesthetic and handling characteristics [Chung, 2008]. Thus, tooth-coloured resin matrix composites containing filler particles are now available for the restoration of posterior stress-bearing cavities as a viable alternative to amalgam [Upadhyay et al, 2006; Prakki et al, 2005]. Due to the major influence of the fillers on the properties of dental composites; their classification is now based on the type of filler used and the particle size thereof [Moszner and Salz, 2001; Cheng, 2008]. Three main classes of dental composites are now based on particle size and distribution: the macro-filled or conventional; micro-filled; and hybrid composites (i.e. micro-and nano- types). These are as illustrated in Figure 2-4.

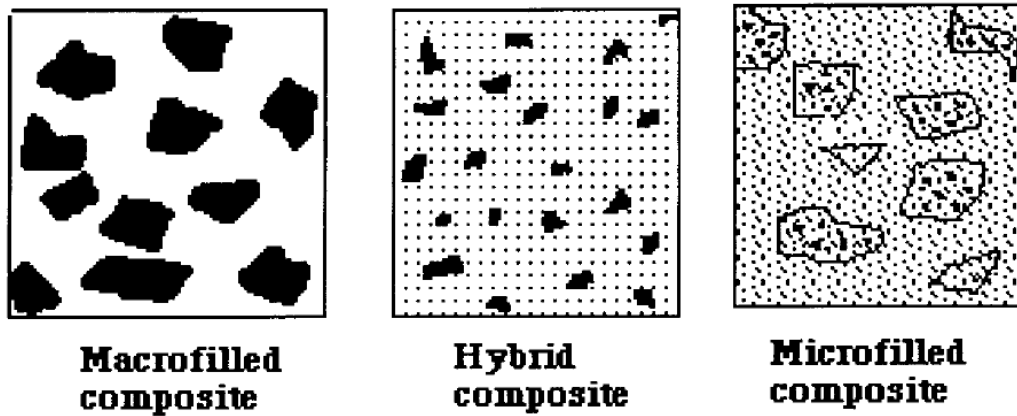


**Figure 2-4** Filler particles in different dental composites [Deb, 1998]  
(not to scale).

The increased variety of commercial composite brands in the market has made it more difficult to group dental composites into these three classes. Currently, commercial dental composites are classified by the type of filler components, which prompts periodically further development in dental composites classification based upon filler size and volume fraction. Microfilled composites have low modulus of elasticity and low fracture toughness. Hybrid composites have higher modulus of elasticity and fracture toughness.

On the other hand, polyacid-modified composite resins, known as compomers, were introduced to the dental profession in the early 1990s and are used for restoring teeth damaged by dental caries [Nicholson, 2007]. With biocompatible fibres and matrix systems, fibrous composites found application as biomaterials, and a number of such materials have been developed for dental applications [Fujihara et al, 2004]. These materials feature the advantage of good aesthetics for dental restoration and are able to bond to tooth structures easily using the acid-etch technique. Table 2-1 summarizes the existing categories of dental composite in the market.

Currently, dental composites are classified depending on their ability to flow. Packable dental composites are those with high viscosity, and they are used for replacing amalgam material in posterior application. In particular, they are used for making large fillings or total replacements of tooth tissue. Flowable dental composites are those used for filling small and/or deep cavities in tooth tissues and are required to easily flow [Abe et al, 2001].



**Table 2-1** Current Unfilled polymers and composites [Zhou and Zheng, 2008]

| Material type                          | Formulation/Processing method  | Typical application  |
|--|--|--|
| Lightly filled or Un-filled composites |  | Adhesives  |
| Macro-filled composites                |  |  |
| Micro-filled composites                | Homogenous micro-filled  | Restorations and crowns of anterior and posterior teeth; in lays and on lays |
|  | Heterogeneous micro-filled   |  |
| Hybrid composites                      | Composed of 70-80% glass fillers and 20-30% nano-fillers polyacid-modified | Obturation materials for dental caries                                       |
| Compomers fibrous composite            | Carbon fibres for the core and glass fibres for sheathing                  | Dental post, orthodontic arch-wires and brackets                             |
| Glass ionomers                         | Resin-modified   | Adhesives, obturation materials for dental caries                            |
|  | Metal-reinforced   | Adhesives, obturation materials for dental caries                            |

### 2.3 Physical and Mechanical Properties of Dental Composites

The physical and mechanical properties of dental composites are used to determine the suitability of the dental restorations in oral applications. Improvements in the formulation and processing of dental composites have significantly enhanced their physical and mechanical properties to match those of a natural tooth. Heintze [2010] conducted a comparative study of the physical and mechanical properties of contemporary dental resin composites, enamel and dentine, and found that properties of the dental composites match well with those of dentine and enamel. Exceptions found were the higher modulus of elasticity of enamel and the higher fracture toughness of dentine. On the other hand, dental composites have higher thermal conductivity than natural teeth. Table 2-2 presents comparative findings from different studies. However, clinical conditions require mechanical properties of restorations be somewhat less than that of natural tooth to prevent wear of the latter [Zhou and Zheng, 2008].

**Table 2-2** Mechanical and physical properties of dental materials [Heintze, 2010]

| Type of property  | Natural Enamel | Natural Dentine | Dental Composites |
|---|----------------|-----------------|-------------------|
| Hardness (micro hardness indentation) (GPa)             | 3.03           | 0.58            | 0.5-0.6           |
| Flexural strength (MPa)                                 | 141            | 172             | 90-170            |
| Compressive strength (MPa)                              | 384            | 297             | 250-400           |
| Tensile strength (MPa)                                  | 10             | 52              | 40-90             |
| Fracture toughness (MPa-m <sup>1/2</sup> )              | 0.77           | 3.4             | 0.6-1.4           |
| Young's modulus (GPa)                                   | 94             | 20              | 3-20              |
| Coefficient of thermal expansion (µm/m°K)               | 11.4           | 8.3             | 14-50             |
| Density (g/cm <sup>3</sup> )                            | 2.97           | 2.14            | 1.6-2.4           |
| Thermo-conductivity(W m <sup>-1</sup> K <sup>-1</sup> ) | 0.93           | 0.57            | 1.09-1.37         |
| Friction coefficient (µ)                                | 0.14           | 0.31            | 0.1-0.6           |

Mechanical properties play a significant role in clinical applications, and in the fatigue and failure of dental composites. Sadeghipour et al [1994] reported that, depending on filler composition and volume, dental composites exhibit an elastic state at room temperature and transforms to an elastic/plastic state at elevated temperature. He further concluded that high filler composition and volume influence brittleness behaviour, and that most dental composite have bilinear properties as depicted in Figure 2-5. So, the key components in studying surface contact fatigue are the types of stress and strain induced during service conditions under the influence of two-body (opposing dentition)

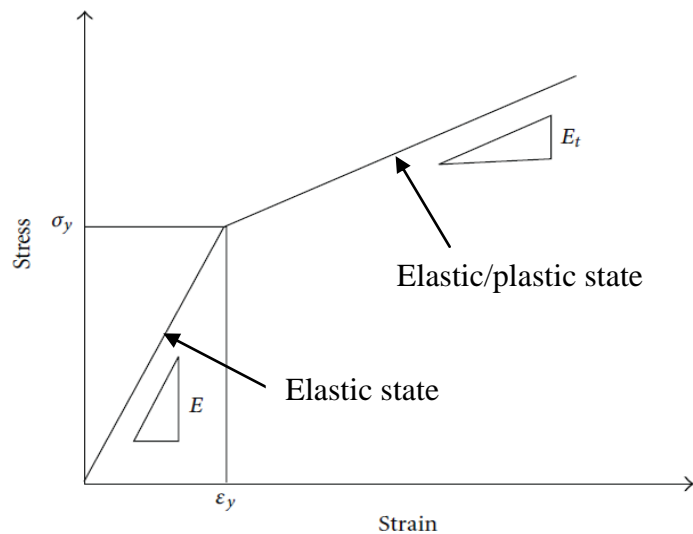


**Figure 2-5** Bilinear properties of polymer-based dental composites

Shrinkage was a major concern in early days of composites, due to the physical characteristics of the filler materials and the degree of polymerization. Such problems have been overcome due to a considerable minimization of the contraction exhibited by modern composites. This has been achieved by using large monomers and filler materials. The use of large monomers reduces the concentration of reactive groups, whereas the filler materials reduce the concentration of reactive species [Zhou and Zheng, 2008].

The absorption of water into composites leads to the release of free monomers and decreased fracture toughness and fatigue life [Barden et al, 1997]. Yield stress and fracture toughness have been reported to decrease by up to 30% if water is absorbed by dental composites. Venz and Dickens [1991] reported that swelling and shrinkage during polymerization and degree of curing are major causes of failure mechanisms in dental composites. They further stated that stress cracks and partial de-bonding increased opacity and altered the aesthetic appearance of dental composites. The leaching out of a composite's monomers may cause sensitization and allergies in some patients as well as the failure of the denture [Spahl et al, 1994]. The increase in stresses due to differences in levels of thermal expansion in the tooth and dental composite can cause fluid filtering at cavity margins [Zhou and Zheng, 2008].

Several studies have reported improvements in mechanical properties resulting from increases in filler volume and size. Xu et al, [2000] reported that increasing filler volume improves the fatigue and flexural strength of dental composites. In another study, Braem et al [2000] found that the modulus and hardness of composites consistently increases with increased filler volume. Garoushi et al (2007) reported that composite with fibre fillers of 3mm in length and 15-25 $\mu$ m diameter doubled flexural strength, increased the flexural modulus and tripled their flexural toughness as compared to micro-filled composites. This improvement was attributed to the ability of the fibre to withstand higher stress and the prevention of crack propagation.

The mechanical properties of the three classes of dental composites are given in Table 2-3 as guidance for comparing the mean values of the mechanical characteristics attained in each class. It has been observed that heavy-filled conventional composites suffer brittle fractures whereas decreasing the filler material can cause ductile fractures. Micro-filled composites with less than 50% of filler volume show yield points at

stresses lower than the fracture stress. However, the yield stress indicates an irreversible breakdown of the material. The amount, type and size of filler material control properties like hardness, roughness and abrasion. Although the characteristic hardness of resin and filler are not affected by the amount of filler, bulk hardness increases for a filled composite.

**Table 2-3** Physical and mechanical properties of dental composites [Anusavice, 1996]

| Property   | Conventional composites | Hybrid composites      | Micro-fine composites  |
|--|-------------------------|------------------------|------------------------|
| Tensile strength (MPa)                             | 50-60                   | 45-90                  | 30-50                  |
| Elastic modulus (GPa)                              | 8-15                    | 7-12                   | 3-6                    |
| Compressive strength (MPa)                         | 250-300                 | 300-350                | 250-350                |
| Hardness (VHN)                                     | 60                      | 70-90                  | 60                     |
| Volume shrinkage (%)                               | 1.67-2.5                | 2.5-3.7                | 3.0-5.0                |
| Water absorption(mg/cm <sup>2</sup> )              | 0.5-0.7                 | 0.5-0.7                | 1.4-1.7                |
| Coefficient of thermal expansion ( <sup>o</sup> C) | 32x10 <sup>-6</sup>     | 30-50x10 <sup>-6</sup> | 50-70x10 <sup>-6</sup> |
| Thermal diffusivity (mm <sup>2</sup> /s)           | 5.0                     | 0.68                   | 0.69                   |

In conclusion, the excessive wear of composite restorations is still a major problem encountered in their use in stress-bearing applications, despite the significant improvements already made [Hu et al, 1999; Yap et al, 2002]. Compared to amalgam and ceramic materials, dental composites still have higher wear rates. This underlines the importance of testing their mechanical properties prior to use.

## 2.4 Tribological Wear Behaviour of Dental Composites

The tribological wear of dental structures develops due to abrasion, adhesion, attrition, corrosion, fretting and fatigue. Studies by Wilson [1990]; Craig [1997] and Kemp-Scholte and Davidson [1998] have established that dental restorative materials within the oral cavity are subjected to severe dynamic situations as a consequence of adverse conditions. The resulting surface wear is due to the complexity of oral the environment and the geometric diversity of the mouth's cavity filled with restorative materials. Accordingly, factors likely to influence the wear of dental composites are the loading force, the size, shape and hardness of the fillers, the strength of the bonding between

fillers and the polymer matrix, the degree of the polymerization, and friction between contacting materials [Heintze, 2010]. However, it is difficult in most scenarios to perform *in-vivo* simulations in order to precisely determine from the wear pattern of the mechanisms promoting the wear. Even so, natural teeth and dental restorations wear could be grouped into physiological wear (vital functions), pathological wear (disease or abnormal conditions), prophylactic wear (preventive conditions) and finishing procedure wear [Powers and Bayne, 1988].

It is important that dental restorative materials have a high resistance to wear so that dental restorations can last longer and look aesthetically acceptable.. Studies by Condon and Ferracane [1997], Pavinee et al [2010], and De Souza et al, [2012], have linked the loss of anatomical shape of posterior restorations with masticatory abrasion, adhesion, compression and attrition. On the other hand, studies by McCabe et al [1997; 2000], Fujii et al [2004] and De Souza et al [2012] have reported that surface contact fatigue of antagonist teeth is the major cause of loss of shape in composite restorations. Nevertheless, there have been efforts to optimize dental composites so as to improve their wear resistance. Nowadays, dental composites are wear-resistant except for wear that occurs on the occlusal contact area (OCA) as shown in Figure 2-6 [Lambrechts et al, 2006; Heintze, 2010].

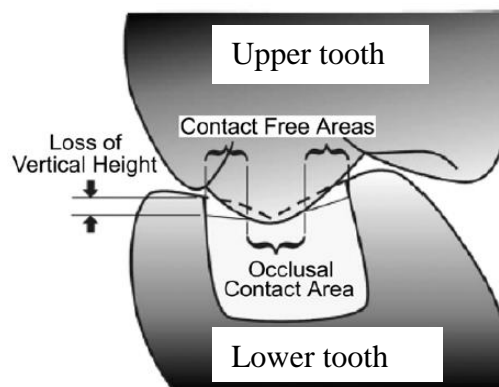


**Figure 2-6** Illustration of tooth occlusal contact and contact free areas [Zhou and Zheng, 2008]

Abe et al [2001] and Yap [2002] have investigated the wear of various dental “composites particularly in the OCA region, using *in vitro* sliding devices. The findings from both studies have shown that the rate of wear of antagonist dental restorations is a function of material composition and that there is a positive correlation between micro-

filled and mini-filled composites. Heintze [2010] concluded that abrasion and chemical degradation dominate the contact-free areas whereas fatigue and adhesive wear prevail on the occlusal contact area [Mair et al, 1996]. The wear pattern shown in dental composites is directly influenced by material composition.

## **2.5 Dental Composite Wear Testing Methods**

Several factors influence the wear pattern of dental composites such as fracture toughness, compression strength and compression fatigue limit, surface hardness, modulus of elasticity, and curing depth. There are three methods for studying the tribological wear behaviour of dental materials: *in-vivo* observation and measurement, *in-vitro* laboratory simulation, and *in-situ* testing. Clinicians use *in-vivo* testing to investigate the wear of teeth and restorations in the mouth. Tribology and dental materials researchers use the *in-vitro* laboratory testing to explore the wear mechanisms of both natural and artificial materials. *In-situ* testing is a newly-developed testing method for dental materials which overcomes the limitations of the other two testing methods [Zhou and Zheng, 2008].

### **2.5.1 *In-vivo* testing**

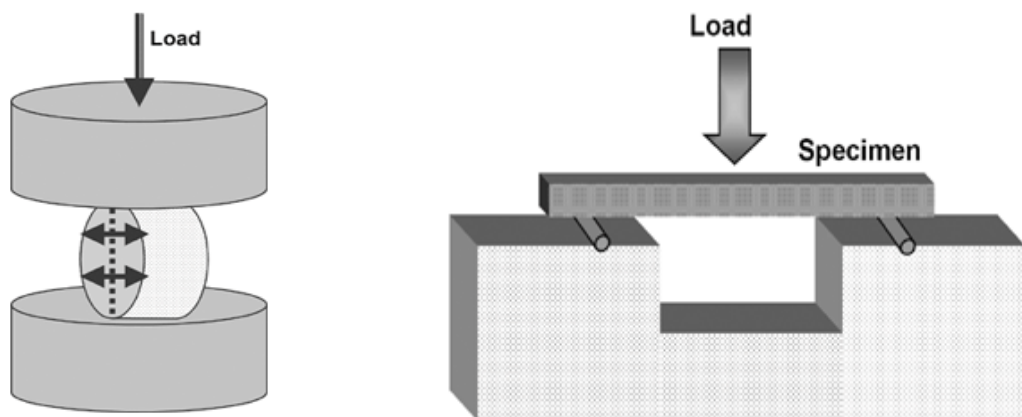
*In-vivo* testing is basically used in clinics. The method is used to examine and determine the tribological behaviour of teeth and restorations resulting from real oral environments and biomechanics [Dwyer-Joyce, 2005]; Lambrechts et al, 2006]. However, *in-vivo* methods cannot isolate and study individual wear processes such as attrition, abrasion, erosion and fatigue. Moreover, these methods cannot create a subjective environment for every wear process, thus making it difficult to interpret experimental data [Mair et al 1996].

Other difficulties with *in-vivo* methods include to controlling influential factors like chewing force, diet intake and environmental factors; hence significantly limiting the use of these methods to understand wear mechanisms [Taylor et al, 1994]. In addition, *in-vivo* methods cannot accelerate the wear processes, and any investigation depends on volunteer compliance, thus making the methods time-consuming and expensive [DeLong, 2006]. Studies by Smith and Knight [1984], Mair et al, [1996] and DeLong, [2006] have also established that *in-vivo* testing cannot accommodate suitably sensitive methods for

measuring the wear of restorations. In conclusion, ethical approval is required for *in-vivo* testing from relevant authorities, thus may prevent, limit or delay testing.

### 2.5.2 *In-vitro* testing

Given the limitations of *in-vivo* testing methods and the increasing diversity of synthetic dental materials, it has been necessary to develop *in-vitro* testing methods in order to predict the optimal clinical performance of restorative materials. Traditionally, *in-vitro* tests include those for tensile strength, diametral compression, compressive strength, flexural strength and hardness. Compressive and flexural strength tests have become the main *in-vitro* methods for establishing the fatigue resistance of dental restorative materials [Braem et al, 1994]. These methods involve testing cylindrical or beam specimens of materials by destruction through cyclic loading, as shown in Figure 2-7. However, studies conducted by McCabe et al [1997; 2000] and De Souza [2012] have shown that it is difficult to discriminate fatigue failure mechanisms of dental composites from the catastrophic fracture patterns resulting from the tests.



(a) Diametral compression test

(b) Flexural strength test

**Figure 2-7** Traditional dental material testing methods [Wang et al, 2003]

Consequently, simulation methods to mimic wear conditions in the mouth, such as the clinical masticatory circle and oral environment, have been developed and used since the 1940s to conduct the *in-vitro* evaluation of dental materials [Randall and Wilson, 1999]. The devices incorporate several liquids to simulate oral lubrication such as distilled water, alcohol, acid, olive-oil, olive-oil/CAF slurry, and artificial saliva with or without the inclusion of bacteria [Lambrechts et al, 2006].

In addition, wear simulation methods range from tooth-brushing devices, two-body wear and three-body wear devices. The tooth brushing machines use a tooth brush and dentifrice abrasion concept with a programmable brushing technique and path and a medium such as dry, wet and dentifrice abrasion slurry [Lambrechts et al, 2006]. The Relative Dentine Abrasion (RDA) technique developed by Hefferren is a well known *in-vitro* method to study toothpaste abrasion and is widely used by manufacturers [Hefferren, 1976]. A schematic of a Pepsodent tooth-brushing machine developed by the Precision Workshop of the University of Sao Paulo, Brazil used for the assessment of dental resin composites wear and surface roughness is shown in Figure 2-8.

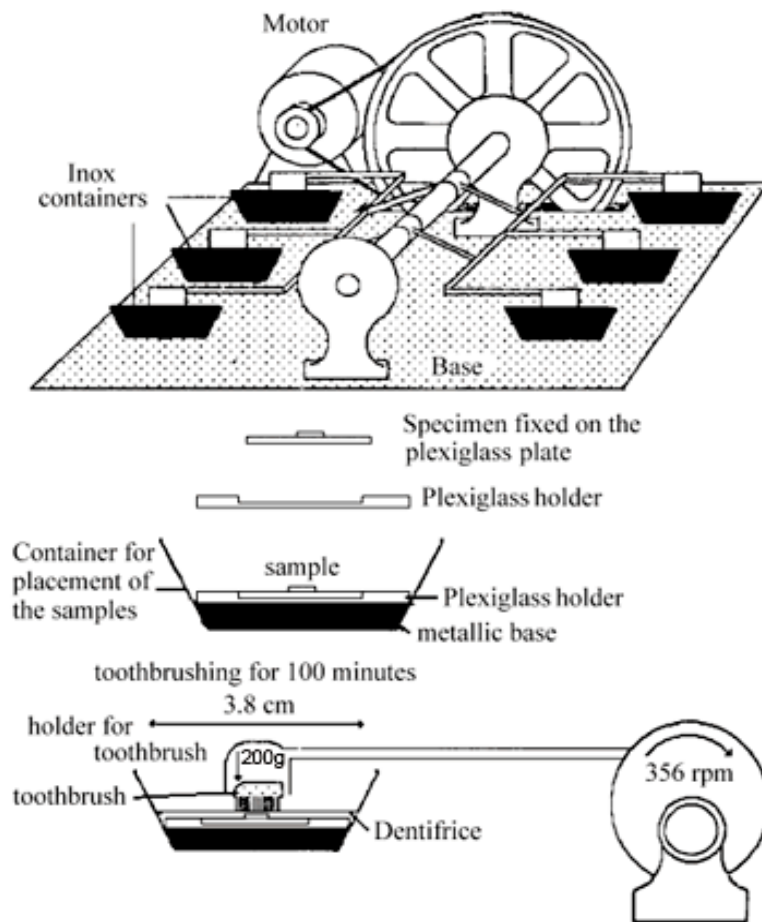
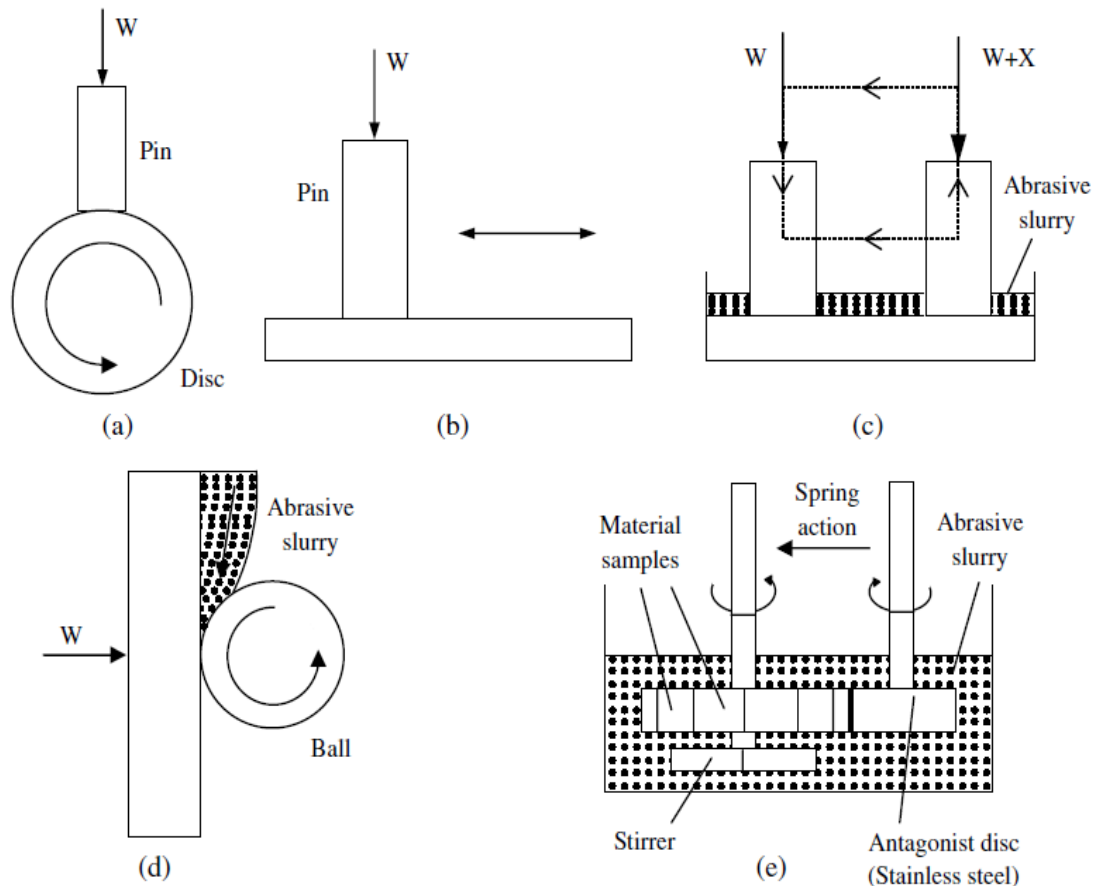


**Figure 2-8** Schematic of the tooth brushing machine [Chimello et al, 2001]

Several two-body wear simulators have also been designed and used with varying degrees of success in imitating clinical wear [Lambrechts et al, 2006]. These include the two-body abrasion single-pass sliding, two-body wear rotating counter sample, table abraser, two-body machine sliding wear, pin-on-disc tribometer, abrasive disc, oscillatory wear test, modified polisher and fretting test, and rolling ball devices [Zhong



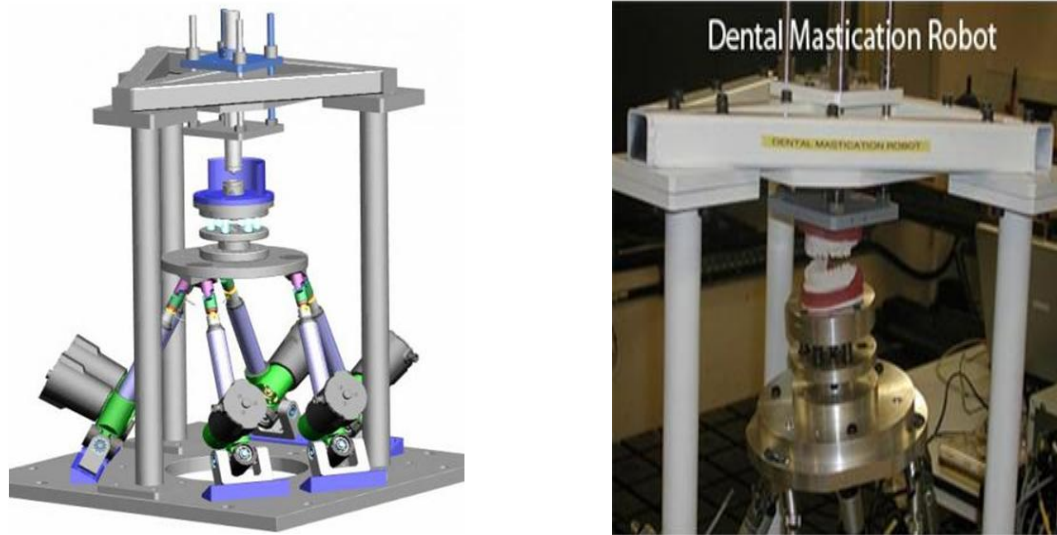
and Zheng, 2008, McCabe et al, 1997]. Illustrations of the two-body wear simulators are depicted in Figure 2-9 (a) and (b).



[(a) pin-on-disc (b) reciprocating (sliding) (c) one-way slide and static end load (d) ball and crate (e) two disc]

**Figure 2-9** Two-body and three-body dental wear simulator configurations Zhou and Zheng [2008.]

Moreover, a number of three-body wear simulators have been developed to stimulate masticatory abrasions which include abrasive slurry that act simultaneously with surface contact as shown in Figure 2-9(c-e). These are the Minnesota MTS wear simulator (i.e. an artificial mouth) [Sakaguchi et al, 1986], the four-stations Alabama three-body wear device [Leinfelder,1989], the Zurich computer-controlled masticator [Krejci et al, 1990], the ACTA wear machine [De Gee and Pallav, 1994], the Oregon Health Science University (OHSU) oral wear simulator [Condon and Ferracane,1996], BIOMAT wear simulator [Yap,1999], Willytec Munich (Muc3) [Kunzelmann et al, 2001] and Chewing robot [Raabe et al, 2009]. Virtual and physical models of the latter are shown in Figure 2-10.



(a)CAD model of the chewing robot (b) Physical model of the chewing robot

**Figure 2-10** Configurations of the Chewing robot [Raabe et al, 2009].

In conclusion, *in-vitro* testing enables much more control to be exercised over experimental variables, provides the opportunity for more accurate measurement and detailed investigation of the wear mechanisms of natural and restorative materials. More comprehensive evaluations of dental materials can be conducted in a shorter period of time in comparison with clinical trials [Lewis and Dwyer-Joyce, 2005]. Nevertheless, *in-vitro* methods use different test rigs with different contact geometries, loads, sliding speeds, lubricants and so on, making it difficult to compare the wear results obtained from different machines. On the other hand, wear simulators may accelerate wear rate than in actual clinical conditions, leading to a wrong conclusion. Moreover, the simulators are sophisticated and expensive; making them inaccessible to research institutions. Currently, there are less than ten wear simulators available in large research laboratories and dental composite manufacturers in Europe and America [Heintze, 2010]. Therefore, there is still room for the development of affordable and appropriate technologies to cater for medium sized dental laboratories and research institutions.

### 2.5.3 *In-situ* testing

An *in-situ* testing method has been developed by West and partners [West et al, 1998] to account between the limitations of *in-vivo* and *in-vitro* testing methods. During *in-situ* testing, specimens are mounted in devices worn in the mouth and finally removed for *ex-vivo* measurement [Lewis and Dwyer-Joyce, 2005]. This exposes the specimen to a natural oral environment and later permits the investigation of the wear process. The

experimental conditions are carefully controlled so that the effects noted can be ascribed to the agent under test [Hughes et al, 2002]. The technique uses sensitive devices such as a profilometer and scanning force microscopy to measure the loss of material from surfaces due to various factors, so that experiments could be conducted over comparatively short time periods.

## 2.6 Overview of Dental Composite Surface Contact Fatigue

The cyclic interactions in the posterior region of the mouth induce local stresses on the surfaces and sub-surfaces of a dental restoration. The nature of contact is initially non-conforming and slowly develops to a conforming type as the surface wear (failure) grows. This is the case because the contact junction is between the cusps and asperity tips of the new restoration. The progressive and localized structural damage on and below the contact area under cyclic loading is termed surface fatigue (surface wear) and is illustrated in Figure 2-11

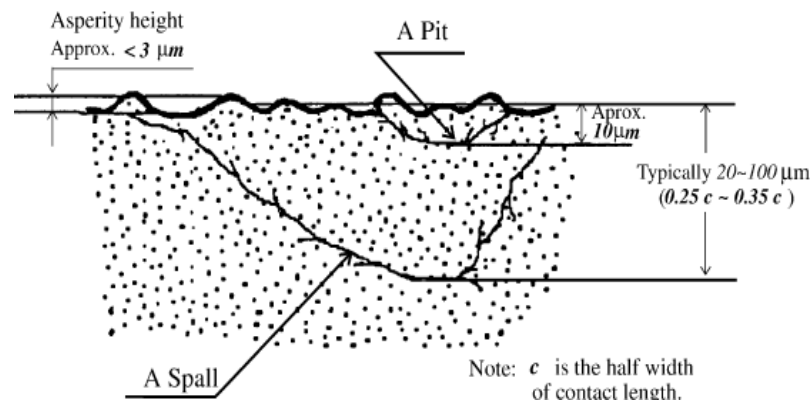


**Figure 2-11** Illustration of pitting and spalling phenomena [Ding and Riegler, 2003]

High concentrations of stresses and strains on the contact area initiate surface and subsurface cracks and voids which grow with time and coalesce to cause pitting and spalling failure. Over time, the deformation alters the nature of contact. Therefore, fatigue is the indication of material failure with time under the influence of stress or strain in static, dynamic and/or cyclic loading.

Fatigue in dental restorations manifests as wear, fractured margins, delamination of coatings and bulk failure. Fatigue has three stages of growth, namely: nucleation, propagation and the coalescence of the crack, as illustrated in Figure 2-12 in which the rate of crack growth per cycle ( $da/dN$ ) is plotted against change in intensity factor ( $\Delta K$ ).

Region I characterizes rapid crack growth after crack nucleation while region II characterizes subcritical crack growth (slow growth rate) in which crack direction is perpendicular to the tensile axis and is well correlated to stress intensity (linear characteristics), thus obeying the Paris law in equation 2.1 [Paris et al, 1961]:

$$\frac{da}{dN} = A\Delta K^m \quad (2.1)$$

where  $A$  and  $m$  are empirically derived constants:  $m$  is the slope of the curve and  $A$  is the coefficient of the intercept of the stress intensity axes. Region III characterizes rapid crack propagation and coalescence leading to pitting and spalling or fatigue failure.

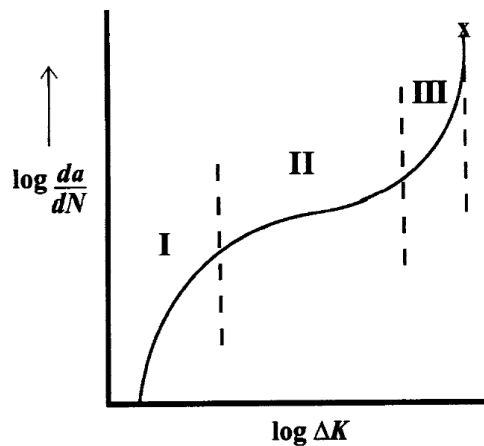


**Figure 2-12** Stages of fatigue growth in structured polymeric composites

The failure mechanism is always governed by material ductility, where brittle restorations (i.e. composites with large percentage volumes of fillers) suffer catastrophic failure, and ductile restorations (i.e. composites with large percentages of polymeric material) undergo plasticity in order to reduce stress concentrations at the crack area. Figure 2-13 illustrates the phenomenological approach of characterizing the fatigue life of dental composite based on subjecting a standard specimen or surrogate structures to a cyclic stresses or strains, and the outcome presented as plots of stress induced, change of stresses or ratio of maximum to minimum stresses, strain or change of strain against the logarithmic of the number of load cycles before failure or fatigue limit. Test variables include temperature, cyclic frequency and wave shape and environment (i.e. dry or wet). The outcome data plots take different form depending on the type and composition of the dental composites as characterized in Figure2-13 where plot (a) shows a polymeric composite exhibiting an endurance limit, plot (b) shows a polymeric

composite with no endurance limit, and plot (c) shows a polymeric composite without crazing characteristics. In addition to the conventional loading techniques such as tension-tension or compression-tension and so on, contact fatigue can be induced using cyclic loading of an indenter into the surface of a material because of its perceived relevance in the study of wear processes.

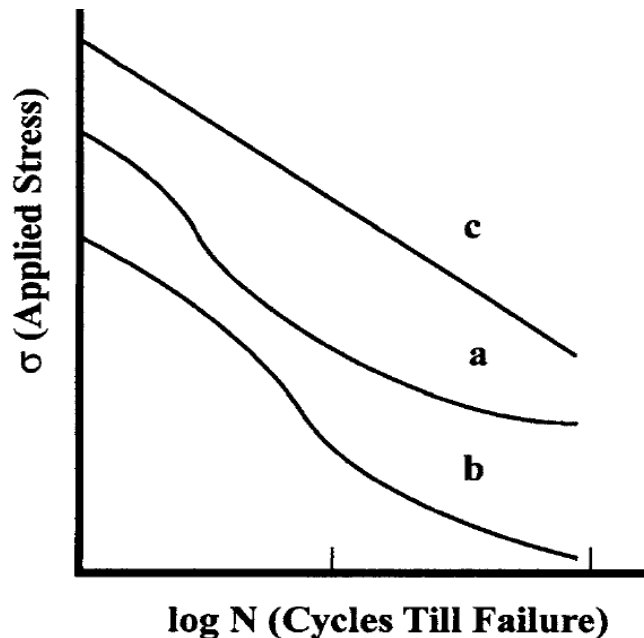


**Figure 2-13** Characteristic curves of polymeric composites failure [Baran et al, 2001]

However, a blunt indenter should be preferred to subject the specimen to a realistic loading mode combining compressive and tensile stresses in order to propagate the crack [Baran et al, 200]. In addition, the selection of the size of the indenter is important in testing polymer and polymeric composites. Indenters with a smaller diameter than the critical diameter of the polymeric material would produce plastic deformation of the material instead of cone -crack deformation [Baran et al, 1994].

Dental composites have random isotropic and amorphous structure of high-modulus, and brittle reinforcing fibres or particles dispersed in a quasi-brittle polymer matrix [Craig et al, 2002]. The strength of dental composites depends on the direction and method of transferring load from the matrix to the reinforcing phase. Depending on the type of reinforcement (i.e. particulate or fibrous), the direction of loading application, the strengths of the various phases and the interfacial strength, several mechanisms may participate in the fatigue failure of dental composite restorations.

These include matrix cracking, matrix deformation, void formation, multidirectional cracking, filler debonding and filler failure. Consequently, scatter in fatigue data for a composite is greater than in monolithic materials, where typically a single damage mechanism is presumed to be active. De-bonding at the filler matrix interface occurs in particulate-reinforced composites at low static stresses, producing a rough fracture surface, while at higher applied stresses which cause higher crack velocities; the crack propagates through the filler and matrix, resulting in a smooth fracture surface. In fibre-reinforced materials, cracks do not propagate for long within the matrix before reaching the fibre interface. Propagation continues along the interface; since the angular distribution of stresses at the crack tip in composites is determined by microstructure, not by the direction of the applied load.

Similarly, the speed of crack propagation is a function of stress intensity and microstructure. The strength gradient at the interface between matrix and filler determines crack growth rate. Due to the fact that a local matrix and interface failure surrounds a dispersed fibre, the fibre itself ruptures and this is followed by transfer of the fracture to neighbouring fibres which in turn rupture. Eventually, the whole composite fails by fatigue. Failure is sometimes localized within a specific area, and this damage is termed “brushed-like cracking” from which ultimate failure of the body proceeds [Bolotin, 1999]. Given a sufficient accumulation of micro-crack damage through the above mechanism, macro-cracks are initiated which thus change the compliance of the bulk composites.

The change in compliance is often useful in defining fatigue life, since the load-bearing capacity of the composite structure deteriorates well before actual failure through the specimen. Strength vs. cycles to failure (S/N) data can exhibit more than one change in compliance. Hence a final failure takes place over a wide variation in final crack sizes at higher applied stresses; short cracks are responsible for failure, while at low stresses, long cracks are responsible for failure. Usually, fibre-reinforced composites show lower fatigue resistance in compression than in tension, because of the cooperative buckling of adjacent fibres and matrix shear [Zhou and Zhong, 2008]. Researchers suspect that crack growth rate measurement may not be an appropriate design approach for predicting the lifetimes of composites, because of the wide variety of fatigue damage modes occurring within them [Baran,2001].

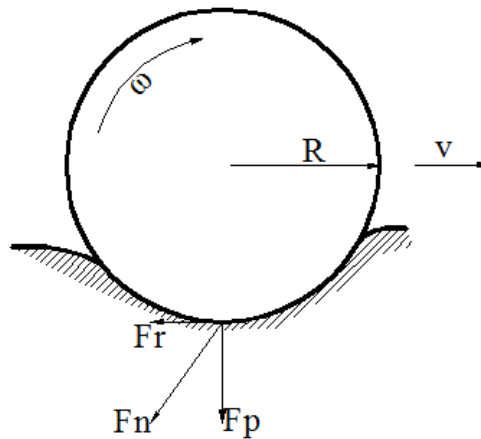
Lambrechts et al [1984] identified two distinct wear regions on posterior composite restorations resulting from abrasion and attrition. It has been further established by Lutz et al [1984] that the attrition wear region is based on the OCA, whereas the abrasion region is on a contact free area (CFA). Condon and Ferrecane [1997] established a combination of several wear mechanisms in the CFA, ranging from abrasion, adhesive and erosion depending on either two-or three-body contact. Similarly, the OCA region comprises a combination of abrasion, fatigue, and adhesion wear mechanisms. Studies by McCabe et al [1997; 2000], Yap [2002], Lambrechts et al [2006], De Souza, [2012] have emphasized that natural and restored teeth suffer contact fatigue (wear) after a period of time from direct contact between teeth, teeth and restoratives, or two restoratives. Other contributing factors are abrasive particles sandwiched between them during mastication, thegosis, bruxism and other functions [Zhou and Zheng, 2008] and cyclic compression stress on antagonistic teeth [Brandao et al, 2005; Shafie at al, 2009].

However, these studies neither quantify nor indicate how the contact mechanism influences the surface contact fatigue (wear) of dental composites in OCA. Therefore, the role of the antagonist tooth in influencing the wear of composite restorations is largely unknown.

## **2.7 Spherical Rolling Contact Application in Materials Characterization**

Rolling contact tests have been used extensively in engineering tribology to characterize surface wear and the wear mechanisms of materials, and to examine and determine the mechanical properties of parts moving relative to one another. The working principle is derived from resistance to roll, sometimes called rolling friction or rolling drag, which occurs when a spherical object such as a ball rolls on a flat surface. According to Hibbler [2007], the main cause of the surface wear of parts in motion is the deformation of the object and/or the surface on which it rolls. Other contributing factors are the object's radius and rolling speed, surface adhesion, and relative micro-sliding between the surfaces of the contact. Factors influencing the rolling contact mechanism are illustrated in Figure 2.14. Rolling is more preferred in characterizing surface wear of structured materials because of its simplicity in application, notably in inducing cyclic loading and localized surface wear on the material being tested. In addition, the circular rolling leads to a proportional smallest size of the test specimens, thus reducing experimental costs. Its relevance to dental composites surface wear testing is accounted

in section 2.8.



[ $F_p$ , light force acting on the ball;  $F_r$  frictional resistance force;  $F_n$ , normal reaction force;  $R$ , ball radius;  $\omega$ , rolling speed;  $v$ , translation speed]

**Figure 2-14** Factors governing spherical rolling contact on materials [Hibbler, 2007].

In tribology engineering, numerous studies have evaluated the surface contact fatigue of rolling ball bearings made from steel or ceramic composites using spherical contact mechanics and modelling. Recent studies of surface/rolling contact fatigue in ferrous and non-ferrous bearing materials were conducted by Zhou and Wu [2009], Miyazaki et al [2009] and Zhong-Yu et al [2010]. Besides this, studies on surface contact fatigue (wear) of polymeric and composite materials have used the rolling ball test to analyze mechanical properties related to the failure of these materials. Kocsis et al [2008] investigated friction, sliding and rolling wear characteristics of thermo-plastic dynamic vulcanizates (TPVs) using a steel rolling ball-on-plate (RBOP) tests rigs where the plate was made of a rubber material, as shown in Figure 2-15.

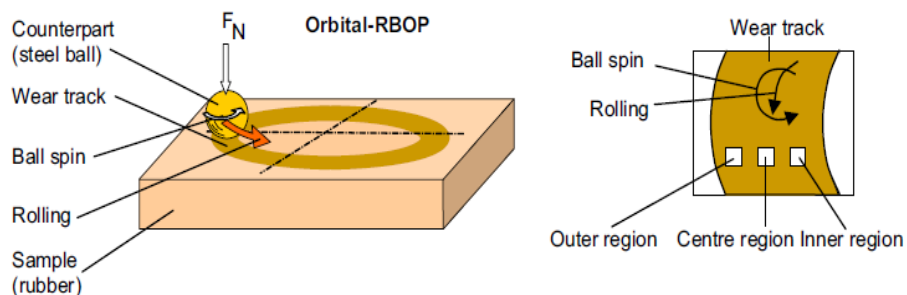


**Figure 2-15** Fatigue test of a polymeric material [Xu and Karger-Kocsic, 2010]

The composition and basic mechanical properties of TPV of varying hardness (Shore A=60°, 70° and 80°) were evaluated. The rubber sheet was worn by one steel ball



(100Cr6) with a diameter of 14 mm and roughness of 1  $\mu\text{m}$ . The ball rolls around a circular path of diameter 33 mm while being pushed against the rubber sheet with a load of 30 N. The test used 100 rpm for duration of 6 hours. The device recorded the COF as a function of time. Of interest in this research is the observed rolling motion. The ball rolled with a lateral spin due to a guiding groove in the upper steel plate. Xu and Karger-Kocsic [2010] reported that SEM photographs of the left and right flanks of the wear track showed different wear characteristics as a result of differences in motion. The rolling ball was superimposed by a friction spin forward (left) and backward (right flank area) respectively. Additionally, patchy patterns with pitting events due to the visco-elasticity and morphology of the polymer were noted, along with plastic deformation on the test groove resulting from the rolling backward spin.

Harrass et al [2010] studied the rolling wear behaviour of unfilled polyimide 6, polyoxymethylene and polyetheretherketone material using different wear testing rigs. In one test, a rolling ball (steel-on-plate) was rolled on the polymer plate surface with a rotational and linear motion as illustrated in Figure 2-16. The steel ball had a diameter of 6 mm and the specimen was 60 mm x 60 mm x 4 mm. The loads ranged from 100 N to 2000 N, and the results revealed three different motions evolving during the revolutions of the ball, which were: rolling on the circular path, rotation around its y-axis, and spinning around the z-axis. In the rolling test, wear on the surface of the polymer materials was initiated by inelastic deformations during rolling contact, as illustrated in Figure 2-17.

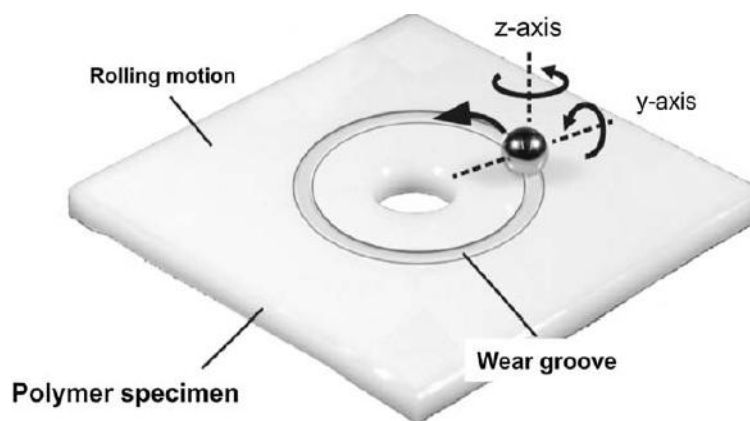
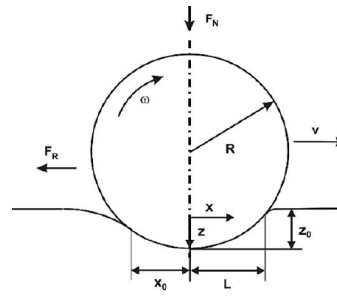


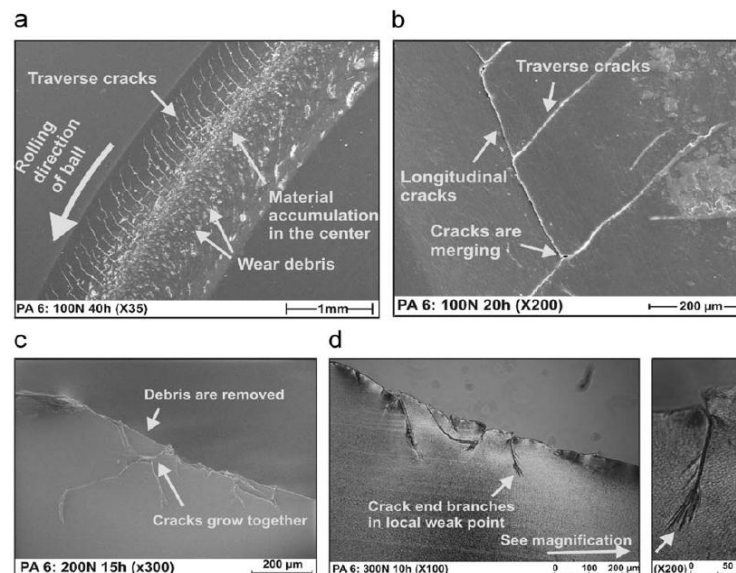
**Figure 2-16** Steel ball rolling on a polymer plate [Harass et al, 2010].



[where  $F_N$  is the normal contact force,  $F_R$  is the frictional resistance force,  $R$  is the radius of the ball,  $v$  is the translational velocity along the orbit,  $\omega$  is the contact rolling angular velocity,  $X_o$  is the sink-in length,  $L$  is the pile-up length and  $Z_o$  is the pile-up height]

**Figure 2-17** Factors influencing distortion mechanism in polymeric materials

Another interesting finding relevant to this study is the differences in wear analyzed by Scanning Electron Microscopy (SEM) which are shown in Figure 2-18. The centre of the groove exhibits an accumulation of wear debris, which evolves from the specific motions of the ball through its revolutions. The forced motions in an orbit cause spinning of the ball whereby the outer regions are worn more than the centre. Compressed particles are found on the inner side of the track, while on the outer area of the groove cracks are present, oriented perpendicular to the rolling direction of the ball, and originating from the centre and propagating to the outer wall of the groove.



[SEM photos of worn Sustamid 6: (a) wear groove in top view; (b) magnified wear groove; (c) polished cross section of the wear groove; (d) thin walled section taken from the groove transverse to the rolling direction [Harass et al, 2010]]

**Figure 2-18** SEM images illustrating wear characteristics of polymeric material

The conclusion drawn from these studies is that surface contact fatigue initiated by a rolling ball has variable patterns depending on its location. In addition the surface fatigue can result from pitting, delamination of the structured layers, fractured margins or the bulk failure (spalling) of the surface. Dental composites contain large proportions of polymer compounds and are likely to suffer surface fatigue by one of the failure mechanisms. Another conclusion is that the circular motion of a rolling ball constrained in a V-shaped groove is a complex phenomenon comprising translation along the circular path, rotation along the y axis, and spinning along the z axis. It is therefore important to discriminate between the components of orbital rolling motion in order to understand the beat frequency acquired by the data acquisition sensor in the rolling ball device for dental composites.

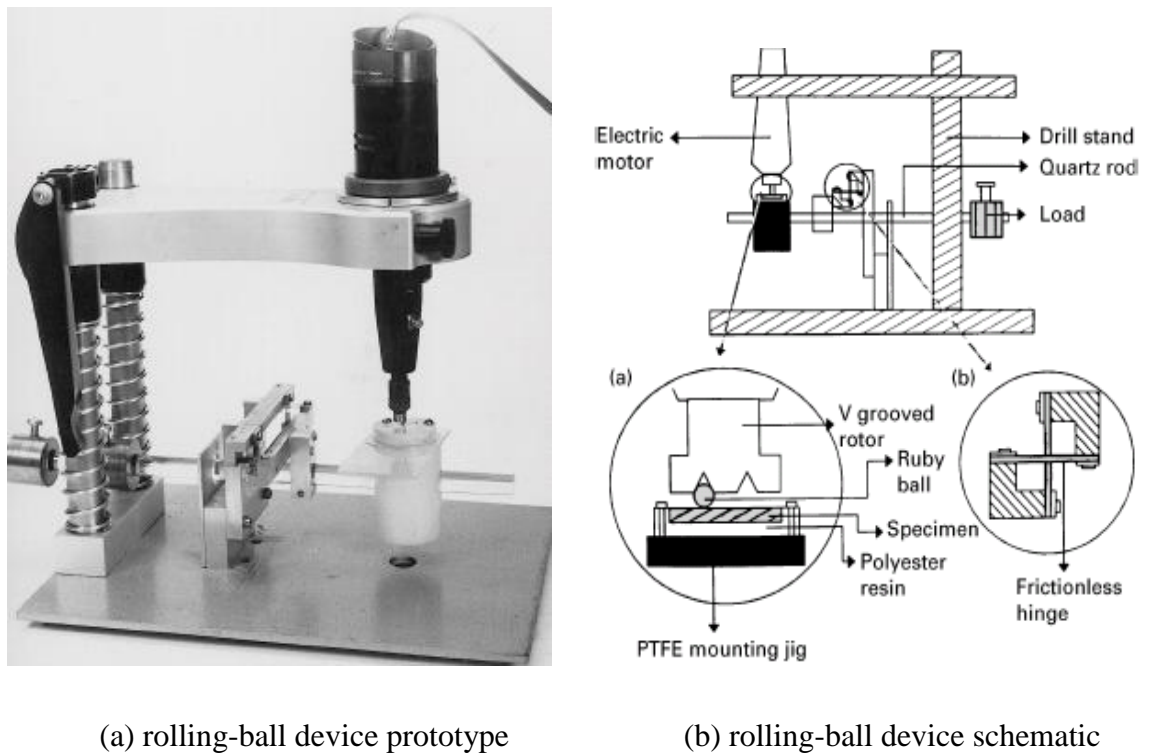
## **2.8 Use of Spherical Contact Rolling in Dental Composite Testing**

The use of spherical rolling contact in testing dental composites is quite rare, and few relevant studies have been reported. This can be attributed to the fact that surface contact fatigue was not regarded as source of failure in dental materials as compared to other sources of wear such as abrasion, adhesion, attrition and flexure. Realizing that the wear process of dental composites was partly due to surface contact fatigue, McCabe et al [1997] embarked on the development of a rolling ball device to simulate surface contact fatigue *in-vitro*. This was intended to overcome the shortcomings resulting from flexural fatigue simulators. Their typical shortcomings include a lack of correlation between the bulk catastrophic failure of specimens and loss of surface material by fatigue wear. Furthermore, the experimental procedures used to cause bulk fracture by fatigue, produce a large scatter in the results, leading to difficulties in establishing differences between materials or requiring very large numbers of test specimens to demonstrate such differences. On the other hand, the fatigue element of the degradation process has often proved to be the most elusive, due to the fact that the characteristics of surface contact fatigue cannot be readily understood from knowledge of bulk fatigue behaviour. McCabe explained that, when two surfaces are in regular intermittent contact, as is the case in the oral cavity, surface and subsurface stresses might eventually lead to crack propagation and loss of surface material due to fractures originating from the subsurface and surface cracks or flaws.

Accordingly, Ferracane et al [1992] established that the fracture and failure of dental

composites occur from a surface or subsurface crack or flaw oriented at an angle with respect to that of the applied load (i.e. modes I and II loading). In another study, Rodrigues et al [2007] established that fracture initiations in bar specimens, such as cracks, voids, inclusions or other defects, are caused by the processing of the dental composite or fabrication methods such as polishing and grinding. The cyclic loading of dental materials has become important due to the fact that dental restoratives in the oral cavity are subjected to repetitive masticatory forces. In addition, many dental restorative materials have shown susceptibility to cyclic loading, including ceramics, glass ionomers cements, fibre-reinforced resins and composites [Braem et al, 1994; Drummond et al, 1998; Bapna et al, 2002].

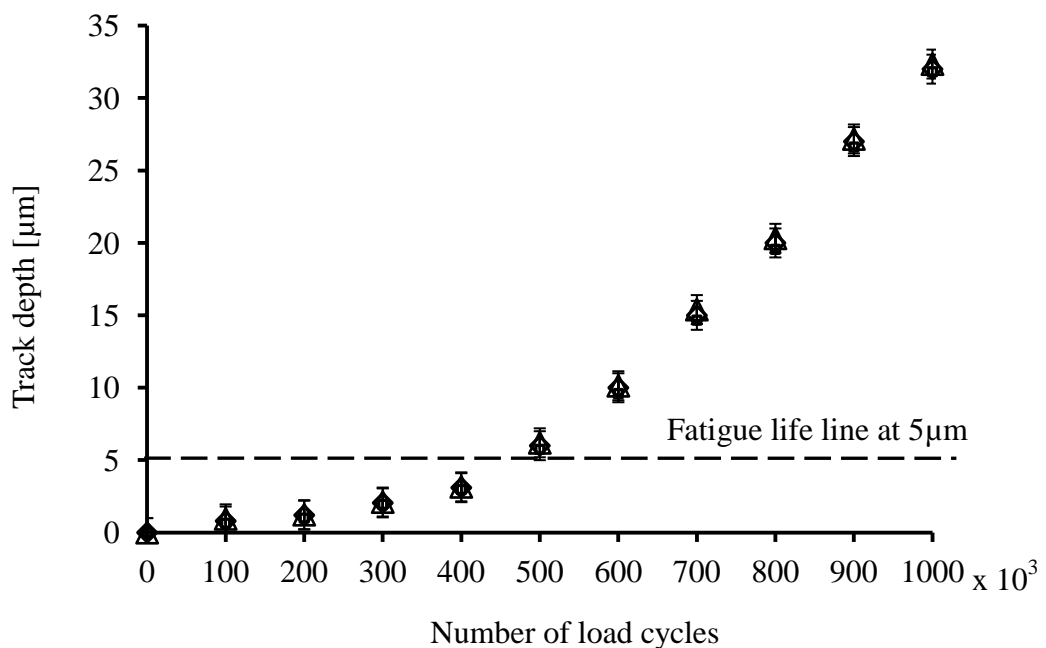
The classic cyclic rolling-ball device shown in Figure 2-19, developed by McCabe et al [1997], used a ruby ball which kept rolling on the flat surface of the specimen with a light compressive force applied. The use of a ball of 2 mm in diameter was intended to provide line contact and minimize friction at the indenter and specimen material interface. The ball was rotated at 2000 rpm approximately using a DC motor for a specific number of load cycles ( $1 \times 10^6$ ) in which the measurement of the fatigue track depth was performed periodically ( $1 \times 10^5$ ) as a function of time. The pre-compressive load of 200 g was achieved by balancing the spring and weight rod.



(a) rolling-ball device prototype (b) rolling-ball device schematic  
**Figure 2-19** Rolling-ball devices for dental composites fatigue [McCabe et al, 1997].

Two specimens, one with unsilanated filler and the second with silanated filler were used. The measured depth of fatigue track was plotted versus the corresponding number of load cycles, as shown in Figure 2-20. The plot shows that the experimental data are reproducible and that the fatigue life of dental composites varies with filler volume fractions, and appearing to be optimized at filler concentrations in the range of 30 to 50 vol%. At low-volume fractions, this could be explained by the relatively high cyclic deformations that occur beneath the rolling ball, eventually leading to micro-cracking. At extremely high volume fractions, there may be an element of increased brittleness leading to additional crack propagation.

The rolling ball device has been shown to have several advantages compared to traditional methods of measuring the surface fatigue of dental materials, and this has led to development of a prototype device at the Dental school, of the University of Newcastle.



(a) silanated glass filler indicating the reproducibility of the test results. Key: (o) Sample A, (□) Sample B, (Δ) Sample C. error bars represent 1% S.D. Linear-linear plot extrapolated from one of the log-linear plots in McCabe et al [1997]

**Figure 2-20** Fatigue track depth for the 57 vol% with silanated glass filler

Capitalizing on the achievements of the first rolling ball prototype, a second version was developed by the team to address the shortcomings of the first prototype as reported by Fujii et al, [2004]. In the modified instrument, loading is provided using a

deadweight and pulley arrangement, as shown in Figure 2-21, instead of the beam used in the previous rolling ball device.

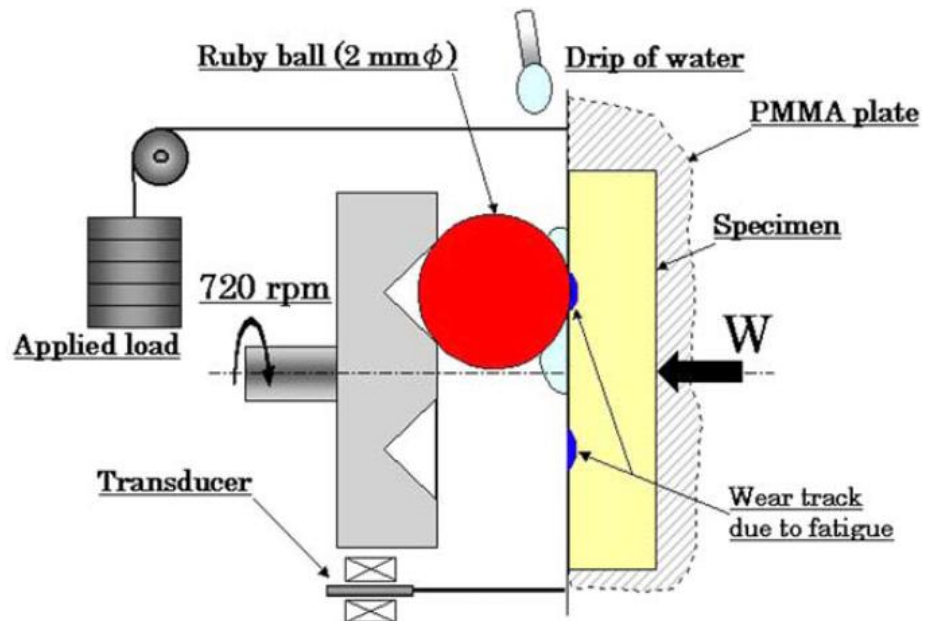


**Figure 2-21** Revised design of the rolling-ball device for measuring contact fatigue  
[Fujii et al, 2004]

The ball is constrained between a mandrel with a V-shaped groove and the test material and rotated at 720 rpm using a DC motor. The testing speed was reduced apparently to meet the electrical specifications of the motor, but was still 10x higher than chewing frequency. This led to a longer testing time and possibly reduced rolling dynamics and consequently less surface fatigue on the dental composite. The specimen and mandrel are maintained in a rigid alignment to avoid twisting and bending stress. Although an LVDT was incorporated in the device, wear measurements were carried out periodically using a profilometer due inability of the LVDT to acquire meaningful measurements. Two dental filling materials, a micro-filled composite (FA) and glass ionomer (GFII), were tested using the revised device. Fatigue life based on the number of load cycles to produce a track 5 $\mu$ m deep was determined by interpolation.

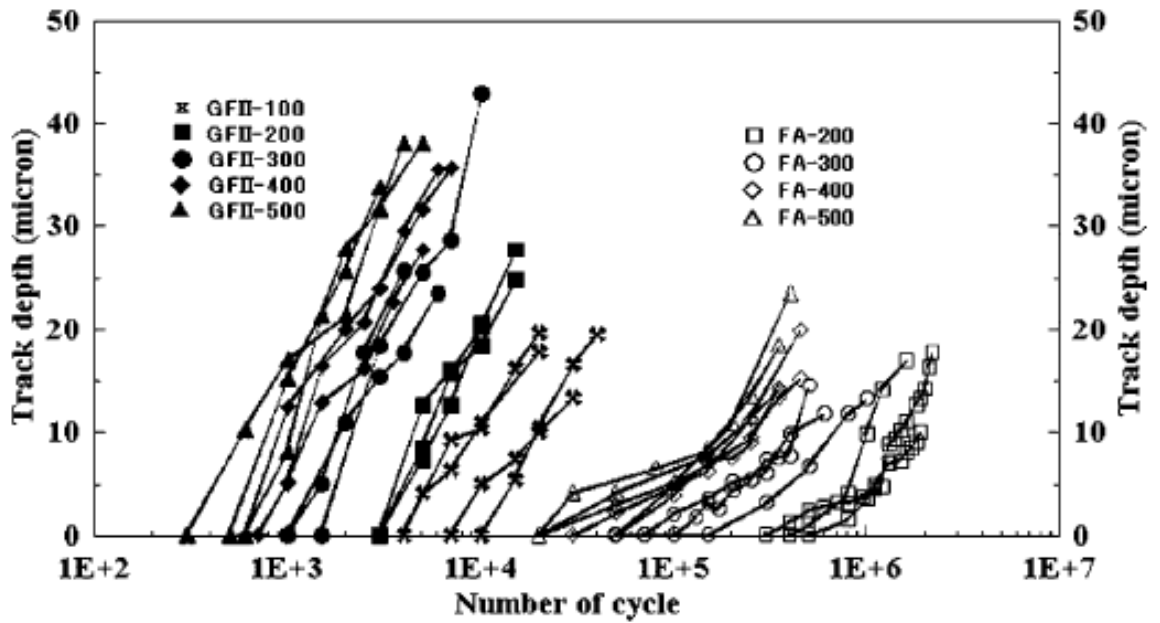


**Figure 2-22** Fatigue track depth against load cycles [Fujii et al, 2004].

Data were statistically analyzed using ANOVA and the T-test at a significance level of 0.05. The variation in wear track depth against number of load cycle for each dental composite is plotted in Figure 2-22. The results show that with loads between 2-5N, FA had a fatigue life ranging from  $0.4 \times 10^5$  to  $0.5 \times 10^5$  cycles, and GFII had a fatigue life of  $0.6 \times 10^5$  to  $1.0 \times 10^5$  cycles when loaded between 1N to 5N. As expected, fatigue life was significantly reduced when test load increased. It was also established that the surface contact fatigue life for FA is about 100 times greater than that for GFII at all loads. The findings from these experiments are considered more reliable and can be attributed to the point of contact perpendicular to the surface of the test specimen. It was concluded that the rolling-ball device is a simple and meaningful device for the study of surface contact fatigue.

However, the equipment has significant limitations, which have required re-engineering and innovations to meet the specifications required for testing the wear of dental materials under the influence of two-or three-body contact listed in ISO/TS 14569-2:2001. Offline measuring and evaluation of surface contact fatigue by manually profiling the wear track after every  $1 \times 10^5$  load cycles subjects the measurement to errors and reduces accuracy, and the open loop control system for the motor drive did not ensure the precise counting of the number of fatigue life cycles. In addition, the LVDT sensor output exhibited a beating oscillation which makes it difficult to digitize and

enable online data acquisition. Other shortcomings are the lack of oral condition and test monitoring systems to determine the onset of surface contact fatigue.

A previous cyclic wear study by Mueller et al [1985] used a pin-on-plate (POP) device with dental amalgams, and established that the wear grooves exhibit a shear mechanism except for gamma-1 phase amalgams in which the main attribute is adhesive welding. The wear pattern was influenced by the existence of wear debris on the contacting surfaces leading to smearing. The findings contradict the 3-body abrasive wear model which suggests that wear is solely due to the abrasive effect of contacting surfaces. De Souza et al [2012] investigated the wear mechanisms of dental composites based on 3-body contact by using ball crater (ball-on-plate) and a linear reciprocating pin (pin-on-plate) devices and an aqueous aluminium oxide suspension (White/Blue alumina<sup>®</sup>, QM Brazil) as an abrasive agent (i.e. a food bolus). The study established that ball-on-plate (BOP) wear is mainly influenced by abrasive and/or adhesive mechanisms which cannot easily be discriminated quantitatively by the authors. The pin-on-plate (POP) test results comprise mainly a fatigue mechanism, with the presence of abrasive and adhesive mechanisms at the onset of the surface wear. After an undefined number of cycles, fatigue mechanism influences the surface wear characteristics leading to severe material loss.

In conclusion, BOP is the best method to simulate surface fatigue of dental composites if the ball rolls without slip because surface contact fatigue dominate the wear behaviour of the dental composites. In BOP other wear mechanisms such as adhesive and abrasive are significantly minimal. These depend on whether a 2-body or 3-body *in-vitro* test is used, material composition, filler type and size. Therefore, different tests with varying load cycles can be used followed up by Scanning Electron Microscopy (SEM) to study the surface texture of the wear tracks.

## **2.9 Use of Finite Element Analysis to Predict Failures of Dental Composites**

Previous Finite element analysis (FEA) studies of micro-indentation processes focused on measuring the elastic properties of materials using sharp indenters such as conical and Berkovich indenters. However, researchers [Mesarovic and Fleck, 1999; Herbet et al, 2001; Park and Pharr, 2004; Taljat and Pharr, 2004] have reported growing interest in measuring the plastic properties of material such as yield, flexural strength, fatigue strength and so on, using spherical indenters simultaneously with finite element analysis



(FEA) prediction models. Although different approaches and assumptions have been used to analyze the results, it has been shown that, in most cases the FEA results tally very well with physical experimental results.

FEA has also been used to predict material damage and to assess subsurface damage and stress distribution using non-destructive and destructive approaches [Mackerle, 2003]. Vasudeva [2009] reviewed the use of FEA as a research tool in the analysis of dental structures and materials dating back to the late 1960s. Currently, the FEA analysis has overshadowed other types of theoretical analysis due to its ability to model even the most complex geometries with immensely flexible and adaptable characteristics.

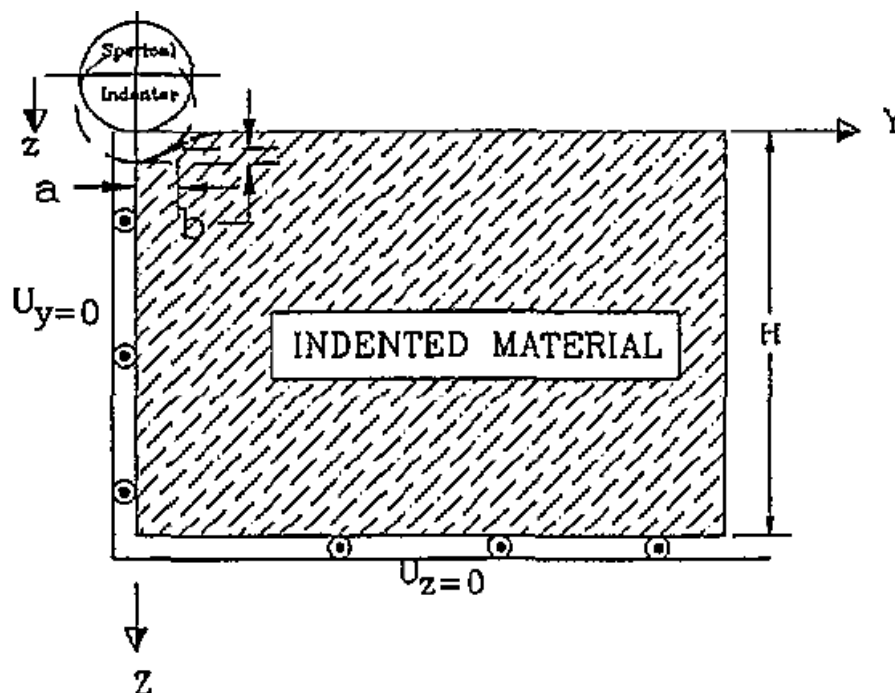
Yasuhiro et al [2006] used three-dimensional finite element (FE) to investigate stress the distributions in a composite resins under loading. The predictions established that flexural strength decreased with the increasing particle size of the filler of the composite resins ( $p < 0.05$ ). They also established that there is no significant difference in Young's modulus among composite resins with various filler sizes ( $p > 0.05$ ), and FEA indicated that stress concentration increased with increasing particle size. The FE predictions agreed well with experimental results for flexural strength. They concluded that the flexural strength of composite resins decreases with increasing filler particle size and evaluated the stress distributions of dental composite resins with various filler sizes.

Chuang et al [2003] used FEA to model the grinding forces and stress fields in the diamond grinding of silicon nitride. It was found that there exists a functional relationship between the depth of the subsurface in the shear failure zone and the depth of cut of the grits. Similarly, a study by Zang and Peng [2000] used an FEA model based on continuum mechanics, and predicted the grinding damage of ceramics under single grit conditions. They found that, when diamond tools were used at a proper negative rake angle and un-cut chip thickness of the order of  $1\mu\text{m}$  or less, chips could be removed from brittle materials through plastic shear, leaving a crack-free machined surface. The damage predicted by the model showed very good agreement with the experimental results. It was concluded that FEA is a vital tool in predicting the nature of surface and sub-surface damage and can be used as a non destructive test method.

Sadeghipour et al [1994] used FEA to investigate the elastic and elastic/plastic behaviour of polymer dental materials using a spherical indentation method. The key

component of the wear modelling of such materials was an understanding of the stresses encountered by dental restorative materials during service, when two-body or three-body interactions cause failure on the surface of dental restorations. The distribution of stresses and corresponding strain behaviour around the contact area was also considered in order to elucidate crack phenomena. The large-deformation analysis was repeated for various indenter penetration depths and a schematic diagram of the experimental set-up is shown in Figure 2-23.

The results show that, at a certain load, the tensile stresses were sufficient to form a ring crack (i.e. circular cracks on the contact surface) in the sample surface around the indenter. A similar analysis was also used to show the formation of other median cracks in the sample. The results were closely matched and verified against those of experimental investigations. By so doing, the study was extended to investigate the unloading process of the micro-indentation. It has been further shown that the unloading process produces residual stresses in the material which are large enough to cause the Hertzian-like ring cracks.



[ $H$ , specimen height;  $z$ , indenter's displacement;  $b$ , penetration;  $R$ , radius of indenter;  $a$ , radius of the contact area [Sadeghipour et al [1994]].

**Figure 2-23** Schematic of the spherical indentation model

Lee et al [2000b] used FEA to evaluate the thermal stress behaviour of a filler-matrix interface. The aim was to compare the FEA results with those of previous study

obtained by using a laser thermo-acoustic technique (LTAT) by Lee et al [2000a]. The same experimental systems (75/25 Bis-GMA/TEGDMA resin reinforced with 0, 25, 50 and 75 wt% 8- $\mu\text{m}$  silanized/unsilanized  $\text{BaSiO}_6$ ) as used in the experimental study by were modelled. The established FEA models were based on a coefficient of thermal expansion (CTE) mismatch phenomenon (i.e. the polarizer light leakage shrinkage due to uneven thermal stress changes). The model assumed that the elastic modulus and thermal expansion coefficient of the silane coupling agent had optimum heat transfer, and the thermal loading was based on steady-state thermal analysis.

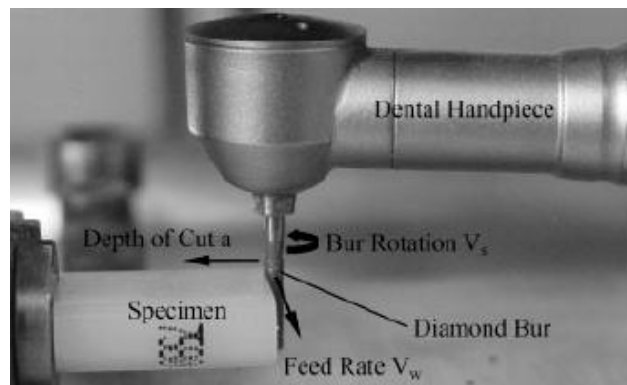
The results showed that the strain energy and interfacial shearing stress calculated from FEM validated the results from the previous LTAT study. In addition, the stress distributions of silanized and un-silanized FEM models were compared. It was established that the acoustic signals in the LTAT study were mainly derived from the de-bonding of the filler-matrix interface of silanized specimens, and from the matrix area of the un-silanized specimens. Hence, it was concluded that FEA is a powerful tool for exploring the thermo-acoustic mechanisms of dental composites.

The flexibility and adaptability of FEA has enabled the modelling of complex geometries such as those used in most dentistry applications. Han et al [2000] studied stress distributions in supporting tissues of clasp-type partial dentures on the transfer of occlusal forces by using a three-dimensional FEA tool. The results showed that the masticatory function can be satisfactorily recovered, and the reasonable rest recess angle for the clasp-type partial denture for the transfer of occlusion force has been found to be about 75 degrees. Oh et al [2002] used fractographic analysis and FEA to determine the crack initiation site and predicted the characteristic strength, location of peak stress concentration, and risk of rupture intensities of ceramic fixed-partial dentures (FPDs). The study established that the tensile stress concentration occurs in the adhesive layer of the crowns and the FDP connectors. Additionally, FEA was used to analyze the Hertzian contact tests and stress of dental bi-layer structures and stress distributions, and it was established that the tensile stresses predominantly drive the fracture in the ceramic coating structure.

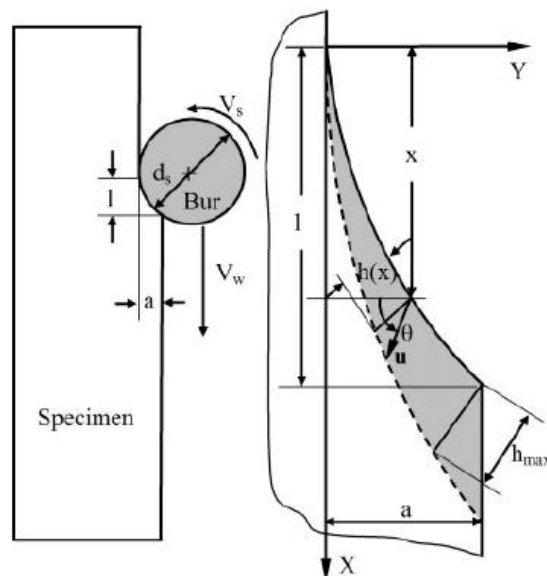
Song et al [2007] used FEA to investigate the stress fields and the degrees of subsurface damage of ceramic prostheses in simulated intraoral dental resurfacing operations using clinical diamond burrs. The set up of the experiment is shown in Figure 2.30. A two-

dimensional finite element model was established with the dental operational parameters and the material properties as input variables. The model enabled the prediction of stress fields and evaluated the depths of subsurface damage in ceramic prostheses as a function of the dental resurfacing operational conditions.

The results indicated that tensile, shear, compressive and equivalent von Mises stresses are all centred under the diamond burr-specimen contact zone. The maximum values of these stresses are concentrated at the diamond grit exit point, decreasing with an increase in depth of cut. The predicted depths of subsurface damage increase with an increase in both the depth of cut and the maximum chip thickness, and are in the range of 30-140 $\mu\text{m}$ . Physical experimental measurement of the depth of cut was also performed using Scanning Electron Microscopy (SEM). It was found that the FEA results match the SEM results.



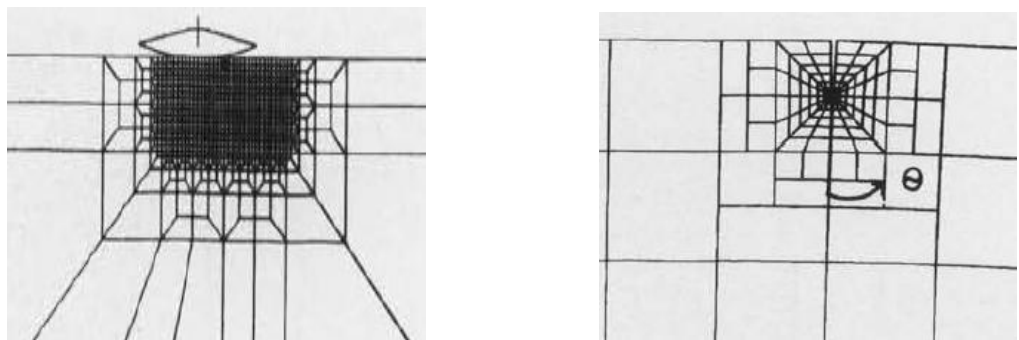
(a) Optical image of the simulated dental resurfacing using a hand piece/burr



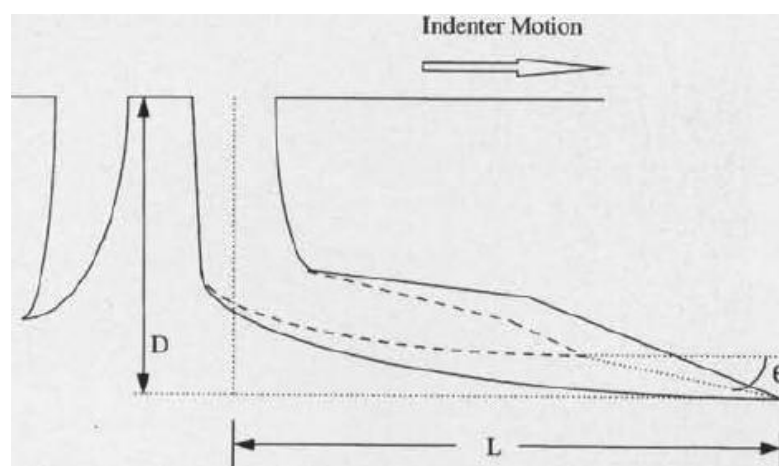
(b) Schematic of the burr-specimen interaction and chip geometry model

**Figure 2-24** Simulated intraoral resurfacing process [Song et al, 2007].

Baran et al [1998] used FEA to study crack propagation in posterior composite restorative materials (see Figure 2-31). The fatigue mechanism was regarded as the primary cause of the accelerated wear in the occlusal contact area (OCA). The study aimed to develop a finite element model enabling investigators to predict the directions of crack propagation in resins used as the matrix material in composites, and to verify these predictions by observing cracks formed during the pin-on-disc wear of a 60:40 BisGMA:TEGDMA resin and an ethoxylated bisphenol-A dimethacrylate (EBPADMA) resin. The experiment used laser confocal scanning microscopy (CLSM) to measure crack locations. CLSM is a high resolution optical imaging at a desired depth in the material. It is also known as optical sectioning. The image is re-constructed using the acquired point to point data by computer software. This was followed by finite element modelling using ABAQUS software. The software modelled a cylinder sliding on a material with pre-existing surface-breaking cracks. The modelling variables included modulus, cylinder/material friction coefficient, crack face friction, and yield behaviour.



(a) Finite element mesh including indenter (b) Illustration of vertical crack opening



(c) Schematic of subsurface cracks with parameters for establishing  $\Theta$ .  $D$ , crack depth;  $L$ , crack length;  $\Theta$ , crack propagation angle

**Figure 2-25** Methods for establishing crack propagation direction [Baran et al, 1998]

The experimental results were surprising, because most cracks occurred in the opposite directions to those in previously published observations. Although the majority of surface cracks were initially orthogonal to the surface, they changed direction to run 20° to 30° from the horizontal in the direction of indenter movement. Thus, FEM established the importance of subsurface shear stresses, since the calculations provided evidence that cracks propagated in the direction of maximum stress intensity, in the same direction as the motion of the indenter, and at an angle of approximately 20°. The findings have provided the foundation for a predictive model of sliding wear in unfilled glassy resins.

In conclusion, FEA is an efficient, economical and viable method for predicting and evaluating the stress responses and failure properties of materials, and particularly of brittle materials. Dental composites contain high proportions of polymer-ceramic compounds in layered systems, and behave like brittle materials under contact loading. However, no work has been reported on the application of FEA prediction and evaluation models to the failure of dental composites due to rolling contact.

## **2.10 Summary**

The foregoing literature review has shown that dental composites are now the preferred dental restorative materials. The optimisation of manufacturing processes for dental composites has led to composite materials with strengths matching those of metal alloys such as amalgam. Currently, dental composites are suitable for both anterior and posterior applications. The challenge now is to establish the mechanical characteristics of different formulations produced in research laboratories. Thus, there is not only growing research interest in the development and optimisation of the material, but also on the development of appropriate devices for testing dental composites.

*In-vitro* testing provides researchers with control over experimental variables and the opportunity to take accurate measurements. Fatigue tests are time-consuming and results cannot readily be available. This makes *in-vitro* testing an ideal method for studying the mechanisms surface contact fatigue in dental composites, because the evaluation of their characteristics can be achieved in a short time compared to in *in-vivo* and *in-situ* methods. However, it is important that all *in-vitro* models replicate the complex oral environment as closely as possible in order to enable the full range of

surface contact fatigue measurements as would be obtained using *in-vivo* (clinical) methods.

Currently, dental composites are tested for tensile strength, shear strength, diametral compression, compressive strength, fatigue strength, and so on. Of these, flexural fatigue strength and compressive strength are most popular. These tests give valuable information about the characteristics of dental composites, but they are limited by the fact that a catastrophic bulk fracture of the specimen cannot provide precise information about the surface failure of the materials, and many tests have to be performed to overcome significant variance in test results. On the other hand, efforts to develop a surface contact fatigue testing device have borne fruit. Nevertheless, there exist a need to extend its capabilities to an automatic operation with online measurement and condition monitoring systems while providing friendly user interface.

It has also been established that the complexity of the oral environment subjects dental restorative material to surface contact fatigue (surface wear). Thus, dental composites must have high resistance to surface wear. However, the trend has been to develop wear simulation devices based on the principles of attrition and abrasion. Nonetheless, such devices are few in number, sophisticated and expensive and will not be available to research laboratories.

The review has established that dental composites are materials composing of heterogeneous structures, and that knowledge concerning the fracture mechanics of homogeneous materials has a limited validity. Stresses vary depending on the location and the nature of the existing bonds. Thus, interpenetration of fatigue data from dental composites is still an issue requiring further research. On the other hand, promising applications of the rolling-ball technique have been used to determine the mechanical characteristics of different materials, including studies of surface contact fatigue in components and structures. Successful automations of the rolling-ball technique have enabled online data acquisition and interpretation in the industrial applications.

Research efforts to apply the rolling-ball technique to determine the surface contact fatigue of dental composites are still ongoing. One interesting finding is that the technique is able to distinguish between different rates and mechanisms of surface contact for different materials. In spite of the interesting research finding; two challenges are apparent. One is to automate the process of surface wear generation in

order to match the clinical oral environment (i.e. temperature and humidity). The second challenge is to enable online data acquisition and processing in order to reduce machine and human error.

The review has also shown that finite element analysis (FEA) is a vital prediction tool used to establish the nature of failure in structures and components. Its applications have extended from the design of structural components to the prediction of surface failure of materials, including dental composites. The complex bonding nature of dental composites necessitates additional testing variables, which hence renders the measurement of surface contact fatigue cumbersome. Thus, it is important to combine FEA prediction models and valid laboratory testing methods to overcome difficulties of data interpretation.

In conclusion, the current research focuses on developing a real-time mechatronic rolling-ball device for testing the surface contact fatigue of different dental composites in order to establish surface contact fatigue resistance. This will be followed by laboratory testing of selected dental composites. Additionally, the research focuses on establishing FEA prediction models for the selected composites so as to predict the nature of surface contact fatigue. Validation of the device's suitability for the testing of dental composites will be based on the experimental results and those of the prediction models along with any available clinical data. The overall aim of the research is to commission an appropriate test device for medium-sized dental research laboratories.



## CHAPTER 3 EXPERIMENTAL VALIDATION OF LVDT SENSOR AND MODELLING OF ROLLING BALL KINEMATICS

This chapter deals with the preliminary experiments to validate suitability of the linear voltage differential transformer (LVDT) transducer to acquire online surface contact fatigue measurements. It also includes modelling of the kinematics of the rolling ball and its influence on the surface fatigue measurements of dental composites. The understanding of the kinematics will enable correct setting of fatigues load cycles, analysis of the sensor data, and supports the understanding of the mechanism induced in the surface fatigue failure of dental composites. The online surface wear measurements will be correlated with those obtained previously using a profilometry technique [McCabe et. al. 1997, 2000; Fujii et. al. 2004]. The chapter describes rig set up, drive and control, the LVDT transducer and preparation its calibration, preparations of the test material, the kinematics modelling of the rolling ball, and surface fatigue measurement and analysis.

### 3.1 Prototype Rig Set Up

The prototype rig illustrated in Figure 3-1 is a modified configuration of a rolling ball device reported by Fujii et al [2004].

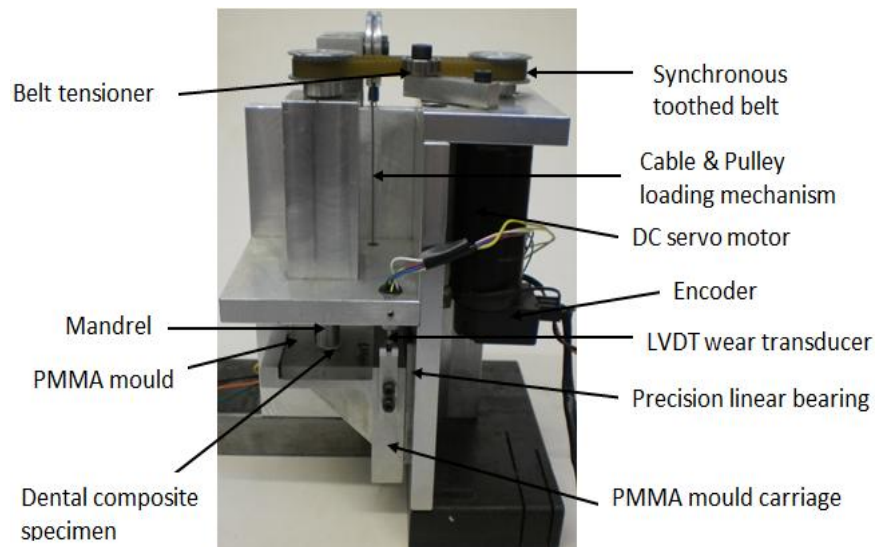


**Figure 3-1** Photo image of the revised prototype rig

The rig integrates two modules to facilitate its operation. A closed loop module drives and controls the DC motor and a second module is used to sample surface fatigue data.

The flow of instructions from the user interface computer to the motion control and data acquisition modules is illustrated in Figure 2-3.

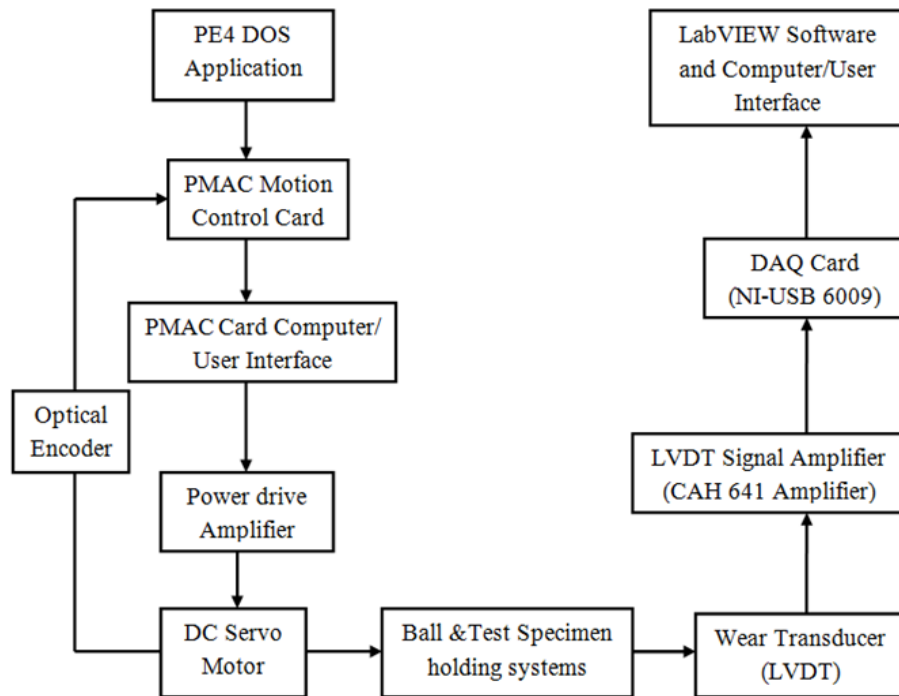


**Figure 3-2** Prototype rig set up and instruction flow.

The mandrel (rotor) was driven by a small DC servo motor (RE-36-118798) using a Programmable Multi Axis Card (PMAC) installed on a 486 PC computer, running under the MS-DOS operating system. The PC provided a user interface with the PMAC card through a dedicated motion control program (PE4.exe). The motor is coupled to the rotor by a synchronous toothed belt. A schematic diagram of the cyclic rolling ball principle and process using the prototype rig is shown in Figure 3.3. The mandrel has a V-shaped groove which provides three point of contact with a precision ruby ball 2mm in diameter to ensure rolling and minimise sliding. The pre-loading of the specimen is achieved using a dead weight and pulley arrangement, where the cable is coupled to the specimen carriage. The specimen carriage is mounted on a precision linear bearing (model: IKO, BSR 20 40 SL) to ensure the constant loading of the dental specimen against the ruby ball.

Wear measurements are recorded using a Solatron LVDT (model SM1) transducer with a linear output of  $\pm 5\text{VDC}$  and range of  $\pm 1\text{mm}$ . The LVDT sensitivity was set at 142 mV/V at a excitation rate of 5 kHz using a Fylde CAH-641 carrier amplifier ( $\pm 10\text{VDC}$  output; maximum ripple of 10mV) to amplify the LVDT output signal which was

acquired and filtered in LabVIEW using a 3<sup>rd</sup> low pass filter with a cut-off frequency at 20Hz. A data acquisition card (DAQ) NI-USB 6009 with a 14-bit resolution and 48 kS/s sampling rate was connected in differential mode.

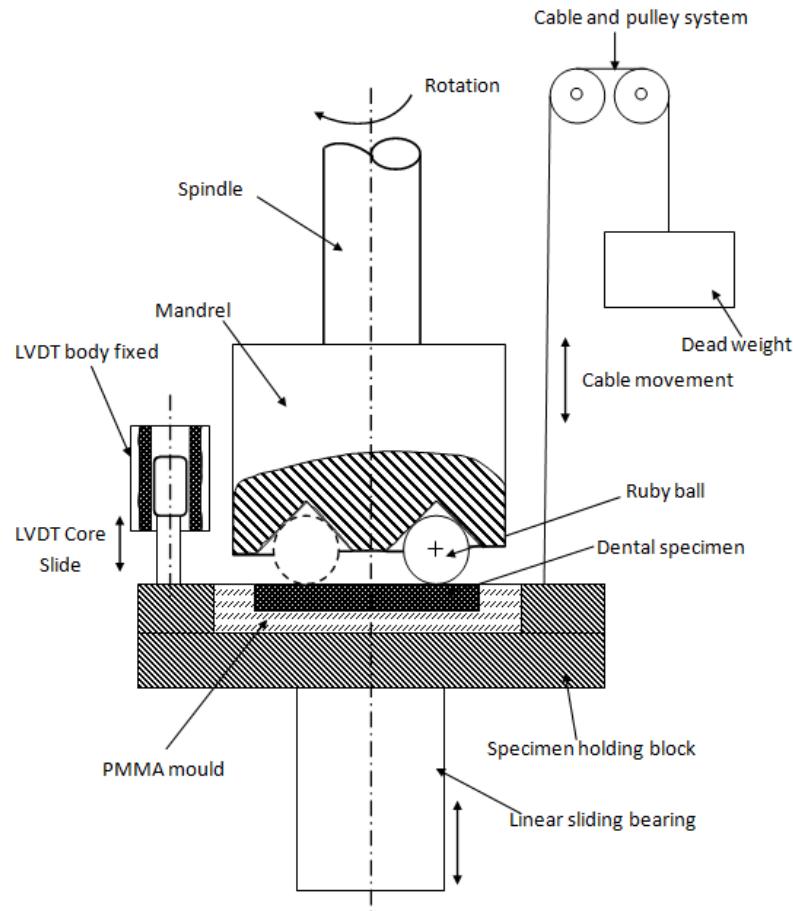


**Figure 3-3** Illustrations of the rolling ball prototype rig (not to scale)

### 3.2 Surface Fatigue Actuation and Data Acquisition

The motor drive was controlled using two dedicated PLC motion programs, which were uploaded to the PMAC card. One program runs the motor at 720 rev/min to create wear on the dental material along the ruby ball's circular orbit. A second motion program runs the motor at 120 rev/min in order to minimize mechanical vibrations during data acquisition. A program for acquiring and compiling measurement data from the transducer was created using LabVIEW (National Instruments). Acquired data were digitized and stored in Excel format. The virtual instrument program for data acquisition and representation in both time and frequency domains is shown in Figure 3-4.

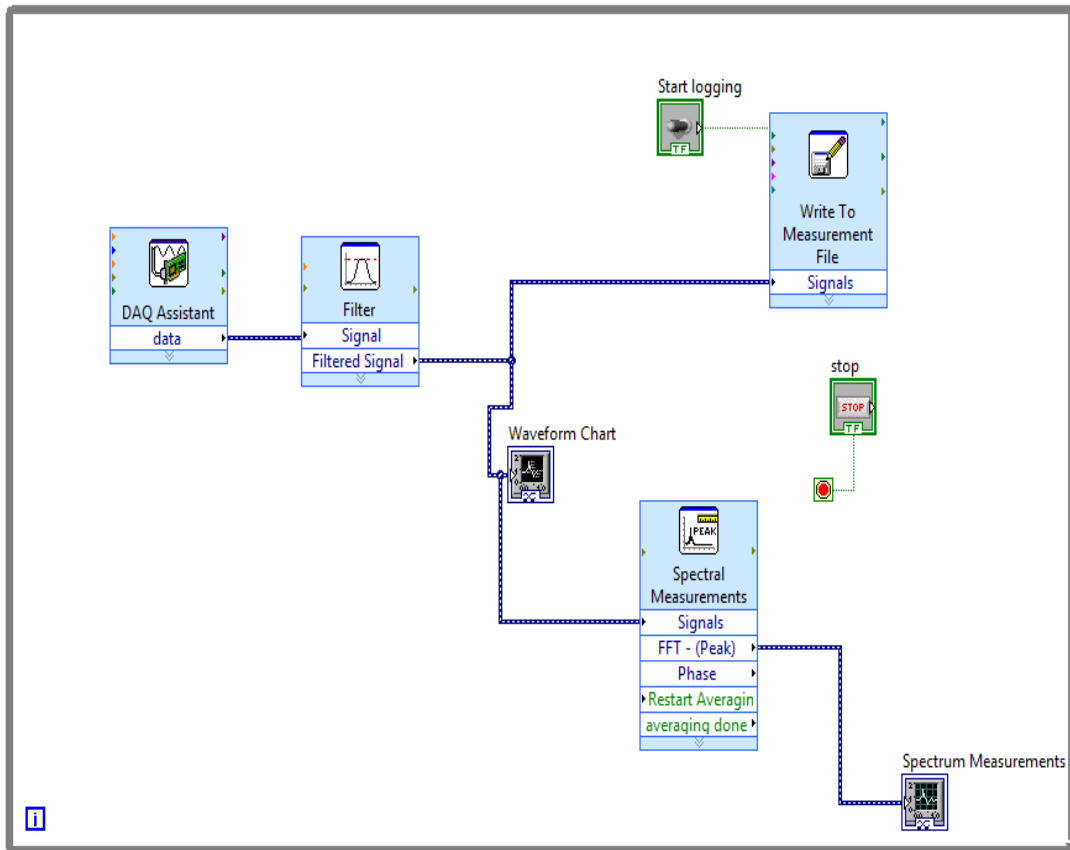


**Figure 3-4** LabVIEW VI for acquiring measurement data

### 3.3 Calibration of the Measurement System

Slip gauges with an accuracy of  $\pm 0.001\text{mm}$  were used to calibrate the measurement system at  $20^{\circ}\text{C}$  ambient temperature, and used to displace the LVDT core. The voltage output was measured using a digital voltmeter and recorded. The calibration graph is shown in Figure 3-5, showing a well-correlated linear relationship between the core displacement and voltage output. The LVDT transducer's calibration included observing the temperature drift against time. The measurement drift due to a temperature change from  $20^{\circ}\text{C}$  to  $25^{\circ}\text{C}$  was  $6\mu\text{m}$ , on average and electrical noise was  $4\text{mV}$  p-p. The measurements were considered to be within acceptable limits for the LVDT and amplifier, which each had a limit of  $10\text{mV}$ .

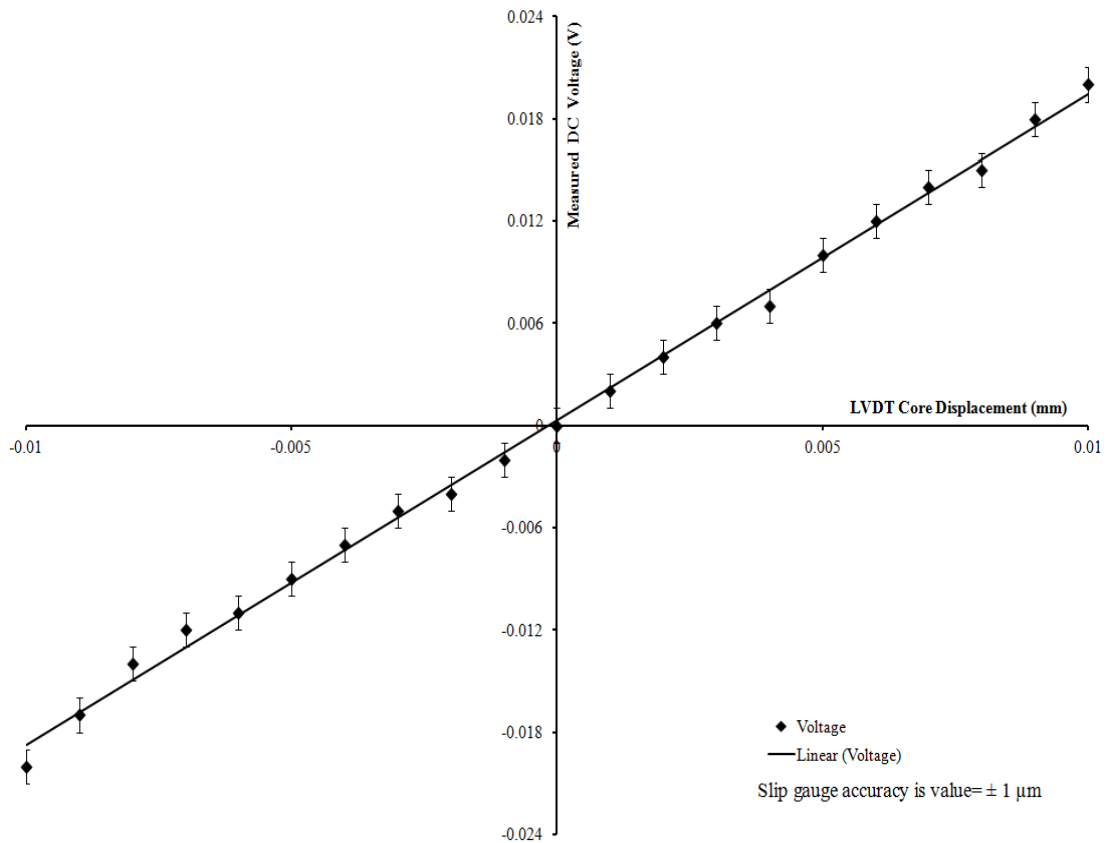


**Figure 3-5** SM1 LVDT calibration graph in the range of  $\pm 10\mu\text{m}$ .

### 3.4 Dental Specimen Preparation and Testing

The test specimens used in the experiments were similar to those used by Fujii et al [2004], and were made from a micro-filled composite material (Filtek TM A110, 3M USA). The dental materials comprised BisGMA monomers, TEGMA monomers and colloidal silica. The specimens were cast into disk moulds 10mm in diameter and 1.5mm deep, supported on PMMA plates of  $40 \times 40 \times 6 \text{mm}^3$ . Excess material was removed using a polyester strip and another PMMA plate. Curing was carried out by using blue light in overlapping exposures of sixty seconds while covering the specimens with polyester strips in a curing unit with an exposure intensity of  $700 \text{mW/cm}^2$ , Luxor 4000 type. The exposure was also applied to the PMMA side of the mould to ensure optimum curing while manipulating the curing variables according to the manufacturer's instructions. After curing, the specimens were ground and polished using wet carborundum paper with 800 and 1000 grits respectively. A final polish using a  $1\mu\text{m}$  alumina material was applied before storing the specimen in water at  $23^\circ\text{C}$  for 24 hours.

The tests were conducted using successive contact loads of 1 N, 2 N, 3 N and 4 N. The load was continuously applied through the 2mm diameter ruby ball by using the cable and pulley mechanism, while the ball was rolling on the surface of the specimen in a dry condition. During testing, the DC servo motor rotated the constrained ball for  $10^6$  load cycles, which is equivalent to  $1.9 \times 10^6$  mandrel rotations at an angular speed of 660 rpm. The ratio of mandrel to load cycles is based on a  $125^\circ$  symmetrical groove mandrel as presented in section 3.5. The effect of pre-loading on the visco-elastic properties of the dental composite was regarded minimal at the room temperature of 20-24°C [Sadephour et al, 2004]. This produced a circular track on the specimen, and over time, a loss of material (wear) occurred on the specimen. After every  $10^5$  load cycles, ( $1.9 \times 10^5$  mandrel rotations), a slow sampling speed of 120 rpm was initiated and wear data was sampled using LabVIEW for a period of 15 seconds at a rate of 1 kHz. Having completed data sampling, another fast cycle program was run. The fatigue process continued to  $10^6$  load cycles or above in successive intervals of  $10^5$  load cycles. The wear data was analyzed in the time and frequency domains using both MATLAB and Excel software.

### **3.5 Kinematic Modelling of the Beating Effect**

Online surface wear measurement required the digitization of the LVDT analog signal. However, the LVDT signal from the rolling ball device exhibited a beat frequency, as illustrated in Figure 3-6 below, and this phenomenon would limit digitization of the LVDT output signal or require expensive digital signal processing. An in-depth analysis of the causes of the beat frequency was necessary before embarking on the mechatronic design of the rolling ball device.

According to Rao [2011], beat frequency is produced when two sinusoids of either audio or sound vibrations move with the same intensity and slightly different frequencies ( $\omega_1 - \omega_2 = \Delta\omega$ ) in the same direction and superimpose on one another to produce another frequency with components at the sum and difference of the two frequencies. He further termed the phenomenon as the “*superposition of two vibrations of different frequencies*”. Mayoof [2009] and Yuan and Järvenpää [2006] reported that the phenomenon was exhibited by two free oscillatory motions and undamped simple harmonic vibrations moving with close frequencies in machine elements such as bearings, rollers, springs, and oscillating parts. They further reported that the main

cause had been uneven rolling or oscillating motions resulting from defective or misaligned elements. They used a vibration analysis technique which involved selecting the vibration signals in time domain and processed them using FFT (fast Fourier transform) analysis to obtain frequency spectra. These were interpreted by relating the measured frequencies with relevant possible causes like imbalance, misalignment, bearing defects and resonance. Thus, for a successful evaluation of the beat phenomenon, analysis of the time and frequency domains of the LVDT output was conducted. A FFT analysis of the sampled data obtained in the time domain as shown in Figure 3-6 was carried out using MATLAB to generate the frequency domain plot depicted in Figure 3-7. The MATLAB program is listed in Appendix A1.1

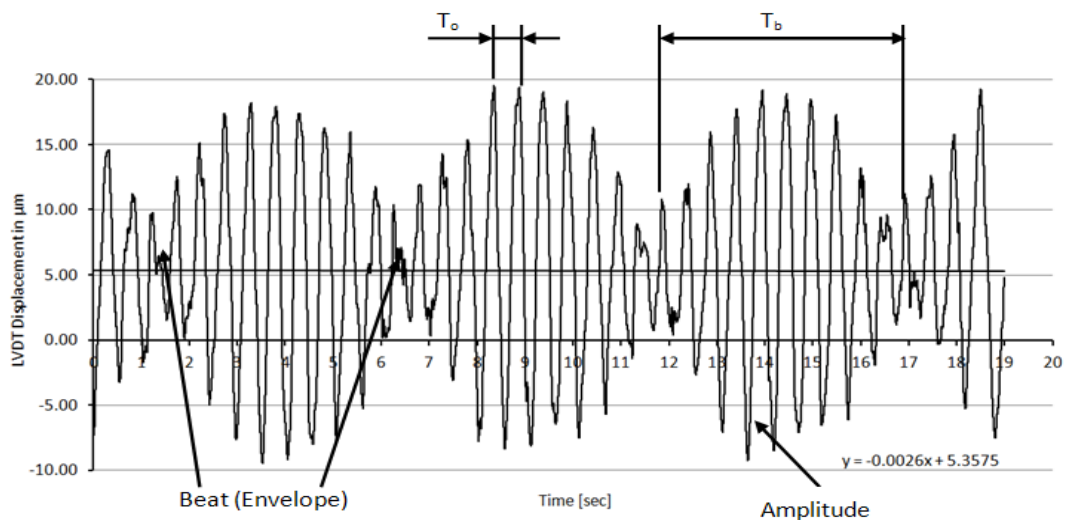


**Figure 3-6** LVDT time domain signal depicting the beating phenomenon.

Figure 3.6 depicts a signal sampled from the LVDT transducer showing a number of orbital rotations of the ruby ball with the ball's orbit period  $T_o$ . The orbit rotations are superimposed into an envelope (i.e. a beat) with an average beating period of  $T_b$ . The FFT transforms plotted in Figure 3-7 show that the LVDT analog signal is made up of two major components, 1Hz and 1.9Hz. The mandrel speed was 120 rpm (2Hz), which is close to the FFT's component of 1.913Hz. The 0.996Hz (approximately 1Hz) component is the ball's orbital rotation. To gain more insight into this scenario, an analysis of the time domain signal was conducted to determine the specific causes of the beating phenomenon. Visual observation of the time domain plot in Figure 3-6 establishes that the average beating period  $T_b$ , and ball orbit period  $T_o$  were 5.3s and 0.5s respectively.

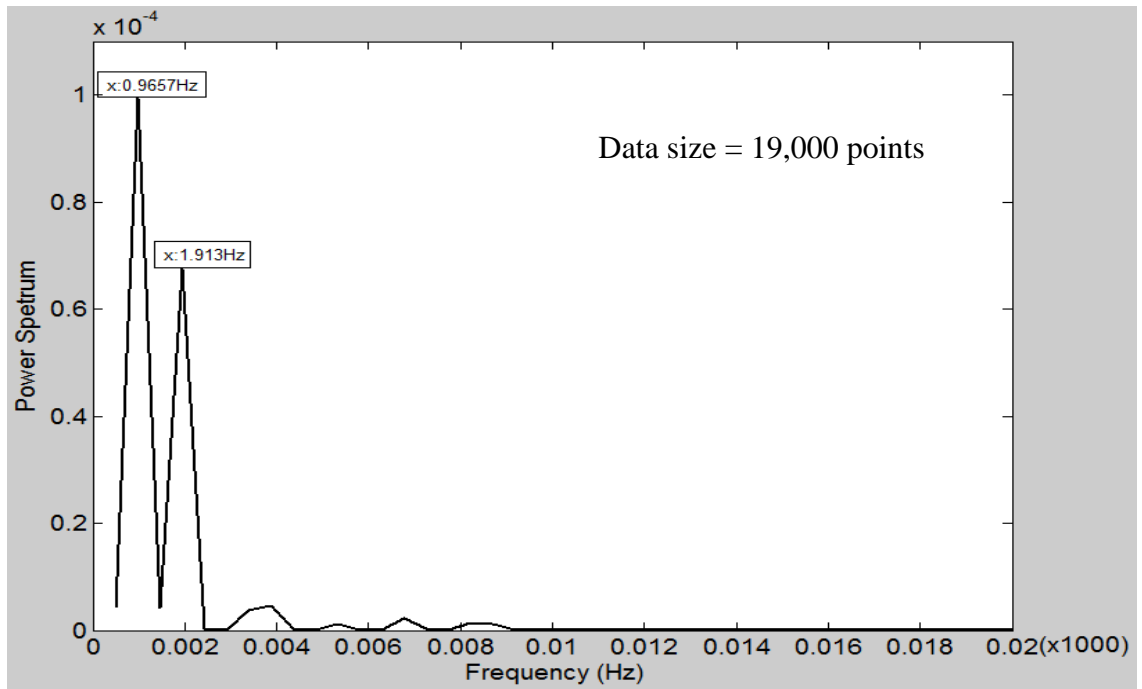


**Figure 3-7** LVDT frequency domain plot depicting the signal's components

Recalling the theory of simple harmonic motion and analysis of vibrating systems, the beating and oscillation periods of two sinusoidal oscillations exhibiting the beating phenomenon can be computed using equations 3.1 and 3.2.

$$\text{Beating period } (T_b) = \frac{2\pi}{|\omega_1 - \omega_2|} \quad (3.1)$$

$$\text{Oscillation period } (T_o) = \frac{4\pi}{\omega_1 + \omega_2} \quad (3.2)$$

If  $T_b = 5.3\text{sec}$  and  $T_o = 0.5\text{sec}$  are substituted into equations 3.1 and 3.2 and solved,  $\omega_1 = 13.16 \text{ rad/sec}$  (2.09 Hz) and  $\omega_2 = 11.97\text{rad/sec}$  (1.91Hz). Thus, 2.09Hz and 1.91Hz are very close to the sampling speed of 12.57rad/sec (2Hz) and can be related to it, but the actual cause and nature of relationship is still unknown. To further explore the source of the beat phenomenon, the kinematics of the mandrel, ruby ball and specimen were studied, as illustrated in Figure 3.8. Adapting the nomenclature and assumptions listed here, the kinematic model of the rolling ball can be derived. In addition, the kinematics of the rolling ball in the rolling ball-on-plate (RBOP) device as discussed by Xu, [2009], are used to simplify the analysis.

$\Omega$  is mandrel speed (rad/s)

$\omega$  is ball orbit speed (rad/s)



$\omega_{xsp}$  is ball spinning speed along the x-axis (rad/s)

$\omega_{zsp}$  is ball spinning speed along the z-axis (rad/s)

$\eta$  is ball rolling speed about its axis of rotation (rad/s)

$v_c$  is the resultant peripheral velocity with respect to the mandrel (m/s)

$v_{ci}$  is the contact point  $P_3$  peripheral velocity with respect to the mandrel (m/s)

$v_{co}$  is the contact point  $P_2$  peripheral velocity with respect to the mandrel (m/s)

$v_b$  is the centre point velocity (m/s)

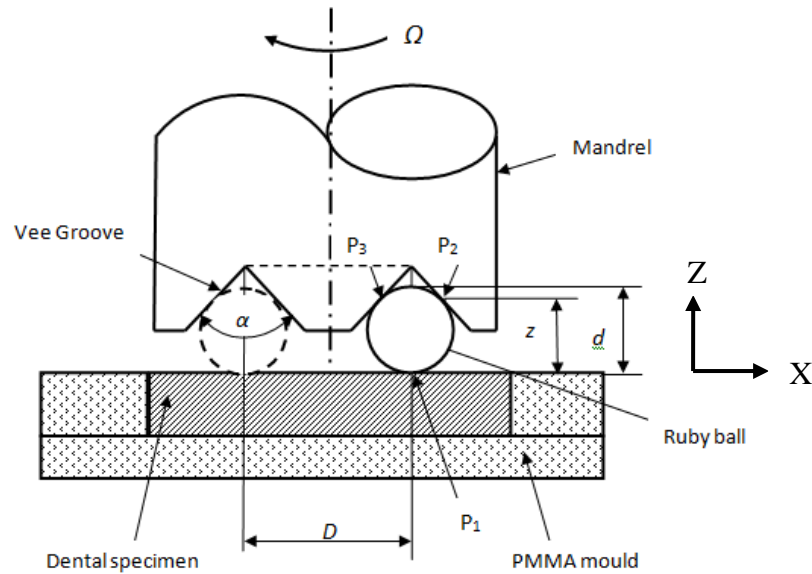


**Figure 3-8** Kinematics of mandrel, ruby ball and dental specimen

(not to scale)

the ball is rolling without slippage in the orbital diameter  $D$

the ball is constrained in a perfect symmetrical groove of angle  $\alpha$

the ball is a perfect sphere of diameter  $d$

the mandrel and specimen axes have no misalignments

tangential contact points exist between mandrel and ball ( $P_2$ ,  $P_3$ ) with contact of radii  $r_i$  and  $r_o$  and between the ball and specimen surfaces ( $P_1$ )

the beating components have the same amplitude

the beating occurs when the frequency of the mandrel ( $\Omega$ ) is approximately equal to the orbital frequency of the ruby ball ( $\omega$ ), such that  $\Omega - \omega \approx 0$ .

Figure 3-9(a) and (b) elaborate on the kinematics of the contacts between the mandrel, ruby ball and dental specimen during rolling along the mandrel's orbit ( $D$ ).

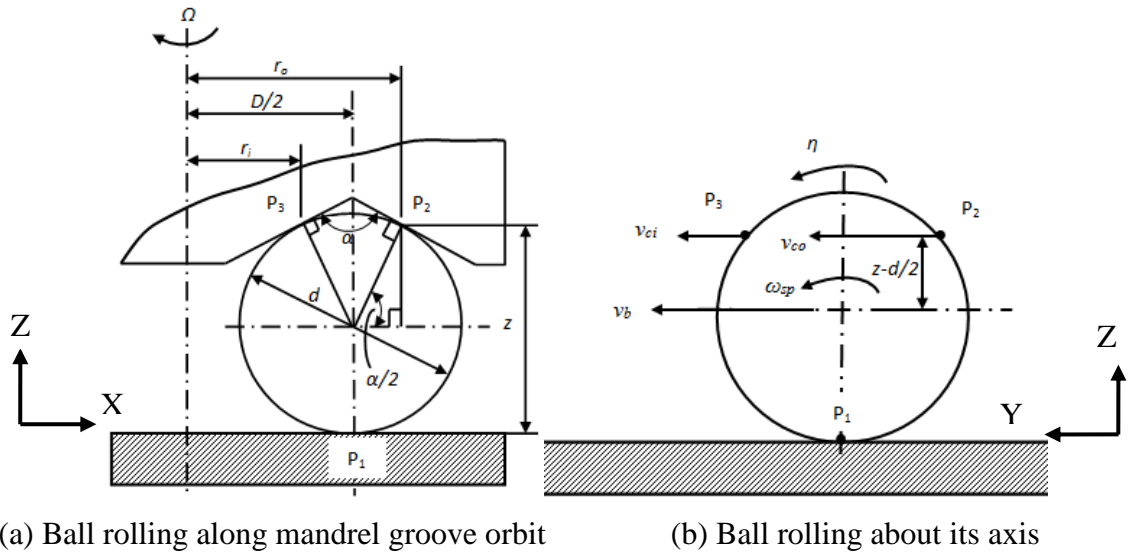


**Figure 3-9** Mandrel and ruby ball contact kinematics during rolling on the dental specimen (not to scale).

From Figure 3-9 (a), if the radius of the ball is  $\frac{d}{2}$ , and the mandrel's groove angle is  $\alpha$ , and  $z$  is the height from the specimen/ruby ball contact point to the respective tangential points of the mandrel/ruby ball, then using trigonometric identities and the similarity of triangles theorem it can be deduced that the perpendicular (shortest) height  $z$  is always a function of half of the mandrel groove angle  $\frac{\alpha}{2}$  and the radius of the ball of  $\frac{d}{2}$ , and can be expressed as:

$$z = \frac{d}{2} \left( 1 + \sin \left( \frac{\alpha}{2} \right) \right) \quad (3.6)$$

The height  $z$  varies from the centre to the apex of the ball as the mandrel groove angle  $\alpha$  increases from  $0^\circ$  to  $180^\circ$ . When  $\alpha=0^\circ$  the ball sits between two parallel surfaces of the mandrel and the specimen with two-points contact, when  $\alpha=180^\circ$  there are two peripheral (i.e. apex) contact points along the ball's diametrical axis. Otherwise, there are three contact points, two on the mandrel and one the specimen surface, governing the relative motion of the mandrel with respect to the specimen surface influenced by the magnitude of the groove angle ( $\alpha$ ) and the contact point height ( $z$ ), as illustrated in Figure 3-10.

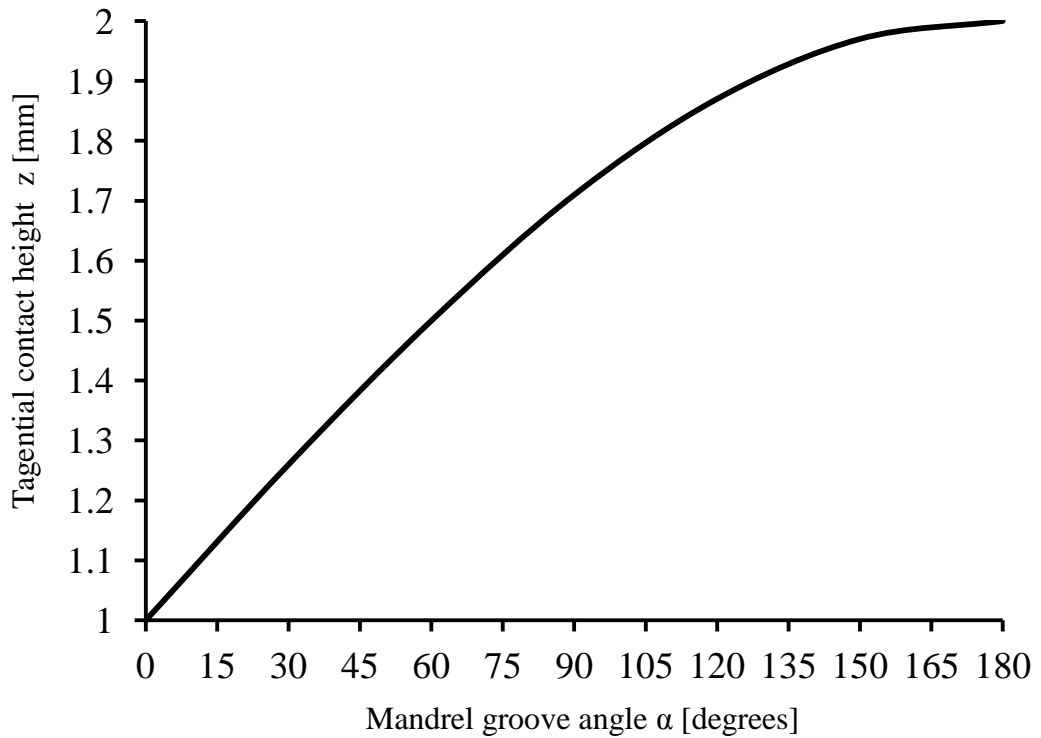


**Figure 3-10** Relationship of mandrel, ball and specimen three point-contact.

The contact geometry illustrated in Figure 3-8 influences relative velocities at the contact-points and determines the number of load cycles on the specimen with respect to mandrel rotation speed. At the contact points of the grooved mandrel rotating at  $\Omega$  speed and the rolling ball, different velocities evolve ( $v_{ci}, v_{co}$ ) because of the difference in contact radii ( $r_i, r_o$ ). The resultant velocity ( $v_c = v_{co} - v_{ci}$ ) generates a spinning motion of the ball ( $\omega_{sp}$ ) about its vertical axis. Besides this, the velocity difference between the top and bottom contacting apexes induces a forward rolling motion of the ball about its centre point ( $\eta$ ). The combination of the rolling and spinning motion of the ball generate a rotation sliding at the contact ellipse where the sliding speed changes. This causes a complex relative displacement causing the ball to roll with stick slip at the lower contact point  $P_1$ . It can be established mathematically that the resultant peripheral velocity ( $v_c$ ) at the mandrel-ball contact points is governed by the ball rolling speed ( $\eta$ ) and the tangential height ( $z$ ) [www.cnx.org/rolling motion-accessed on 25/09/2011]. To clarify these design parameters, a kinematic modelling of the relative velocities of contact-points was conducted. The resultant peripheral velocity ( $v_c$ ) of the ball as it rolls about its axis of rotation (Figure 3-7(b)) is expressed as:

$$v_c = v_b + v_{cb} \quad (3.7)$$

Where  $v_c$  is the linear resultant velocity of the peripheral contact points P2 and P3, and

$v_b$  is the centre point linear velocity. But,  $v_b = \frac{\eta d}{2}$  and  $v_{cb} = \eta \left( z - \frac{d}{2} \right)$ . Substituting  $v_b$  and  $v_{cb}$  in equation 3.7, the peripheral velocity becomes:

$$v_c = \eta z = \frac{\eta d}{2} \left( 1 + \sin \left( \frac{\alpha}{2} \right) \right) \quad (3.8)$$

Peripheral velocity with respect to the mandrel is also:

$$v_c = \frac{\Omega D}{2} \quad (3.9)$$

If slip is neglected and combining equations 3.8 and 3.9, equation 3.10 is yielded.

$$\Omega = \frac{\eta d}{D} \left( 1 + \sin \left( \frac{\alpha}{2} \right) \right) \quad (3.10)$$

Similarly, the orbit velocity can be related to the centre point velocity such that

$v_b = \frac{\omega D}{2} = \frac{\eta d}{2}$  and this leads to equation 3.11:

$$\eta = \frac{\omega D}{d} \quad (3.11)$$

Substituting ball rolling speed  $\eta$  in equation 3.10, and using equation 3.11, leads to a new equation that relates the mandrel speed to the ball's orbital speed. Equation 3.12 shows that the speed relationship depends on the mandrel groove angle and is independent of the mandrel groove and ball diameters  $D$  and  $d$  respectively. This is somewhat counter-intuitive, as it would be expected that there should be a link between the mandrel groove and ball diameters to their respective speeds. Thus, the number of mandrel rotations can be established if the designer sets the number of load cycles per test on the specimen surface (i.e. the ball orbital frequency( $\omega$ ) and mandrel groove angle ( $\alpha$ )). Assuming no slip, then the ratio of mandrel speed to ball orbital speed is obtained using equation 3.12:

$$\frac{\Omega}{\omega} = \left( 1 + \sin \left( \frac{\alpha}{2} \right) \right) \quad (3.12)$$

Figure 3.11 shows that the relationship between the relative angular speed of the mandrel with respect to the ball orbit speed which is influenced by the mandrel groove angle ( $\alpha$ ), as illustrated in Figure 3-10. In addition, the kinematics modelling found that increasing the ball diameter reduced the ball rolling speed. Increasing the orbital diameter would increase the ball rolling speed, as well. Interestingly, the ball rolls about itself once for one orbital rotation if the ball diameter equals the orbital diameter.

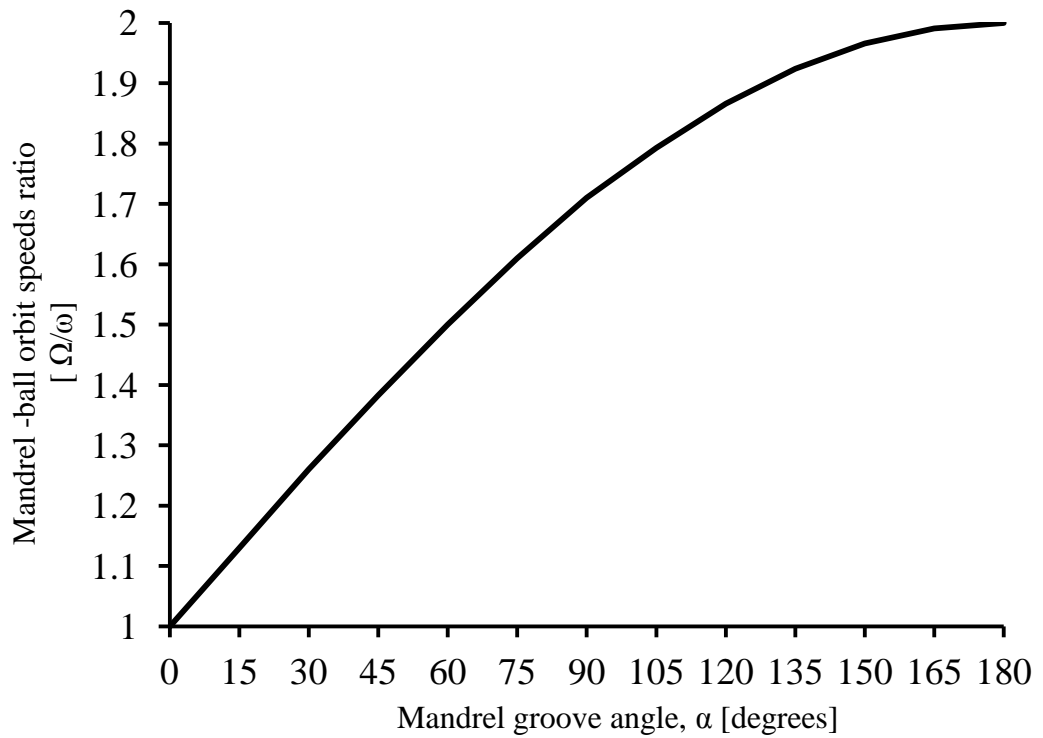


**Figure 3-11** Influence of mandrel groove angle on mandrel-ball orbit speeds ratio.

Vertical height variations ( $h_s$ ) during ball rolling resulting from any misalignment of the specimen mounting and/or carriage, as illustrated in Figure 3-12. The variations in misalignment ( $h_s$ ) can be expressed as:

$$h_s = D/2 \sin \gamma \quad (3.13)$$

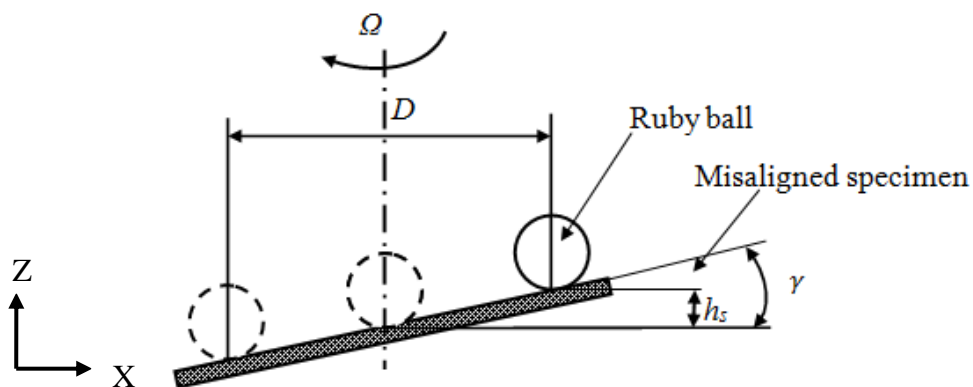


**Figure 3-12** Schematic illustration of specimen misalignment (exaggerated)

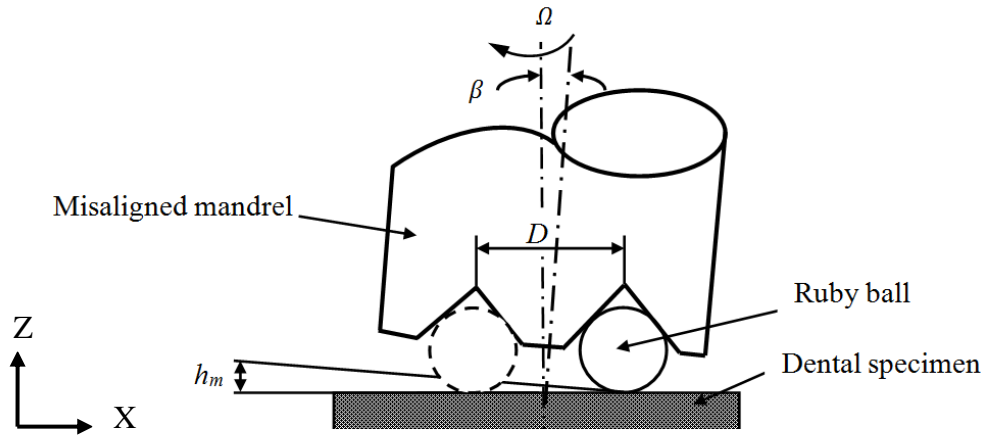


**Figure 3-13** Schematic illustration of mandrel misalignment (exaggerated)

Similarly, small mandrel misalignments ( $h_m$ ) due to spindle/mandrel run out, also contribute to fluctuations of the vertical height during rolling. The amplitude of the mandrel misalignment  $h_m$  is illustrated in Figure 3-9(b) and can be expressed as:

$$h_m = \frac{D}{2} \sin \beta \quad (3.14)$$

The variations in height due to the combined misalignments yield a total misalignment ( $h$ ), because harmonic motions with close frequency to one another produce a beat if added linearly to one another [ Rao, 2011] and can be expressed as follows:

$$h = h_s \sin \omega t + h_m \sin \Omega t \quad (3.15)$$

If both  $\gamma$  and  $\beta$  are small, then  $\sin \gamma \approx \gamma$  and  $\sin \beta \approx \beta$  respectively, this leads to mandrel misalignments  $h_s = \frac{D}{2} \gamma$  and  $h_m = \frac{D}{2} \beta$ .

Substituting  $h_s$  and  $h_m$  in equation 3.15 leads to equation 3.16:

$$h = \frac{D}{2} (\gamma \sin \omega t + \beta \sin \Omega t) \quad (3.16)$$

Equation 3-16 was simulated using MATLAB (see Appendix A1.2) using the experimental set up parameters, from section 3.5, i.e.  $\Omega = 2$  rev/s,  $D = 2.50$  mm, and  $\alpha = 125^\circ$ , giving mandrel-ball contact rolling as 1.84 rev/s, and an assumed misalignment magnitude of  $\beta = \gamma = 0.1$ . The output ( $h$ ) is plotted in Figure 3.14 and shows the integral effect of mandrel and specimen misalignments and the spinning motion of the ball due to the grooved mandrel.

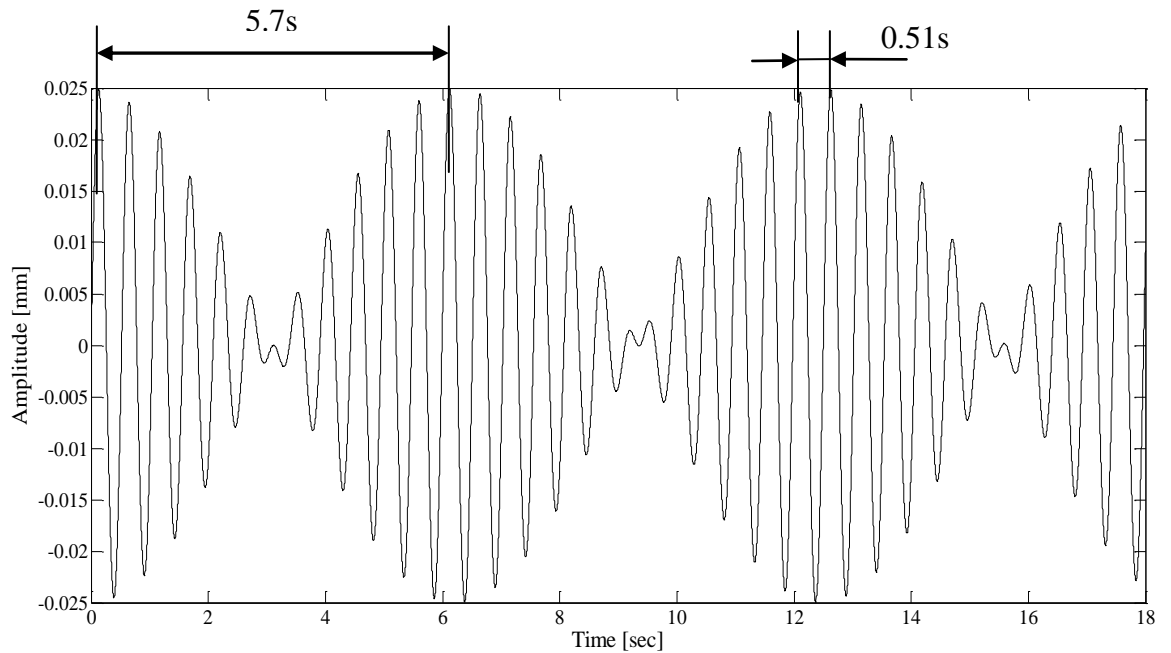


**Figure 3-14** Combined effect of mandrel and specimen misalignment with  $\alpha=125^{\circ}$

It was noted that the observed beat phenomenon existed when the values of  $\beta$  and  $\gamma$  were small and similar and the ball spinning speed ( $\omega_{sp}$ ) was approaching the mandrel speed ( $\Omega$ ). The beat period is 5.7 seconds which is close to the computed period of 5.3 seconds and oscillation period for the simulated graph is the same as in Figure 3-6 and is at 0.51 seconds. To ensure the ball rolls without slip, three-point contact using a mandrel with a groove angle of between  $120^{\circ}$ - $150^{\circ}$  has evaluated to be optimal. A best fitting algorithm is then used to sample the LVDT data taking into account the beat phenomena.

To summarize this analysis has shown that the beating effect is as a result of the angular misalignment between the spindle and the specimen surface and is particularly pronounced when the misalignments are similar in magnitude.

### 3.6 Preliminary Surface Contact Fatigue Results and Discussion

Experimental results are presented in plots of fatigue life (in number of load cycles) against the induced depth of the fatigue track for the 2-4N contact loads. Four trial (N=4) tests were carried out for each contact load and a mean of the wear tracks computed from the mean of each 2000 LVDT sample data. The data obtained are the mean (average) of the LVDT wear measurement at every  $10^5$  load cycle intervals over the total ( $\times 10^6$ ) load cycles. The 1N contact load did not induce any notable surface fatigue

on the specimen throughout the  $10^6$  load cycles and consequently this data is not recorded. The tests are not intended to show the magnitude of the surface fatigue failure on the dental specimens, as in the results previously published by McCabe et al [1997; 2000]; Fujii et al [2004], but tests were intended to ascertain the ability of the LVDT transducer to measure wear resulting from surface contact fatigue, with a view to adapting the measurement transducer in the proposed mechatronic system. The results and discussion are based on the correlation between the LVDT transducer measurements and those obtained by profilometry techniques by the above-mentioned researchers.

The results for the three different loads are plotted as illustrated in Figure 3-15. The average measurement deviations due to temperature drift was  $5^{\circ}\text{C}$  during testing leading to measurement uncertainty of  $\pm 3 \mu\text{m}$ . It can be deduced from the plots in Figure 3.15 that a good correlation between the LVDT surface wear measurements and the results using the profilometry technique was achieved, and the measurement data has a 54% reproducibility using ANOVA single factor analysis ( $p < 0.05$ ).

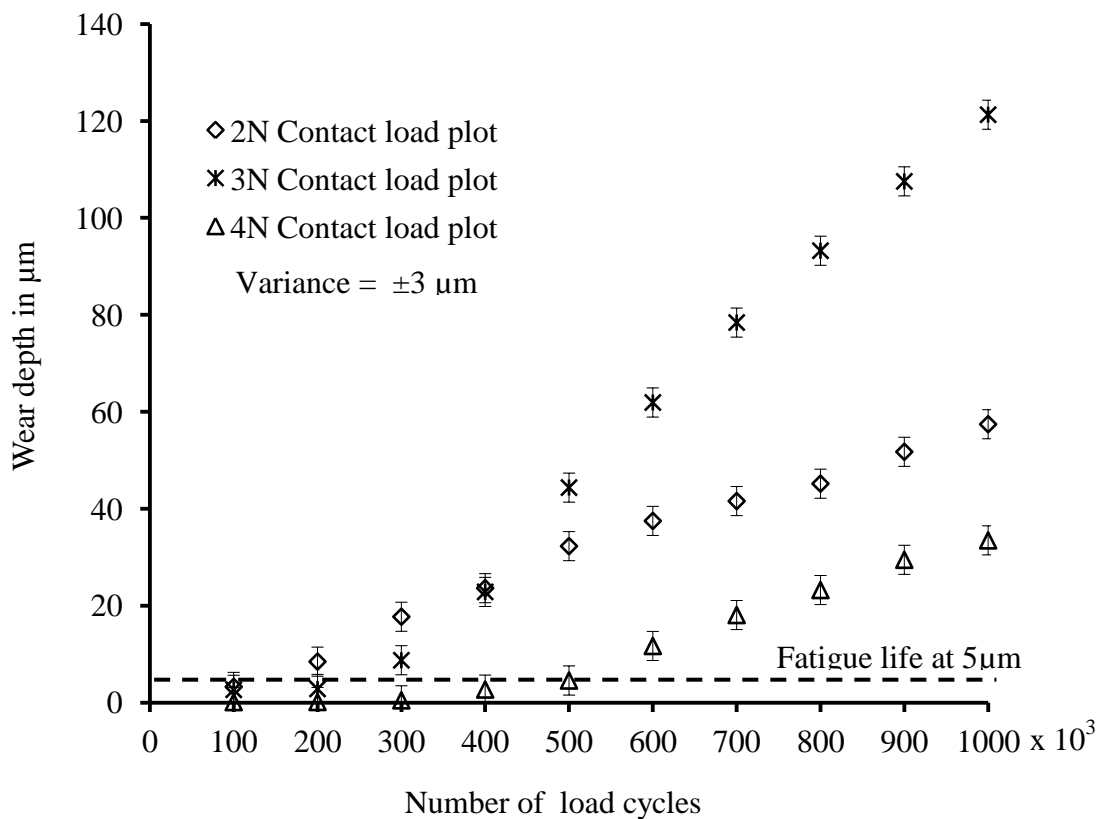


**Figure 3-15** Fatigue wear data recorded using LVDT measurement transducer



The plots show that the dental specimens tested can withstand several hundred thousand of load cycles before any notable surface degradation occurs, followed by a rapid rate of material removal after the onset of surface degradation. The number of load cycles to produce a wear track of 5  $\mu\text{m}$  depth lies between  $1 \times 10^5$  and  $8 \times 10^5$  load cycles for the three contact loads. The tests were terminated after  $10^6$  load cycles, and the depth of the surface fatigue track for the 3 N contact load was 121  $\mu\text{m}$  (0.121 mm) whereas those of 2 N and 4 N contact load were 45  $\mu\text{m}$  (0.045 mm) and 57  $\mu\text{m}$  (0.057 mm) respectively.

The two distinct regimes (i.e. 2 N and 4 N contact loads) correlate very well with those obtained in previous tests by McCabe et. al. [1997; 2000] and Fujii et. al. [2004], as described in Section 2.8 (see Figure 2-20 and 2-22) in which it was established that approximately  $10^5$  load cycles had to run before any notable surface wear was induced on the micro-filled composite specimens. McCabe et. al used a contact load of 2N whereas Fujii et. al used contact loads ranging from 1N to 5 N. A profilometry technique was used in both studies to analyse the experiment data, where the specimen was physically removed and then remounted. The specimens used in the preliminary tests were several years old and it is speculated that this may have influenced the 3 N contact load inducing more surface fatigue on the specimen than the 2 N and 4 N contact loads. It is hypothesized that surface ageing may have resulted in different levels of hardness on the surface skin of the specimens and eventually led to the varying rate of fatigue wear. Surface ageing in dental composites is caused by several factors such as light exposure, age of the specimen, curing process used, time, and storage conditions. The degree of surface hardness of the specimens could not be established in this study and is subject to further investigation.

On this occasion, a Denford CNC router (2600 PRO) fitted with a laser scanner/profiler was used to profile the surface fatigue depth on the tested specimens. The profiling resolution was 0.001mm (smallest possible) in steps of 0.05 mm and the profiling speed was 100 mm/min. The profiled data were analyzed using Matlab codes in Appendix A1.3 and presented in 3D plots. The plot depicted in Figure 3-16 is for the 3 N contact load and shows that the reference datum is 0.40 mm, and the surface fatigue track is approximately 0.25 mm below the reference; giving a track depth of 0.15 mm. The visualization is aided using the attached coloured legend.. Figure 3-16 provides a reasonable approximation to the LVDT transducer readings in Figure 3-15. However, actual wear depth could not be established with certainty because laser light penetrated

into the translucent dental specimen and PMMA mould. Gold sputter should be used to coat the specimens and moulds in the future in order to prevent light penetration and increase the quality of the profiled data [McCabe et al, 2000].

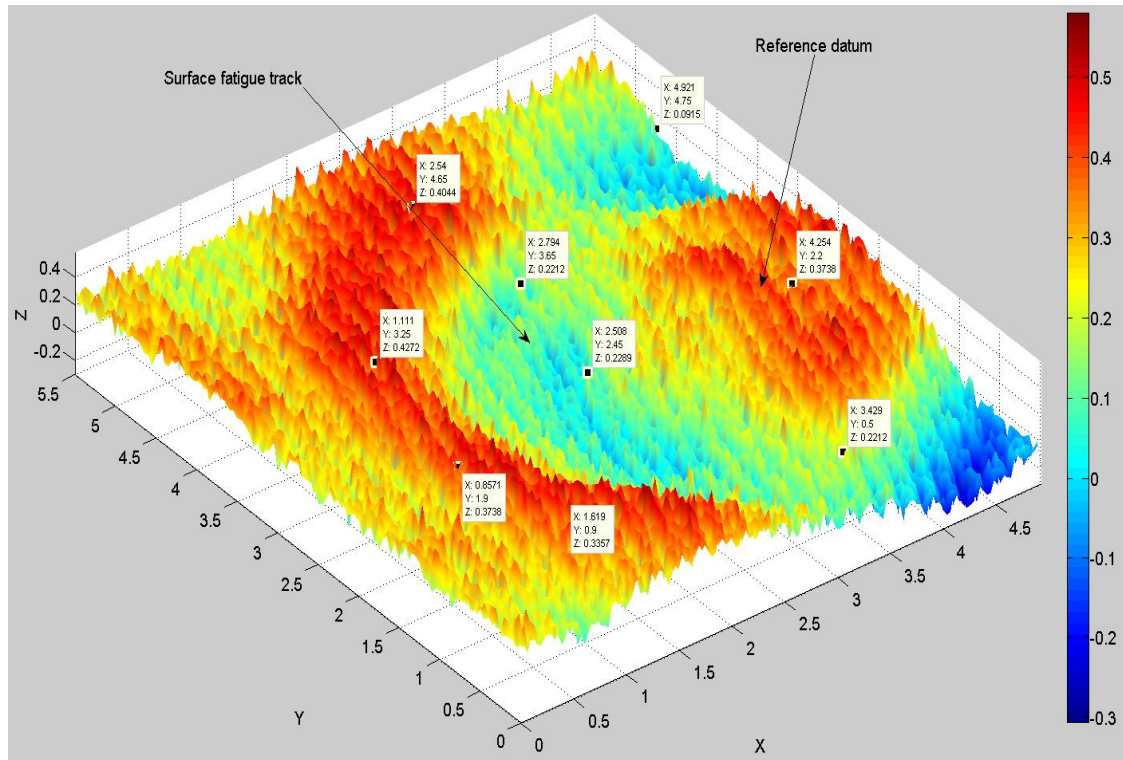


**Figure 3-16** Matlab 3D model plot of the surface wear track for a 3 N contact load on the dental specimen

Legend: X and Y are respective length of the profile in x and y axes. Z is the depth of the profile in z axis.

### 3.7 Summary

The preliminary findings provide important data for optimizing the existing prototype. The insights gained have proved very useful towards the aim of achieving a low-cost mechatronic surface fatigue measurement system. A milestone achievement is the viability of online (i.e. real time) data acquisition using an LVDT transducer. The prototype surface fatigue device will be now be re-designed and optimized to mimic the human oral cavity in terms of temperature and lubrication to meet ISO/TS 14569-2:2001 specifications, thus giving data that are clinically more meaningful. The mechatronic system will incorporate features to take the device further towards meeting the criteria set for the validation and qualification of testing dental materials as outlined by the ISO/TS 14569-2:2001 specifications.

## CHAPTER 4 ROLLING BALL FINITE ELEMENT ANALYSIS

Understanding the mechanisms of the evolution of surface contact fatigue, and the associated fatigue life of dental composites, is important in ensuring longevity and the optimum clinical service. Difficulties in modelling the *in-vivo* stresses and strains of restorative materials in-service have necessitated finite element analysis (FEA) of *in-vitro* cyclic loading. Two-body interaction is used to evaluate the mechanism of rolling ball contact which underlies the surface contact fatigue of dental composites, including establishing the stress and strain parameters in order to predict fatigue life.

### 4.1 Basis of Surface Contact Fatigue Modelling

Surfaces in rolling contact under loading experience surface fatigue. This is caused by changes in the microstructure of the material, which subsequently leads to the initiation and propagation cracks influenced by time and loading [Baran et al, 2001; Sraml et al, 2003; Sadeghipour et al, 2003]. Fatemi and Lyang [1998] analyzed several theories used to predict fatigue damage in homogeneous materials with load cycles applied. Discussing concepts of crack growths and continuum damage mechanics models, they concluded that fatigue damage was cumulative with the number of load cycles applied. Protocnick et al [2010] established the fatigue life of double slewing ball bearing unit is based on load distribution and maximum contact force on rolling contact elements using FE modelling. They found that the deformation stresses on the deformed part were influenced by external loading and the hardness of the material. In addition, the fatigue life of the deformed part was influenced more than parts which were not deformed. On the other hand, Singh et al [2011] used 3D-FE to predict fatigue damage at the dentine-adhesive interface using the analysis of localized micromechanical stresses and found that loading amplitude, microstructure and the mechanical properties of the material components have a significant influence on such fatigue damage. They concluded that FE modelling can provide information on the mechanisms that control the degradation of the dental materials by fatigue.

For the rolling ball on a dental composite, circular contact rolling in a defined orbit is complex and cannot be easily handled using available software resources. Therefore, a representative linear segment of orbital contact rolling is considered, as illustrated in Figure 4-1. It can be deduced from Figure 4-1 that the rolling of a ball on a planar half specimen is initially a non-conformal contact (i.e. between curved surfaces). In this

simplest case of a ball rolling on a planar dental composite, a superposition of translation and rotation occurs at the point of contact during the rolling motion. The rotating axis of the ball moves parallel to the planar surface and causes the instantaneous contact point to also move a finite distance at every instantaneous short time. Ultimately, the contact point, which can be also regarded as the rolling centre, is displaced in a pseudo-stationary fashion along the contact orbit. Subsequently, the tangential velocity of the contact point is zero, and it increases as its peripheral position changes during rolling to twice the level at the apex of the ball. The centre point of the rolling ball moves with half of the tangential velocity ( $v$ ) of the apex. The non-conformal contact of the ball on the planar surface of the dental specimen is termed Hertzian contact, which is derived from Hertz contact theory [Johnson, 1985; Fischer-Cripps, 1999]. Using this theory and assuming an ideal (frictionless) contact, indicative values of parameters such as contact length, depth, pressure, distribution, stiffness, deformation and compressive stresses can be evaluated for contact between the rolling ball and dental composite. However, actual values are determined by including other factors such as the elasto-plastic properties of the ball and dental composite, surface roughness, effect of normal force ( $F_N$ ) and tangential friction force ( $F_R$ ) and the velocity of the rolling motion ( $\omega$ ).

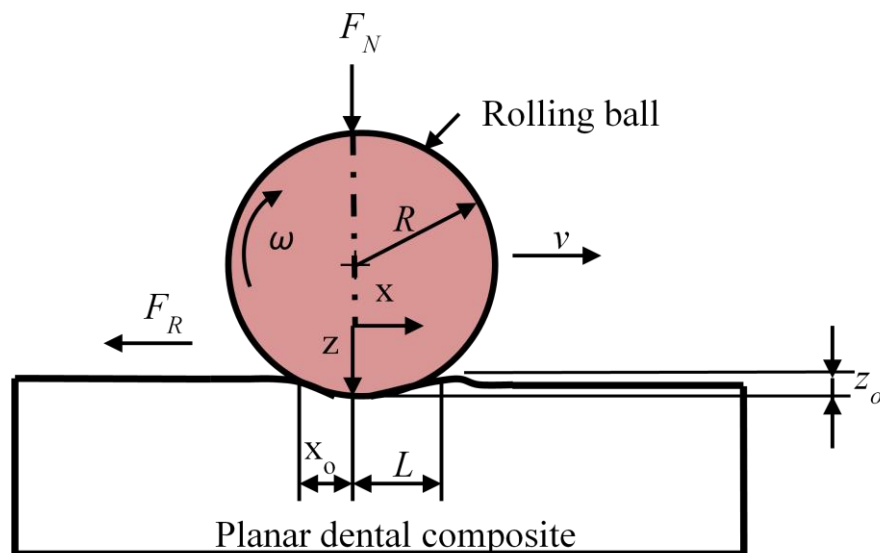


**Figure 4-1** Illustration of cyclic rolling and induced elasto-plastic deformation

Figure 4-1 shows a rigid ball rolling on a plane surface of an elasto-plastic polymeric dental composite. The resistance against the rolling of the ball initially evolves by hysteresis losses due to the elastic deformation of the elasto-plastic dental composite.

Material just ahead of the rolling ball is compressed and forms a pile-up region with height ( $z_o$ ), while behind this rolling ball expands to cause a sink-in as a function of relaxation time [Harass et al, 2010]. The process generates energy loss in the form of heat which is taken up by the dental composite and ball. The ratio of the sink-in length ( $x_o$ ) to the pile up length ( $L$ ) is characterized by the normal load applied, rolling velocity ( $\omega$ ) and the elastic-plastic modulus of the dental composite as it undergoes elasto-plastic hardening.

Consequently, the modelling of cyclic contact loading is conducted in two phases. Phase one involves loading the ball statically against the dental composite so as not to induce any permanent deformation, and in the second phase the rolling ball is cyclically loaded (negligible slip) on the specimen as in Figure 4-1. The deformation stresses are analyzed on the basis of Hertzian theory [Johnson, 1985], whereas the frictional forces are characterized using the Coulomb friction law.

#### 4.2 Ruby Ball and Dental Composite Analytical Modelling

A general framework of the nomenclature of contact deformation between the (rigid) ruby ball and a deformable dental composite specimen is illustrated in Figure 4-2

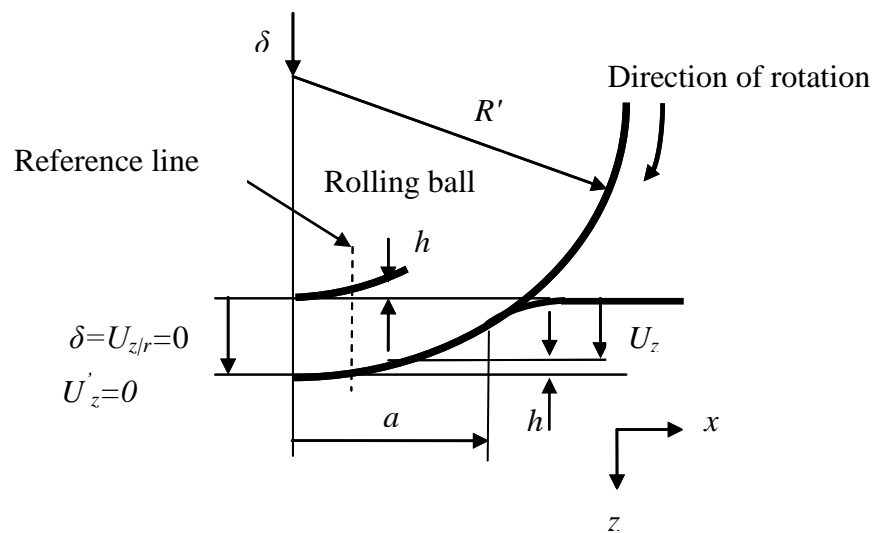


**Figure 4-2** Symmetry contact nomenclature of rolling ball and dental composite

The ruby ball and planar half-space model of the dental composite are initially in contact at an infinitesimal width (i.e. a point). However, as soon as a load is applied to bring them together, the elastic nature of the two bodies causes local deformation at the interface, and the area of contact increases. The local strain due to deformation leads to

the development of stresses in the dental composite specimen and ruby ball. Eventually, the dental specimen fails because its stiffness is significantly lower than that of the ruby ball. However, there are important assumptions for a classical analysis using Hertzian contact theory. Based on the assumptions and mechanical properties of the ball and dental composite given in Table 4-1, analytical and FEA solutions for contact deformation and subsequently rolling contact fatigue are established.

**Table 4-1** List of used mechanical properties of ruby ball and dental composite

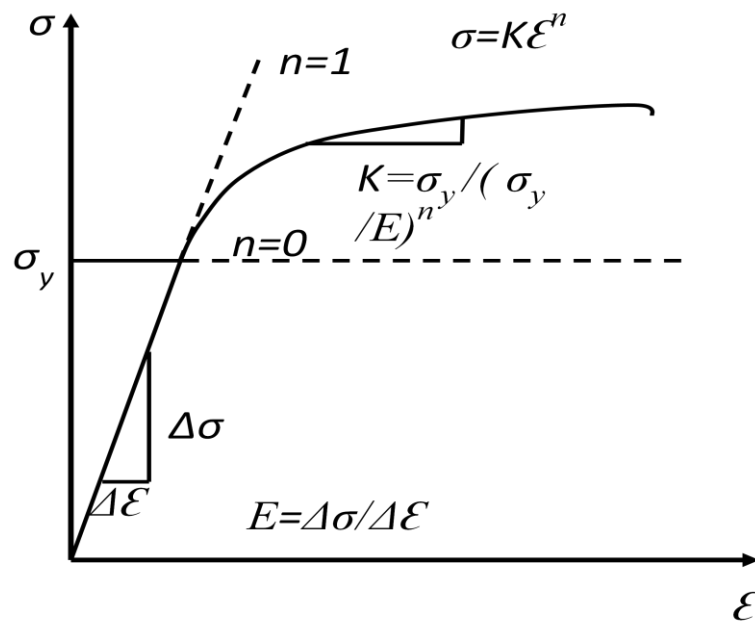
| Physical quantity                          | Ruby ball indenter               | Dental composite half-space        |
|--|----------------------------------|------------------------------------|
| Dimensions                                 | Diameter 2 mm                    | 3 mm x1 mmx1 mm                    |
| Modulus of elasticity ( $E$ )<br>(Average) | $380 \times 10^3 \text{ N/mm}^2$ | $12.25 \times 10^3 \text{ N/mm}^2$ |
| Poison ratio ( $\nu$ )                     | 0.17                             | 0.28                               |
| Density ( $\zeta$ )                        | $3990 \text{ kg/m}^3$            | $2000 \text{ kg/m}^3$              |

The assumptions are:

- (i) the distribution of the matrix volume to each individual filler is perfect and continuous.
- (ii) there are many filler particles and their distribution is uniform, so that the dental composite is regarded to have random isotropic and quasi-homogeneous
- (iii) the polymer matrix and fillers are elastic, isotropic and homogeneous.
- (iv) surfaces are continuous and non-conforming, leading to initial point contact.
- (v) strains are small and within elastic limits, assuming that the contact radius is very small compared to the radius of curvature.
- (vi) the contact surfaces are smooth and frictionless, and therefore cannot penetrate into each other ( $\sigma_x = \sigma_y = 0$ ).
- (vii) the ball is ideally stiff, and thus it can only undergo elastic deformation, whereas the dental composite may experience both elastic and plastic deformation.
- (viii) the stiff ball and deformable half space are semi-infinitely large bodies; hence,  $a \ll R$ .
- (ix) significant deformation occurs, and thus minute asperities are isotropic and can be neglected.
- (x) the indentation process is isothermal.

- (xi) dental composite specimens have linear elasticity within the test temperature range (20-37<sup>0</sup>C) which is far lower than their glass transition temperatures (120-160<sup>0</sup>C) and hence the effect of their strain rate on fracture and on yield, and modulus ratios are minimal at room temperature [Putick, 1973, 1978].
- (xii) there are no body forces on the dental specimens.
- (xiii) dental specimens have a continuous interface between the filler matrix and resin polymer.
- (xiv) the dental specimen has a complete adhesion between the filler and matrix (as simulated).

Based on the above, it is assumed that the deformation induced on the dental specimen by the rolling-ball is linear-elastic within the elastic limit and develops to elastic-plastic beyond the yield point, as schematically shown in Figure 4-3.



[ $\sigma$ : stress in dental composite,  $\epsilon$ : strain in dental composite,  $\sigma_y$ : the material yield stress,  $E$ : Elastic modulus,  $K$ : Bulk (tangential) modulus,  $n$ : work hardening index (Meyer's index),  $\Delta$  indicates difference/change of stress or stress]

**Figure 4-3** Stress-strain in a pre-and post-deformed elasto-plastic dental composite

It can be deduced from Figure 4-3 that rolling compression loading induces a linear deformation with a proportional stress and strain relationship until the yield stress is reached. Ideally, the deformation is recoverable when the load is removed. Beyond the yield stress, the dental composite starts to harden depending on factors such as loading force, the composition of the material and the coefficient of friction. The rate of growth

of the strain is no longer linearly proportional to stress and depends on the hardening index ( $n$ ). The elastic-plastic nature of the dental composite grows rapidly, and degradation begins in the critically strained location. According to Oliver and Pharr [1992] and Giannakopoulos and Suresh [1999], the elastic-plastic hardening can be determined using the sink-in or pile-up region and shape of the indenter. From Hertzian contact theory; the distribution of the normal contact pressure in the contact area is given by equation 4.1:

$$p(x) = \frac{2F}{\pi a} \sqrt{1 - \frac{x^2}{a^2}} \quad (4.1)$$

where  $F$  is the normal contact force, and  $a$  is the contact radius computed using equation 4.2:

$$a = \left( \frac{3FR}{4E} \right)^{\frac{1}{3}} \quad (4.2)$$

where  $E$  is the equivalent Young's modulus of elasticity and  $R'$  is the equivalent radius of contact given by equations 4.3 and 4.4 respectively:

$$E = \left( \frac{1-\nu_1^2}{E_1} + \frac{1-\nu_2^2}{E_2} \right)^{-1} \quad (4.3)$$

$E_1$  and  $E_2$  are the moduli of the rolling ball and dental composite, and  $\nu_1$  and  $\nu_2$  are their respective Poisson ratios. The analytical model assumes a rigid spherical indenter,  $E_1 \gg E_2$ , which gives an equivalent modulus approximating the modulus of the dental composite,  $E_2$ .

$$R' = \left( \frac{1}{R_1} + \frac{1}{R_2} \right)^{-1} \quad (4.4)$$

In this case, a spherical indenter with a radius  $R_1=R'$  is in contact with a planar specimen,  $R_2= \infty$ . Similarly, the normal stiffness ( $k$ ) of the deformable half-space specimen is obtained by differentiating the deflection with respect to load to obtain compliance, and is given by:

$$k = 2Ea = \left( 6FR'E^2 \right)^{\frac{1}{3}} \quad (4.5)$$

The maximum contact pressure  $P_{max}=p(x=0)$  acting between the rolling ball and dental composite specimen is found by differentiating equation 4.1 and it occurs at the centre of the interface. It is also known as the unit of stress and is shown in equations 4.6a and 4.6b:



$$P_{\max} = \frac{2P}{\pi a} \quad (4.6a)$$

or

$$P_{\max} = \sqrt{\frac{FE}{\pi R'}} \quad (4.6b)$$

This gives the displacement (penetration) of the contact point as:

$$\delta = \frac{a^2}{R'} \quad (4.7)$$

Hertzian contact occurs if, and only if, the contact variables  $a$  and  $\delta$  satisfy  $a^2 = R'\delta$ .

Referring to Figure 4.2 above, the displacement of a point on the surface in contact between an originally even surface and the rolling ball is given by

$$U_z = \delta - \frac{r^2}{2R'} \quad (4.8)$$

where the radius of displacement point,  $r$  is given by the expression,  $r = \sqrt{x^2 + y^2}$ . In addition, there is an important parameter associated with the contact of the rigid sphere and the elastic half space. This is called the potential energy, a parameter which governs the relationship between the stresses and strain of the half space material as it transforms from the elastic to elastic-plastic state due to deformation. The potential energy,  $U$ , induced by the elastic deformation is expressed as:

$$U = \frac{8}{15} E_2 R_1^{1/2} \delta^{5/2} \quad (4.9)$$

In the physical contact rolling process, partial sliding can occur due to complex loading conditions, and the geometry and surface roughness of both the ball and dental specimen. Accordingly, the partial slip can be accounted for using the Coulomb law,

such that the traction force is given by:

$$q(x) = \mu^* p(x) \quad (4.10)$$

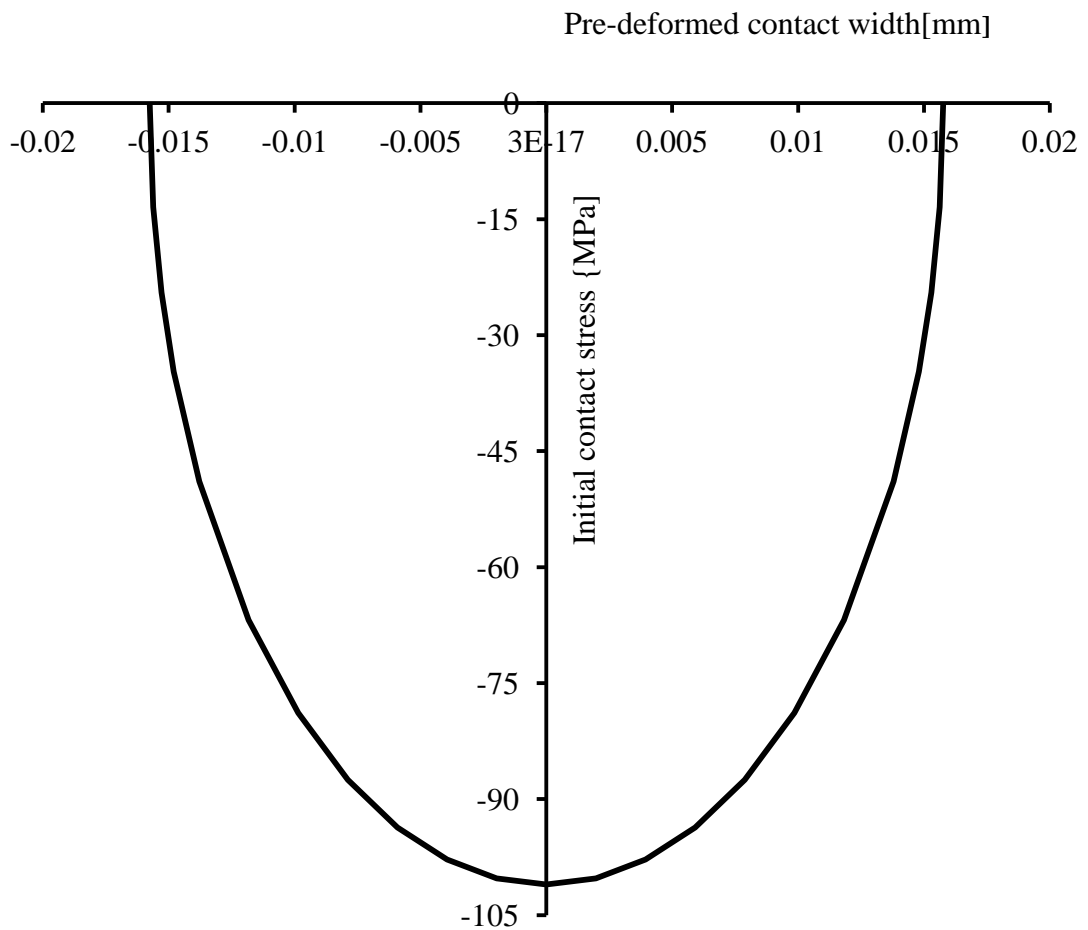
where  $\mu$  is the coefficient of friction between the rolling ball and dental specimen, which is approximately 0.2 for both wet and dry contact [Frunza et al, 2011].

Using a contact load of 2.5 N, which is the mean of the 1- 4 N contact load range [Fujii et al, 2004], with the geometrical dimensions and properties given in Table 4-1, static deformation was predicted using Hertzian contact theory for frictionless contact to provide a comparison with the FEA analysis. The reduced elastic modulus ( $E$ ) was 12.81 GPa and the reduced radius of curvature ( $R'$ ) was 1mm. From Table 4-2, it is evident that all pre-deformed contact parameters and stresses are below their respective deformed values. Although the contact stiffness remained steady, the Hertzian contact stresses increased significantly and transformed the dental specimen from the elastic to elastic-plastic state. The mean compressive yield strength for Synergy D6 composites is estimated at 238MPa [Davari et al, 2012]; however, with a 2.5N contact load and penetration of 2.80 $\mu$ m, the induced von Mises stress was 270MPa, which was somewhat higher than the compressive yield strength. This indicates the dental composite deformed plastically. The induced von Mises stress and cyclic contact loading on the dental composite strain-hardened the material, thus increasing its brittleness and ultimately leading to surface wear and failure.

**Table 4-2** Static contact deformation parameters and stress for a load of 2.5N

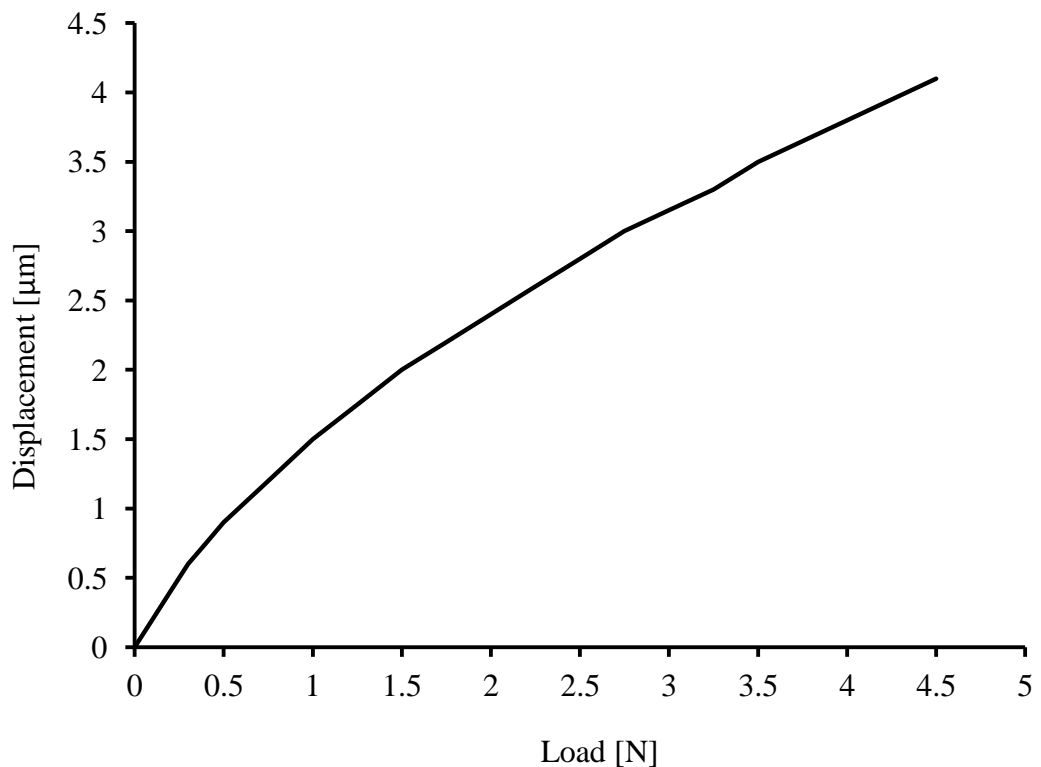
| Contact Parameters and Stresses         | Pre-deformed results | Deformed results |
|---|----------------------|------------------|
| Contact radius $a$ ( $\mu$ m)           | 15.76                | 52.70            |
| Initial penetration $d$ ( $\mu$ m)      | 0.25                 | 2.80             |
| Contact stiffness (N/mm)                | 1350.46              | 1352.60          |
| Contact pressure (MPa)                  | 101                  | 429.84           |
| Maximum von Mises stress $\sigma$ (MPa) | 31.32                | 270.50           |
| Contact strain                          | 0.016                | 0.053            |

Figure 4-4 shows that the maximum elastic contact stress was predicted to be 101MPa before the deformation of the contact region. The distribution of initial contact stress along the contact region is elliptical with a peak at the mid contact point reducing to zero towards the boundary of the contacting circle, as established by Johnson [1985] and Fishers-Cripps [1999]. The smooth distribution results from the assumption that the surface finish of the contacting bodies (ball and specimen) were sufficiently smooth.



**Figure 4-4** Contact stress distribution on the uniformly loaded half-space.

The influence of the indentation load on the depth of deformation was evaluated using equations 4.2 and 4.7. Figure 4-5 shows that the relationship is non-linear and is influenced by the contact pressure and stiffness of the specimen. However, it can be considered that large contact load causes large deformation and non-linear increase of contact area which leads to non-linear plasticity. This imparts more brittleness to the dental composite, causing surface and subsurface micro-cracks and culminating in surface wear and the failure of the material.



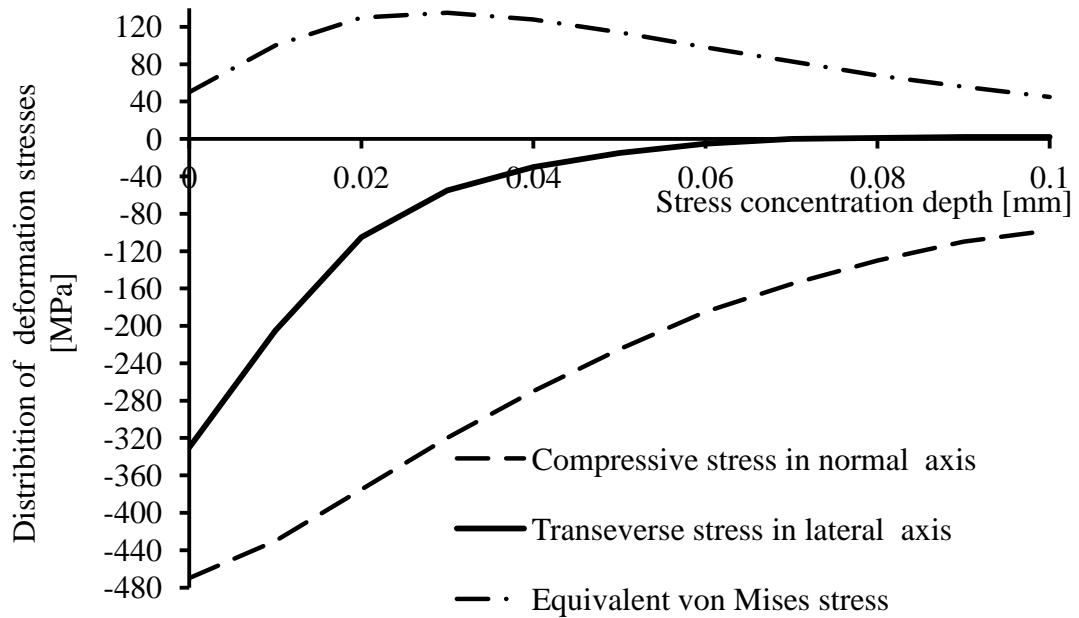
**Figure 4-5** Displacement versus load relationship for the dental composite

Figure 4-6 shows the relationship between normal compressive stress, transverse compressive stress and equivalent von Mises stress along the loaded area of the composite. The transverse compressive stress is caused by the localized compression of the material at the contact point. The normal compressive stress is at a maximum (480MPa) at the surface and declines with the increased depth of contact to about 120MPa at 0.1mm.

Furthermore, it can be observed that the transverse compressive stress falls to zero at about 0.06 mm from the contact point. The compressive stress is the same in both transverse axes. However, the von Mises stress is at a maximum at 0.025mm below the surface, reaching 120MPa, which is about three times that on the surface. It has been established that, for maximally smooth material, the maximum von Mises and shear stresses occur at a distance equivalent to 0.48 of the contact width. This is the principal cause of pitting or spalling and leads to subsurface damage before propagating and emerging on the surface.

From the analytical modelling it is apparent that the relationship between the normal load pressing the ruby ball into the deformable dental composite is also non linear, as

given by equation 4.6b, where  $P_{\max} \propto \sqrt{F}$ . Maintaining the area of contact as constant, a logarithmic relationship is realized similar to that of contact load versus displacement. This means that, as the dental composite deforms, the radius of curvature increases, thus distributing the load over a larger area than before.



**Figure 4-6** Ruby ball and dental composite contact nomenclature

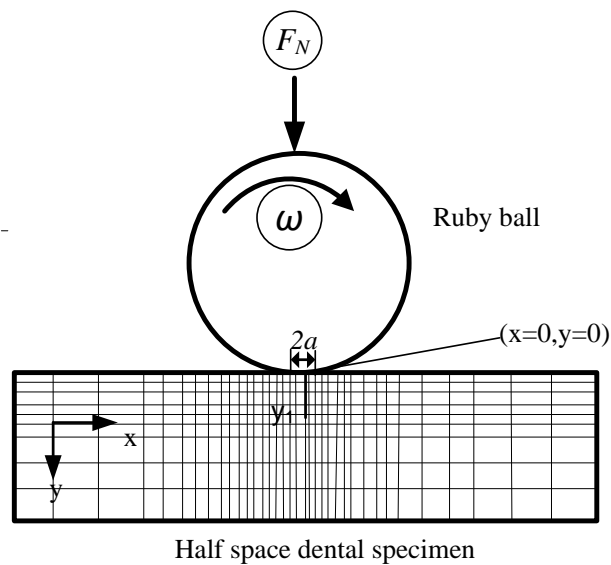
### 4.3 Finite Element Analysis (FEA)

FEA was modelled based on the elastic-plastic deformation of dental composites using static and cyclic loading in an attempt to demonstrate rolling contact fatigue. The model was designed based on the half-3D model, so that both stress and strain can be analyzed and, as expected, the contact strain increased with the depth of penetration. Shallow or small deformations exhibited elastic loading, which developed into the elastic-plastic state with increased deformation.

#### 4.3.1 Modelling and meshing

The rolling contact simulation comprised two steps, as shown in Figure 4.7. The first step was to apply a normal load on the ball and specimen which did not permanently deform the dental composite. In the second step, the rolling-ball displaced the contacting nodes over the specimen surface without slip. The induced cyclic compressive stresses along the contact region were analyzed and used to establish the

number of rolling cycles required to initiate surface contact fatigue. A coefficient of friction was applied in the model to enable the ball to roll without slip. The friction coefficient between the rolling-ball and dental specimen was set at 0.2, as obtained from Frunza et al [2011]. Other coefficients of friction, such as 0.15 and 0.25, were also used, but did not show any significant difference in the results, demonstrating that high friction did not influence the results in any meaningful way.



[ $F_N$ : static normal force pressing on the dental composite,  $\omega$ : cyclic rolling of the ball on the surface,  $a$ : the ball's non-conformal contact width,  $x=0$ ,  $y=0$  indicate initial contact position of the rolling ball]

**Figure 4-7** Schematic of the FEA Set-Up

The rolling contact was modelled using ANSYS 13. The ruby ball was represented as a stiffer hemisphere of radius 1mm and the dental composite as a deformable half-space planar of dimensions 3x1x1mm, as illustrated in Figure 4-8. To minimize the computational demand and solution time, a symmetrical boundary condition was applied along the axis of symmetry of the 3D model, and SOLID 186, a higher order 3-D 20-node solid element with quadratic displacement behaviour, was used to mesh the solid geometries. A key attribute leading to the selection of the model in this application is its ability to simulate the deformations of nearly incompressible elasto-plastic materials. It can also be used for homogeneous structured solids and provides uniform reduced integration in order to minimize computational time and to allow the region of interest adjacent to the contact interface to have the greatest concentration of elements. Throughout the modelling, surface-to-surface rigid/deformable contact was used to allow the stiffness of the ruby ball and dental composite model to characterize

deformation on the two bodies. Besides this, by indicating stress concentration on the ruby ball, the surface-to-surface flexible modelling offered a converging solution which proved difficult with rigid-flexible modelling and it also overcomes the limitations of the PC RAM memory.

To characterize the contact region, TARGE 170 and CONTA 174 were assigned to the contact areas using the contact wizard. TARGE 170 is a 3-D (surf to surf) segmented set of target elements used to pair and associate with CONTA 174 elements overlaying the contacting area, and it enables translation and rotational displacements. CONTA174 is a 3-D 8-node-to-surface contact element representing contact and sliding between 3-D rigid and deformable surfaces, and it permits macro-sliding between contacting surfaces. It also permits ramped-on initial penetration and frictional sliding behaviour, amongst other important characteristics required in this application [ANSYS, 2011]. The contact and target elements were applied only adjacent to the contacting area, in order to reduce the total number of elements.

Figure 4-8 shows the 3D half-model, with the mesh and designation of the contact pair between the ruby ball and the entire half-space planar model. A total of 2639 quadrilateral elements were used to mesh the volumes with an element size as small as 0.03 mm in the contact zone.

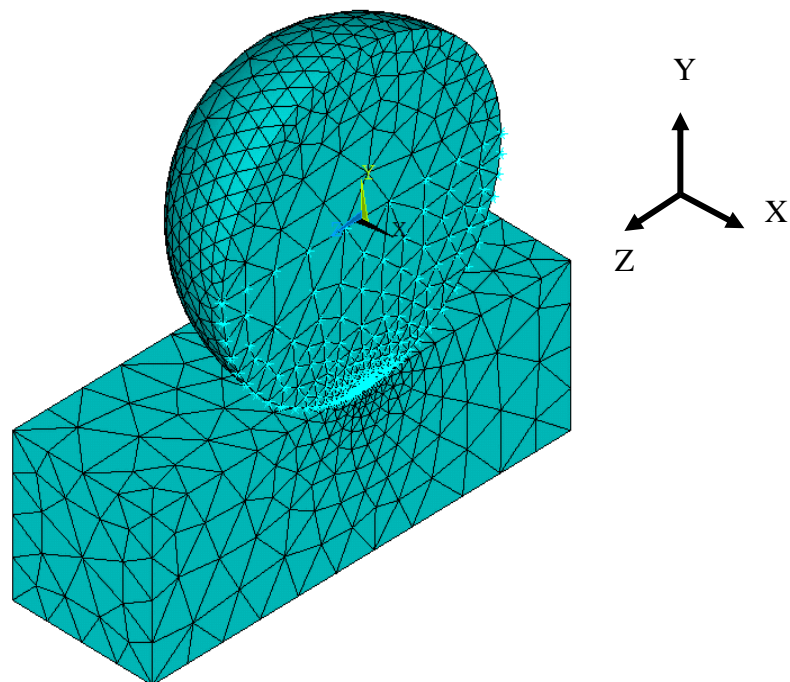


**Figure 4-8** Half 3D FE model of the rolling ball and planar dental composite

### 4.3.2 Boundary and loading conditions

Boundary conditions are derived from the stress equilibrium equations governing loading conditions between a rigid sphere and elastic-plastic body. Different approaches have been used by different researchers, such as considering a very small volume element of the deforming elastic-plastic half-space [Johnson, 2003], considering transverse isotropic elastic half-space [Liao and Wang, 1997] or considering theory of elasticity [Timoshenko and Goodier, 1951]. This study uses Johnson [2003] approach to develop a mathematical model of the boundary conditions. Schematics showing the initial condition, loading condition and after loading are shown in Figure 4.9.

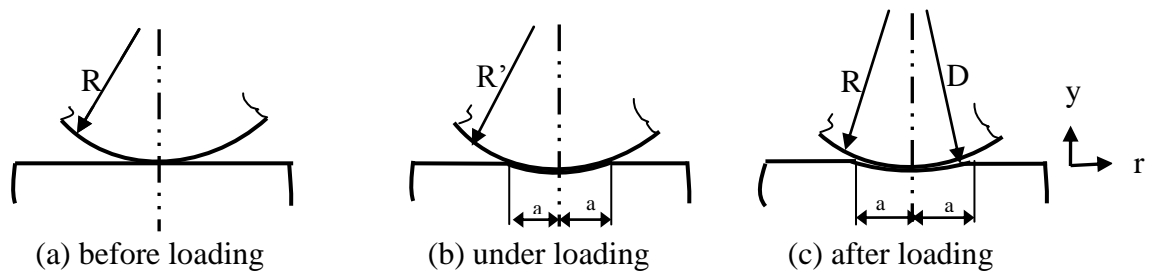


**Figure 4-9** Contact loading boundary conditions

It is assumed that during loading the elastic half space goes well into the plastic range and the deformation differences between loading and unloading is no longer small. Despite the large plastic deformation, it is intuitive to expect the unloading process is perfectly elastic. The indentation loading has an equivalent radius  $R'$  that is somewhat larger than the radius  $R$  due to elastic compression of the specimen. Upon removing the loading, a shallow indentation is noted on the specimen due to the elastic recovery of dental specimen with a permanent radius  $D$  which is also larger than  $R'$ . If the unloading is elastic and reversible, a repeat loading behaves elastically when the radius  $R$  is pressed into the contact with the concave spherical shape of radius  $D$ . For shallow indentation, Hertzian contact theory still applies and the permanent radius  $D$  and depth of penetration can be related to the radius of indentation ball [Johnson, 2003]. It is emphasized that the process has limitations because it assumes the pressure distribution before unloading obeys Hertzian distribution and the recovered profile is an arc. Unloading will always leave the dental composite in a state of residue stress. Therefore, it is important to know the stress at the end of the plastic loading. This can be accurately done using FEA [Fischer-Cripps, 1999].



During the plastic indentation, the material of the dental specimen beneath the ruby ball experience permanent compression in the direction perpendicular to the surface and radial expansions parallel to the surface. Releasing the ball causes the stresses normal to the surface to relieve where as the permanent radial expansion of the deformed specimen induces a radial compressive stress. The compressive stress is applied by the surrounding elastic material of the dental composite. Thus, the residual compression stresses in the boundary layer of the filler and polymer matrix in the subsurface and surface region propagates the fatigue damage. Hence, during plastic and elastic unloading of the half-space, the deformation stresses can be deduced along the axis of symmetry as outlined in equation 4.11 and 4.12 respectively:

$$|\sigma_y - \sigma_r| = Y \quad (4.11)$$

$$|\sigma_r - \sigma_y| = KP_m = KcY \quad (4.12)$$

Where  $\sigma_y$  and  $\sigma_r$  are normal and radial stresses in the contact region,  $K$  is a constant which depends on the mean contact pressure ( $P_m$ ) at the end of loading and upon the depth below the deformed surface of the half space and  $Y$  is the yield stress of the dental half space and  $c$  is the elastic-plastic boundary radius. Equating 4.11 and 4.12 gives the residue stress differences due to the permanent deformation as shown in equation 4.13

$$|\sigma_r - \sigma_y|_r = (Kc - 1)Y \quad (4.13)$$

The boundary conditions at the contact surface are set as follows:  $(\sigma_y)_r = 0 \text{ N-mm}^{-2}$  when  $y = 0 \text{ mm}$ , and its value in the subsurface region is very small compared with  $(\sigma_r)_r$ . During full plastic deformation,  $c \approx 3$  and the pressure distribution is approximately uniform, giving  $K=0.65$  at  $y=0.64a$ . This makes  $(Kc-1) \approx 0.95$  confirming strain hardening effect and the dental composite cannot elastically return to its original form. On the other hand, at the immediate contact surface, a different scenario exists. Considering uniform contact pressure  $p$ ,  $\sigma_y = -p$ ,  $\sigma_r = \sigma_\theta = -(p-Y)$ . Elastic unloading set over the surfaces stresses  $\sigma_y = p$ ,  $\sigma_r = \sigma_\theta = 0.5(1+2\nu)p \approx 0.8p$ , similarly leaving residual stresses equivalent to  $(\sigma_y)_r = 0 \text{ N-mm}^{-2}$ ,  $(\sigma_r)_r = (\sigma_\theta)_r = Y - 0.2p$ . In indentation,  $p=3Y$  for a fully plastic deformation, giving  $(\sigma_r)_r = (\sigma_\theta)_r \approx 0.4Y$  which is a tensile stress. Otherwise, the stresses in the plastic zone outside the contact area are given by the cavity model

where  $a \leq r \leq c$ . In this case  $c$  is the elastic-plastic boundary radius and  $c > a$  [Johnson, 2003]. Note that  $r$  is the maximum radial contact length ( $r = a_{max}$ ) at the maximum depth of penetration. The analysis deduces that the rigid-elastic-plastic half space contact induces a multi axial stresses and strains on the deformable dental composite. Principally, the contact stresses due to an elastic-plastic indentation in which the strains remain small can calculated or evaluated using FEA.

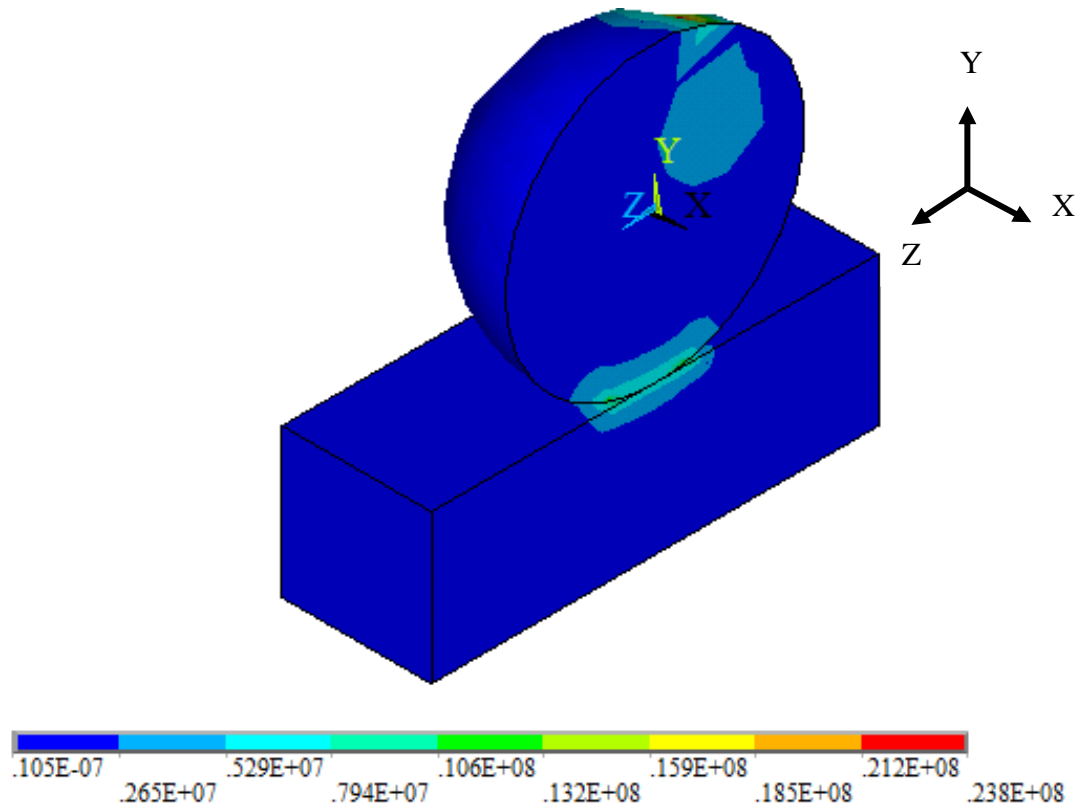
The 3D planar model was constrained in all DOFs except along the symmetrical axis and the faces forming the contact pair. One analysis using the highest contact load of 4N was simulated and analysed as a representation of the 2-4N test range. Important parameters evaluated from the FEA included initial and final deformation, nodal stress, principal and von Mises stresses and contact pressure. The stresses resulting from the displacement of the contacting node were used in real stress loading cycles of the material in order to theoretically determine the loading cycles and contact fatigue.

#### **4.3.3 Convergence test**

Convergence was checked by beginning with a coarse mesh (default size 6) and then refining to finer meshes of sizes 3 and 1, while observing the contact force convergence criteria of 0.001. It was noted that the nodal solution for mesh sizes 6 and 3 varied by 5%, whereas that of mesh size 1 did not converge during the entire run time. Therefore, the mesh 3 solution was considered optimally sufficient for the simulation.

#### **4.4 FEA results**

The FEA results are presented in two parts. The first part shows the stress concentration when the contact load is just brought into contact with the specimen. Only one contact load of (4N), which is the maximum predicted testing used in this research, is simulated in the static and rolling simulation. Figure 4-10 shows the contour nodal solution of the contacting bodies brought in contact with a 2N (or equivalent total 4N) force, without rolling. Owing to the static nature of the loading, principal and von Mises stresses were analyzed because the shear stress components were expected to be small.



Contour stress display is in  $\text{N/m}^2$

**Figure 4-10** Static loading von Mises stress contour plot

Figure 4-10 shows that deformation is virtually non-existent, at only  $0.435\mu\text{m}$  depth. The average von Mises stress is  $10.6\text{MPa}$  which is significantly low in terms of permanently deforming the dental composite despite the maximum being  $23.8\text{MPa}$ . The results obtained from the static FEA can be inferred along with those of the undeformed analytical analysis using a  $2.5\text{N}$  load in Section 4.2.

Figure 4-11 shows the principal and von Mises stresses summarized in a distribution plot below the contact point within the dental composite. The principal stresses are at a maximum on the contact surface and reduce logarithmically to zero with an increase of the nodal distance from the contact surface. The stresses are mainly compressive along the direction of applied load (y axis), reaching a maximum of  $5.9\text{MPa}$  at the contact surface. In contrast, the von Mises stress is somewhat higher at  $7.1\text{MPa}$  peak on the contact surface, decreasing with depth to  $0.5\text{MPa}$  at  $1\text{mm}$  depth.

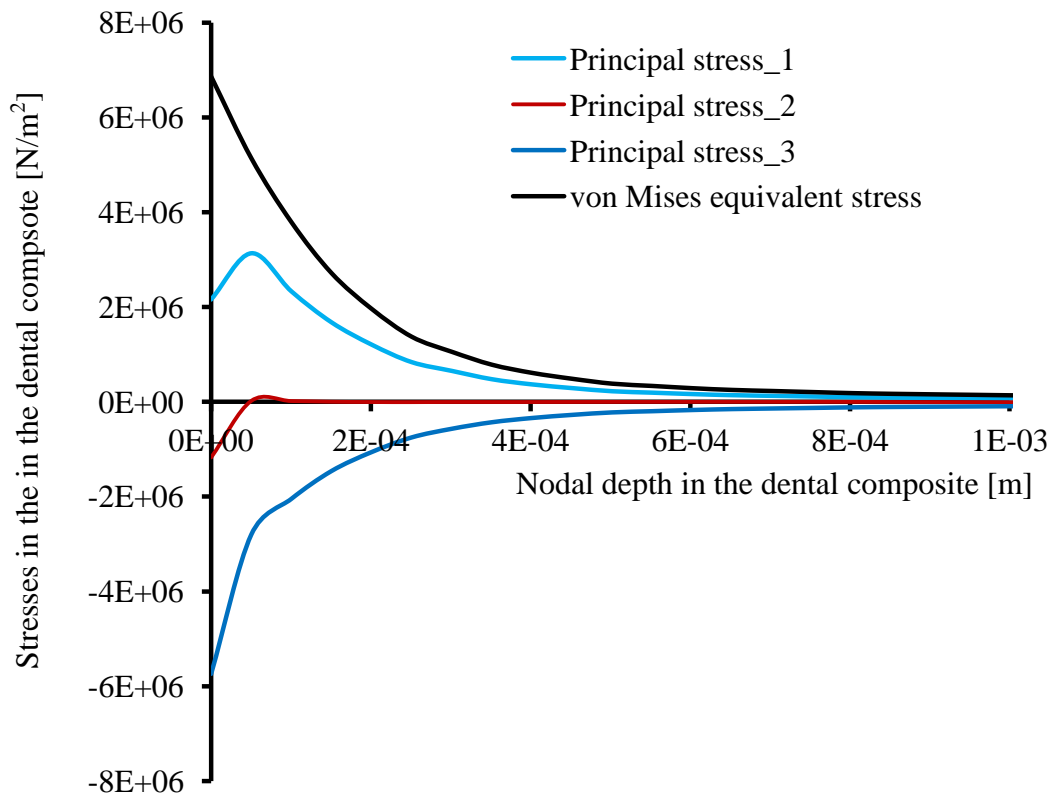


**Figure 4-11** Stress distributions along the contact region in static loading

The second stage simulates rolling contact and analyzes the stresses induced on the dental composite specimen. The axial stresses can be observed from the contour plots in Figures 4-12 to 4-15 in the three axes during the rolling motion. The non-conformal rolling of the ruby ball on the surface of the dental composite induced a localized, three-dimensional state of stress, as described in the literature [For example, Johnson, 1985, Alfredsson, 2000] The equivalent fatigue stress is derived solely from the normal maxima and minima stresses for the three axes; therefore, the equivalent fatigue stress is derived from them using the von Mises failure criteria.

It can be observed that the stress field translates through the dental composite as the ball rolls due to compression-tension effects. Figures 4-12 to 4-13 show stress distributions along the axis of symmetry. Combined tension-compression is noted due to the rolling motion. As the ball rolls, the material ahead of the ball and underneath the contact zone is squeezed and then released after the passing of the ball. This is shown by the piling-up nature of the dental composite in the rolling direction. The cyclic tension-compression induces high subsurface stresses which initiate micro-cracks along the material subsurface interlayer boundaries.

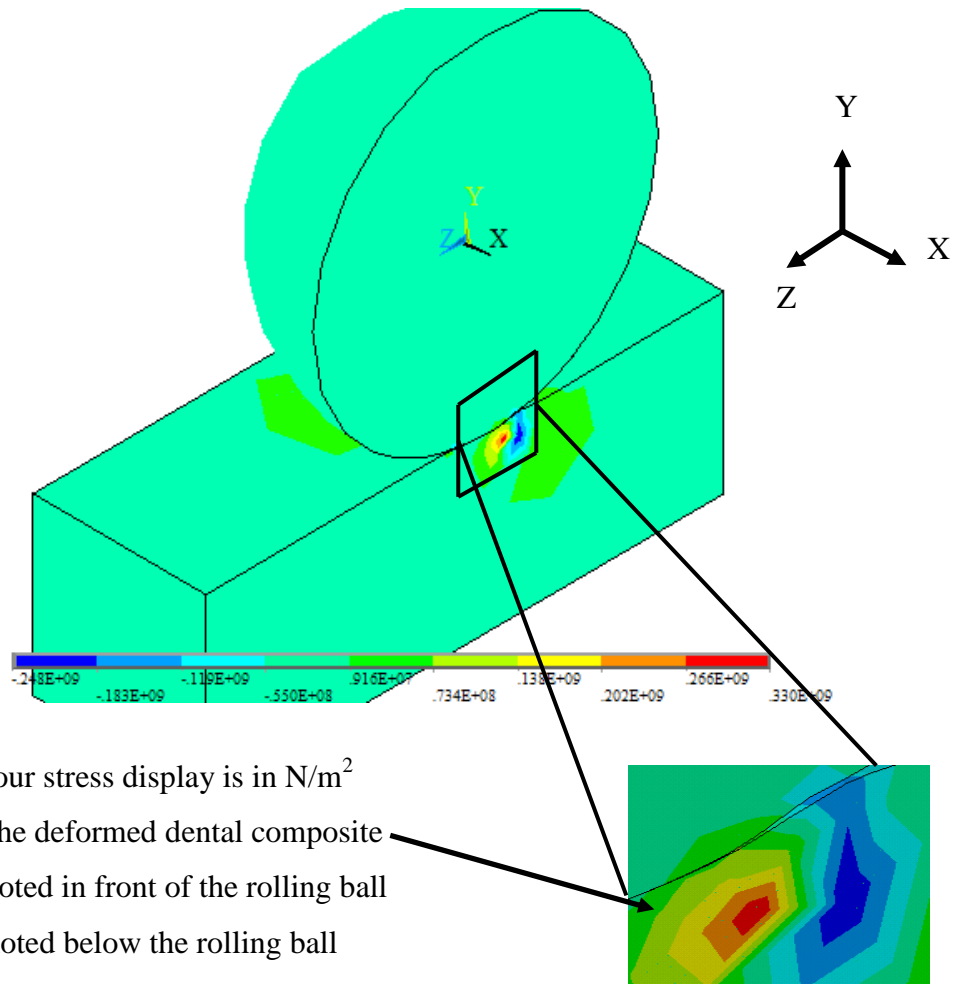
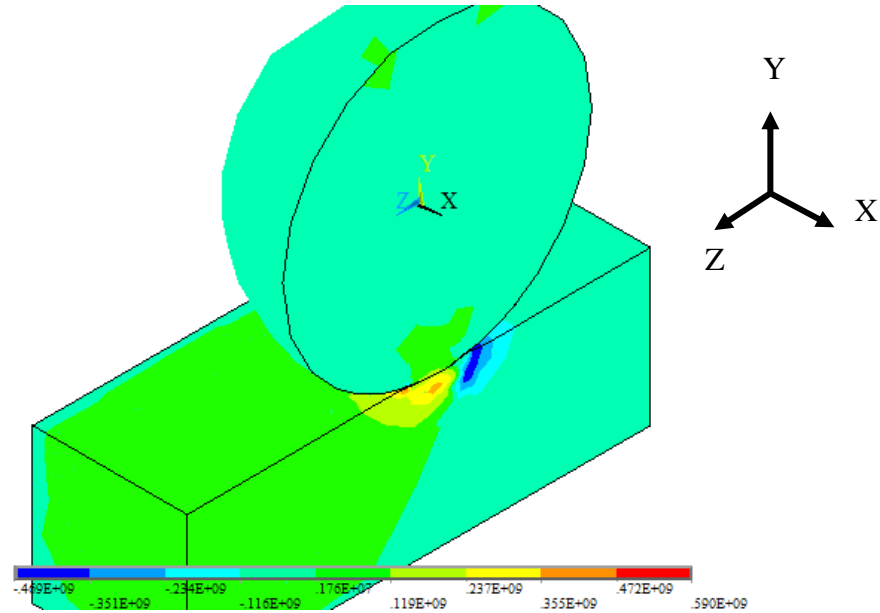


**Figure 4-12** Distribution of stress contour in x-axis direction

Eventually, the subsurface micro-cracks propagate to the surface to form a relatively large spall. Normally, the weak points are glass fillers and resin matrix bond interfaces. They have maximum shear stress and can exhibit weakness resulting from the mechanical finishing processes [Baran et al, 1998]. The micro-cracks grow with time to the surface and cause spalling failure. Spalling failure is the dominant mode of failure in rolling contact in finely polished materials such as dental composites [Slack and Sadeghi, 2010; Santus et al, 2012]. Compressive-tensile stresses due to the compression of the material in front of the rolling ball and expansion due to relaxation just behind the ball are shown along the x and z axes in the contour plots in Figure 4-12 and 4-13 respectively. Whereas a maximum compressive stress of 248MPa exists along the x-axis, the compressive stress is much higher along the z-axis (i.e. the rolling direction) with a maximum value of 469 MPa in the pile-up region ahead of the ball as shown in Figure 4-13. The maximum deformation on the dental composite was 142 $\mu\text{m}$ .

In contrast, a maximum tensile stress of 590MPa exists immediately before the pile-up in the x-axis and behind the rolling ball in the z-axis due to the expansion and relaxation of the material structure, as explained by Harass et al [2010]. This demonstrates the complex deformation the material undergoes during rolling contact.

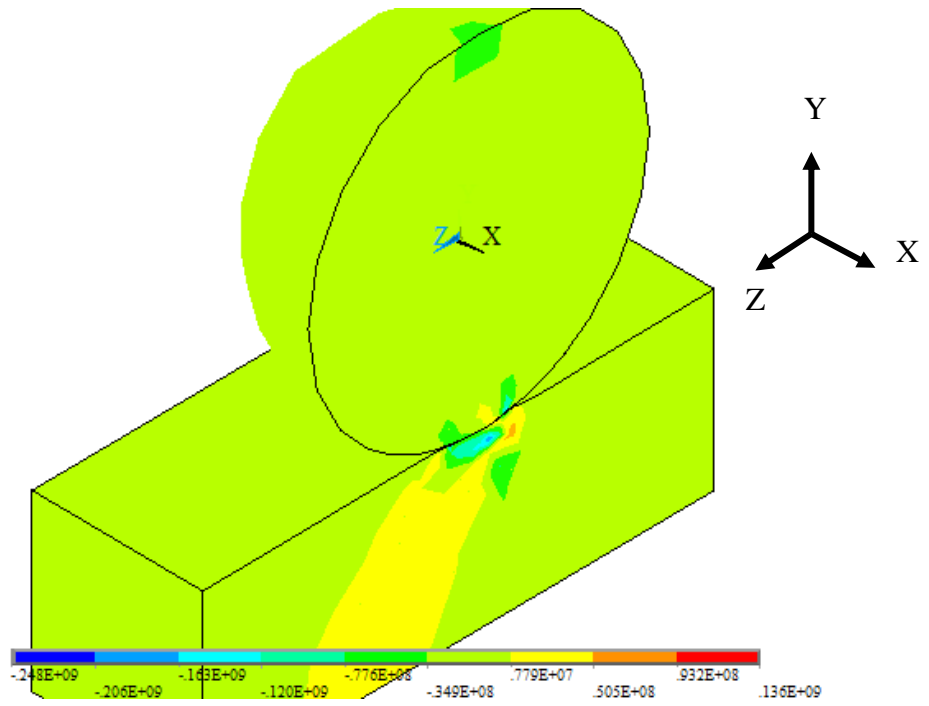


Contour stress display is in  $\text{N/m}^2$

Rolling motion is in -Z direction

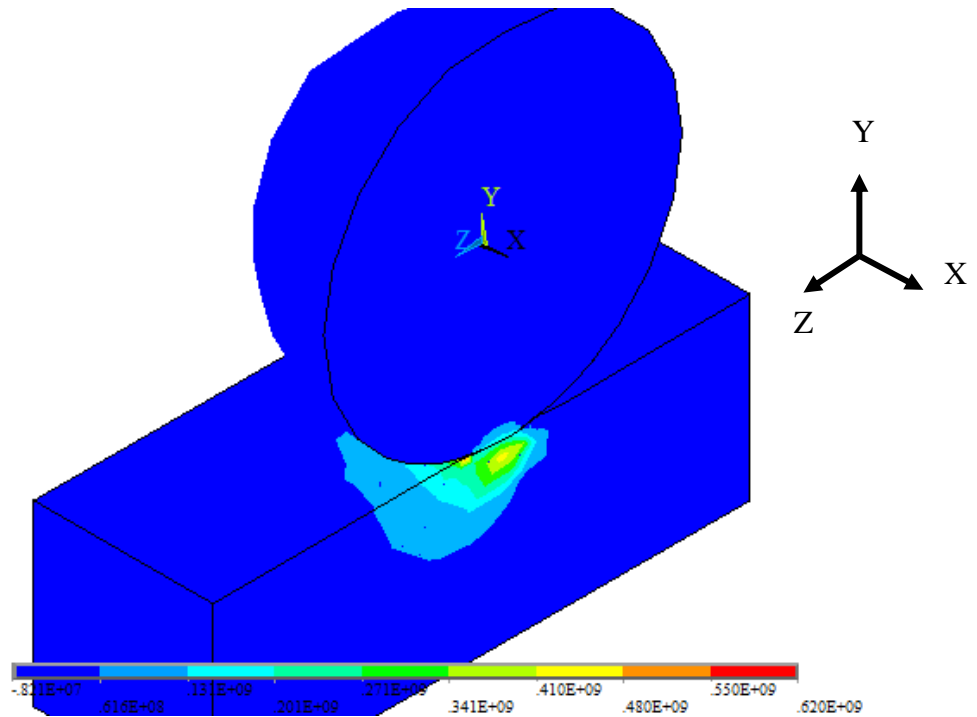
**Figure 4-13** Distribution of stress contour in z-axis direction

Figure 4-14 shows combined compression-tension under the contact surface with a maximum compressive stress of 248MPa, which is somewhat higher than the yield strength of the dental composite. Based on the level of stresses observed, it is expected that the dental composite is transformed from the elastic to the elastic-plastic state due to the rolling motion of the ball, thus increasing the amount of hardening. Figure 4-15 displays a contour plot of the equivalent von Mises stresses, which are higher than the axial and transverse stresses with a maximum value of 620MPa. The complex multi-axial loading combining compressive, tensile and shear stresses prompts the use of von Mises failure criteria to evaluate the equivalent fatigue stress in computing the fatigue life of the dental composite.



Contour stress display is in N/m<sup>2</sup>  
 Rolling motion is in -Z direction

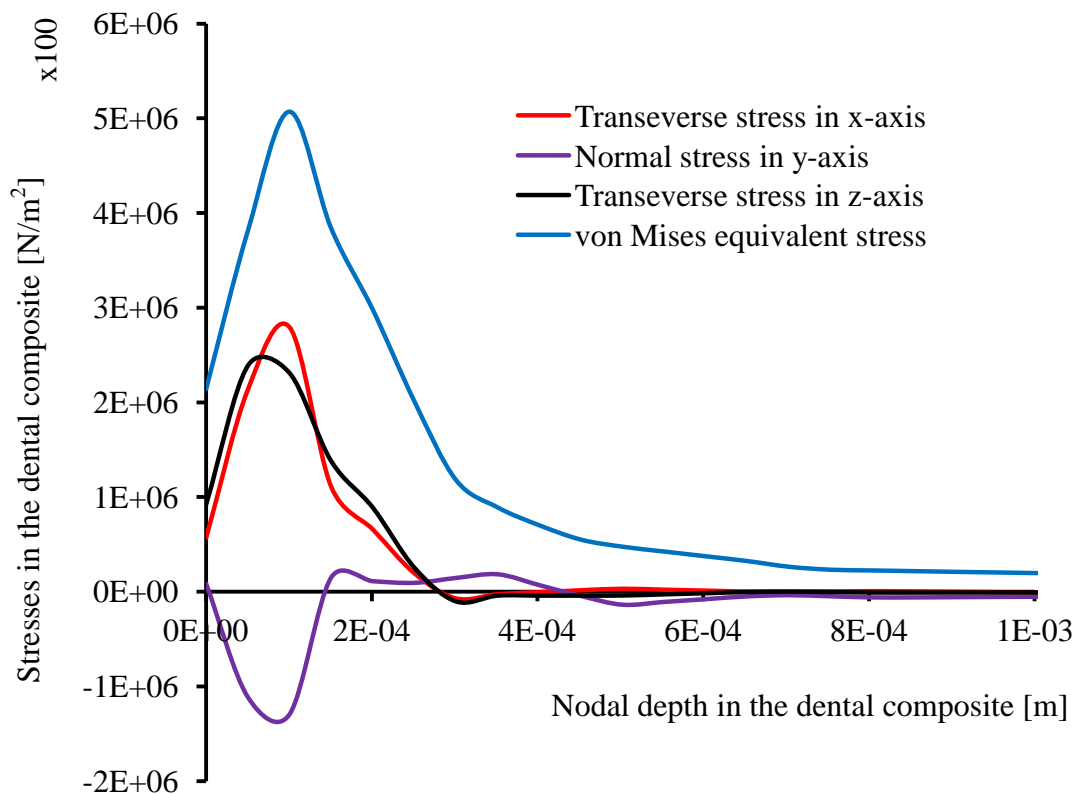
**Figure 4-14** Distribution of stress contour in y-axis direction



Contour stress display is in N/m<sup>2</sup>  
 Rolling motion is in -Z direction

**Figure 4-15** Distribution of von Mises stress contour plot

A corresponding graphical comparison of the subsurface and surface axial and von Mises stresses below the rolling contact is shown in Figure 4-16. The plot complements the observations in Figure 4-12 to 4-15 by showing that the maximum stresses in the transverse x and z axes are tensile stresses and maximum compressive stress exists in the normal loading axis. In contrast to static contact, the rolling contact stresses do not rise and fall together. A number of factors, such as lack of proportionality in the localized phase change, micro-plasticity, the applied load, induced residual stresses, fillers orientation and the size and composition of the filler material as well as the curing treatment, all contribute to the variation of stress concentration during rolling contact [Sadephour et al, 2003]. The normal and von Mises stresses due to rolling agree very well with the analytical solutions and indentation test results. It is further observed that the peak stresses are at 0.1mm below the surface.



Stress magnitude is in hundreds (x100)

**Figure 4-16** Stress distributions along the contact region in cyclic loading

It is further noted that compressive stresses exist below the surface, while tensile stresses dominate the x and z axes on nodes near the rolling contact ball. All the stresses rise to their maximum peak at 0.1 mm depth and fall to their constant magnitude of



7.5MPa at 0.5 mm depth. The evolution of spalling emerges after numerous rolling cycles, requiring a fatigue model to predict the failure time of the dental composite under rolling contact.

#### 4.5 Fatigue Life Prediction Based on FEA Analysis

The fatigue life of dental composites under rolling contact is predicted using the stress-based life approach and the Basquin relationship [Kim, 2003; S raml et al, 2003 Anastasios and Keller, 2011; Singh et al, 2011]:

$$N = \left( \frac{\sigma}{2^b * \sigma'_f} \right)^{\frac{1}{b}} \quad (4.14)$$

where  $N$  is number of stress cycles to failure,  $\sigma$  is the equivalent fatigue stress,  $b$  is the fatigue strength exponent which ranges from -0.04 to -0.125, and  $\sigma'_f$  is the fracture compressive strength of the material undergoing fatigue testing. The method is proposed as an alternative to the empirical estimation line method used by McCabe et al [1997; 2000] and Fujii et al [2004].

Often, the prediction of the fatigue life of materials uses two approaches: stress-based fatigue life, also known as high cycle fatigue (HCF); and strain-based fatigue life or low cycle fatigue (LCF). In addition, the stress-based fatigue life approach differentiates between the formation (initiation) and propagation (growth) of the surface contact fatigue cracks. The two approaches are schematically shown in Figure 4-17. It can be deduced from Figure 4-17 that the LCF regime comprises early crack formation and a prolonged propagation time, whereas the HCF regime comprises prolonged crack formation and a short propagation time (i.e. rapid crack growth) in relation to total life. Depending on the material properties concerned and crack formation models used, the low cycle fatigue (LCF) approach is more suitable for brittle materials and those experiencing crack formation in less than  $100 \times 10^3$  load cycles, while stress-based or high cycle fatigue (HCF) models apply to ductile materials or those experiencing crack formation after more than  $100 \times 10^3$  load cycles.

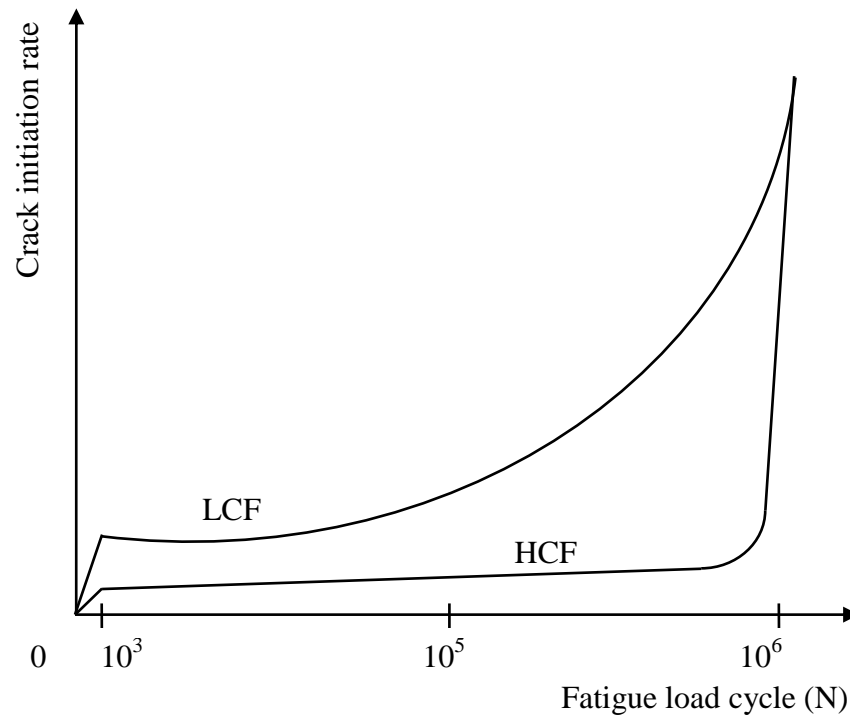


**Figure 4-17** Conceptual differences between LCF and HCF [Kim et al, 2003]

Previous research by McCabe et al [1999; 2000] and Fujii et al [2004] has established that dental composites can withstand tens of thousands of load cycles before any surface fatigue is initiated. The fatigue failure scenario indicated that the material failed due to high cycle fatigue (HCF), and thus a stress-based fatigue life approach, (HCF) was used to predict the fatigue life of the specimen under rolling contact.

Dental composites exhibit combined levels of ductility and brittleness depending on their composition, curing method and service conditions. Moreover, it has been established using FEA that rolling contact causes a pulsating compression-tension on the dental composite specimen. The equivalent fatigue stress ( $\sigma$ ) to use in the Basquin equation must be derived using the Goodman diagram shown in Figure 4-18 and the FEA multi-axial stresses induced by the rolling contact. Referring to Figure 4-18,  $\sigma_u$  and  $\sigma_y$  are respectively the ultimate tensile/or compressive and yield strengths of the material. The equivalent fatigue stress is evaluated from the FEA multi-axial stresses due to the cyclic compression in front of the rolling ball and cyclic tension from the expansion and relaxation of the material behind the rolling ball, using equation 4.15:

$$\sigma = \frac{\sigma_a}{1 - \frac{\sigma_m}{\sigma_u}} \quad (4.15)$$

Additional interpretation of the parameters of equation 4.13 is elaborated in Figure 4-19, in which  $\sigma_a$  and  $\sigma_m$  are the equivalent alternating and mean stresses as expressed in equations 4.16 and 4.17 for the uni-axial loading.

$$\sigma_a = \frac{\sigma_{\max} - \sigma_{\min}}{2} \quad (4.16)$$

$$\sigma_m = \frac{\sigma_{\max} + \sigma_{\min}}{2} \quad (4.17)$$

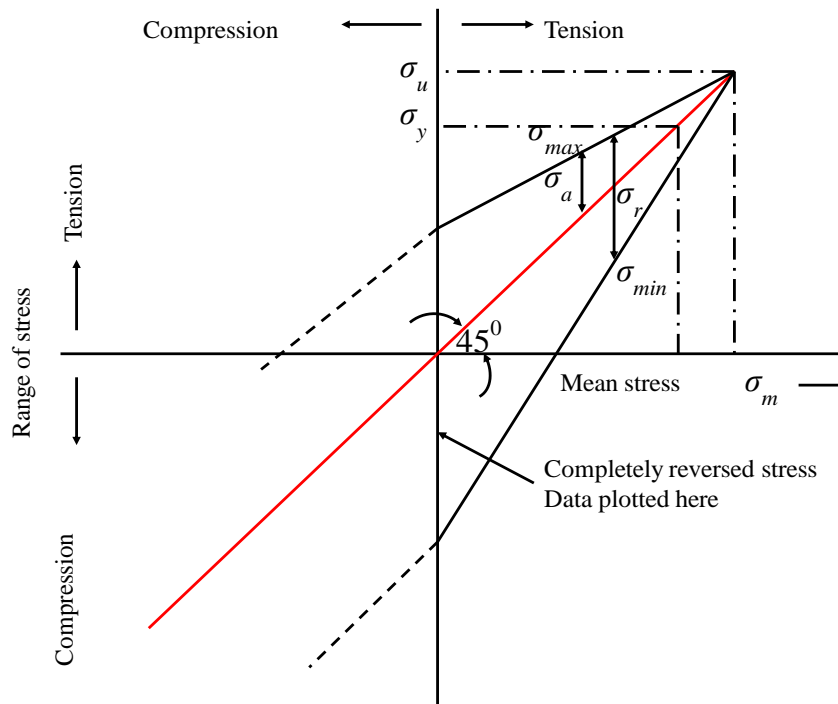
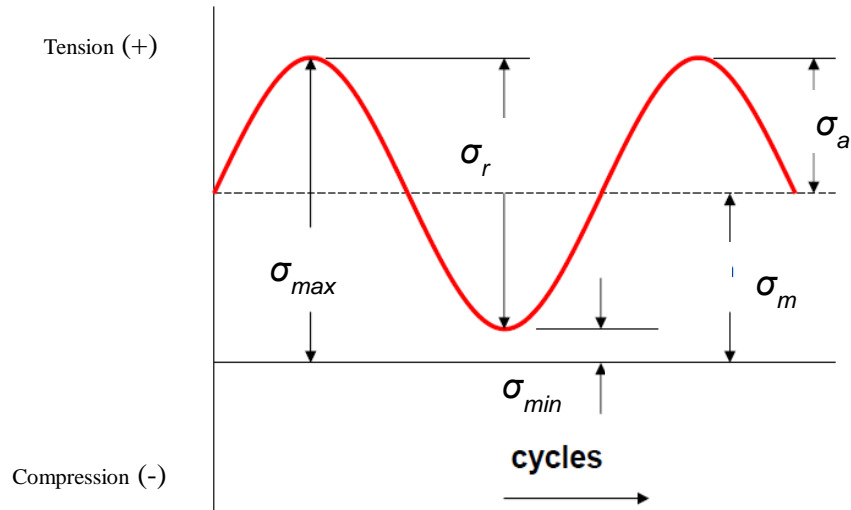


**Figure 4-18** Modified Goodman diagram showing limit and range of stresses

It is difficult to measure the compressive yield strength of the dental composite in the actual experiment. Referring to the MSDS [[www.coltene.com](http://www.coltene.com) accessed on 12.09.2013], the compressive yield strength is 392MPa. The indicated value is for the material yielding only, and often much higher values are needed to fracture the dental composite under compressive rolling. Thus, the maximum plastic strength (i.e. the maximum work hardening strength) is chosen as the fatigue strength coefficient.



[Legend:  $\sigma_{max}$  is maximum stress,  $\sigma_{min}$  is minimum stress,  $\sigma_r$  is stress range,  $\sigma_a$  is alternating stress,  $\sigma_m$  is mean stress]

**Figure 4-19** Nomenclature of fluctuating stress parameters in fatigue loading

This corresponds to the maximum contact pressure under the ball (Hertzian stress) obtained from indentation experiments. Table 4-3 shows the mean results of five hardness tests ( $N = 5$ ) conducted on one of the dental composites used in this research, where Synergy D6 was used to establish the mechanical properties of the specimen. The indentation test depth was  $30\mu\text{m}$  using a 200gm load. The row labelled  $\bar{x}$  contains the mean value, and  $s$  indicates the standard deviation and  $v$  the variance of the test parameters.

**Table 4-3** Laboratory hardness test for Synergy D6 composite

| Series<br>$n = 5$ | HM<br>N/mm <sup>2</sup> | HMs<br>N/mm <sup>2</sup> | H <sub>IT</sub><br>N/mm <sup>2</sup> | HV(H <sub>IT</sub> ) | E <sub>IT</sub><br>kN/mm <sup>2</sup> | W <sub>total</sub><br>Nmm | W <sub>elast</sub><br>Nmm | C <sub>IT</sub><br>% | R <sub>IT</sub><br>% | $\eta_{IT}$<br>% | Begin $m$ (hr)<br>N | End $m$ (hr)<br>N |
|-------------------|-------------------------|--------------------------|--------------------------------------|----------------------|---------------------------------------|---------------------------|---------------------------|----------------------|----------------------|------------------|---------------------|-------------------|
| $\bar{x}$         | 438                     | 490                      | 620                                  | 58.58                | 12.64                                 | 0.009                     | 0.003                     | 5.68                 | -2.43                | 36.31            | 1.87                | 1.18              |
| $s$               | 48                      | 13                       | 77                                   | 7.28                 | 0.83                                  | 0.000                     | 0.000                     | 0.41                 | 0.37                 | 0.24             | 0.02                | 0.01              |
| $v$               | 10.95                   | 2.70                     | 12.43                                | 12.43                | 6.58                                  | 1.29                      | 1.17                      | 7.25                 | -15.23               | 0.67             | 0.84                | 0.84              |

[HM: Martens hardness, HMs: Martens hardness (slope of force/indentation depth curve), H<sub>IT</sub> : Indentation hardness, E<sub>IT</sub>: Indentation modulus, W<sub>total</sub>: Total indentation work, W<sub>elastic</sub> :Elastic indentation work, C<sub>IT</sub> : Indentation creep, R<sub>IT</sub> : Indentation relaxation,  $\eta_{IT}$  : Indentation elastic share, Begin  $m$ : beginning force (load), End  $m$ : ending force (load)]

The FEA has demonstrated that rolling contact involves multi-axial loading stresses and strains. The equivalent alternating and mean stresses induced on the deformed dental

specimen are estimated based on the von Mises criterion as defined in equations 4.18 and 4.19, in which  $\sigma_{ai}$  and  $\sigma_{mi}$  are the alternating principal stresses and mean stresses:

$$\sigma_a = \frac{1}{\sqrt{2}} * \sqrt{(\sigma_{a1} - \sigma_{a2})^2 + (\sigma_{a2} - \sigma_{a3})^2 + (\sigma_{a3} - \sigma_{a1})^2} \quad (4.18)$$

$$\sigma_m = \frac{1}{\sqrt{2}} * \sqrt{(\sigma_{m1} - \sigma_{m2})^2 + (\sigma_{m2} - \sigma_{m3})^2 + (\sigma_{m3} - \sigma_{m1})^2} \quad (4.19)$$

Equation 4.18 is not sensitive to hydrostatic stresses and always produces a positive equivalent mean stress. This is resolved by using another approach to evaluate equivalent mean stresses by summing the principal stresses, as in equation 4.20 [Potocnick et al, 2010]. This equation is often used in compressive loading, and provides a better representation of the beneficial effect of the compressive mean stresses that result in crack closing and lead to slower crack propagation:

$$\sigma_m = \sigma_{m1} + \sigma_{m2} + \sigma_{m3} \quad (4.20)$$

Based on the multi-axial maximum and minimum principal stresses evaluated by the rolling contact FEA analysis and equations 4.18 and 4.19,  $\sigma_a$  and  $\sigma_m$  have been established mathematically to be 300MPa and 45.5MPa respectively. The maximum work hardening strength is obtained from Table 4-3 as 620MPa. The Basquin exponent ( $b$ ) varies between -0.04 and -0.06 for multi-directional glass fibre composites [Anastasios and Keller, 2011]. Smaller values of  $b$  indicate a steeper S-N curve. However, Basquin exponents ranging between -0.05 and -0.048 were used with equation 4.14 to establish the Synergy D6 composite fatigue life ranged from  $209 \times 10^3$  and  $359 \times 10^3$  load cycles. The Synergy D6 composite fatigue life correlates well with previous experimental results from McCabe et al [1997; 2000] and Fujii et al [2004] evaluated using the arithmetic line estimation method at  $5\mu\text{m}$  with micro-filled and hybrid composites.

In addition, the FEA and the Basquin equation yield a qualitative estimation of surface contact fatigue as it relates to the occurrence with spalling. Moreover, the FEA modelling has demonstrated that it is possible to combine theoretical analysis and actual rolling ball tests to predict the fatigue life of dental composite specimens. This is a timely and cost effective method. Based on the findings, the prediction of the fatigue life of dental composite restorations in service can be established in advance and managed.

## **4.6 Summary**

The stress-based approach to predict surface contact fatigue and the fatigue life of dental composite restorations is quite encouraging. Future work will characterize more precisely surface contact fatigue parameters by using Voronoi tessellation finite element (Voronoi FE) with the capability to incorporate additional clinical conditions such as microstructure properties, microstructure crack spalling simulation, surface roughness, bilinear properties, residue stress and progressive cyclic loading and number of cycles. Additionally, the development of a quadrilateral element with the ability to re-mesh the contact surface after each pass can provide the stable simulation behaviour of the hydrostatic stress.

## **CHAPTER 5 DESIGN OF THE MECHATRONIC MEASUREMENT SYSTEM**

The mechatronic measurement system is derived from the prototype device by optimizing its mechanical, electrical and electronic hardware. The optimized design is integrated with embedded control hardware and software systems in order to enable real time control and data acquisition. Systematic design approaches [Pahl and Beitz, 1996] as summarized in Figure 5-1 and from Pugh [1991] were used to select optimum mechanical and electrical hardware, whereas a modular design concept [Tseng and Jiao, 1997] was applied to develop the electronics for the embedded hardware. The design optimisation process focused partly on conceptual design and especially on embodiment design, because the ground design tasks have already been accomplished in the previous design prototypes.

### **5.1 Mechatronic Design Specifications**

From the preliminary investigation and experiments, several areas for improvement have been established. The key attributes of the envisaged mechatronic system are to establish a real-time operation and control of the drive system, online acquisition of the test data and post processing, and the ability to mimic the oral environment and monitor the surface fatigue process. Addressing these attributes; the following preliminary design requirements were set:

- (a) The system should run continuously for a defined number of load cycles (typically  $10^6$ ); enabling online data sampling after every  $10^5$  load cycles.
- (b) The device should provide a continuous light compression force (i.e. 1-10N) throughout the test process.
- (c) The device should be based on an embedded processor and have a suitable graphical user interface (GUI).
- (d) The main actuator should be a small servo-motor operating in a speed control mode.
- (e) The device should have an automatic monitoring and data acquisition system.

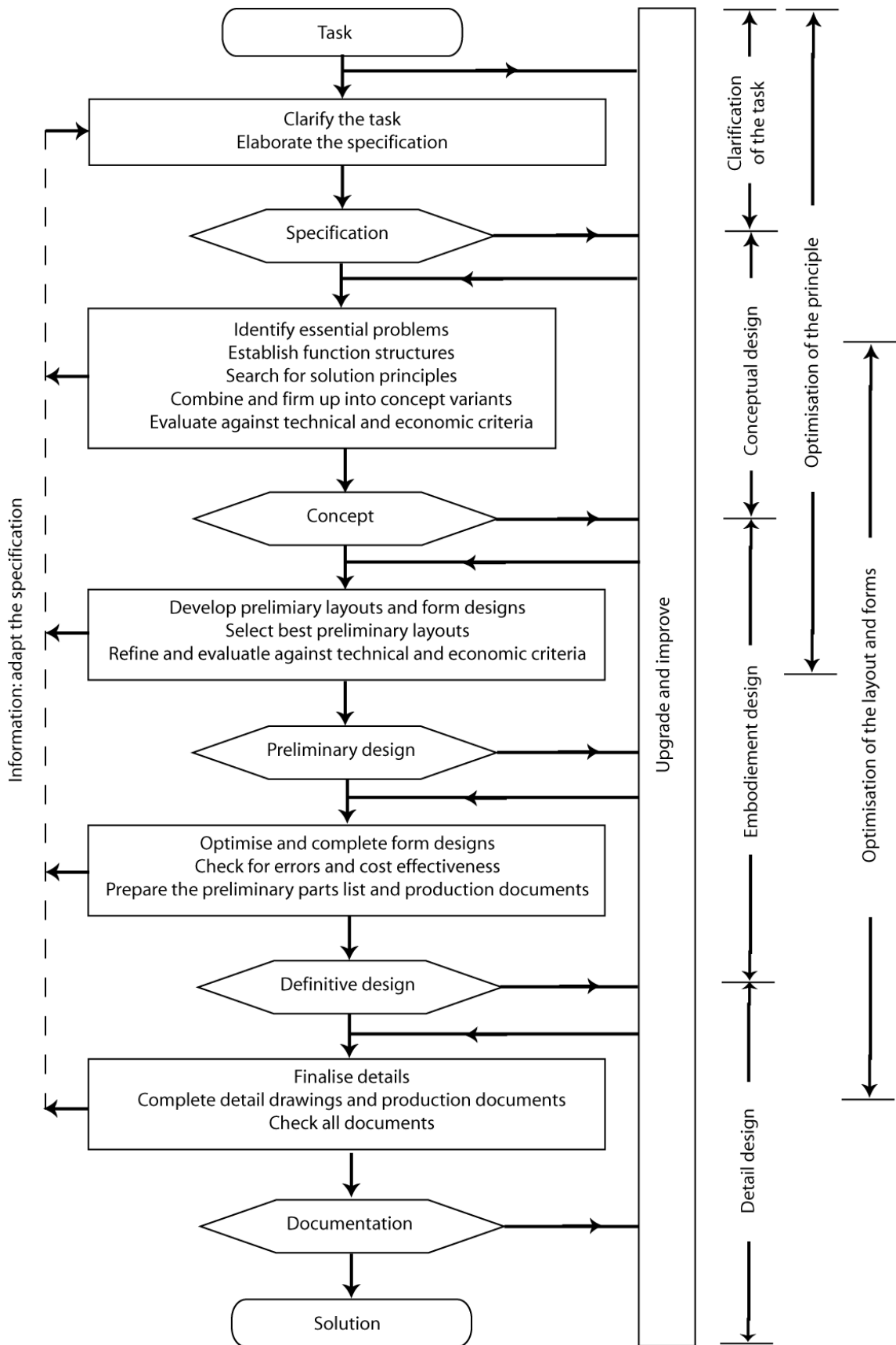


**Figure 5-1** Systematic design approach method [Pahl and Beitz, 1996]



- (f) The device should simulate the real oral environment in terms of temperature and lubrication
- (g) The device should enable the quick setting of the specimen and the ball on their holding accessories.
- (h) The device should be stable, compatible, portable and have scope for module upgrading and multi-station integration.

The requirements apply to fields across mechanical, electrical, electronic and embedded systems design. Therefore, a multidisciplinary design optimization (MDO), is illustrated in Figure 5-2, was simultaneously used to exploit the interactions between disciplines to enhance throughput of the design process.

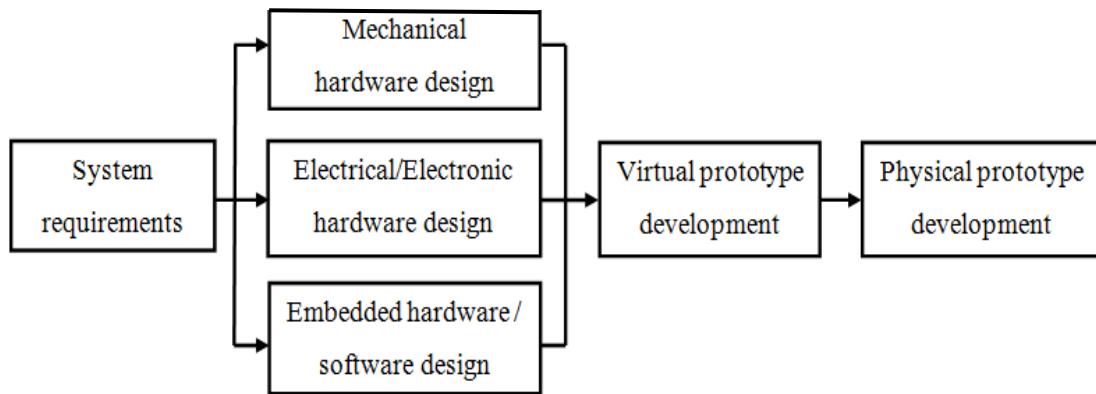


**Figure 5-2** Design synthesis and optimization process flow

The specific design requirements were clarified to suit the selection of each component or configuration. Several specific requirements were established, as listed in Table 5-1. The specific requirements were synthesized based on ISO/TS 14569-2:2001 and ISO 3:1973 specifications for preferred numbers and functionalities gathered from the previous prototypes. This led to the retention of some features of the previous prototypes and optimization of others to develop a mechatronic system to meet the ISO/TS 14569-2:2001 specifications.

**Table 5-1** Clarified design requirements for the mechatronic measurement system

| No | Group                    | Design requirements and constraints                              |
|----|--------------------------|--|
| 1  | Layout and configuration | 1. Vertical layout<br>2. Horizontal layout<br>3. Inclined layout |

| No | Group                                | Design requirements and constraints   |
|----|--------------------------------------|---|
| 2  | Fatigue actuator                     | 1. Brushed dc servo motor<br>2. Brushless dc servo motor  |
| 3  | Sensing                              | 1. Displacement sensors<br>2. Optical sensors<br>3. Ultrasonic sensors<br>4. Accelerometers   |
| 4  | Control and data sampling technology | 1. PIC microcontroller<br>2. DSC microcontroller<br>3. Digital signal processor (DSP)   |
| 5  | Load/Force (1-10N)                   | 1. Dead weight and cable loading<br>2. Pneumatic loading<br>3. Beam and spring loading  |
| 7  | Medium of and size                   | 1. Steel ball<br>2. Ceramic ball<br>3. Aluminium oxide  |
| 8  | Test temperature                     | 1. Ambient (20-25 <sup>0</sup> C)<br>2. Constant (20 <sup>0</sup> C or 37 <sup>0</sup> C)<br>3. Thermo-cyclic (5-55 <sup>0</sup> C) |
| 9  | Nature of test and friction          | 1. Wet test (distilled water, saliva has 99.5% of pure water [ De-Almeida et al, 2008)<br>2. Dry test                               |
| 10 | Performance                          | 1. Constant frequency<br>2. Variable frequency  |
| 12 | Operation                            | 1. Manual<br>2. Semi-automatic<br>3. Fully automatic  |
| 13 | Human machine interface (HMI)        | 1. Graphical user interface (GUI)<br>2. Command driven interface (CDI)<br>3. Human-machine switching console                        |
| 14 | Noise and vibration                  | 1.No noise and external vibration   |

### 5.1.1 Design synthesis and trade-off analysis

In the evaluation and selection of appropriate configurations, components, subsystems, operation, off-the-shelf parts, materials and manufacturing process, an iterative process was employed which involved the evaluation of possible alternatives against specific set criteria to recommend an optimum configuration, components or process. The iteration process is summarized in the flow chart in Figure 5-3.

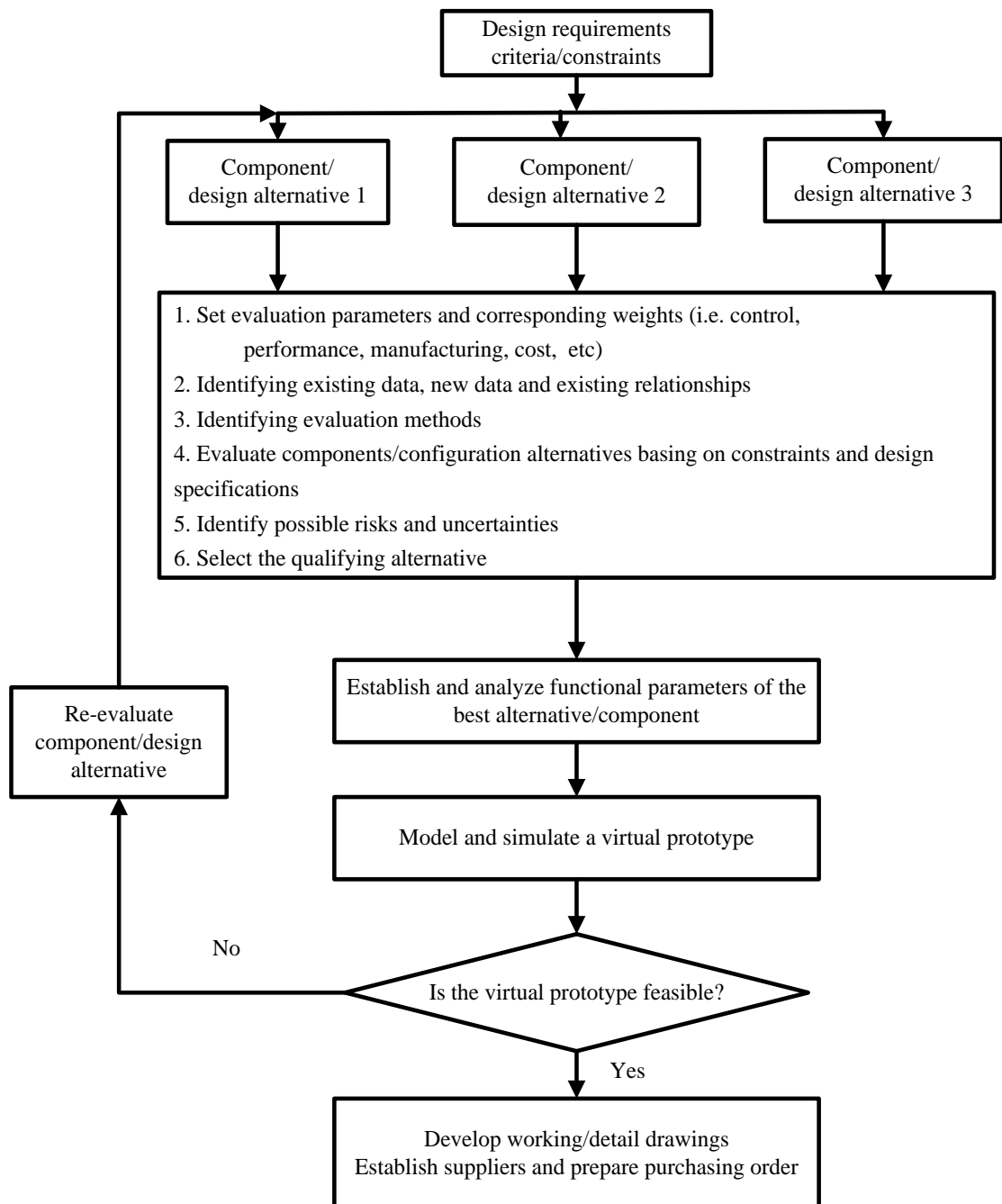


**Figure 5-3** Mechatronic system design optimisation flow

## 5.2 Mechatronic Hardware Design

The hardware design involved the selection and synthesis of mechanical, electrical and electronic components. The emphasis on the design process was on the selection and the integration of standard and off-shelf calibrated parts from manufacturers to enhance design optimization. Therefore, this section focuses on the rationale behind the selection of the following hardware: (a) device structural frame (b) actuator and mandrel drive train (c) sensors and data acquisition unit (d) specimen holding carriage (e) quick release clamp fixture (f) lubrication system (g) heating and control system and (h) vibration isolation module.

### 5.2.1 Working principle and frame design

The principle of the surface fatigue process using a rolling ball is presented in Figure 5-4. The ruby ball is held between a grooved mandrel and the dental specimen using a dead weight, cable and pulley pre-loading system. The cable is firmly attached to the specimen carriage which is mounted on a low-friction linear bearing.

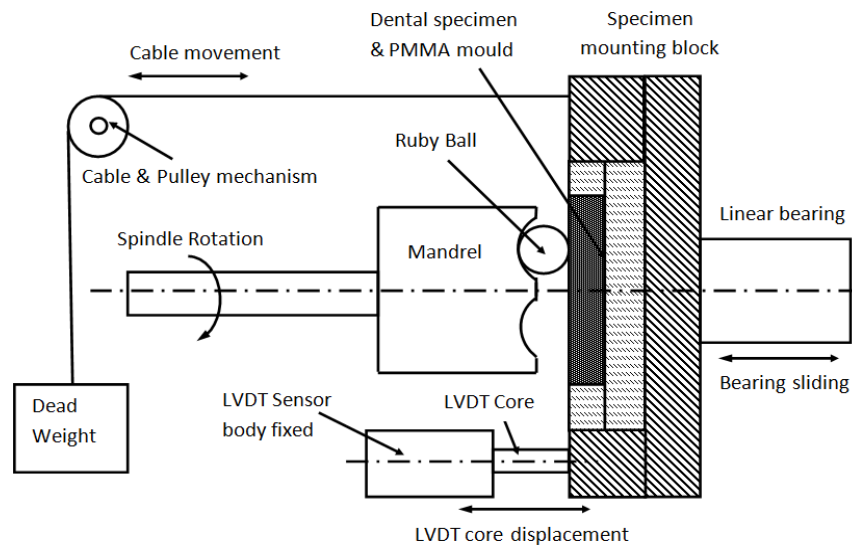


**Figure 5-4** Schematic of the cyclic rolling ball surface fatigue process

The LVDT transducer body with a through bore is mounted and locked onto the device frame, and its magnetic core is mounted on the specimen carriage. This allows the transducer core to displace freely within the transducer bore when the specimen carriage translates. The LVDT modulator/demodulator outputs a DC voltage proportional to the transducer's output, which is acquired and processed by a data acquisition system. The

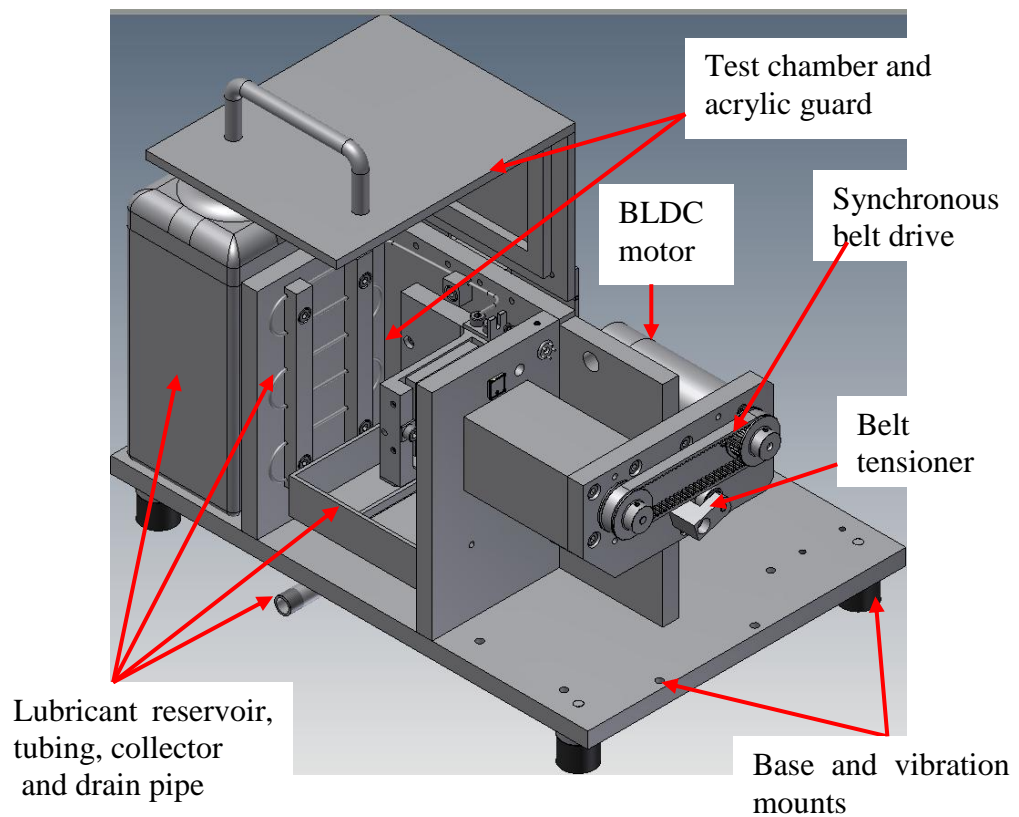
transducer operation is detailed in Section 6.4. The displacement (in  $\mu\text{m}$ ) measured after a specified number of load cycles by the LVDT transducer determines the depth of the surface fatigue track on the dental specimen. The depth characterizes the resistance to wear of the dental material specimen. The mandrel drive is provided by a synchronous toothed belt and an electric DC motor. Referring to Figure 5.4, the device can be mounted vertically, horizontally or inclined, preferably at  $45^\circ$  to take advantage of the vertical and horizontal layout. Nonetheless, an optimum layout can only be deduced by synthesizing the merits and demerits of each layout. The device layout contributes to a user-friendly human-machine interface, the manufacturing costs, ball and specimen loading, compatibility, portability, and so on. Three layouts are feasible, and a decision matrix analysis (DMA) was used to compare the selected aspects of merit against each layout alternative, as depicted in Table 5-2. Ranking was based on +1 to indicate that the merit has a positive influence on the layout, -1 to indicate the merit has a negative influence on the layout, and 0 to indicate a neutral influence.

**Table 5-2** DMA for evaluating the mechatronic device frame

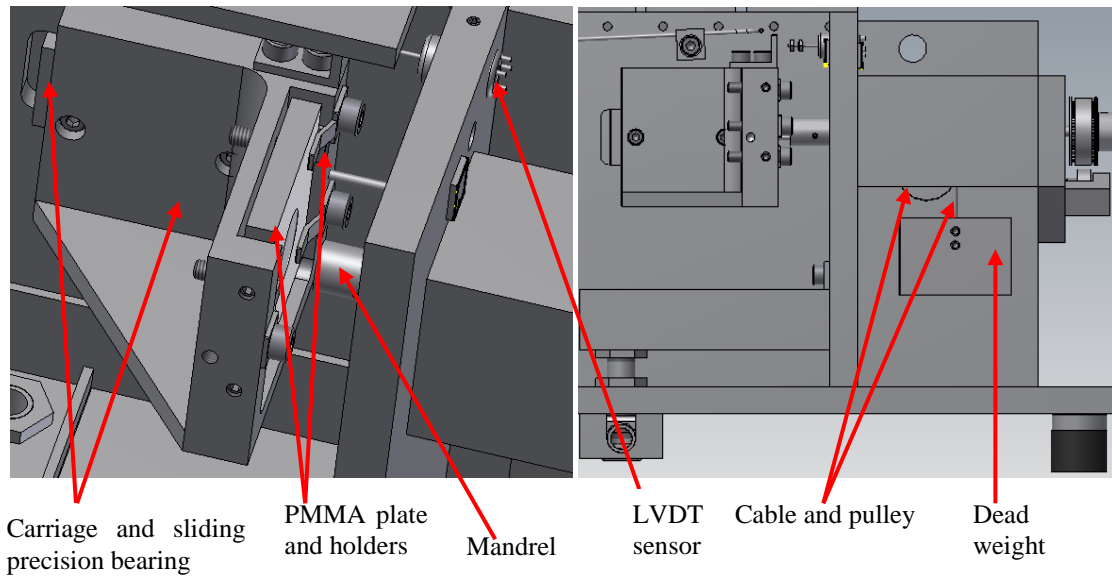
| No  | Aspects of merit              | Weighting (%) | Vertical frame | Horizontal frame | Inclined frame |
|-----|-------------------------------|---------------|----------------|------------------|----------------|
| 1.  | Design simplicity             | 15            | +1             | +1               | -1             |
| 2.  | Ease of manufacturing         | 15            | +1             | +1               | -1             |
| 3.  | Manufacturing costs (low)     | 12            | +1             | +1               | -1             |
| 4.  | Easy ball loading             | 10            | +1             | -1               | +1             |
| 5.  | Easy specimen loading         | 10            | 0              | +1               | +1             |
| 6.  | Stability and rigidity        | 10            | -1             | +1               | +1             |
| 7.  | Fatigue debris free falling   | 10            | -1             | +1               | +1             |
| 8.  | Spindle inertia loading (min) | 9             | +1             | -1               | +1             |
| 9.  | Compatibility and portability | 5             | 0              | 0                | 0              |
| 10. | Maintainability               | 7             | +1             | +1               | +1             |
|     | Total                         | 100           | 0.46           | 0.58             | 0.12           |

From Table 5-2, the horizontal layout emerged with the highest positive ranking, followed by a vertical frame design. While the horizontal layout would allow free falling (self-washing) of fatigue debris and maintain good stability, the vertical frame design would perform better in retaining the ruby ball in position. Therefore, the horizontal layout was selected for the embodiment design.

The device frame is subject to small static loading and does not require strength analysis under load. Emphasis was put on a simple design which could be easily manufactured and assembled at low cost. Bearing in mind, the stringent conditions for designing medical devices, materials for the frame were selected to meet these requirements. KASTAL 300 which is an improved 5000 series aluminium alloy plate of 10mm thickness was used for the manufacturing the frame. This material has high strength and is pre-milled on both sides to very close thickness and flatness tolerances. KASTAL 300 is recommended for medical application devices, and its typical mechanical and physical properties are detailed on the Kastal 300 data sheet. A virtual model of the designed mechatronic rolling ball device is presented in Figure 5-5.



(a) Drive-side (right side) view



(b) Sliding carriage concept                      (c) Cable and dead weight concept

**Figure 5-5** Interaction of different parts' models of the rolling ball device

### 5.2.2 Contact fatigue actuator drive

The cyclic rolling actuation of surface contact fatigue on the dental specimen narrows the choice of actuators to electric servo motors. Maxon's DC servo motors have robust and compact design with improved performance characteristics compared to other servo motors of the same specifications due to the ironless winding technology used, as described in Maxon's Ironless winding technology data sheet [Maxon, 2011]. It was also necessary to choose between brushed and brushless servo motors, which prompted the designer to synthesize the performance characteristics of the two types of servo motors with respect to the desired application. The performance characteristics tabulated in Table 5-3 were used to optimize the selection.

**Table 5-3** Characteristics of BLDC and Brushed DC motors

| Feature                      | Brushless DC servo motor                            | Brushed DC servo motor                                    |
|------------------------------|---|---|
| Commutation                  | Electronically commuted using hall position sensors | Electrically commutated using carbon brushes (Slip rings) |
| Motor control                | Complex and expensive                               | Simple and inexpensive                                    |
| Life                         | Longer  | Shorter   |
| Speed/torque characteristics | Flat  | Moderately flat, reduce with increase speed               |

| <b>Feature</b>            | <b>Brushless DC servo motor</b>              | <b>Brushed DC servo motor</b>  |
|---------------------------|--|--|
| Output power/weight ratio | High due to superior thermal characteristics | Moderate to low to enable air cooling gap                              |
| Manufacturing costs       | High due to permanent magnets on the rotor   | Low  |
| Motor efficiency          | High, no voltage drop across brushes         | Moderate   |
| Speed ranges              | High, no brushes/commutator limitations      | Low, mechanically limited by brushes                                   |
| Maintenance               | Less, there is no brushes                    | Requires periodic maintenance  |
| Control requirements      | Controller is needed to keep motor running   | No need of controller except for variable speeds                       |
| Rotor Inertia             | Low, improves dynamic responses              | High, limits dynamic responses   |
| Electrical noises         | Low noise, no brushes                        | High noise caused by brush generated electromagnetic inductance (EMI). |
| Reliability               | High   | Low  |

To enhance actuator optimisation, the selection criteria were broadened to include commutation and motor control, speed-torque characteristics, output power-weight ratio, dynamic responses (influence of inertia load), motor efficiency, speed ranges, and initial costs. The weighting of each characteristic was ranked basing on +1 for a positive influence of a characteristic, -1 for a negative influence of a characteristic, and 0 to indicate a neutral influence of a particular characteristic with regard to the design requirements.

Referring to Table 5-4, the BLDC servo motor was a preferred actuator because it has significantly improved characteristics compared to the brushed DC servo motor. Its high initial cost, expensive commutation and control technology can be overcome by savings in performance reliability and low maintenance costs.



**Table 5-4** Decision matrix table (DMA) for selecting optimum DC servo motor

| No  | Characteristic of Merit      | Weighting (%) | Brushed DC servo motor | Brushless DC servo motor |
|-----|------------------------------|---------------|------------------------|--------------------------|
| 1.  | Performance reliability      | 15            | 0                      | +1                       |
| 2.  | Low electrical noises        | 15            | -1                     | +1                       |
| 3.  | Inexpensive motor technology | 12            | +1                     | -1                       |
| 3.  | High motor efficiency        | 10            | +1                     | +1                       |
| 6.  | Motor initial cost           | 10            | +1                     | -1                       |
| 7.  | Low maintenance              | 10            | -1                     | +1                       |
| 4.  | Speed/torque characteristic  | 10            | 0                      | 0                        |
| 8.  | Low inertia losses           | 6             | +1                     | +1                       |
| 9.  | Output power/weight ratio    | 6             | 0                      | +1                       |
| 10. | Speed ranges                 | 6             | 0                      | 0                        |
|     | <b>Total</b>                 | 100           | 0.17                   | 0.4                      |

To select an appropriate size for the BLDC servo motor, speed and torque requirements had to be decided upon. It was important to decide the type of mandrel drive to compensate for the axial expansion of the motor shaft, due to changes in motor temperature. Fortunately, a solution to this problem had been realized in the immediately preceding prototype rig, in which a synchronous toothed belt drive was designed and successfully applied. The same drive was adapted in this design.

Three parameters were used to estimate the motor size, peak torque required for the application ( $T_P$ ), root mean square torque ( $T_{RMS}$ ), and operating speed range. The peak torque was calculated by summing the load torque ( $T_L$ ), torque due to inertia ( $T_J$ ) and torque required to overcome friction ( $T_F$ ). A safety factor of 20% was added to the peak torque to account for miscellaneous losses. Equation 5-1 was used to estimate the peak torque requirements of the servo motor:

$$T_P = (T_L + T_J + T_F) * 1.2 \quad (5.1)$$

The schematic of the mandrel drive system is illustrated in Figure 5-6 whereas Figures

5-7 and 5-8 show velocity vs. time and torque vs. time curves that have been used to estimate the peak and RMS torques.

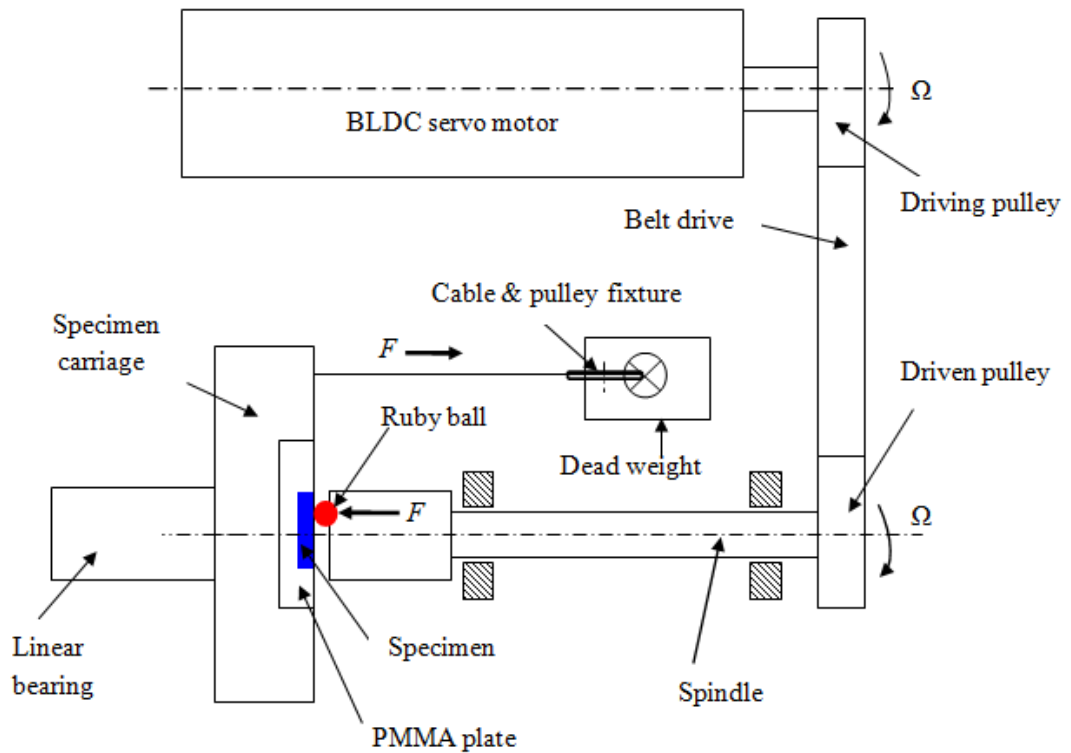


**Figure 5-6** Illustration of the synchronous toothed belt drive system

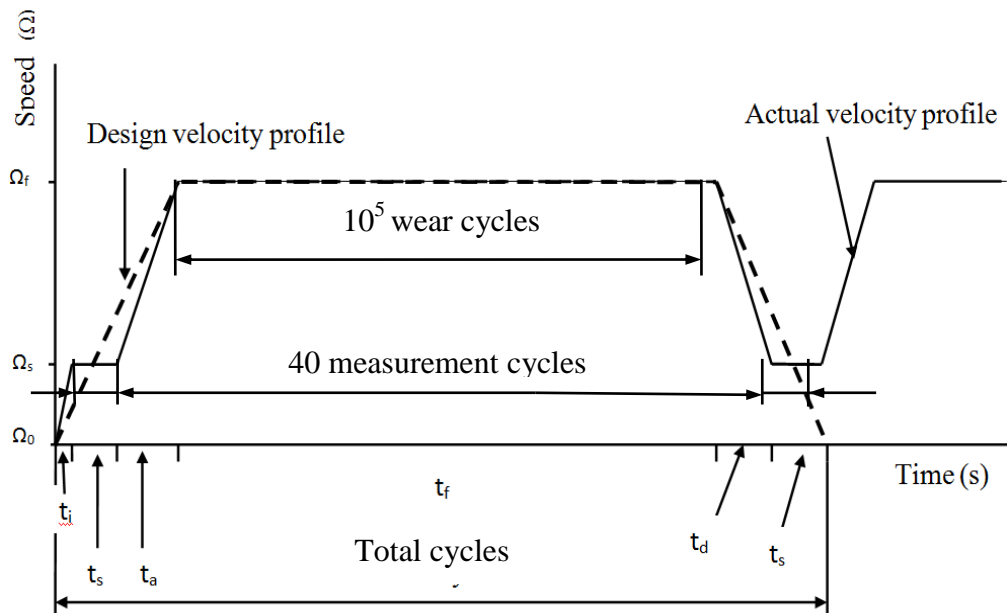


**Figure 5-7** BLDC servo actuator trapezoidal speed profile

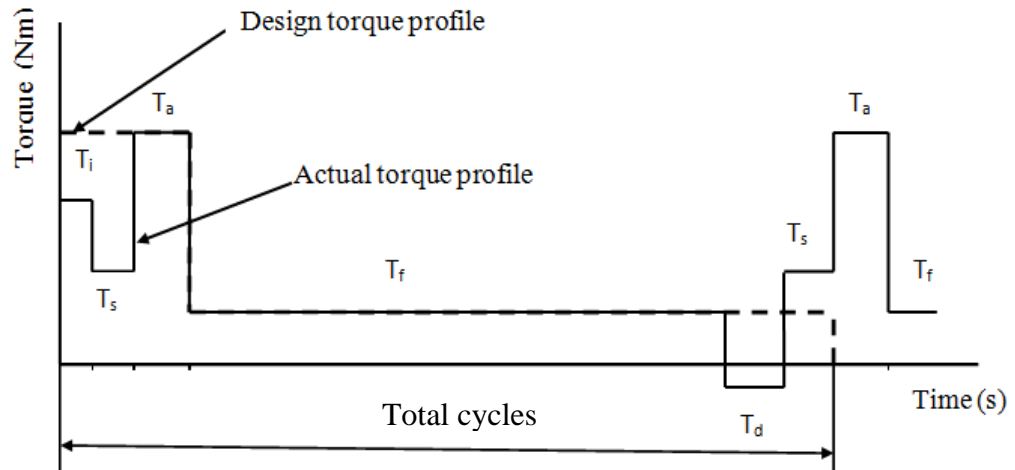


**Figure 5-8** BLDC servo actuator torque profile

$t_i$ : initial acceleration time (s)

$T_i$ : initial acceleration torque (Nm)

$t_s$ : sampling time (s)

$T_s$ : sampling speed torque (Nm)

$t_a$ : surface fatigue acceleration time(s)

$T_a$ : fatigue speed accelerating torque (Nm)

$t_f$ : surface fatigue actuating time (s)

$T_f$ : surface fatigue actuating torque (Nm)

$t_d$ : surface fatigue deceleration time (s)

$T_d$ : the deceleration torque (Nm)

$\Omega_0$ : standstill position (zero speed) (rpm)

$\Omega_s$ : sampling speed (rpm)

$\Omega_f$ : surface fatigue actuating speed (rpm)

Considering Figure 5-7, the actual velocity profile one cycle which include sampling cycles and fatigue actuation cycle is shown. The inertia effect of every mechanical elements making-up the drive train as shown in Figure 5-8, including driving shaft and the force exerted by the pre-loading system were used to estimate the load and friction torques. The estimated load torque is 25.4 mNm based on the quantitative design analysis in Appendix A2.1. Using the torque calculated, the desired peak voltage and current were estimated at 5.242V and 1.97A as shown in the analysis in Appendix A2.1. Using Maxon BLDC servo motor catalogue, EC-max 30-model 272766 was chosen rated supply voltage and current of 12V and 2.83A respectively. The EC-max model 272766 is shown in Figure 5-9 with shaft extension in both ends was selected. The short shaft extension mounts an encoder for measuring speed whereas the long extension mounts driven elements such as pulleys, mandrels and gears.



**Figure 5-9** EC-max 30 (model 272766) brushless dc servo motor [Maxon, 2011]

### 5.2.3 Contact force loading and sensing module

The mechatronic rolling ball device includes a pre-compression loading unit comprising a linear bearing, a LVDT transducer to measure wear depth, a specimen mounting carriage, and a dead weight attached to a pulley and rope mechanism. The dead weight and cable and pulley arrangement has been synthesized and optimised against the pivot beam, spring and pneumatics loading arrangement in the second prototype design, and thus it has been adapted in this new design with slight layout modifications.

### 5.2.4 Precision linear sliding bearing

An IKO Precision linear sliding bearing (re-circulating ball type BSR 2040SL) shown in Figure 5-10 was selected to provide a linear displacement of the specimen mounting carriage. It has a light weight and compact linear rolling motion guide, and is made from a stainless steel sheet by precision forming. Other features are its high accuracy, high performance, safety and durability, which make it the correct choice for this application. See Appendix A2.2 for more details.

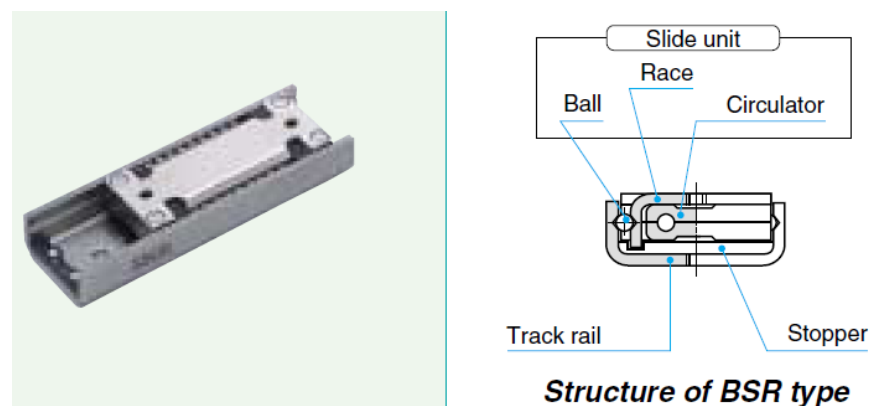


**Figure 5-10** Schematic of precision linear bearing [www.ikont.co.jp]

### ***5.2.5 LVDT wear transducer***

The surface wear due to surface fatigue is detected and measured using a linear voltage differential transformer (LVDT), model SM1 M922935A233-03 from Solatron Technology with a linear output range of  $\pm 1$ mm. The specimen carriage is mounted on the precision linear bearing and the sliding core of the LVDT is clamped onto the carriage using a fixture. The LVDT's body is clamped firmly on the intermediate cross bracket and aligned with the core. A cable and pulley mechanism ensures constant the pre-loading of the specimen against the cyclic rolling ball during the test. See Appendix A2.3 for detailed specifications.

### ***5.2.6 LVDT Hybrid Simulator and Demodulator***

The LVDT transducer uses a hybrid oscillator and demodulator (see Figure A2-3) to provide the excitation voltage and output signal conditioning. The oscillator provides a sine carrier of 5Vrms at 5 or 10 kHz for driving the transducer and a square wave reference for the demodulator. The demodulator amplifies the output from the transducer and converts it to a DC voltage. It provides a nominal 5V DC output which can be linear up to 10V for inputs ranging from 0.5Vrms to 7.0Vrms. The output characteristics were refined using external components. Further details are provided in the data sheet.

### ***5.2.7 Specimen carriage***

The specimen carriage is a vital part of the mechatronic rolling ball device since it aligns the dental specimen and provides smooth axial displacement of the LVDT core along its bore. It also connects the dead weight, cable and pulley mechanism to ensure constant and light pre-compression of the specimen against the cycling rolling ball. The carriage contains threaded holes for mounting M4 mm screws. The screws have spherical rolling ball end to provide point contact mounting. The illustration in Figure 5-11 highlights the key features of the specimen carriage. It is machined from KASTAL 300 material to meet lightweight design criterion and resistance to corrosion and oxide scaling.

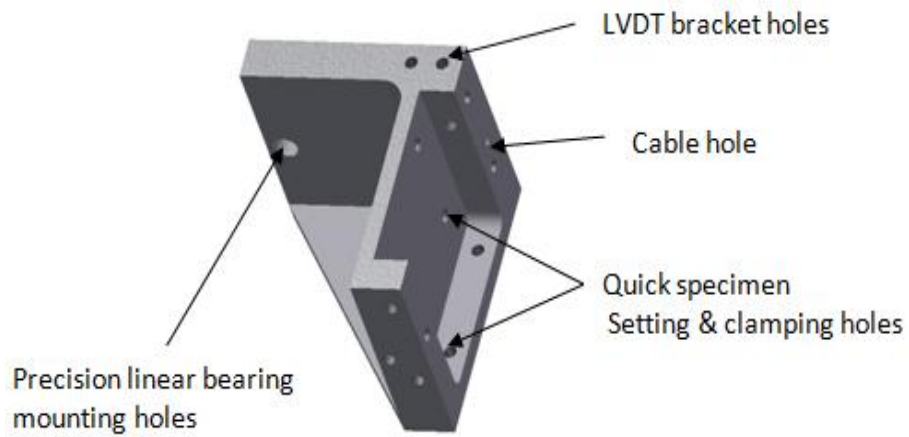


**Figure 5-11** Versatile specimen carriages (not to scale)

Dental specimens are moulded on cavities of diameter 18mm x 1.5mm deep machined on the sides of an acrylic (PMMA) plate of 40 mm x 40 mm x 6 mm, as shown in Figure 5-11. Curing and polishing are performed using the manufacturer's specifications. The carriage's mounting pocket and acrylic plate shown in Figure 5-12 allow four tests on one specimen cast in the mould cavity and a total of eight tests per one PMMA mould plate. The acrylic plate is held and aligned on the carriage using set screws. The dental specimens are cast on the two recesses with a diameter of 18 mm and depth of 1.5 mm as detailed in section 7.5.3.

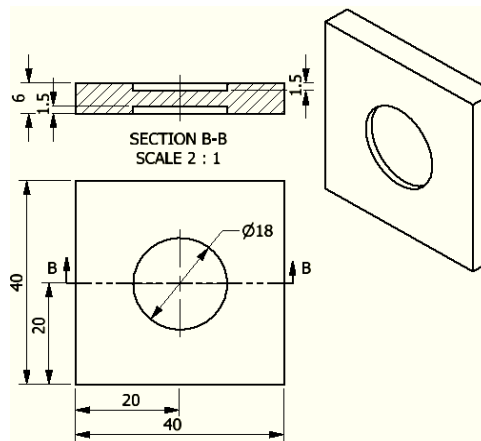


**Figure 5-12** PMMA mould plate for dental specimen (not to scale)

### 5.2.8 Heating System

One of the requirements of the ISO/TS 14569-2:2001 specifications for dental material testing is that in-vitro tests should mimic the oral environment in terms of temperature and lubrication. Tests can be conducted at a constant temperature of 20<sup>0</sup>C or 37<sup>0</sup>C (i.e. ambient or oral temperatures) and/or in thermo-cyclic cooling and heating between 5<sup>0</sup>C

and 55<sup>0</sup>C [Lambrechts et al, 2006].

A number of heating alternatives were assessed, including hot water-bath, cartridge heaters and silicone mats. Cartridge heaters are designed to fit in metal blocks and provide heating through conduction. Silicone heating mats are flexible and available in a variety of shapes to suit different configurations. Having a thin cross-section and light weight, silicone heating mats have low thermal mass and hence provide rapid heat-up characteristics with fast response to temperature control. Each of the heating systems has advantages depending on the nature and type of application.

**Table 5-5** Decision matrix table (DMA) for evaluating heating system

| No | Figure of Merit      | Weighting (%) | Water-bath heating | Cartridge heating | Silicone heating mat |
|----|----------------------|---------------|--------------------|-------------------|----------------------|
| 1. | Initial cost         | 15            | -1                 | +1                | +1                   |
| 2. | Ease of installation | 14            | -1                 | -1                | +1                   |
| 3. | Power consumption    | 13            | -1                 | +1                | -1                   |
| 3. | Uniform heating      | 10            | 0                  | 0                 | +1                   |
| 4. | Heat loss saving     | 10            | +1                 | +1                | -1                   |
| 5. | Sensor and control   | 10            | -1                 | +1                | +1                   |
| 6. | Reliability          | 10            | -1                 | +1                | +1                   |
| 7. | Safe application     | 9             | +1                 | -1                | +1                   |
| 8. | Maintainability      | 9             | -1                 | +1                | +1                   |
|    | <b>Total</b>         | 100           | -0.52              | 0.44              | 0.54                 |

These include initial cost, ease of installation, power consumption, uniform heating, heat loss, sensor and control technology, system reliability, safe application and system maintainability, as given in Table 5-5. The advantages of each heating system were considered as aspects of merit and synthesized for their suitability in the current use. From the decision matrix table, the heating mat scored 54% and emerged as more suitable for the current application. Although high initial heating costs are anticipated for raising the temperature of the heat sink, over time the costs will be offset by the heat stored in the sink. Consequently, savings is achieved by the periods of off-heating. The lubricant reservoir is located close to heating system to utilize radiant heat from the mat in pre-heating the lubricant. The suitability of cartridge heaters is limited by the fact that

installation in a wet and humid environment may significantly compromise reliability and safety, and hence special design considerations are needed. Significantly, the circulating water-bath has shown not cost-effective for this application.

Overall, the heating wattage required is estimated at 89.5W as detailed in Appendix A2.4. From the data sheet an etched foil heater (self-adhesive heating mat model SRM-120x80), whose main features are illustrated in Figure 5-13, was selected for the heating application. It has dimensions of 120 mm x 80 mm, a supply voltage 15Vdc and power rating of 90W. Other specific details can be found in Drawing QB96 [Tecnologic UK (2012)]. The self-adhesive silicone mat is directly mounted on the 80 mm x 130 mm x 10 mm side plate using the adhesive glue. The heat is conveyed to the test chamber by conduction from the side plate which also serves as the heating sink.

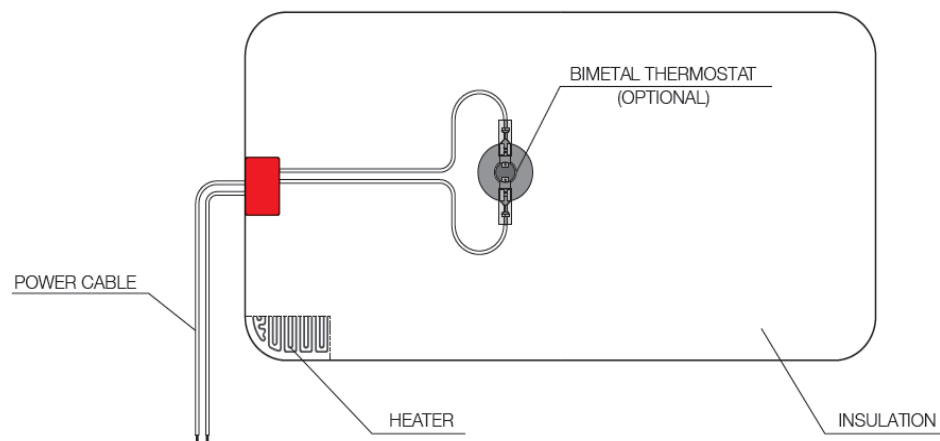


**Figure 5-13** Self-adhesive silicone heating mat (not to scale)

### 5.2.9 Lubricating system

A lubricating system has been incorporated to meet ISO/TS 14569-2:2001 specifications requiring the in-vitro testing of dental composites to mimic the oral cavity in terms of temperature and lubrication. The lubricant, which is distilled water is stored in a lubricant reservoir (a clear HDPE bottle) and is pumped to the test area by a micro-range peristaltic pump using viton rubber and copper tubing of 0.8mm internal diameter. The lubricant flows to the test area to wash off fatigue debris that have broken from the surface wear track. Besides washing the test area, the lubricant minimizes friction between contacting parts and keeps the dental composite under wet conditions during testing. This phenomenon is typical in human oral environments in which saliva always lubricates the contact surfaces of antagonist teeth.



The lubricant is collected in a PTFE reservoir and discharged through the discharge pipe at convenient time intervals. The micro-range peristaltic pump has a self priming capability of up to 10 m. The selected pump (100 series pump, model 102-005-012-008/4) has a flow rate of 0.08 ml/min, with 4 rollers, and runs at 5 rpm using a 12 VDC and 60 mA. The tubing has a size of 0.8mm internal diameter and is made from Viton® material [Williamson, 2008]. A configuration of the peristaltic pump is shown in Figure 5-14.

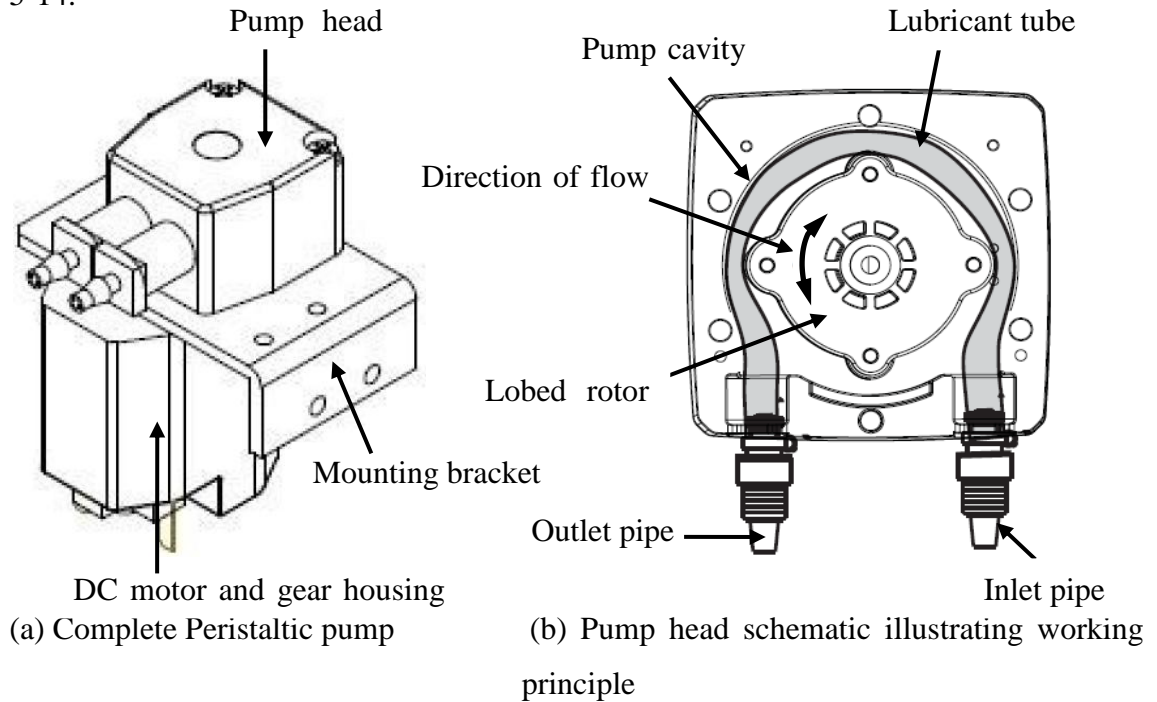


**Figure 5-14** Peristaltic pump [Williamson, 2008] (not to scale)

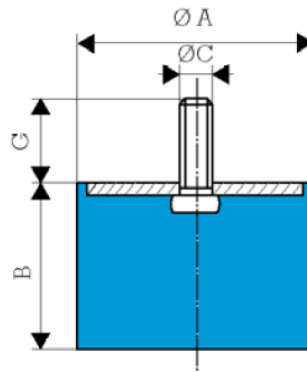
To optimise the lubrication process, it was decided not to re-circulate the lubricant as re-circulation was deemed expensive and could contaminate the test area.

### 5.2.10 Vibration Isolator

Rubber anti-vibration mounts have been added to the base of the mechatronic rolling ball device to isolate it from vibration produced by adjacent systems. Rubber mounts are preferred because they provide a good sideways stability in a limited space. The designer opted for the Radiaflex mount (Paulstra, model no. 521178) which has greater radial elasticity than axial elasticity as described in the data sheet. The mount works in compression, shear and in combined compression and shear loads. .

Figure 5-15 illustrates the mounts adapted for the mechatronic rolling ball device. Each can withstand an axial compression load of up to 300 N with a deflection of 5mm. The

mass of the mechatronic rolling ball device is approximately 10 kg. The four vibration mounts are mounted in the four corners of the base plate sharing the axial compression load. Therefore, each vibration mount is compressed axially by a compression load of 24.53N, which is less than 10x its capacity, thus giving reliable and durable isolation. Mounting specifications and instructions are available in the product data sheet (at [www.hutchinsonrubber.com](http://www.hutchinsonrubber.com)-accessed on 10.09.2011).



B =20mm, G =16.5mm, A=20mm, C= M6 threads

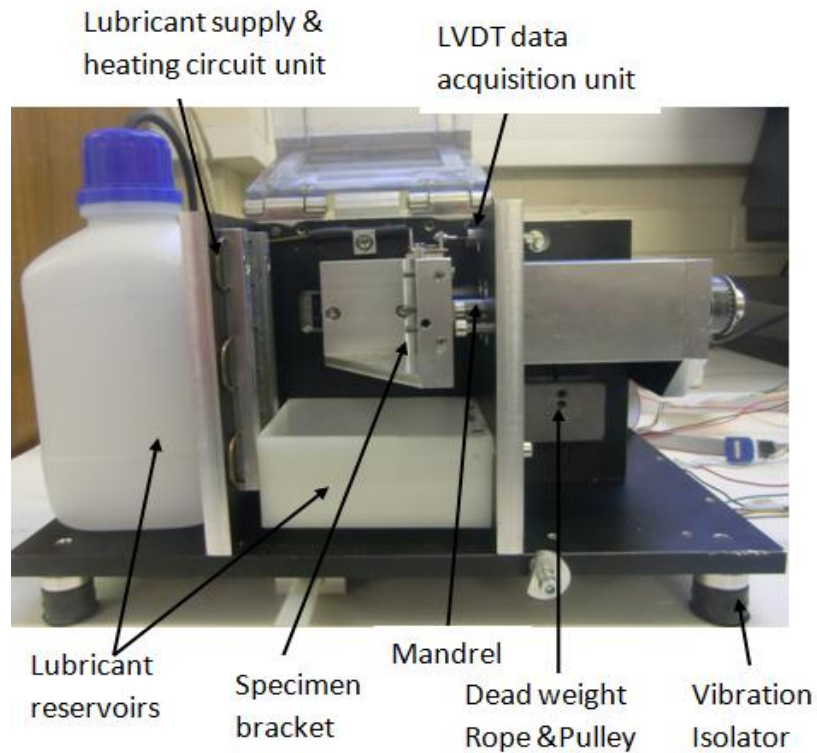
**Figure 5-15** Male Radiaflex vibration mounts (not to scale)

### 5.3 Modelling, engineering drawings and prototype manufacturing

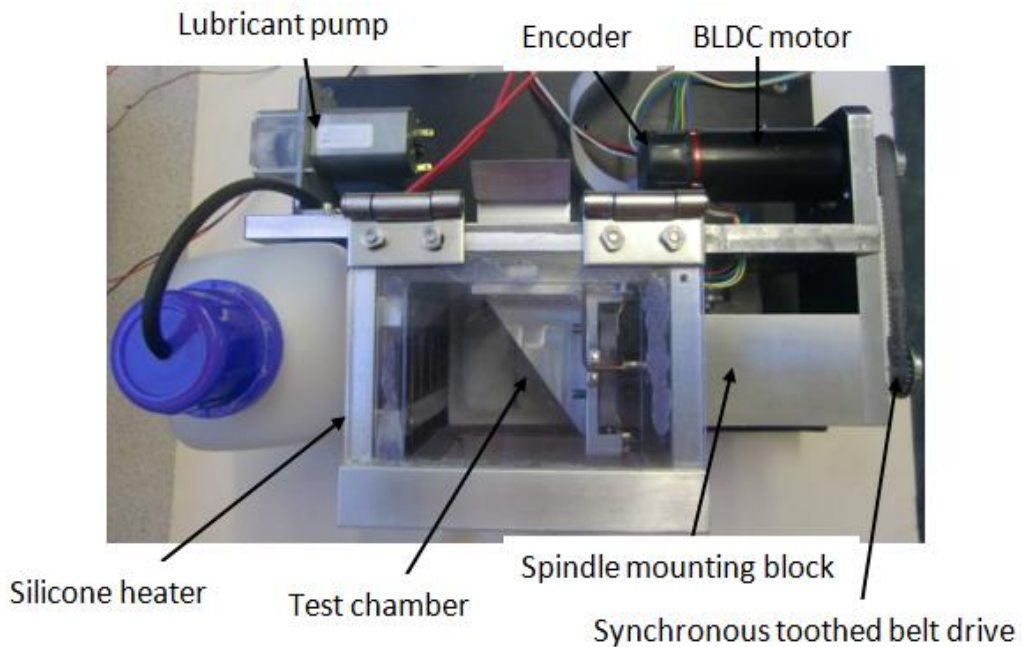
Having completed the conceptual and embodiment design, a CAD package, Autodesk inventor was used to produce a 3-D solid model of the parts and assembled mechatronic rolling ball device to appreciate how the design would fit together and the parts move relative to one another when in use. Owing to insignificant dynamic loading, structural analysis was deemed unnecessary. Working and assembly drawings for the prototype were derived from each 3-D model to represent convenient views for manufacturing.

Complete standardized drawings were made specifying the prototype's parts based on their design. The drawings represent all non-standard parts in detail with regard to dimensions, form, shape and surface finish. They included other details such as the number of parts in the assembly, their location, method of joining, material, surface finish, and so on. The process included preparing specifications to acquire standard parts from manufacturers. Detailed assembly drawings are presented in a single sheet showing the part details in order to describe visually the integrated device and facilitate the assembling processes. Finally, a detailed manufacturing process plan was written to guide the manufacturing process. An assembly drawing showing the views of the

mechanical hardware with overall dimensions and corresponding part list are shown in Appendix A3.1 and A3.2 respectively. Photographic images of the mechatronic rolling ball device are shown in Figure 5-16.



(a) Prototype front and test chamber view (not to scale)



(b) Prototype top view showing BLDC motor, drive and pump layout (not to scale)

**Figure 5-16** Pictorial representation of the mechatronic rolling ball device

## **5.4 Summary**

The chapter has described the approach used for developing the mechatronic hardware, including specifications setting and evaluation, concepts synthesis and evaluation, embodiment design based on the qualitative and quantitative analysis. Eventually, a 3D CAD model of the successful concept and related parts were developed and assembled to appreciate functional interactions. Following a satisfactory simulation, detail working drawings were developed for the parts to manufacture and off the shelf ordering. Having acquired the parts, the physical mechatronic hardware was built into a one product system and tested. Successful testing of the mechatronic hardware, initiated the development of the embedded control hardware and software.

## CHAPTER 6 DESIGN OF THE EMBEDDED CONTROL AND DATA ACQUISITION SYSTEMS

The previous chapter concentrated on the design of the mechanical and electrical hardware with emphasis on part selection and integration into a functional system. This chapter focuses on the design of the electronic hardware which makes up the embedded control, data acquisition and monitoring systems. Motion controllers drive the actuators (i.e. the BLDC servo motor, Brushed DC pump, etc.) and sensors (i.e. the LVDT transducer, accelerometers, etc.) to monitor and acquire measurement data from the system. The peripherals are integrated with the central system controller, which is a Digital Signal Controller (DSC).

### 6.1 Embedded System Specific Requirements

The key attributes of the envisaged mechatronic system are real-time operation and control of the drive system, online data acquisition, data processing and display. Other functional requirements are the ability to mimic the oral environment and monitor the surface fatigue process. Addressing these attributes, the specific requirements for the embedded system were set as follows:

- (a) the system should have two-speed control: sampling speed of 240 rpm to minimize vibration during sampling, and surface fatigue actuation speed of 2040 rpm to accelerate the surface fatigue testing [McCabe et al, 1997].
- (b) the system should have an automatic data acquisition, data processing and storage system.
- (c) the Central Processing Unit (CPU) must simultaneously control the functions of the systems, and acquire and process measurement data.
- (d) the system should be based on an embedded processor with sufficient peripheral features (i.e. I/O pins, timers, ADC module, UART module, etc.) to interface with auxiliary devices and have a suitable graphical user interface (GUI).
- (e) the processor must have high instruction processing speed, preferably of 40 MIPS, to provide real time control and processing, including high data throughput, an enhanced instruction set and support for digital signal processing.

The first task was to select a suitable microcontroller for the embedded system to control peripheral devices, monitor the test environment and perform data sampling.

Several options for microcontrollers exist, ranging from Peripheral Interface Controllers (PICs), Digital Signal Controllers (DSCs) and Digital Signal Processors (DSPs). Each of these has its strengths and weaknesses depending on the nature and type of application concerned. Extensive information is available on their design, architectural layouts and configurations [Huddleston, 2007; Carryer et. al, 2011], which is summarized here to establish their suitability for this application.

According to Carryer et al [2011], microcontroller devices (i.e. PICs) have the CPU, program and data memory, communication modules and peripheral features such as digital inputs/outputs, timers, etc, integrated in a single-chip computer. Microprocessors have a CPU on-chip whereas the program and data memory, communication modules and peripherals features are separate and require the designer to integrate them into the microprocessor. The DSP is a microprocessor specifically designed to perform signal processing at high speeds. On the other hand, DSCs are high performance microcontrollers optimized to combine the characteristics of PICs and DSP on a single chip. The combination enables the device to perform deterministic behavioural control and high speed data acquisition and processing at the same time [Microchip, 2005; Huddleston, 2007].

There are no straightforward criteria for choosing the semiconductor technologies, and the choice largely depends on the application requirements. In order to select an optimum device, the author set criteria to evaluate the three technologies with respect to the current application. These included processing speed, versatility, costs, software interface, hardware interface, power consumption, enhanced functionality, development support and memory, signal processing capabilities, robustness, and support instructions algorithms. The percentage weighting of each criteria was ranked based on +1 for the most suitable criteria, 0 for moderate suitability and -1 for the least suitable criteria for the three different processor types; namely, PIC, DSC and DSP. The evaluation process is tabulated in Table 6-1.

**Table 6-1** Semiconductor technologies evaluation matrix

| No  | Criteria   | Weighting (%) | PIC  | DSC | DSP |
|-----|--|---------------|------|-----|-----|
| 1.  | Speed  | 10            | 0    | 0   | +1  |
| 2.  | Versatility  | 10            | 0    | +1  | 0   |
| 3.  | Low cost   | 10            | +1   | +1  | -1  |
| 4.  | Hardware interface   | 10            | +1   | +1  | +1  |
| 5.  | Software interface   | 5             | +1   | +1  | +1  |
| 6.  | Power consumption  | 5             | +1   | +1  | -1  |
| 7.  | ADC resolution   | 5             | 0    | +1  | +1  |
| 8.  | Development support  | 10            | +1   | +1  | 0   |
| 9.  | Memory space   | 10            | -1   | +1  | +1  |
| 10. | Fixed integer / Floating point<br>(signal processing) format | 10            | -1   | 0   | +1  |
| 11. | Robustness   | 5             | +1   | +1  | +1  |
| 12. | Support programming library                                  | 10            | +1   | -1  | +1  |
|     | Total  | 100           | 0.35 | 0.6 | 0.5 |

Referring to Table 6-1, and desired combinational control and data processing, the DSC microcontroller is the best suited due to its ability to provide powerful mathematical processing performance close to the level of a pure DSP but with the highly deterministic behaviour of a standard PIC microcontroller. That is to say, it can optimally suit the specific design requirements listed above. Although DSPs from Texas Instruments and Analog devices have higher performance than DSC from Microchip, the dsPIC<sup>TM</sup> DSC has been selected because it provides a low-cost solution, combining huge computational capabilities of the DSP processor with the deterministic control behaviour of the 16-bit microcontroller unit (MCU) to provide a compact single chip, single instruction semiconductor for embedded system design [Microchip, 2011]. To optimize both control and data processing as specified in the specific requirements, the author opted for the general purpose sensor family dsPIC33FJ256GP710A in a thin quad flat pack (TQFP) chip. The dsPIC33FJ256GP256A belongs to the dsPIC33F family of 16-bit microcontrollers and is available in a 100-pin. The numerical specifications of the main features of the DSC are tabulated in Table 6-2.

It operates at 3.0V-3.6V, -40<sup>0</sup>C to +125<sup>0</sup>C, DC with a processor speed of up to 40 MIPS.

Alternatively, detailed information can be sourced from the dsPIC33FJ256GP710A data sheet available at [www.microchip.com](http://www.microchip.com) [accessed on 22.07.2013].

**Table 6-2** Summary of the key dsPIC33FJ256GP710A specifications

| No. | Features  | Specification   |
|-----|---|---|
| 1.  | Data bus  | 16-bit  |
| 2.  | Clock speed   | 7.37 MHz  |
| 3.  | Timers: numbers   type of bits  | 9   16-bits,32-bits   |
| 4.  | Memory: program flash memory<br>SRAM<br>DMA-RAM                               | 256 kB<br>30kB (DMA-RAM inclusive)<br>2kB   |
| 5.  | Power characteristics: supply voltage   | 3.0-3.6V  |
| 6.  | Communication interfaces and ports:<br>Serial interfaces<br>Digital I/O ports | ECAN; I <sup>2</sup> C; SPI; DCI; UART (2 each)<br>85   |
| 7.  | A/D converters: bits  | 2 modules, 32ADC channels with<br>10/ 12-bit  |
| 9.  | Peripherals   | Watch dog timers; PWM; Input Capture; Output Compare; Interrupt Controller; Power Saving Mode; Low Voltage Detector |

## 6.2 DsPICDEM™ 80-Pin Starter Development Board

To reduce development time and resources, a development board was acquired to interface the peripheral devices to the dsPIC33FJ256GP710A using a Plug-in Module (PIM). It comprises a header for mounting the 80-pin PIM for either the 80-pin dsPIC30fxxxx or 100-pin dsPIC33FJxxxxxxxx DSC chip for various embedded circuits applications. Key features of the dsPICDEM™ 80-Pin Starter development board with significance for the current application include the following:

- (a) a 80-pin header to accommodate 80-pin PIM for the 100-pin dsPIC33FJ256GP710A device.
- (b) 3.3/5V voltage regulator to provide  $V_{DD}$  and  $AV_{DD}$  from a 9V DC power supply
- (c) MPLAB ICD 2 in-circuit debugger jack.



- (d) RS-232 serial port
- (e) temperature sensor and analog potentiometer to simulate A/D inputs
- (f) 3 push button switches and 4 LED indicators to simulate digital input/ output
- (g) external crystal oscillator for different clocking requirements
- (h) 80-pin I/O port header

The board includes several other components for prototyping as illustrated in Figure 6-1, thus significantly saving prototyping resources and time.

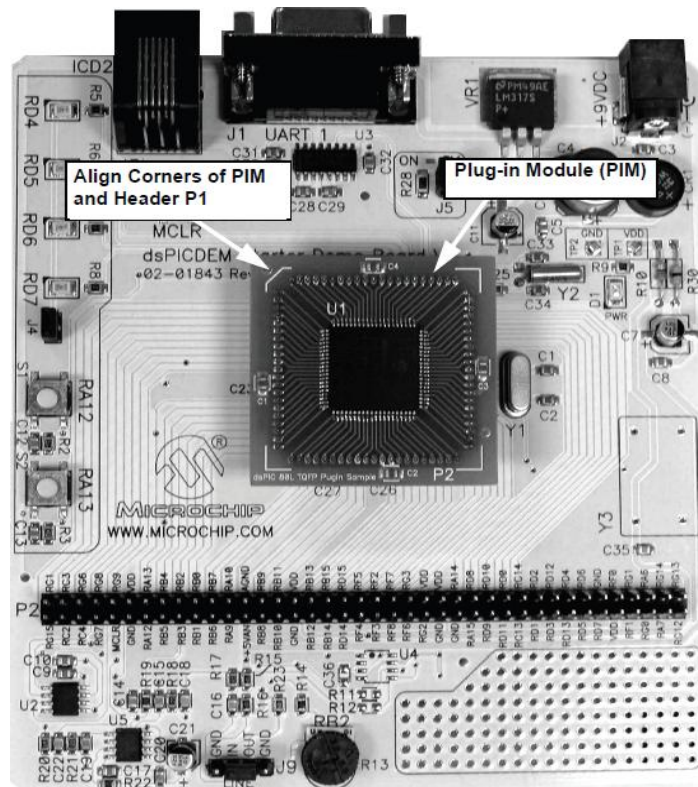


**Figure 6-1** DsPICDEM™ 80-pin starter development board [[www.microchip.com](http://www.microchip.com)].

The dsPIC33FJ256GP710A device has multiple peripheral functions multiplexed on its pins. Therefore, it was important to configure the board to match the current application. Configuration was facilitated using software and jumpers to set up the application interface for the dsPIC33FJ256GP710A.

### 6.3 Embedded Hardware Design

The optimal functioning of the embedded system plays a crucial role in a successful mechatronic design. This required the correct selection and integration of the main controller and external devices such as actuators, sensors, and controllers. Having

selected the main controller according to the system requirements listed in section 6.2, the next task was to design the interface to the controller, actuator and sensor systems through its peripherals to establish an embedded control system for the surface fatigue measurement device. The peripherals included a 3 phase BLDC motor driving board for the BLDC motor, an LVDT transducer conditioning circuit for sensing wear track depth, an accelerometer module for sensing wear vibration, a temperature sensor; an L293N driver board for the brushed dc pump and an RS 232 protocol for communicating with the host computer. The use of external drivers for the BLDC motor and lubricant pump relieved the DSC from direct control of the devices in order to enable sufficient memory and speed for data sampling. A schematic layout showing the integration of the embedded hardware is shown in Figure 6-2. Below listed features were accessed via their respective headers on the dsPICDEM™ 80-pin starter development board. For clarity of the layout, only features of the development board applicable to current design have been shown.

- (a) Timer 1, T1CK1: to capture the up count of the encoder at pin 16 (RC 14).
- (a) Timer 2, T2CK2/3: used to set the servo update time base and interrupt service routine (ISR) at pin 14 (RC 13).
- (b) Timer 3, T2CK2/3: used to set the PWM time-base at pin 15 (RC 13)
- (c) Timer 4, T4CK4/5: used to set the ADC sampling period ISR.
- (d) Timer 5, T4CK4/5: used to set the accelerometer sampling ISR.
- (e) Timer 6, T6CK6/7: used to set the temperature sampling and printing ISR.
- (f) Universal asynchronous receiver/ transmitter 1 (UART1) port: interface GUI window. Rx is connected to pin 26 (U1) RF2 and Tx to pin 25 (RF3) via UART1 header (H4) at pin.

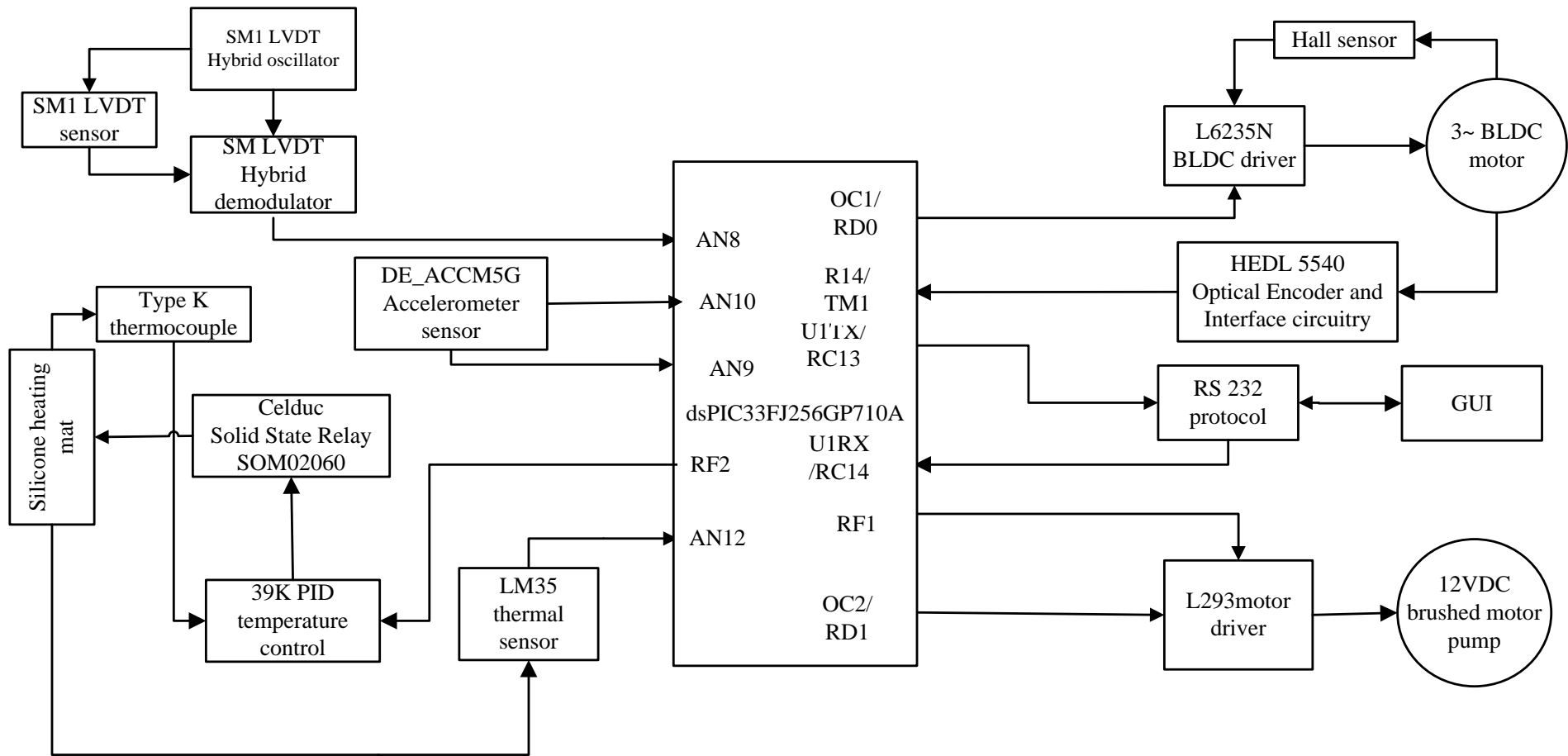


**Figure 6-2** Embedded hardware layout using dsPIC33FJ256GP710A device

- (g) The ADC module provides 32 channels with 12-bit resolution located at ports A, B, and C. The LVDT is connected to RB8 (AN8), the accelerometer to RB10 (AN10) and RB11 (AN11) and the temperature sensors to RB9 (AN9), RB12 (AN12) and RB 13 (AN13).
- (h) Other bi-directional register pins (i.e. RA, RC, RD, RF, RE and RG) are configured as digital I/O pins as a need arises.

Configuring the development board to 3.3V settings automatically connects dsPIC33FJ256GP710A to the 3.3V DC supply and ground voltages via  $V_{DD}$  and GND pins.  $AV_{DD}$  and  $AV_{SS}$  are ADC reference voltage pins with 3.3V and 0V respectively. There are two external clock options available for 7.37MHz and 40 MHz speeds. The current application uses the external crystal in a primary phase locked loop (Pr\_PLL) mode to provide a clock speed of 80MHz, equivalent to 40MIPS. For the RESET circuit, the *MCLR* pin is connected to 3.3V when switch S1 is pressed, and when released, the DSC chip will reset.

### **6.3.1 BLDC motor drive and control interface**

Following the design analysis, optimum speeds of 2040 rpm and 240 rpm were established for the high speed fatigue and low speed sampling phases. It is important to note that the 2040 rpm speed selection is based on the need to accelerate the surface fatigue testing as recommended in *in-vitro* testing and used in the conventional prototype [McCabe et al, 1997; Lambrechts et al, 2006; Zhou and Zeng, 2008]. On the other hand, the 240 rpm was selected based on the need to reduce mechanical vibrations during data sampling and it was obtained by laboratory testing. Although much higher speeds could be used and would reduce testing cycle time, the ball dynamics such as bouncing and impacting on the specimen would impair the nature of surface fatigue wear and the cyclic rolling process. Notwithstanding the motor size evaluation in Section 5.2.2, the immediate availability of off the shelf, a Maxon 3-phase BLDC servo motor EC-max 30 (model 272765) with a rated voltage of 8-48Vdc, rated current of 1.41A and a rated torque of up to 65.3mNm at a speed of 8120 rpm prompted its application in the design. Consequently, the relatively low load demands ensured reliable operation for long durations and large contacting loads.

The motor has integrated hall sensors to control the sequence of commutation and subsequently its speed and direction. The L6235N device is a fully integrated 3-phase

BLDC motor driver and was selected to interface the main controller board and provide the peripheral control characteristics required to commutate the motor. The chip combines DMOS power transistors with CMOS and bipolar circuits. It has logic inputs of CMOS/TTL technology, built in constant off-time Pulse Width Modulation (PWM), inputs for single-ended hall sensor and decoding logic circuitry. The electrical characteristics of the L6235N are listed in its data sheet. The L6235N chip was mounted on an evaluation board, EVAL6235N (see Figure 6-3 and appendix A3.2), which provided the driving circuit and interface connections. A detailed description of the EVAL6235N is available in the AN1625 data sheet [[www.st.com](http://www.st.com)-accessed on 20.10.2011].

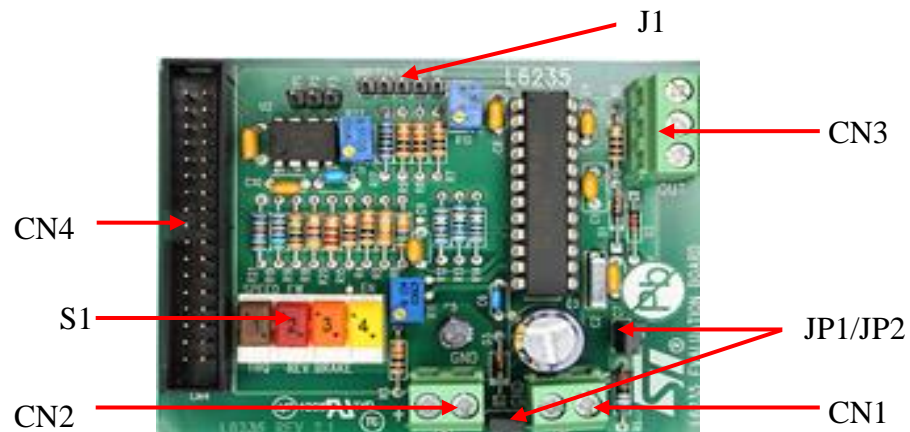


**Figure 6-3** EVAL 6235N 3-phase BLDC motor evaluation board

Key to Figure 6-3:

CN1: connector for board power supply (Vs).

CN2: connector for logic power supply (5V).

CN3: connector for Half-bridge power outputs (V).

CN4: 34-pin connector for interfacing communication (Vs).

S1: quad DIP switches to enable the L6235N chip run the motor in torque or speed mode, for motor direction and to enable motor braking or TACHO functions.

JP1 and JP2: jumpers to facilitate on board 5V supply generation.

J1: hall effect sensors signal input and power supply (5V).

The current application requires uni-directional motor rotation, which is effected by the quad switch S1 forward direction button. The EVAL6235N low pass filter circuit shown in Figure 6-4 is connected to a PWM signal from the dsPIC33FJ256GP710A using pin 31 of the CN4 connector and converts to an analog reference voltage ( $V_{ref}$ ). The low-pass filter components are  $R_{LP} = 20k\Omega$ ,  $R_{DIV} = 2.2k\Omega$  and  $C_{LP} = 68nF$ , as specified on the

data sheet. If the duty cycle is estimated to be 80% during high speed drive, and the voltage output switches between 0V and 5V, the low pass filter reference voltage can be established using equation 6.1. An AN1625 note recommended a reference voltage range of 0V to 1V for a similar application, and thus the established reference voltage 0.4V is a reasonable starting point.

$$V_{ref} = \frac{5V * D_{\mu c} * R_{DIV}}{R_{LP} + R_{DIV}} = \frac{5V * 0.8 * 2200}{20000 + 2200} = 0.4V \quad (6.1)$$

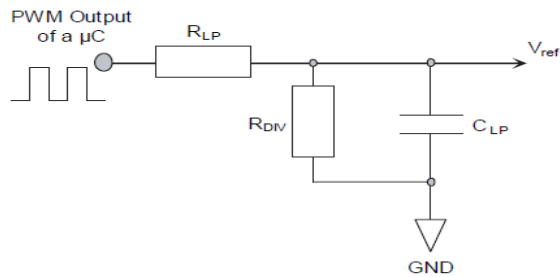


**Figure 6-4** EVAL6235N low pass-filters for the reference voltage ( $V_{ref}$ )

To sense the speed of the motor drive in a closed loop, an optical encoder model HEDL 5540 A13 from AVAGO Technologies with 500 counts per revolution was attached to the motor.

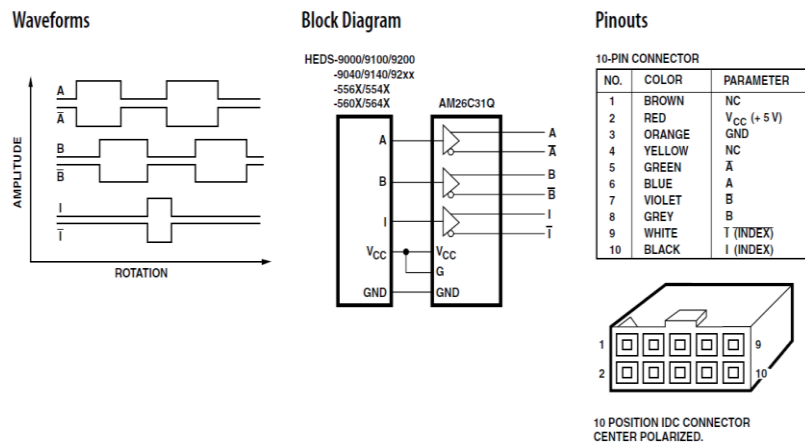


**Figure 6-5** Encoder HEDL 5540 functional characteristics [[www.avagotech.com](http://www.avagotech.com)- accessed on 13.05.2012].

The encoder utilizes differential quadrature inputs and has a single 5V supply (see Figure 6-5). Complementary outputs from channels A, B and I are connected to differential amplifiers (model: AM26LS32) to suppress electrical noise. The outputs of channels A and B from the differential amplifiers are connected to a D flip-flop, as

shown in Figure 6-6, to decode the quadrature pulse train into up-pulse output shown in the timing diagram in Figure 6-7, before being input to the dsPIC333FJ256GP710A 16-bit timer module. The connection provides a clockwise rotation of the BLDC motor. The reference position of the motor shaft is not important; hence the index channel is not connected.

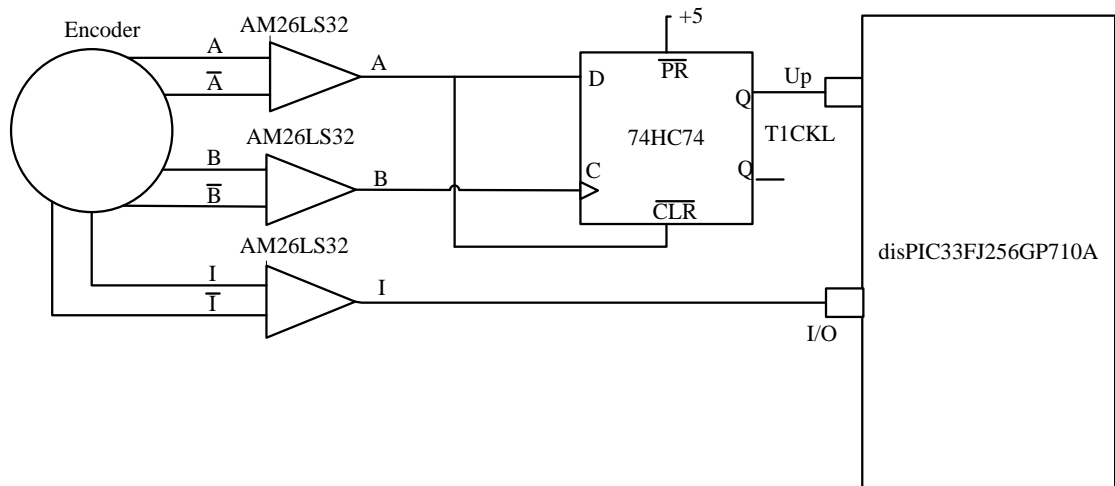


**Figure 6-6** Encoder interface schematic

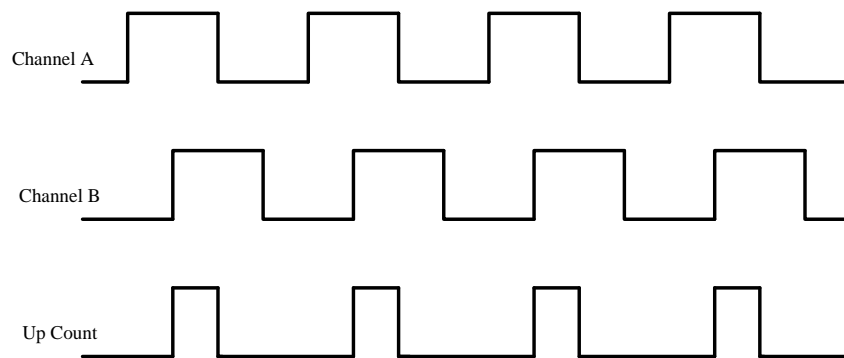


**Figure 6-7** Encoder timing schematic

### 6.3.2 BLDC motor speed and position control

The BLDC motor speed control is an important part of the mechatronic rolling ball device, because the motor must maintain steady speed running at the set speed, irrespective of load dynamics which can vary from increased rolling friction due to change in dead weight, rolling path degradation and broken debris or worn out mandrel. In other words, speed control is likely to increase good dynamic responses of the system and lead to improved test results accuracy. Position control ensures the target is reached

with reasonable accuracy. A combination of speed and position control (i.e. motion control) provides a smooth trapezoidal transition from a set speed to the next speed. The speed and position control has two loops. An outer loop keeps track of the speed and position with respect to set values, and an inner loop controls the torque value (PWM signal). The inner loop is integrated on the BLDC driver board, constituting a closed PI current PWM control loop for commutating the motor through hall sensor feedback as detailed in the EVAL6235N data sheet. The configuration of the two-speed control loops are illustrated in Figure 6-8.

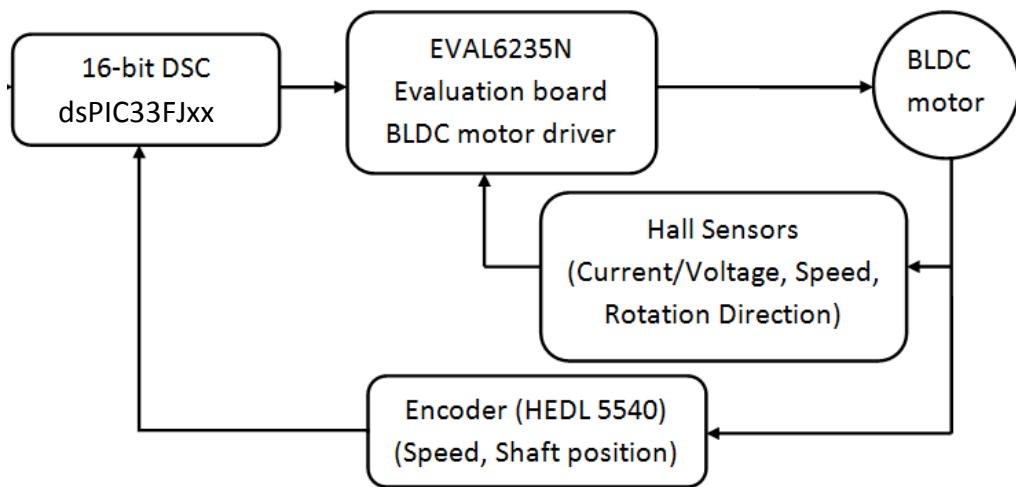


**Figure 6-8** Schematic illustration of the main actuator closed loop control system.

The control loop was re-tuned to match the current application’s requirements. The outer loop is based on an incremental rotary encoder (quadrature/optical encoder) with signal conditioning circuit and linked to the EVAL6235N driver board and main controller dsPIC33FJ256GP710A for precise control of spindle speed. The encoder is mounted on the motor shaft. The accuracy of speed measurements is essential for a good dynamic response to avoid stability issues.

Basically, there are two common methods of speed measurement methods using an incremental encoder. Pulse timing measures the time interval between successive pulses by using a high frequency timer/counter (i.e. Method 1), whereas Pulse counting counts the pulses during a prescribed time (i.e. Method 2). The two methods are achieved by using a microprocessor system clock and timer/counter module. Method 1 gives accurate low speed measurements but inaccurate high speed measurement. In Method 1, the motor speed of  $N_m$  given in rpm is calculated using equation 6.2:



$$N_m = \frac{60}{T_p * N_p} \quad (6.2)$$

in which  $T_p$  is the measured time between two successive pulses and  $N_p$  is the encoder resolution given as pulses per revolution (PPR). Therefore, at high speeds,  $T_p$  is small, and at low speed it is high, leading to quantization errors when used to measure a wide range of speeds.

Method 2 accurately measures medium and high speeds but inaccurately for low speeds. The motor speed for Method 2 in rpm is given by equation 6.3:

$$N_m = \frac{60}{T_s * N_p} * N_s \quad (6.3)$$

in which  $T_s$  is the fixed sampling time,  $N_p$  is the encoder resolution given as pulses per revolution (PPR), and  $N_s$  is the number of pulses in the sampling time given as pulses per sample. In this method, the product of  $T_s$  and  $N_p$  determines the quantization error of the estimated speed, thus making the sampling time an important factor in accurate speed measurement.

In order to overcome the shortcomings of the two techniques, a combination M/T method is adopted by synchronously integrating a high speed frequency timer with the encoder pulse generator, as depicted in Figure 6-9. Referring to the schematic, P is the pulses per revolution from the encoder generator,  $f_c$  is the high frequency reference timer pulse,  $T_s$  is the sampling time,  $\Delta T$  is the compensating time (usually in milliseconds),  $T_d$  is the effective sampling time, and M1 and M2 are counted encoder and clock pulses respectively. In the M/T method, motor speed can be estimated using equation 6.4:

$$N_m = \frac{60 * f_c * M_1}{P * M_2} \quad (6.4)$$

The M/T method requires rather complicated hardware and software but offers accurate speed measurement over a wide speed range. Therefore, a trade-off of the costs and speed accuracy needed determines the best solution for an intended application.

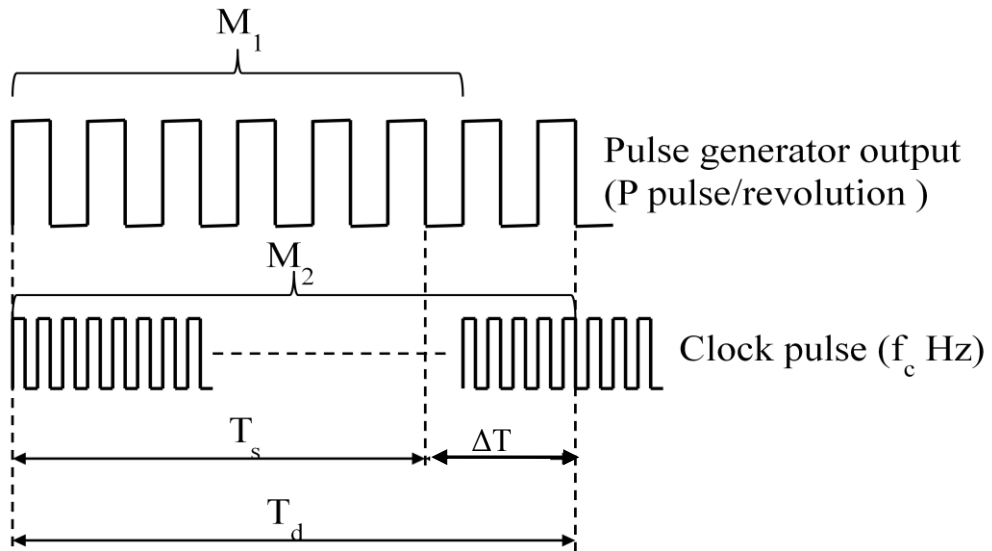


**Figure 6-9** Schematic illustration of the M/T speed measurement method

As the mechatronic testing device is required to operate at low and high speeds (i.e. 240 and 2040 rpm), it was necessary to test the suitability of the speed estimation in order to adopt a suitable method for this application. Speed tests were conducted for different speeds, as illustrated in Figure 6-10, and speed variations from the set point recorded. Percentage speed error was calculated using equation 6.5.

$$\text{Speed fluctuation [\%]} = \left( \frac{\text{Maximum speed} - \text{Minimum speed}}{\text{Actual Speed}} \right) * 100\% \quad (6.5)$$

From Figure 6-10, it is evident that the pulse timing method provides excellent speed control at low speeds but has unacceptably high speed fluctuation at high speeds. On the other hand, the pulse counting method works very well at high and medium speeds, but has large speed fluctuation at low speeds. Therefore, the pulse timing method was used to measure speed at 240rpm for capturing LVDT transducer data, the counting method to control running speed at 2040 rpm, and 720rpm was chosen as the change-over reference.

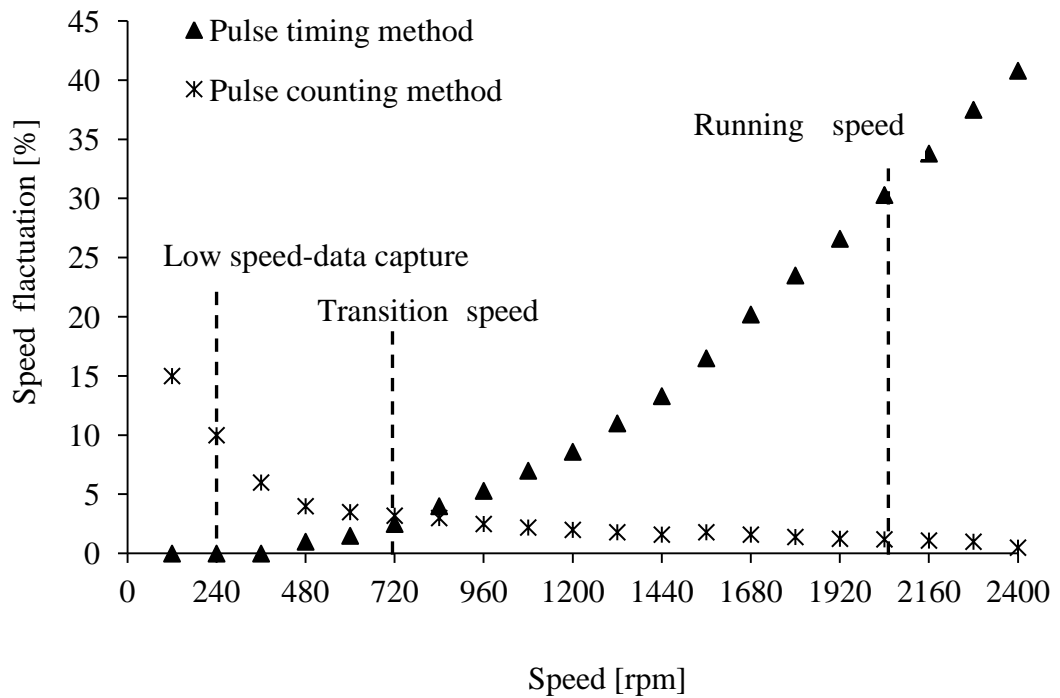


**Figure 6-10** Speed fluctuation for pulse timing and pulse counting methods

### 6.3.3 Updating speed and position

The speed and position of the motor is updated using a servo update loop. The motor is set to run clockwise; therefore only the up-count pulse stream from the encoder is captured by the *timer1* counter after being conditioned by the encoder interface circuit (as discussed in section 6.4.1). The captured pulse count is saved in a 16-bit variable *count* (i.e. *timer1*), which is capable of storing 65536 pulses per sample. Nevertheless, the maximum number of samples captured depends on the speed of the motor and sampling period. In this application, the sample time was set at 10ms, equivalent to an update rate of 100 kHz, provided by the *timer2* interrupt service routine (ISR). The encoder has 500 PPR, and thus the number of pulses per sample period was 20 counts for 240 rpm and 170 counts for 2040 rpm. A combined pulse timing and counting method was used to control the motor speed in order to achieve excellent speed control at both 240rpm and 2040rpm. Pulse timing speed control at 240 rpm utilized the input capture module. Velocity updating was achieved proportional to the motor speed as opposed to regular time updates as used in conventional pulse counting methods. A fixed encoder's pulse width was set by capturing successive rising edges of channel A's pulse train. The width between the rising edges was determined using the 240 rpm

(4rev/s) speed, an MCU clock speed of 40 MIPS and encoder resolution (500 PPR) using equation 6.6:

$$v(k) \cong \frac{X}{t(k) - t(k-1)} \quad (6.6)$$

where  $v$  is velocity,  $X$  is a fixed position interval (width) of the incremental encoder,  $t$  is time, and  $k$  is the discrete-time index. The number of revolutions per pulse was given as

$$\frac{1}{500PPR} = 0.002 \text{ revolution per pulse. At 240 rpm, the pulse width was estimated as:}$$

$$\frac{0.002rev}{4rev/s} = 0.0005s \text{ (0.5ms). With a microcontroller clock of 25ns (i.e. the}$$

DSPIC33FJ256GP710A's clock speed is 40 MIPS) and a pre-scalar of 64 on *timer 2*, the velocity in counts per pulse was given using the microcontroller clock counts as in equation 6.7:

$$v(k) \cong \frac{0.0005}{1pulse * 64 * 25 \times 10^{-9}} \cong 312.5 \frac{counts}{pulse} \quad (6.7)$$

The conventional pulse counting method was used at 2040 rpm due to its inherited accuracy at high speed. The velocity control loop was updated every 10ms. The velocity estimation is based on equation 6.8:

$$v(k) \cong \frac{x(k) - x(k-1)}{N * T * T4\_Prescaler} \quad (6.8)$$

where  $v$  is velocity,  $T$  is a fixed time interval (10ms),  $x$  is position, and  $k$  is the discrete-time index. At 2040 rpm, this is equivalent to 34 rev/s, and with 500 PPR as encoder resolution, and 25ns microcontroller clock and using timer 4 with a pre scalar of 8.

$$34rev/s \cong \frac{x(k) - x(k-1)}{500PPR * 10^{-3}s} \quad (6.9)$$

Ultimately, the velocity is obtained is 170 pulses/sample time. The demand velocity ( $D\_Velo$ ) variable was assigned to 312 pulses of *timer\_2* for the speed of 240 rpm and 170 counts of the encoder pulses read using *timer\_1* was assigned to the speed of 2040 rpm. The position moved is a cumulative sum of encoder pulses acquired, and assigned to a variable *count* and passed to a variable *SimCount* before a new reading is captured.

Total rotation is established by the accumulated sum of encoder counts in a new 32-bit variable, named *SimCount* .

The external speed control servo loop shown in Figure 6-8 in section 6.3.2 uses a PI velocity controller algorithm to determine the amount of correction for a corresponding magnitude of speed fluctuation,  $e$ . The proportional gain determines the speed of response of the velocity feedback system and reduces steady-state error. However, too large a proportional gain causes oscillation and instability. The integral term is added to eliminate the steady-state error and allows the controller to maintain the desired speed. The digital PI algorithm implemented in speed control is based on the incremental algorithm derived below. The PI algorithm is preferred in speed control because of its stability in practical applications in not containing the derivative term which is sensitive to noise. During operation, the controller receives the signals from the encoder and computes the corrective action to send to the actuator. The computation is based on the error (proportion) and the sum of the previous errors (integral). The mathematical model of the PI controller is derived as follows:

$$u(t) = K_p \left[ e(t)dt + \frac{1}{T_i} \int_0^t e(t)dt \right] \quad (6.10)$$

where:

$u(t)$  output of the PI controller

$e(t)$  input of the PI controller; which is the error between the desired input speed and the actual output speed,

$K_p$  proportional gain,

$T_i$  integral time or integral gain.

As the software control method uses sampling to calculate the control signals with regard to error at the sampling point, the controller integral must be discretized to obtain the expression in equation 6.11:

$$u(k) = K_p \left[ e(k) + \frac{T}{T_i} \sum_{j=1}^k e(j) \right] \quad (6.11)$$

in which:

$k$  sampling number  $k=0, 1, 2 \dots$

$u_k$  output value sampling at the  $k$  times

$e_k$  error sampling at  $k$  times

$\sum_{j=1}^k e(j)$  accumulative error sampling from the first time to the  $k$  times

$T$  sampling period

A recursive formula ( $\Delta u(t)$ ) for the incremental PID algorithm is applied to avoid calculating the sum of errors, so that  $\Delta u(k)=u(k)-u(k-1)$ . From equation 6.11,  $u(k-1)$  for the PI controller can be expressed by equation 6.12.

$$u(k-1) = [K_p * e(k-1) + K_i * T \sum_{j=1}^{k-1} e(j)] \quad (6.12)$$

Subtracting equation 6.12 from equation 6.11 leads to equation 6.13:

$$\Delta u(k) = K_p [e(k) - e(k-1)] + K_i * T * e(k) \quad (6.13)$$

An alternative form of equation 6.13 is presented in equation 6.14.

$$\Delta u(k) = K_p \left\{ [e(k) - e(k-1)] + \frac{T}{T_i} * e(k) \right\} \quad (6.14)$$

$$\Delta u(k) = K_p * \Delta e(k) + K_i * e(k) \quad (6.15)$$

in which  $K_i = \frac{K_p}{T_i} * T$

Ultimately, the overall gain ( $U_k$ ) of the incremental PI speed controller algorithm is as shown in equation 6.16; essentially meaning that the current control gain is calculated as an increment of the previous control gain, thus differentiating it to the time domain (conventional) PI controller.

$$U(k) = U(k-1) + \Delta u(k) \quad (6.16)$$

Using the Ziegler–Nichols heuristic tuning method, PI controller gains are established experimentally by setting the integral gain to zero. The proportional gain was obtained by increasing  $K_p$  from zero until it reached the ultimate gain  $K_u$ , at which the output of the control loop oscillated with a constant amplitude, as depicted in Figure 6-11. Critical gain,  $K_u$ , and the oscillation period  $T_u$  were recorded using the real-time LabVIEW program to be 100 and 3.6s, for 2040rpm. The same procedure was used to obtain  $K_u$  and  $T_u$  for the 240rpm to be 330 and 1s. Actual parameters for the two speeds were estimated using the mathematical expressions depicted in Table 6-3. Finally,  $K_p$  and  $K_i$  were optimised to 30 and 3 for the 240 rpm and 80 and 16 the 2040 rpm using the retuning technique and visual observation based on the Lab VIEW application attached in Appendix A6.2.

**Table 6-3** Ziegler-Nichols method mathematical expressions

| <b>Ziegler-Nichols method</b> |                         |                         |                         |
|-------------------------------|-------------------------|-------------------------|-------------------------|
| <b>Control type</b>           | <b><math>K_p</math></b> | <b><math>K_i</math></b> | <b><math>K_d</math></b> |
| P                             | $K_u/2$                 |                         |                         |
| PI                            | $K_u/2.2$               | $1.2K_p/T_u$            |                         |
| PID                           | $0.6 K_u$               | $2K_p/T_u$              | $2K_p T_u /8$           |

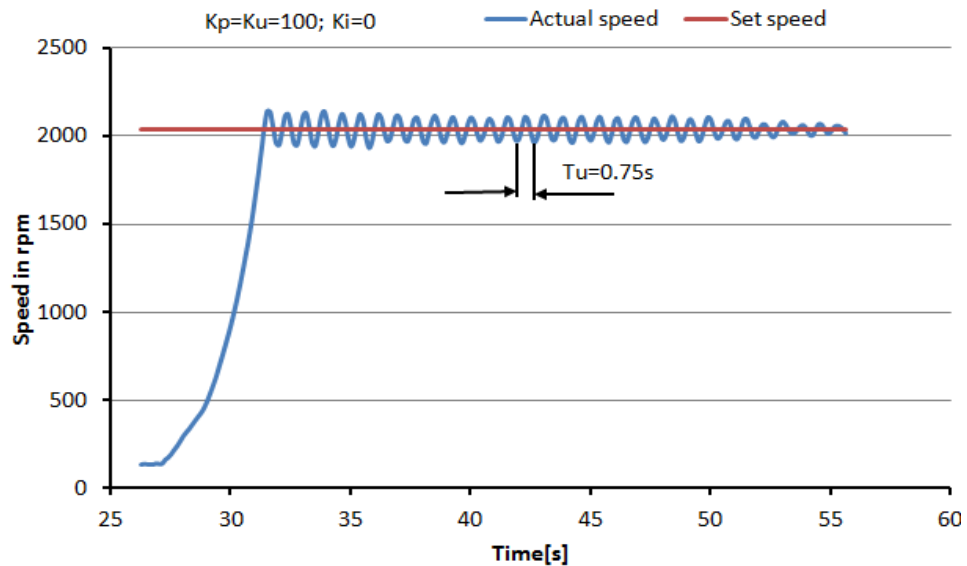


**Figure 6-11** PI Controller loop ultimate gains for the 2040 rpm

The tuning process was concluded by observing the speed fluctuation at the two speeds of 20 counts/s and 170 counts/s. In both speeds the encoder count error was on average  $\pm 1$  counts. This gave an approximate speed fluctuation of  $\pm 5\%$  at 240 rpm and less than  $\pm 1\%$  at the high speed of 2040 rpm. Trapezoidal speed control was used to ramp the speed up or down from one set point to another by providing 50 incremental servos updates of the PWM when the PI interrupt service routine is updated.

#### 6.4 LVDT Wear Transducer Interface

The LVDT transducer is a low voltage AC sensing device, which utilizes a Solatron hybrid oscillator/demodulator LVDT signal conditioning module (model 005900-RS and 005901-RS). The oscillator produces an accurate, stable amplitude and frequency sine wave carrier voltage to drive the transducer and a square wave for referencing the demodulator. In this application, the carrier voltage (5 VRMS at 5 kHz) was used to energize the primary coil using the circuit illustrated in Figure 6-12.

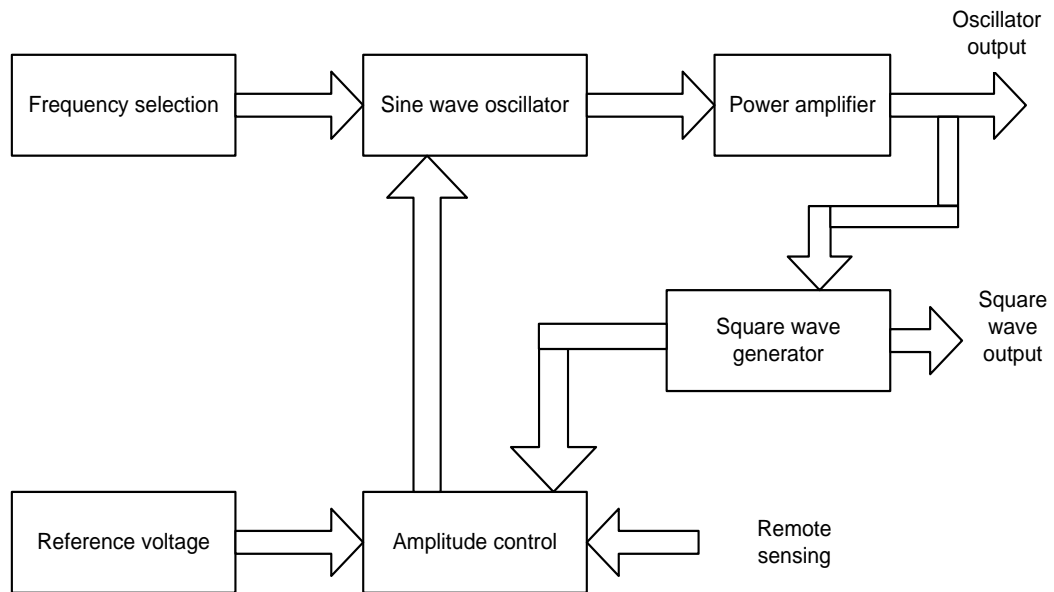


**Figure 6-12** Block diagram of the hybrid oscillator [solatrontechnologies.com]

Depending on the position of the core, the differential AC voltage output is induced by the demodulator for conditioning and amplification. The demodulator shown in Figure 6-13 amplifies the output from the transducer, and converts it to a DC voltage.

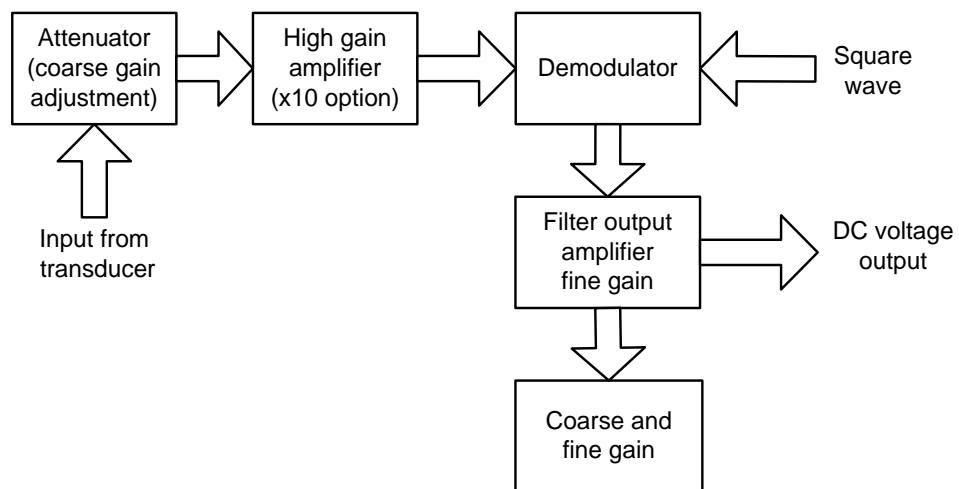


**Figure 6-13** Schematic of the hybrid demodulator circuit [solatrontechnologies.com]

The demodulator provides a nominal 5 VDC output (linear to 10 V) for inputs from 2.5 mV to 5VRMS (from 0.5 mV/V to 750 mV/V for 5 V primary coil energising input). The electrical noise sensitivity is less than 10mV/V. The current application for the oscillator-demodulator configuration to drive the LVDT is shown in Figure 6-14.



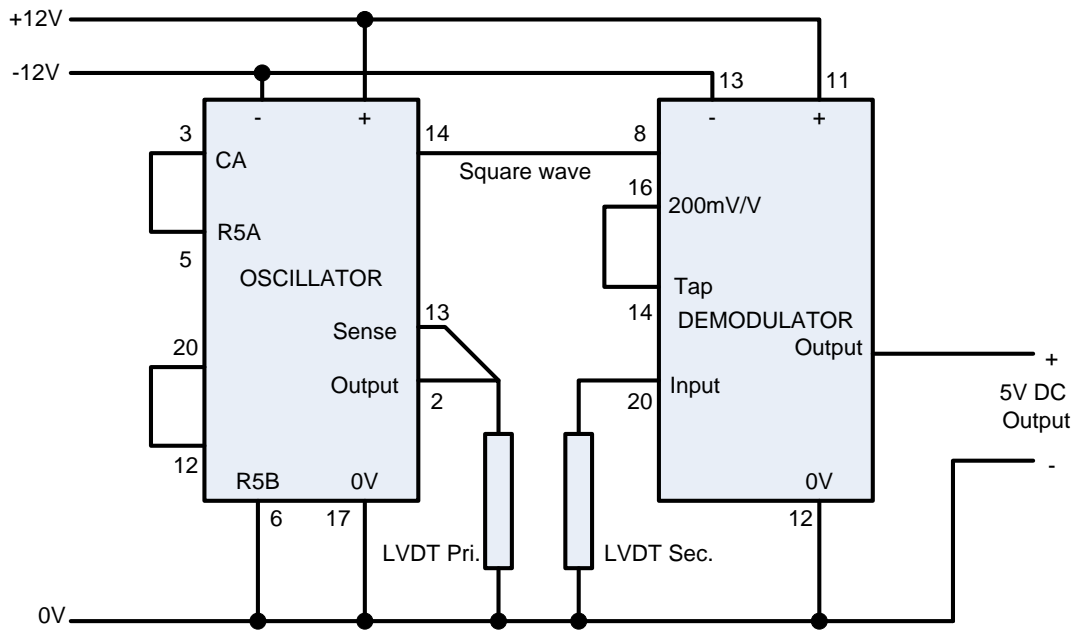


**Figure 6-14** Circuit schematic for the 5 V<sub>DC</sub> output and 5 kHz frequency

The demodulator output is acquired by channel AN8 of the dsPIC33FJ256GP710A for sampling, and the block diagram in Figure 6-15 highlights the sequence of events in the sampling process.

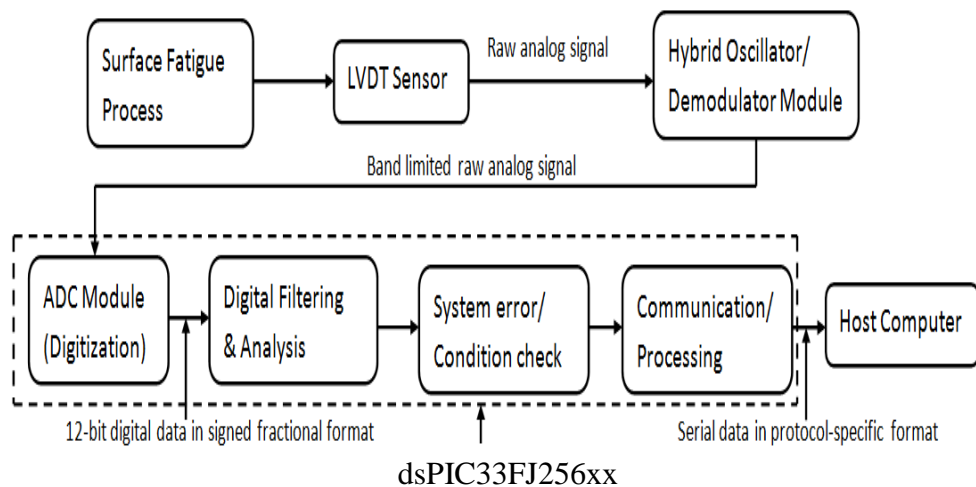


**Figure 6-15** Layout of the surface fatigue data processing.

Wear measurements are conducted at a low speed of 240 rpm in order to minimize dynamics. The minimum LVDT excitation frequency is set to the sub-system frequency, which is 2.5 kHz. This excitation frequency is within the LVDT transducer's frequency range of 1-15 kHz. The SM1 LVDT transducer was calibrated at 3V, 5 kHz; prompting a 5 kHz frequency selection in this application. According to the data sheet and preliminary tests, a  $\pm 12V$  supply voltage to the hybrid oscillator produced an accurate, stable sine carrier wave of  $5V_{RMS}$ , 5 kHz, which was used to energize the LVDT

transducer. The SM1 LVDT transducer has an infinite resolution, an accuracy of  $\pm 1$  microns in the  $\pm 1$ mm measurement range and a repeatability of 0.3microns.

## 6.5 Lubricating Pump Driver Interface

The lubricating pump uses a DC motor rated at 12V and a current of 60mA is interfaced to the dsPIC33FJ256GP710A through a L293D dual H bridge DC motor driver as shown in Figure 6-16, (circuit see appendix A3.3) and it is controlled by a separate timed loop derived from the servo update loop. The pump is connected to M1 configurations.

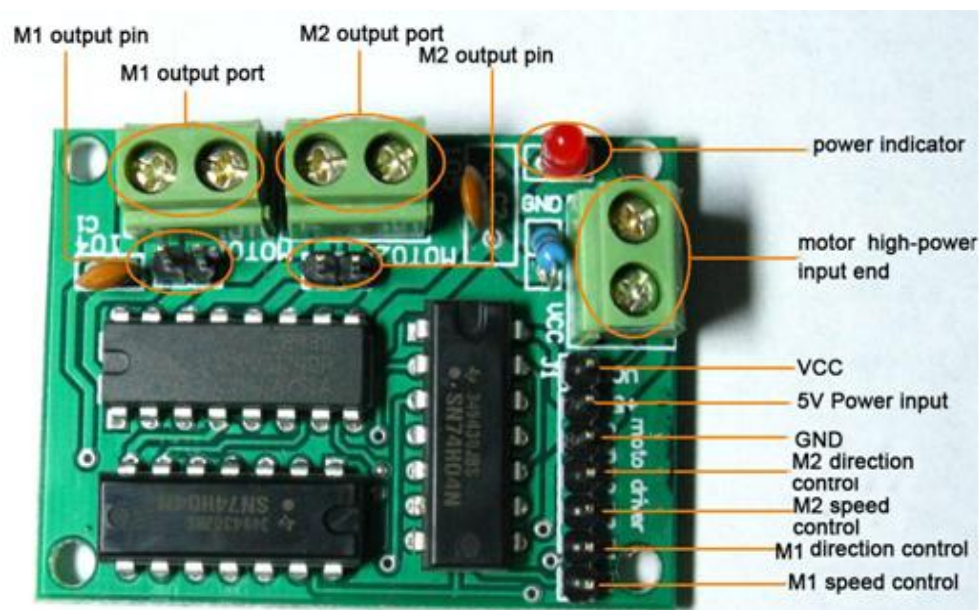


**Figure 6-16** L293D dual motor driver board for driving the peristaltic pump.

The pump runs at 5 rpm and has a flow rate of 0.08ml/s. This gives a drip of 1 ml in every 15 seconds. The pump cycle off-time is set at 15 seconds, and the pump operates twice in a minute. This is sufficient to lubricate and wash out any broken debris. The pump is set to run during the high fatigue cycle (i.e. 2040 rpm). The DsPIC33FJ256GP710A's output-compare module 2 (OC2) configured on pin register RD1 delivers a 5 kHz PWM signal with a 90% duty cycle to operate the pump in a forward direction. Figure 6-17 presents the pump driving and control algorithm.

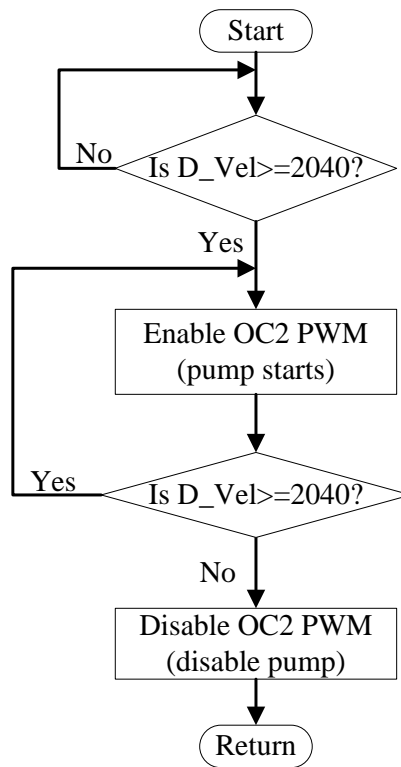


**Figure 6-17** Pump brushed DC motor control algorithm

## 6.6 Heating Circuit Interface

The test chamber is designed to partially simulate oral conditions in terms of temperature (i.e. 37<sup>0</sup>C) and moisture when required during testing. It is also possible to attain other temperature settings between 15<sup>0</sup>C-55<sup>0</sup>C. A schematic of the heating circuit is illustrated in Figure 6-18. The heating system is built using an off-the-shelf self-adhesive backing silicone heating mat, model SRM-120x80, 15V, 90W, a type K (Pt 100) exposed welded junction thermocouple, a Celduc DC Solid State Relay (SSR-model SM06020 as in Appendix A3.5) with a rated capacity of 20A and 5-40 V<sub>DC</sub> switching, an integrated timer and a dual LCD display TK 39 PID temperature controller and a supply rating of 24 V<sub>AC/DC</sub>. The TK 39 PID controller (see appendix A3.4 for connection) is automatically controlled by the dsPIC33FJ256GP710A through the SRD-05VDC-SL-C SSR with an optical-coupler using an input from the RG8 pin. In addition, a toggle switch serves as a safety switch to the controller. Once the toggle switch and an input from dsPIC33FJ256GP710A are on, the PID temperature controller regulates the on and off intervals of the Celduc SSR depending on the PID settings and the temperature sensed by the thermocouple.

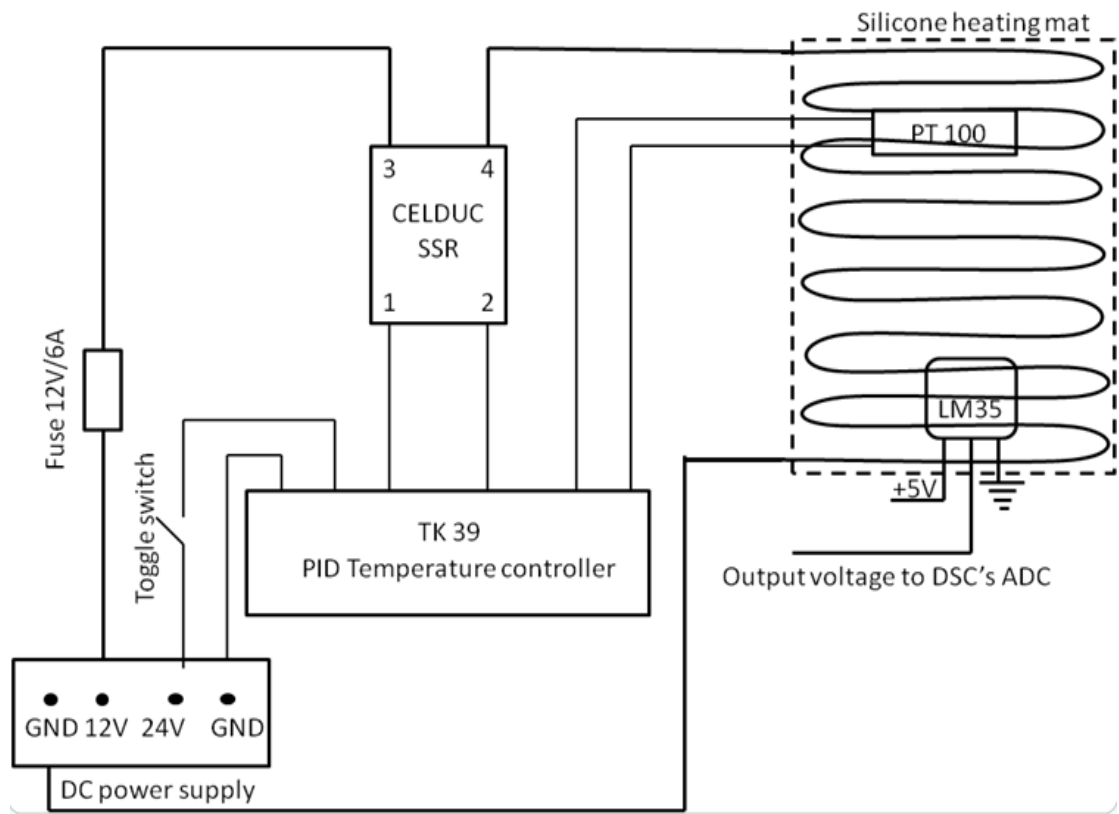


**Figure 6-18** Heating system accessories connection layout

In addition, LM35 sensors have been fitted in the test chamber, actuator and pump locations to monitor temperature using the AN9, AN12 and AN13 channels of the dsPIC33FJ256GP710A. The LM35 is a low-cost temperature sensor with a linear output of  $10\text{mV}/^\circ\text{C}$  and an accuracy of  $\pm 0.5^\circ\text{C}$  at  $25^\circ\text{C}$ , and is operated at  $5\text{V}$  using a sampling rate of  $0.015\text{Sa/s}$  (i.e.  $1\text{Sa/minute}$ ).

The flow chart in Figure 6-19 highlights the algorithm for sampling temperature. The measured temperature ranges from  $15^\circ\text{C}$  to  $55^\circ\text{C}$ , corresponding to the LM35's output of  $400\text{mV}$ . The ADC temperature conversion is based on an  $A_{V_{DD}}$  voltage of  $5\text{V}$ , and ADC 12-bit resolution. This gives a resolution of  $1.22\text{mV/count}$ . The AN8 digital output varies from 123 to 451 counts for the  $15^\circ\text{C}$ - $55^\circ\text{C}$  temperature range, which fits well within the ADC 12-bit resolution. The flow chart in Figure 6-19 highlights the algorithm for sampling temperature.

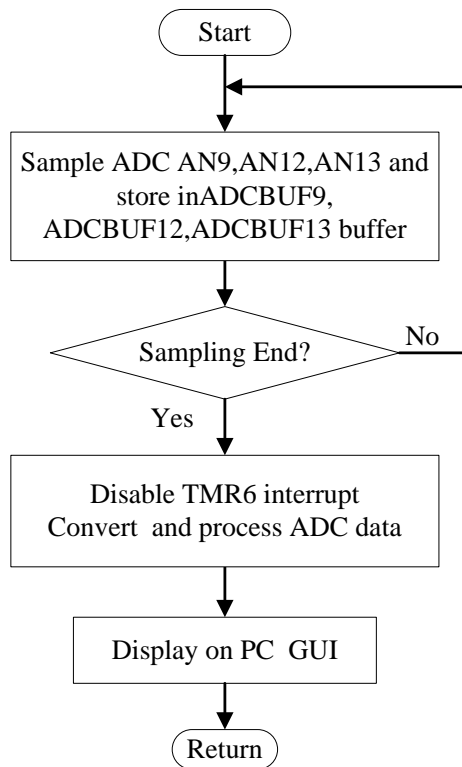


**Figure 6-19** Temperature sampling algorithm flowchart

## 6.7 RS 232 Serial Communication Port

The dsPIC33FJ256GP710A uses a Universal Asynchronous Receiver Transmitter (UART) RS 232 serial communication protocol to transmit and receive data to and from the host computer. In this application, RS 232 communication is achieved through the serial port UART1 on the development board and pins 25 and 26 of the DSC. The port gives full duplex serial communication with 8 or 9-bit communication and baud rates of between 38bps to 1.875Mbps and 30MHz instruction rate. Even, odd or no parity can be used for 8-bit data. A stop bit length of 1, 1.5, or 2 bits can be used. Figure 6-20 illustrates the simplified main elements of the UART such as a baud rate generator, asynchronous transmitter and asynchronous receiver. The board also includes the logic to interface the UART to DSC and the RS-232 line drivers. The UART data transfer rate configuration is set at the bit rate of 9600 bps, 8 data bit, zero parity stop and no flow control. The dsPIC33FJ256GP710A also has a second asynchronous serial port (UART 2), Serial Peripheral Interface (SPI), Intra-integrated circuit (I<sup>2</sup>C) and Controller Area Network ports (CAN) channels, to support future needs for external peripherals communication.

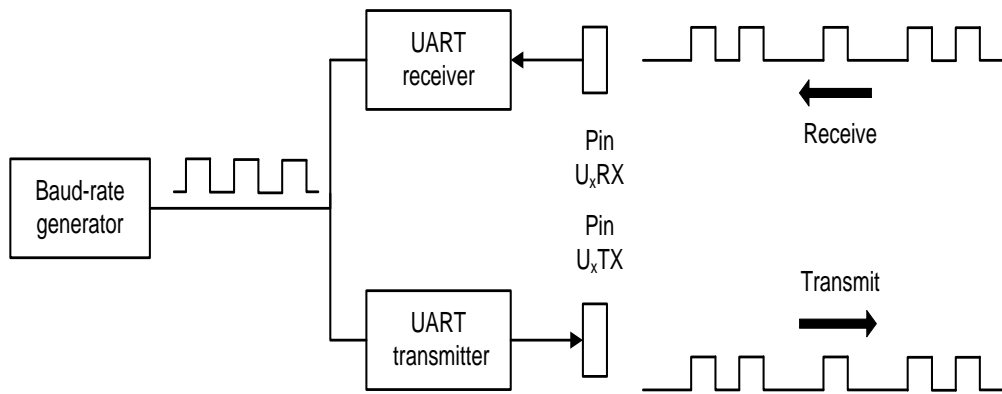


**Figure 6-20** dsPIC33FJ256GP710A DSC UART serial port

The UxBRG register controls the period of a free-running 16-bit timer and for this application, the reference baud register bit is estimated to 260 using equation 6.17.

$$\text{Baud rate} = \frac{F_{cy}}{16 * (U_xBRG + 1)} \quad (6.17)$$

$$U_xBRG = \frac{F_{cy}}{16 * \text{Baud rate}} - 1 = \frac{40 \text{ MHz}}{16 * 9600} - 1 = 260$$

The implementation uses a buffered interface in order to free the application from the need to block on transmission or reception of messages that are longer than the UART 4-byte receive and transmit buffers. A summarized flow chart of the RS 232 protocol is presented in Figure 6-21.

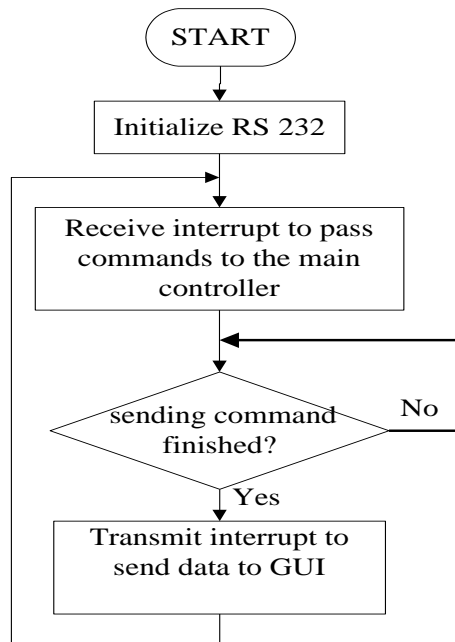


**Figure 6-21** RS 232 Communication sub routine

## 6.8 Embedded Software Design

The embedded software comprises software to provide user access to the measurement system via a Graphical User Interface (GUI), and real time software with sub-programs for motor control and sampling measurement data from the sensors. The software interrelates and functions together as highlighted in Figure 6-22. Efficient communication between the software is based on the following criteria:

- (a) There should be a data identification format for transferring and receiving data between the two programs to enable coherent communication.
- (b) The correct data format should be used to allow the RS232 protocol to code the data into ASCII code. Coded string data should not be more than 16-bit long to allow the DSC microcontroller to convert them to integers or characters.
- (c) An interrupt triggers data conversion timing in the DSC microcontroller. The GUI program should have a special thread program to check and read received data.

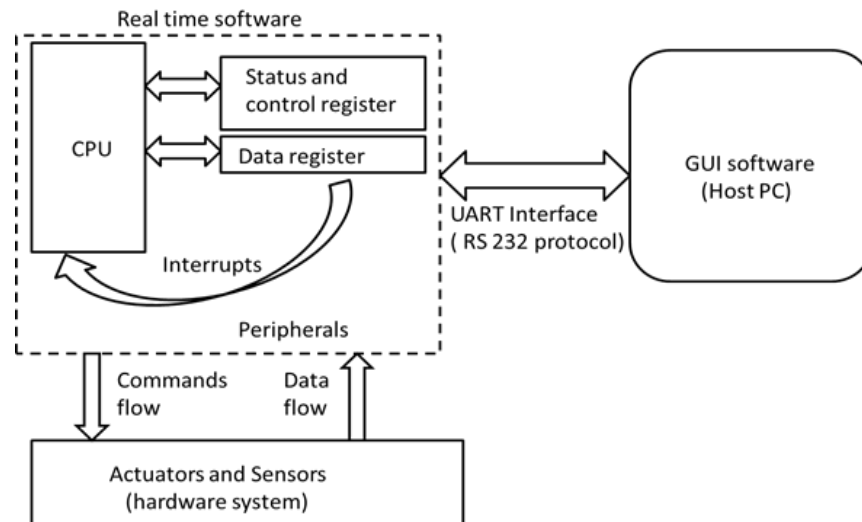


**Figure 6-22** Schematic of embedded software functional relationship

### 6.8.1 Embedded real time program

The real-time programs were developed using the MPLAB IDE v8.60 C platform and CCS compiler and uploaded to the dsPIC33FJ256GP710A DSC microcontroller. MPLAB IDE v8.60 is an integrated environment for developing embedded C software programs that run on a PC to develop applications for Microchip microcontrollers such as the Microchip PICmicro<sup>®</sup> MCU or dsPIC<sup>®</sup> Digital Signal Controllers (DSCs). The

MPLAB IDE is integrated with CCS MPLAB IDE plug-in software to facilitate compiling the programs using a CCS PCD compiler. The CCS PCD compiler is a third-party C compiler for Microchip's 24-bit operation code family of microcontrollers, including the dsPIC30, dsPIC33 and PIC24 families. The compiler is specifically designed for the unique applications of the dsPIC<sup>®</sup> microcontroller. The choice of the compiler allows application programs to be designed in a more readable, high-level language in the shortest time. In addition, the compiler has been optimized to write and compile normal C instructions, input/output operations, bit operations, bit arrays, multiple address space handling and the effective implementation of constant data in ROM to generate code effectively. Schematic showing the CCS\_PCD/MPLAB IDE platform is appended in appendix A4.1.

The real-time program comprises dedicated functions to execute specific tasks which are initiated by the main program in a pre-defined sequence using interrupt service routines (ISR). These include system initialisation, transmitting and receiving data to/from the GUI, controlling the BLDC motor through the L6235N, counting encoder pulses, the ADC sampling of outputs from the LVDT, accelerometer and temperature sensors, and driving the lubricant pump and PID temperature controller. The overall program flow chart is included in Appendix A4.3. The sub-programs are called by the main program and initialized using interrupt routines upon which the main program continues running on the completion of the sub program.

### ***6.8.2 Program and interrupt routines configurations***

The development board uses an external crystal for the dsPIC33FJ256GP710A with a frequency of 7.37 MHz, operating in a primary phase locked loop (PR\_PLL) mode to clock the dsPIC33FJ256GP710A chip at 80MHz. Each dsPIC33FJ256GP710A program instruction requires 2 clock cycles to execute, thus giving the chip a processing speed of 40MIPS. The interrupt routines are installed as peripherals and initialized by an interrupt flag. The main program involves hardware and software system initialization, hardware setting configuration, and RS232 communication. Subroutines for PI speed control pump control, the LVDT data accelerometer and temperature data acquisition are sequentially monitored and executed by the main program using interrupts. The availability of input capture, output compare, timers and ADC peripheral modules facilitates pulse timing for low speed measurement and pulse counting for high speed



measurement, PWM configuring, ADC sampling, and pump and temperature control. A flow chart of pulse timing and pulse counting for the two speeds control is shown in Figure 6-23.

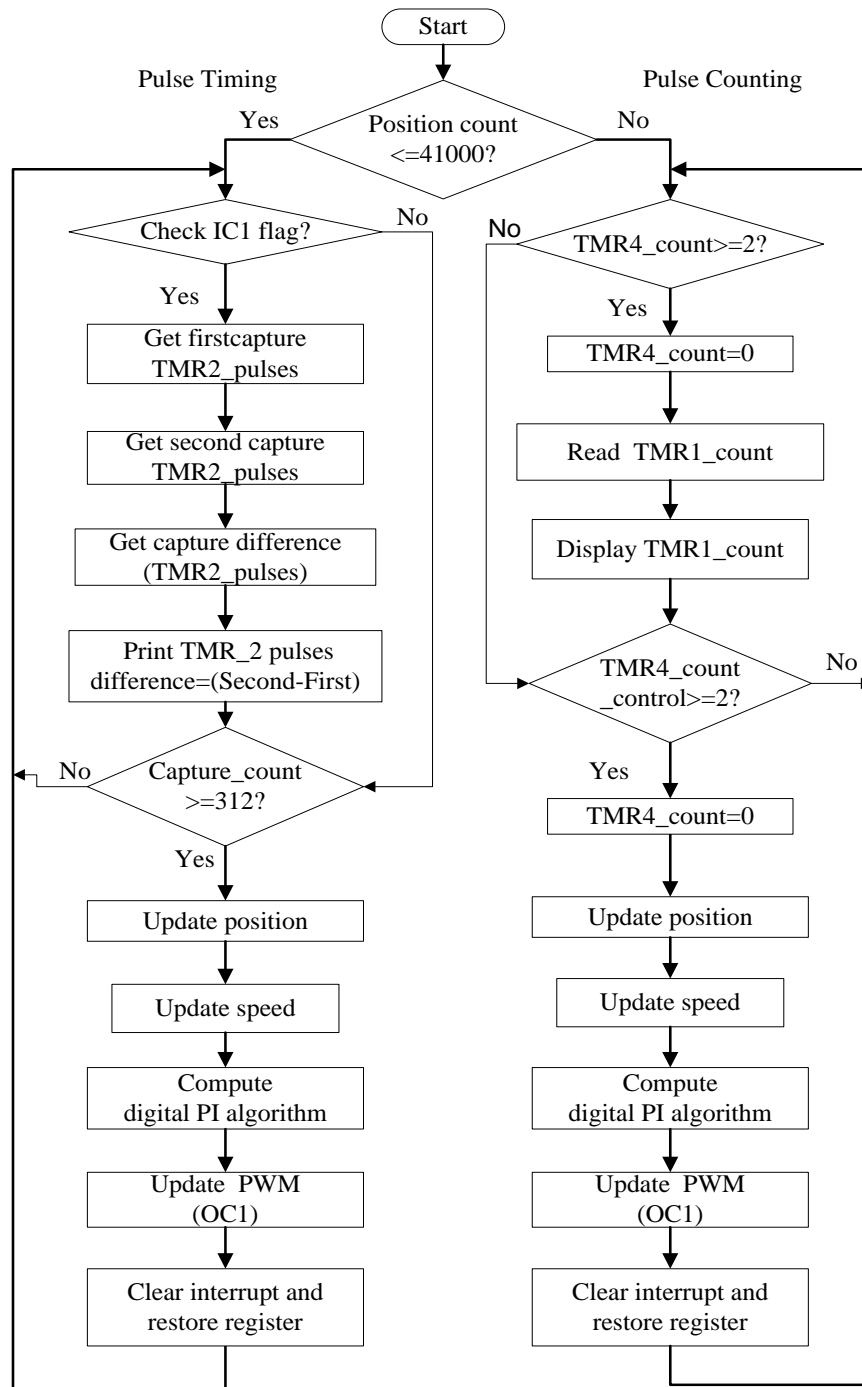


**Figure 6-23** Combined pulse timing and counting algorithm flowchart

The algorithm for speed control uses position counts accumulated in the *SimCount* variable as detailed in section 6.3.3, to switch between low speed-pulse timing and high speed-pulse counting methods. The switching is facilitated by polling a flag when the position count reaches 41000 pulses. The position counts are obtained from the *Timer\_1*

up-count pulses of the encoder. During pulse timing method at low speed, the input capture module\_1 (IC1) captures the falling edge of the *Timer\_2* by interrupting on every second pulse capture. The width of the pulse (or period) is established by the difference of the first and second capture. The result is in counts (i.e. 312 counts for a speed of 240 rpm) corresponds to the measured speed of the motor. The speed counts are passed to the proportional integral (PI) subroutine for updating and regulating the desired speed to ensure a steady state running through the output compare (OC\_1) PWM\_ module. Pulse counting starts at a speed greater or equal to 720 rpm in which timer\_4 interrupts every 10 ms to read pulses (i.e. counts) of the motor speed. The counts are checked against those of the desired speed by the PI speed control subroutine which updates the PWM signal accordingly. This is implemented using output-compare module (OC\_1). The flowchart for the *timer\_4* interrupts service routine (ISR) for motor speed control is in Appendix 4.2.

### 6.8.3 Configuring PWM port

The dsPIC33FJ256GP710A's OC1 is configured to generate a PWM signal, which the low-pass filter of EVAL6235N driver converts to a variable voltage reference for the internal PWM current control circuit. This is achieved by configuring the PWM frequency using the *Timer3* module to give the time base for the PWM signal with reference to the crystal clock. The dsPIC33FJ256GP710A has an instruction cycle period ( $T_{cy}$ ) of 25ns. The *Timer3* register is 16-bit, thus requiring a periodic register value ( $PR_x$ ) to be <15:0>. If the selection starts by setting the time pre-scale factor ( $TMR_xPSF$ ) to 1, and using equation 6.12, a PWM frequency ( $F_{PWM}$ ) of 610 Hz is obtained from the 16-bit timer resolution.

$$F_{PWM} = \frac{1}{[(PR_x)+1]*T_{cy}*TMR_xPSF} \quad (6.12)$$

A rule of thumb is that PWM should be set at least 10 times faster than the motor time constant to give a smooth response of the motor. The EC-max 30, model 272765 has a time constant of 4.17 ms, and therefore a frequency of at least 2.4 kHz PWM is required. Tuning and observing the output characteristics with an oscilloscope led to the selection of a PWM of 5 kHz. The correct value of the period register is given by equation 6.13:

$$PR_x = \frac{F_{cy}}{F_{PWM}*TMR_xPSF} - 1 \quad (6.13)$$

This gives a Timer 3 register value( $PR_x$ ) of 7999. The PWM duty cycle value to load to the duty cycle register pin is calculated using equation 6.14:

$$Duty\ cycle = \frac{PDC_x - DT}{PR_x + 1} \quad (6.14)$$

$DT$  is dead time, and in this application is considered null (0s), and  $PDC_x$  is the duty cycle register value. The duty cycle register value to give a continuous high switching (i.e.100% duty cycle) is determined as 7999. The PWM period is 0.2 ms. If 75% of the period is chosen as the high time during PWM switching, the duty cycle register value ( $PDC_x$ ) is 5999. The initial settings were adjusted to obtain a smooth motor response during system implementation at 5850, which is equivalent to a 73% duty cycle.

#### 6.8.4 Configuring Timers

The dsPIC33FJ256GP710A supports 9 timers which can be configured as either timers or counters. All of these share common characteristics, but each also has special features dedicated to certain types of task. *Timer1* has a 16-bit module; whereas other timer modules have 32-bit which can be configured as a single 32-bit timer/counter or two timers/counters of 16-bit each. The timers can be configured as timers or synchronous and asynchronous counters as detailed in the dsPIC33FJ family reference manual [[www.microchip.com](http://www.microchip.com)-accessed on 22.07.2013]. In this application, *Timer1* is the counter which counts the encoder's UP pulse. *Timer2* is configured as a 16-bit free running timer for setting the time width of the Input capture module *IC1* and *Timer3* is set as a 16-bit timer used for setting the PWM time base. *Timer4* is configured as a 16-bit timer for the 10ms servo updates interrupt routine to time the encoder pulses. *Timer5* is configured as 16-bit timer for the 10ms sampling loop for the LVDT sensor. *Timer5* and *Timer6* are configured as 16-bit timers for the accelerometer and temperature sensors sampling period. *Timer7* is configured as a 16-bit timer for providing the interrupt service routine to send data to the host PC through RS232 serial communication. The *Timer8/9* modules are reserved for future use.

#### 6.8.5 Configuring ADC sampling, online and offline data processing

The dsPIC33FJ256GP710A has 32 input analog channels, available in 2 ADC modules, and can be configured into 12-bit resolution single sample and hold amplifier or 10-bit

resolution multiplexed into four sample and hold amplifiers. The output of the sample and hold amplifier is the input into the converter which generates the digital output. Port B analog channel pins were configured as ADC input pins for this application. Register pin B8 is used to sample the LVDT transducer, B10 and B11 are used to sample data from the accelerometer's X and Y axes, and register pins B9, B12 and B13 are used for sampling LM35D temperature monitoring sensors for the testing chamber, motor and pump. The rest of port B channels are used for other I/O connections or reserved for future analog input configuration. The port is configured to 12-bit resolution single sample and hold amplifier, and initialised appropriately to execute alternate sampling depending on the software requirements.

The LVDT sensor sampling is based on the number of load cycles per second expected to be acquired (i.e. 2.1 rev/s). Based on these requirements, channel AN8 was sampled at 100Hz for the LVDT. Three temperature samples are conducted at a rate of 15 MilliHertz (mHz) or approximately 1 sample per minute due to slow rate of change. Primarily, the sampling is for temperature monitoring purpose. The ADC conversion clock and sampling time are estimated using the instruction clock frequency of 40 MIPS. Therefore, the clock period is  $T_{CY} = 25\text{ns}$

$$\text{Sampling time} = \text{Acquisition time} + \text{Conversion time} \quad (6.14)$$

The recommended minimum sampling time  $T_{AD}$  is 75ns for dsPIC33FJ256GP710A for a clock speed of up to 500 kSa/s and  $V_{dd}$  ranging from -0.4V to 4.0 V. Correct ADC data conversion requires the number of the ADC conversion period to be  $14T_{AD}$  for a single channel of the 12-bit ADC module.  $T_{AD}$  is derived from  $T_{CY}$  using equation 6.15:

$$T_{AD} = T_{CY}(ADCS + 1) \quad (6.15)$$

If  $ADCS\langle 7:0 \rangle$  is set to the highest numeric value of the 8-bit ADC clock select register of 256, the actual  $T_{AD}$  period can be calculated:

$$T_{AD} = (25 * 10^{-9} * (256)) = 6.4 \mu\text{s}$$

Thus, A/D module conversion period per channel is  $14 * T_{AD}$ , equivalent to 89.6 $\mu\text{s}$ , which is rounded to 90  $\mu\text{s}$  (11 kHz sampling rate per channel). Subsequently, the total time for each sample/convert sequence can be determined. LVDT sensor sampling frequency is 100Hz, which is equivalent to 10ms. Therefore, a conversion of 90 $\mu\text{s}$  allows a

maximum of 9.9ms as acquisition time. The acquisition time is sufficient for effective LVDT sensor sampling. Similar analysis has shown that, for accelerometer sampling at 1 kHz, 0.9 ms acquisition time is used and satisfies the sampling requirements. Because temperature is sampled at a slow rate of 15 mHz, there is enough acquisition time. The algorithm for the LVDT wear transducer and accelerometer sampling programs are depicted in Figure 6-24 with numbers 8/10/11 and 4/5 indicating respective ADC sampling channels and timer modules for sampling time . The sampled data are stored in the respective ADC buffers, digitized and post-processed online for time-domain features.

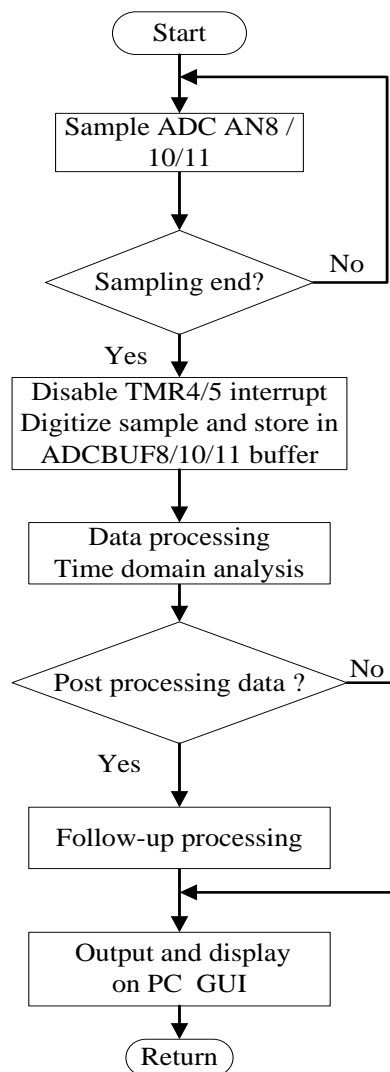


**Figure 6-24** Sensors ADC sampling algorithm

Figure 6-25 shows a schematic block diagram with time-domain features which are processed online by the embedded processor and frequency-domain features which are processed offline using the host PC GUI and data analysis software.

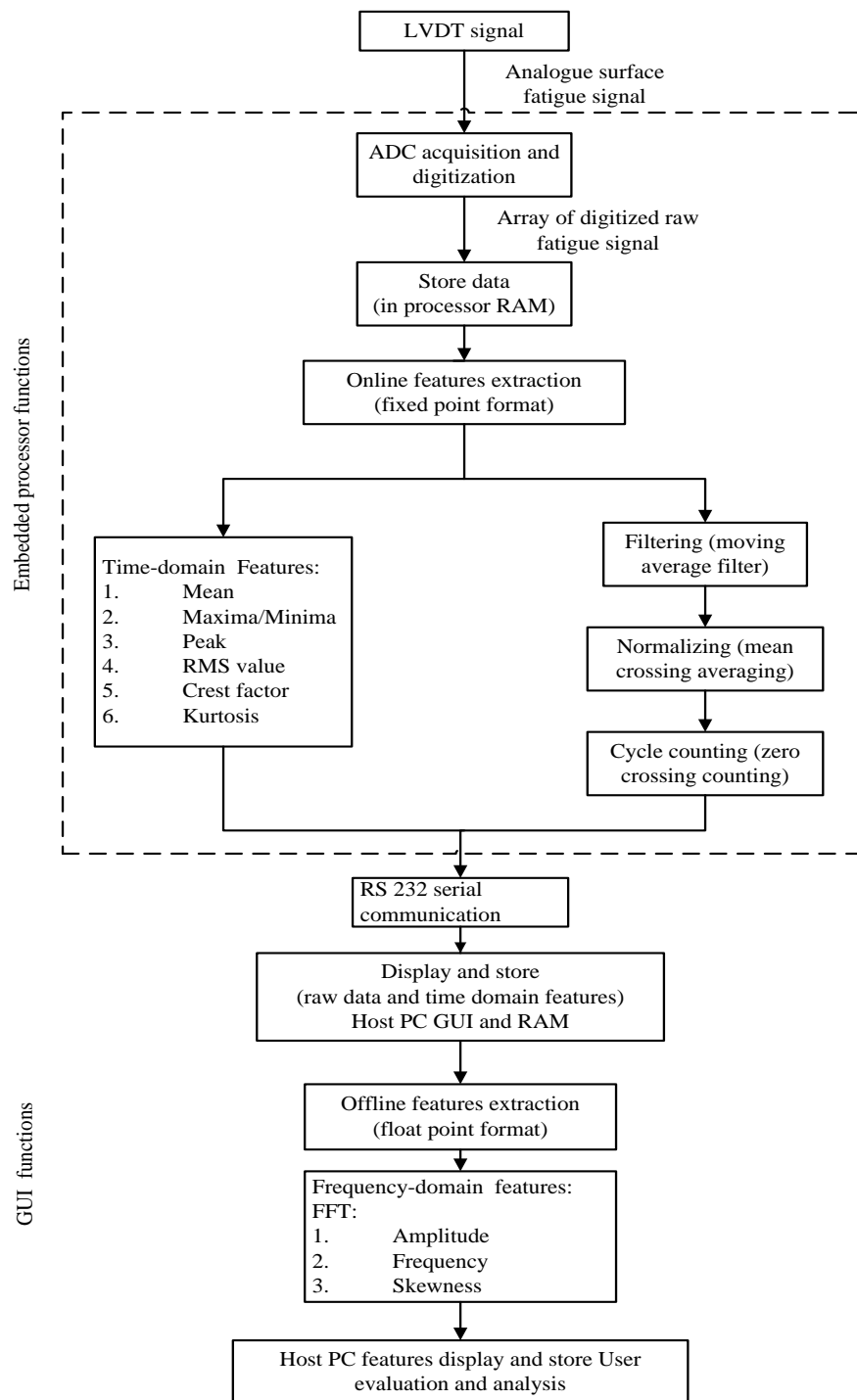


**Figure 6-25** Block diagram of the LVDT online and offline features extraction

The time-domain features are processed online because they are fixed point format and hence less demanding in terms of chip processing power and memory capability. The frequency-domain features are floating point format and demands high processing power and memory which cannot be provided simultaneously with speed control functions by the low cost embedded processor. MATLAB software is installed on the host PC and used for offline processing and analysis. The time-domain online

processing algorithm is integrated with the subroutines for data sampling and main program software into the processor chip.

The LVDT data is acquired and digitized at the speed of 240 rpm and temporarily stored in array format in the RAM of dsPIC33FJ256GP710A, including corresponding register addresses. Because the data is in an unsigned integer 16 format and 2000 samples are read, processed and stored per one sampling, 8 kBytes of the RAM memory are consumed, leaving limited RAM memory for processing the data and performing speed control functions. After accelerating and attaining a constant to 2040 rpm, data processing subroutines calls the stored raw data, process and extract online time-domain features outlined in Figure 6.28 in order to instantly indicate the amount of surface fatigue damage on the dental specimen. The raw data and processed time-domain features are subsequently transmitted to GUI in the host PC through serial RS 232 communication. The transmitted data is sent in buffered transmitted data is received by the VISA function the LabVIEW which is the GUI software and displayed through the terminal while being stored in excel format in the host PC RAM.

Upon storage of the raw data on the host PC RAM, the user can perform frequency-domain analysis using MATLAB software based on fast Fourier transforms (FFT). Through FFT, frequency-domain features such as frequency components, amplitudes (maxima and minima), skewness, energy and linear correlation of the raw data signal can be extracted in order to establish relevance to the critical surface contact fatigue moments of initiation against the number of load cycles. The analyzed features distinguish patterns of induced vibration in order to indicate surface degradation due to pitting and/or spalling with defined number of load cycles.

#### ***6.8.6 LabVIEW Graphical User Interface***

LabVIEW software from National Instruments was used to develop the GUI application to enable users to access and control test parameters as well as monitor, post-process and store measurement data in Excel format. LabVIEW contains functional nodes and wires to create data flow programs instead of lines of codes. This makes it simpler and more flexible, convenient and user-friendly than pseudo-code driven software such as Visual Basic and MATLAB. In-built VISA functions and libraries were used to create GUI serial communications compatible with the dsPIC33FJ256GP710A's UART RS232. VISA provides the programming interface between hardware and software.

LabVIEW software is populated with tools and configuration utilities for VISA, thus making it simple to interface with the RS232 protocol of the dsPIC33FJ256GP710A. The user interface window is linked to the flow code window to enable ready-made virtual instruments and functions to write communication software. The layout of the DSC and LabVIEW interface configuration is summarized in Figure 6-26.

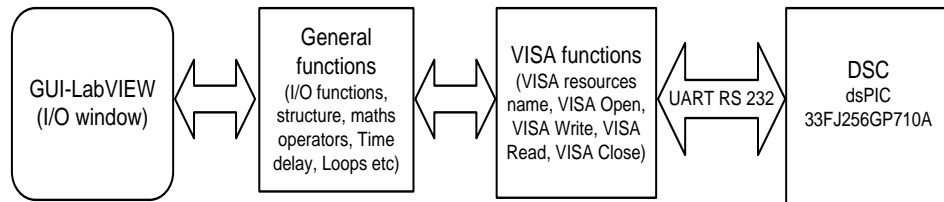


**Figure 6-26** Schematics of GUI program and device interface

### 6.8.7 Serial Communication Interface

Virtual Instrument Software Architecture (VISA) sequentially writes to and reads from the RS232 serial port before closing the session upon completing the I/O task. The data flow flowchart shown in Figure 6-27 and the VISA event protocol, shown in Figure 6-28 enable the stable reception of serial data. The VISA event protocol enables an event triggering when a termination character is received. In so doing, data transmission is made easy and consequently allows the serial port input buffer to read data at a desired rate. In addition, the overflow and/or fragmentation of input buffer data are eliminated. The DSC serial communication interfacing VISA has been discussed in Section 6.8.

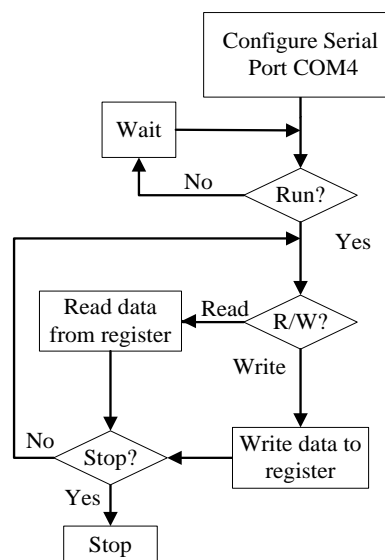


**Figure 6-27** LabVIEW and DSC serial communication algorithm flowchart



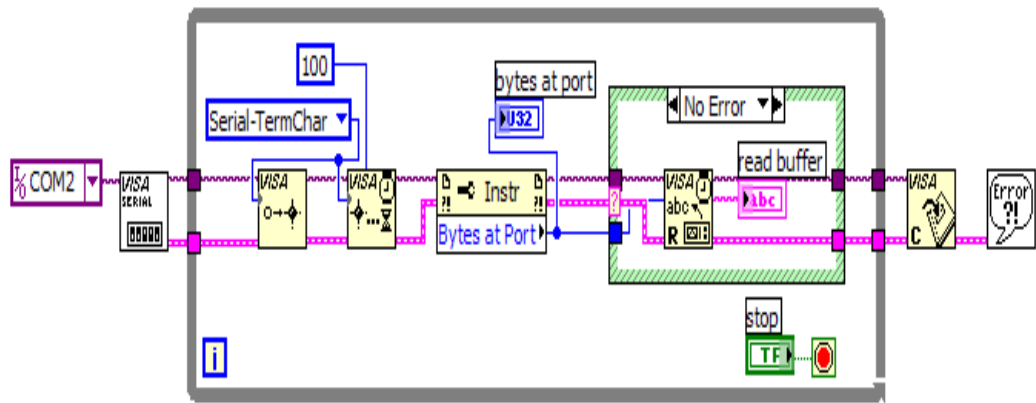


**Figure 6-28** Schematic of VISA Event serial data communication [www.ni.com]

### 6.8.8 Program modules and data storages

The virtual instruments are modularized into related functions and data activities to facilitate maintenance and future expansion. In-built subVIs enables data input/output, conversion and flow from one node to another depending on the task. The program includes sub-virtual instruments for the motor control and drive, LVDT data acquisition, the accelerometer measurement, lubrication pump and temperature monitoring for motor and pump. A first in first out (FIFO) buffer handles cluster of arrays of the digitized data incoming from the sensors to facilitate post-processing. Thus, there is a loop for reading serial data from the GUI and passing it to the DSC, and another loop based on event interrupts to receive digitized data from the microcontroller. The content of the front panel of the GUI is outlined below, followed by a pictorial presentation in Figure 6-29.

- (a) The GUI for the BLDC motor shows the following parameters:
  - set motor speed
  - show current motor speed
  - i. On/off switch and LED indicator
  - ii. Indicators showing the motor's operation in manual or automatic mode
- (b) The GUI for LVDT and accelerometer data indicates the following parameters:
  - i. Indicator showing last stored and current depth of wear track
  - ii. Button to measure the current wear track
  - iii. Indicator showing accelerometer readings over a specified time interval
  - iv. Indicators showing the operation status of the LVDT and accelerometer

- (c) The GUI for the lubricant pump displays the following parameters:
- i. On/off switch and indicator
  - ii. Indicator showing the motor's operation of the pump
- (d) The GUI for the RS 232 communication port shows:
- i. Indicators for baud rate, number of bit, parity number and flow control,
  - ii. Button to initiate writing and reading operations
  - iii. Indicators to show VISA Write and VISA Read status and content

The GUI window has a VISA resources configuration terminal, switches and displays for reading and writing commands, motor and pump switches and their status display terminals, displays for the set number of load cycles, and the instantaneous load cycle display.

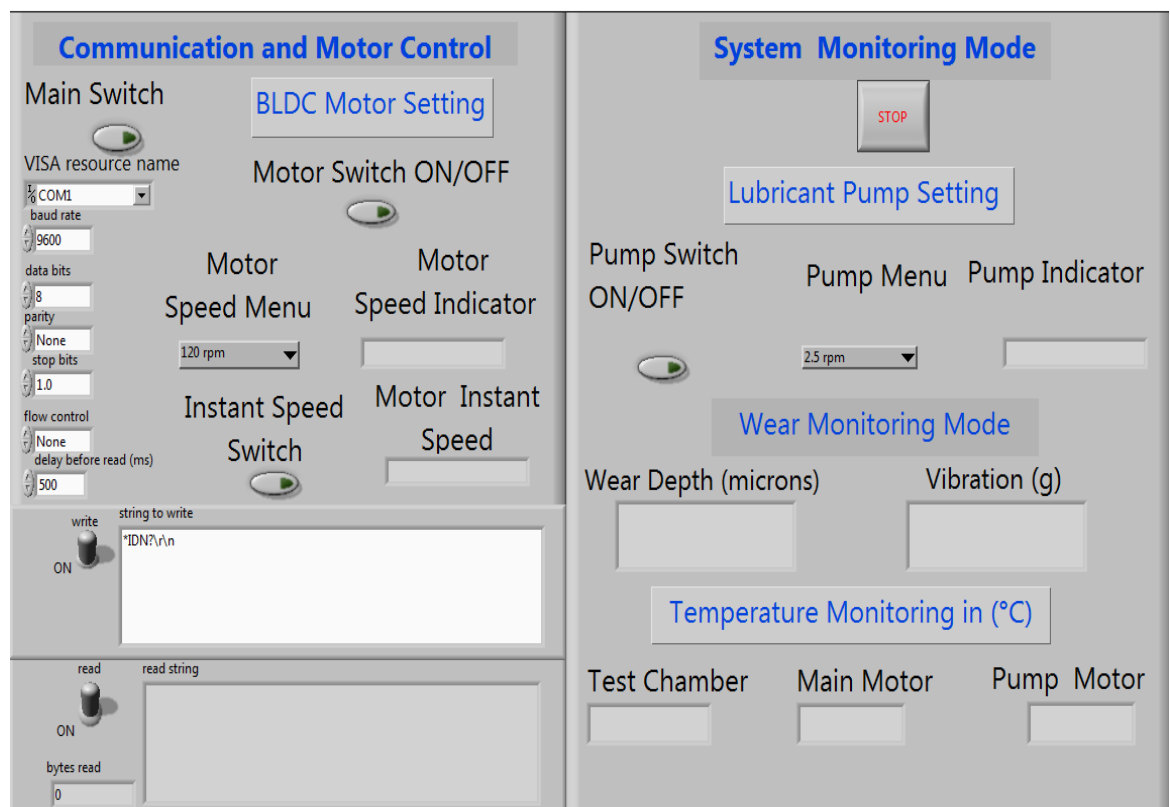


**Figure 6-29** Schematics of GUI program and device interface

### 6.8.9 Embedded software integration

A bottom-up approach was used to integrate the hardware and software systems in two phases. Phase one involved C code compilation to establish that written C codes were

working at respective module levels as per the module specifications. Tasks involved running sub-programs, checking boundary conditions, minimum and maximum limits reached and exceeded, and initialization of the sub-program. Phase two involved integration of the embedded system modules to check their compatibility. Activities included altering program codes and re-writing to integrate different embedded modules. Integration with the mechanical hardware followed a successful testing of each embedded module.

## **6.9 Summary**

This chapter has detailed the design approach to realise the embedded system for the mechatronic rolling-ball device. The approach integrated conventional and modern electronic applications to enable part selection and acquisition. Electronic and embedded hardware designs have been optimised based on the insights gained from the previous prototypes. Embedded software uses a high performance RISC DSC microcontroller to enable the mechatronic system to automate and control the testing processes, data processing and storage. A GUI has been designed based on LabVIEW software to enable inexpensive and flexible enhancement of the GUI in future. The next chapter describes the operation of the mechatronic rolling ball device.

## **CHAPTER 7 MECHATRONIC ROLLING BALL DEVICE SET-UP, OPERATION AND EXPERIMENTAL RESULTS**

The chapter describes the set-up and operations of the rolling ball device including a testing program and results for the qualification of the measurement system. The functionalities of the measurement system are tested in order to qualify and validate its performance.

### **7.1 Mechatronic System Set-up**

The block diagram in Figure 7-1 outlines the subsystems listed below which make up the mechatronic system:

1. Main microprocessor unit (MCU) controller.
2. Actuator and its controller.
3. Data acquisition sensors
4. Monitoring and conditioning subsystem
5. Communication and GUI module

All the modules, including peripheral controllers, are controlled by the main controller, which is a dsPIC33fj256gp710a Microchip Digital Signal Controller (DSC). The system uses 5VDC, 9VDC,  $\pm 12$ VDC and 24VDC power supply inputs depending on the power requirements of each part. The power supply inputs are indicated using plus (+) and minus (-) signs. A full design description and the specifications of the system have been covered in Chapter 5. The GUI software (see Figure 6-29) is built on a host PC to enable user-machine interaction. The user interacts with the GUI to transmit commands and input parameters to the system as well as retrieving data from the system. The Virtual Instrument Software Architecture (VISA), which is a standard interface library in LabVIEW with an RS 232 communication protocol, transmits and receives data to/and from the main controller. The data includes the time domain features of the wear measurements from the LVDT transducer and accelerometer and temperature readings which are displayed on the GUI. Concurrently, the data is stored in a data file in Excel format for post-processing and visualization. The communication port set-up variables are configured on the GUI and commands are executed using virtual switch icons on the GUI.

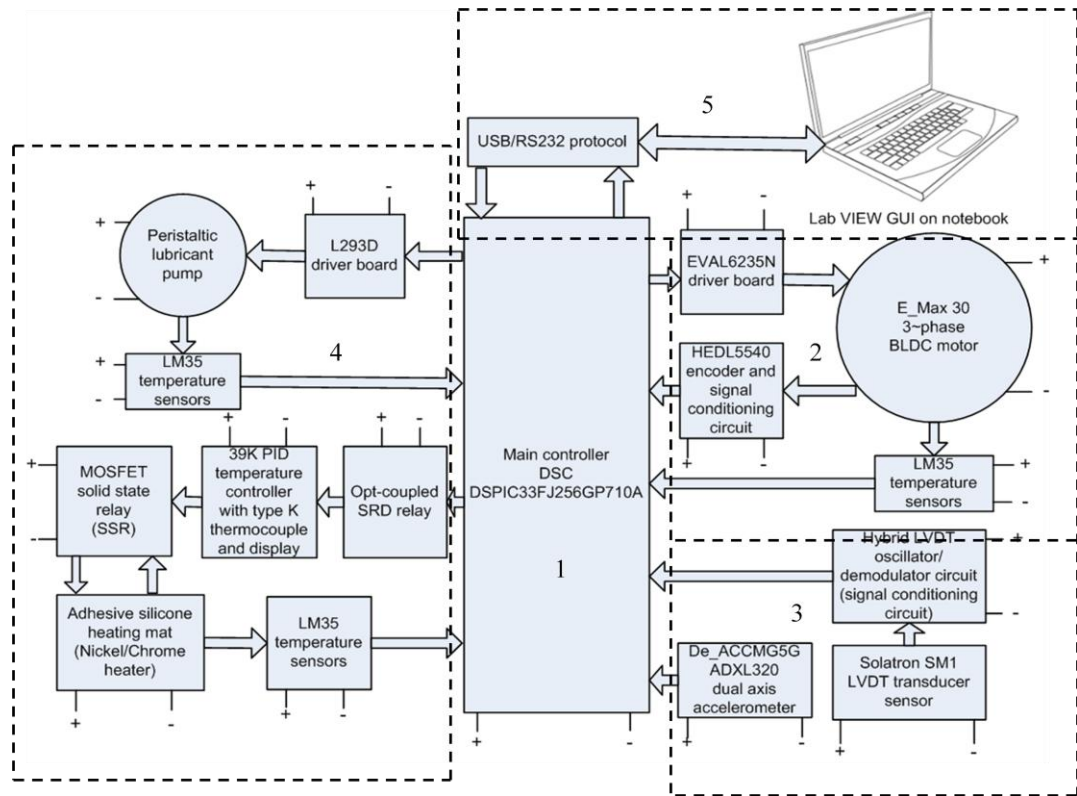


**Figure 7-1** Interaction and layout of mechatronic sub-systems

The module which actuates surface contact fatigue uses a trapezoidal speed control with three control levels, as shown in Figure 7-2. The speed control starts and ends at 0rpm after a series of eleven sampling cycles and ten surface fatigue cycles totalling  $10^6$  load cycles. The speed control loop has a sampling time of 10ms. The lower speed of 240 rpm is used to acquire the LVDT transducer output in order to minimize measurement error resulting from the dynamics of the ball (i.e. bounce, drift, etc.) and mechanical vibrations of the specimen carriage. The plot in Figure 7-2 indicates the speed profile for successive three intervals of sampling cycles and two intervals of surface fatigue with 100,000 load cycles each, which are orbital rotations. The actual speed of the ball and the speed ratio between the mandrel and ruby ball was difficult to measure online, using a sensor due to the small size of the ball (i.e. diameter 2 mm) and constraining groove which limit the clearance between the specimen and mandrel to only 0.5 mm. In order to establish the ball speed, a hand-held Stroboscope was used. The kinematical modelling in Chapter 3 has established the speed ratio between the mandrel and ball to be 1.87. The spindle is coupled to the motor and encoder shaft using a synchronous toothed belt giving a driving ratio of 1:1. The mandrel's symmetrical groove of  $120^\circ$  ensures three-point contact in order to minimize slip and reduce the wear of the ball.

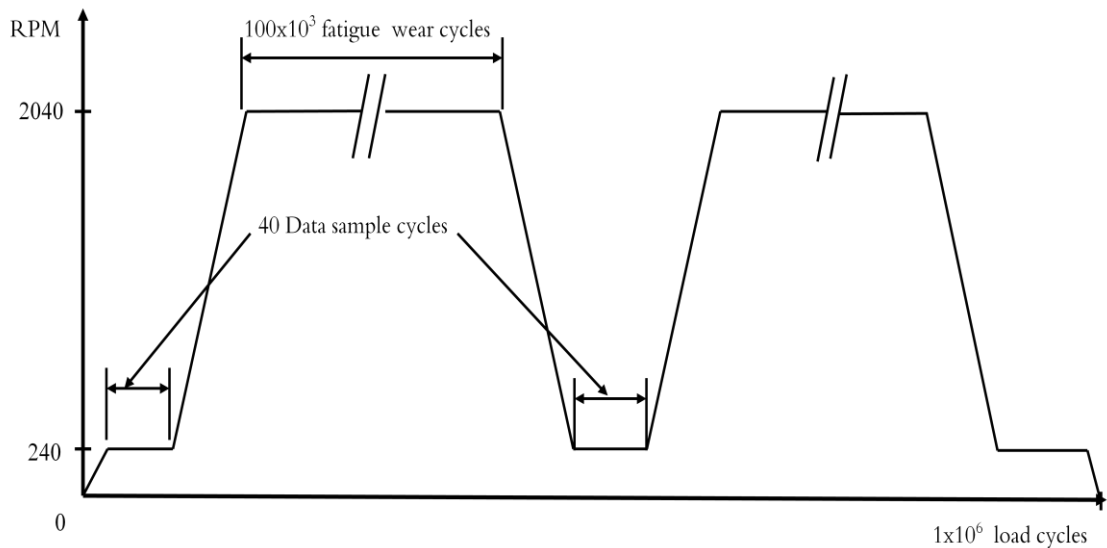


**Figure 7-2** BLDC motor for the actuator speed profile curve

It was important to establish the speed relationship between the mandrel and ruby ball during rolling, and actual speed measurements were conducted using new and worn mandrels with a symmetrical V-groove of  $120^\circ$ . The worn mandrel had been used for a testing cycle equivalent to  $5 \times 10^6$  load cycles, and has suffered a moderate contact wear on the groove. A Stroboscope (model: DAWE, TYPE: 1214B) was used to measure the mandrel and ball speeds in dry and wet conditions while the specimen was held at an inclination of  $1.5^\circ$ . Inclining the specimen provided a non-erratic and uniformly shaped beat signal from the LVDT transducer. The measured speeds in wet and dry rolling are shown in Table 7-1. In each case five measurements were taken ( $N=5$ ) and averaged.

**Table 7-1** Stroboscope speed measurements for the mandrel and ruby ball

| Mandrel status | Mandrel speed RPM [RPS] | Ruby ball speed: RPM [RPS] |             |             |             |
|----------------|-------------------------|----------------------------|-------------|-------------|-------------|
|                |                         | Dry                        | Speed ratio | Wet         | Speed ratio |
| New            | 2040 [34]               | 1065[17.75]                | 1.92        | 1075[17.92] | 1.90        |
| Used/worn      | 2040 [34]               | 1045[17.42]                | 1.95        | 1050[17.50] | 1.94        |

It can be deduced from Table 7-1 that a new mandrel and lubricated conditions provided the highest ball speeds and the lowest mandrel/ball speed ratio, which is very close to the theoretical value of 1.87. On the other hand, a worn mandrel and dry conditions provided the lowest ball speed and highest mandrel/ball speed ratio. These observations are supported by the fact that a new mandrel provides a point contact with the ball and

the shortest contact height, eliminating speed losses due to surface traction and relative contact height between mandrel and specimen. On the other hand a worn mandrel provides a surface contact with longer contact length between the mandrel and the specimen, which lowers the ball speed. Based on the findings from the speed measurements, a speed ratio of 1.9 between the mandrel and ruby ball was fixed for this research as it matches the theoretical speed ratio of 1.87 which was obtained from kinematical modelling in Chapter 3.

## 7.2 System Operation Procedures

In order to achieve the semi-automatic operation of the system, a sequential operational procedure was designed as shown in Figure 7-3. The user first sets and clamps the PMMA mould containing the test specimen in position. Next, the user inserts the ruby ball between the mandrel and specimen and sets a reference datum. Afterwards, the user initializes the hardware and software systems to enable the device to warm up for half an hour. If desired, a manual pre-wash of the specimen and ruby ball is carried out prior to initial sampling. The test cycle starts with the motor increasing to 240 rpm over a period of 1s, and it then runs at a constant speed for 20s. The control loop updates at 100 Hz (10 ms).

The LVDT sensor sampling frequency is set at 100 Hz to match the control loop update frequency of 100 Hz. The signal is acquired, digitized and stored in a buffer through channel AN8 of the 12-bit ADC module, having been initiated by the *timer5* interrupt. After initial sampling, the actuator ramps up to a speed of 2040 rpm in 3.6s and continues running at this speed for  $100 \times 10^3$  load cycles. This is equivalent to  $95 \times 10^6$  encoder counts, which takes approximately 1.55 hours. During the 2040 rpm running time, time-domain features of the previous sampled data are processed online to establish progress of the surface fatigue wear on the dental specimen, which is displayed and stored on the GUI through the RS232 serial communication module. The raw data is also transferred during this time for storage. Upon completion of the  $100 \times 10^3$  load cycles, the motor decelerates to 240 rpm and another sampling run is initiated and stored in the DSC RAM for online processing upon accelerating to a speed of 2040 rpm. The next ten sampling runs include the time-domain statistical features only. The sequence is repeated until  $10^6$  load cycles are completed.

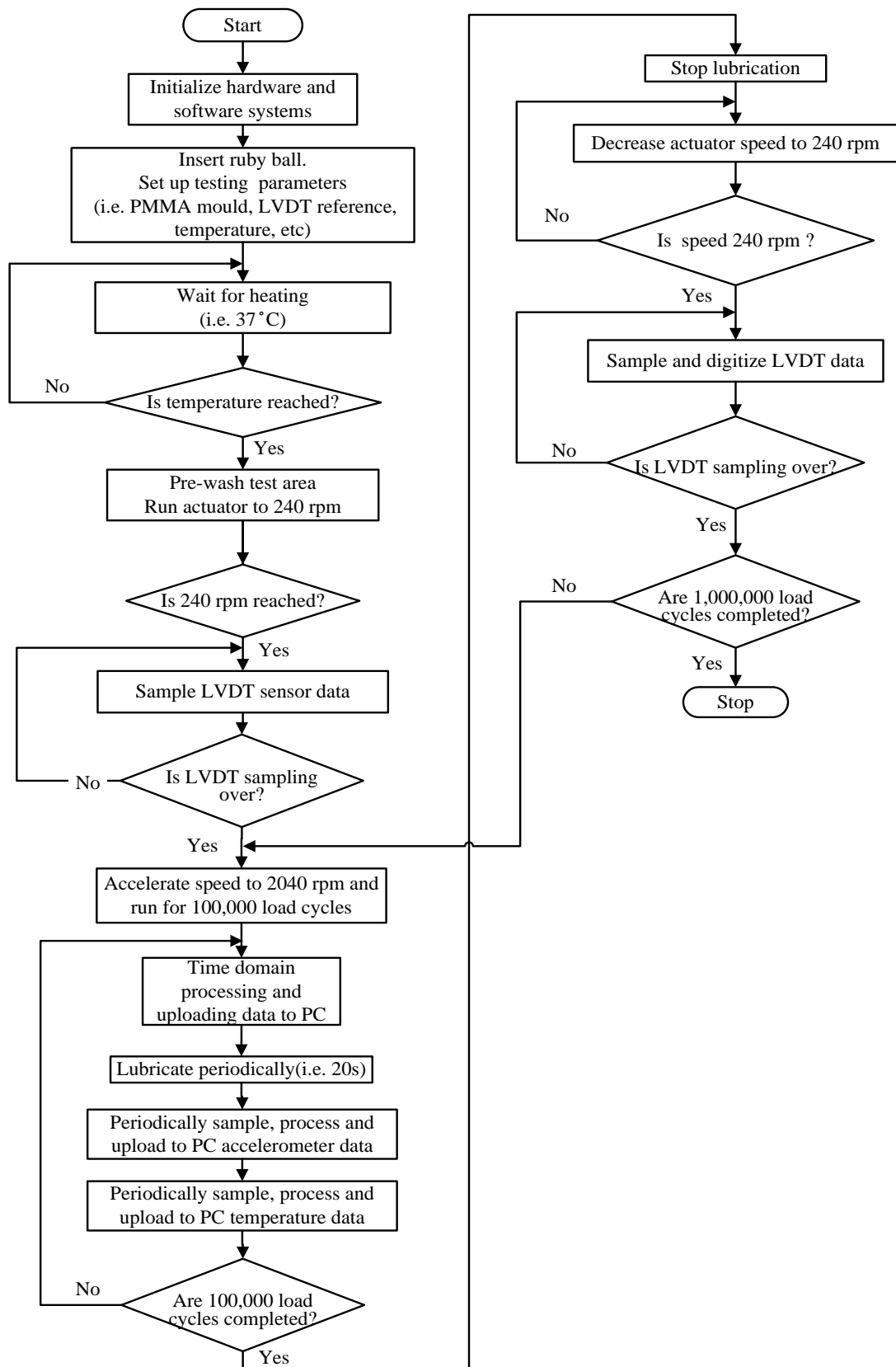


**Figure 7-3** Sequence of operations of the mechatronic measurement system

The tests are planned at temperatures of 20<sup>0</sup>C and 37<sup>0</sup>C in dry or wet conditions. In wet testing, a peristaltic pump supplies distilled water during the 2040 rpm speed interval



and delivers a drip of approximately 1ml every 15s. Human saliva constitutes 99.5% pure water [Del Vigna de Almeida et al, 2008], which is why distilled water was deemed more suitable. The heating system is controlled by a separate PID temperature controller (model 39K) using a type K thermocouple. Also, an LM35ADZ temperature sensor monitors the test temperature using channel AN9 of the DSC's ADC module. An axial compressive load of 2N to 4N with increments of 0.5 N is applied using the rope and pulley arrangement attached to the specimen carriage.

### **7.3 Sensor Calibration**

Although the sensors are calibrated and tested in the factory prior to supply, there exists a need for an *in-situ* calibration to ensure that the manufacturer's specifications are adhered to during installation. In addition, the *in-situ* calibration provides useful information with regards to the application conditions, such as vibration, electromagnetic interference (EMI) noise and temperature drift.

#### **7.3.1 LVDT transducer calibration**

The LVDT transducer required re-calibration due to the change of the powering, control and signal reconditioning circuit. The re-calibration was carried out as described in Section 3.3. The results of the calibration are shown in Figure 7-4 and shows a linear trend within the calibrated range, which agrees well with the LVDT data sheet. Some non-linearity is evident near the null voltage indicating measurement instability, and is avoided by offsetting the reference position from the null voltage. Therefore, a usable range of  $\pm 0.8$  mm was available for use. LVDT measurement drift, due to temperature change from 20<sup>0</sup>C to 25<sup>0</sup>C was on average 6 $\mu$ m and electrical noise was 8mV p-p, below the design specification of 10mV. The demodulator gain was set at 200mV/V and the gain of 207mV/V was evaluated from the calibration plot, giving a correlation factor of 0.9976 and a percentage error of 3.5%.

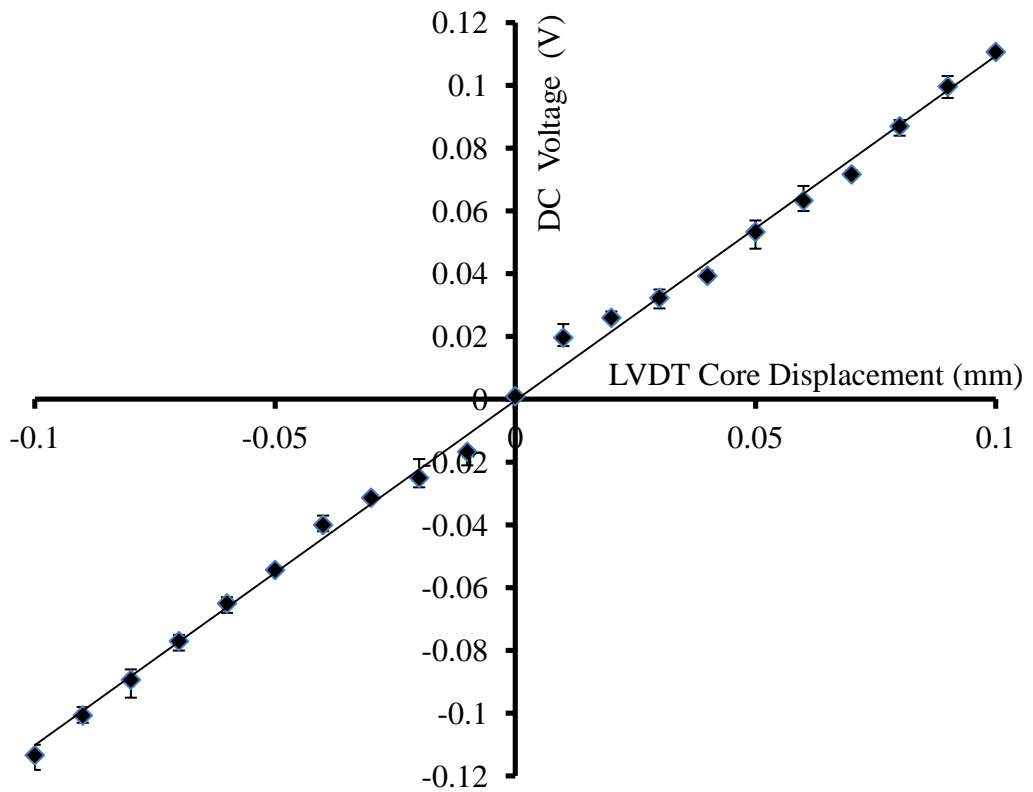


**Figure 7-4** Re-calibrated SM1 LVDT transducer and hybrid modules plot.

### 7.3.2 Accelerometer calibration

The 2-axis accelerometer (model: DE-ACCM5G) was initially mounted on the spindle block adjacent to front bearing; however the signal amplitudes were found to be very small and insignificant. The accelerometer was subsequently relocated on the specimen carriage, as shown in Figure 7.5.

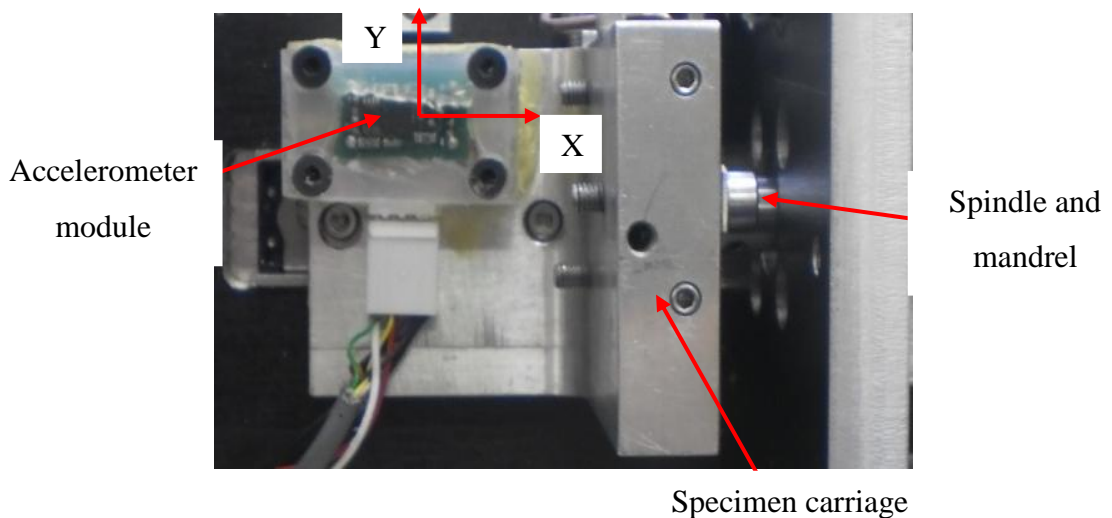


**Figure 7-5** Accelerometer mounted on the specimen carriage

During calibration, dynamic readings in both axial and radial directions were recorded using LabVIEW application (flow code is presented in Appendix A6.3). The calibration was carried out at the running speed of 2040 rpm. The accelerometer bias voltage is 1.65 V when powered at 3.3V, providing a sensitivity of 174 mV/g and a bias deviation less than 2%. The accelerometer outputs were captured simultaneously at sampling frequency of 1 kHz, with filtering using a 50 Hz low-pass filter. A sample of the output of the two axes in the time domain is shown in Figure 7.6.

FFT Matlab was used to analyze the data, with the horizontal axis ( $x$ ) yielding the speed amplitudes relating to the ball-specimen and mandrel-ball rolling contacts, and reduced noise and amplitudes relating to rolling path deterioration due to surface contact fatigue, as shown in the FFT plots in Appendices A6.4 and A6.5. Owing a limitation in memory of the embedded processor, only the axial data (X-axis) was sampled and processed to establish the progressive surface contact fatigue of the dental specimen undergoing testing.

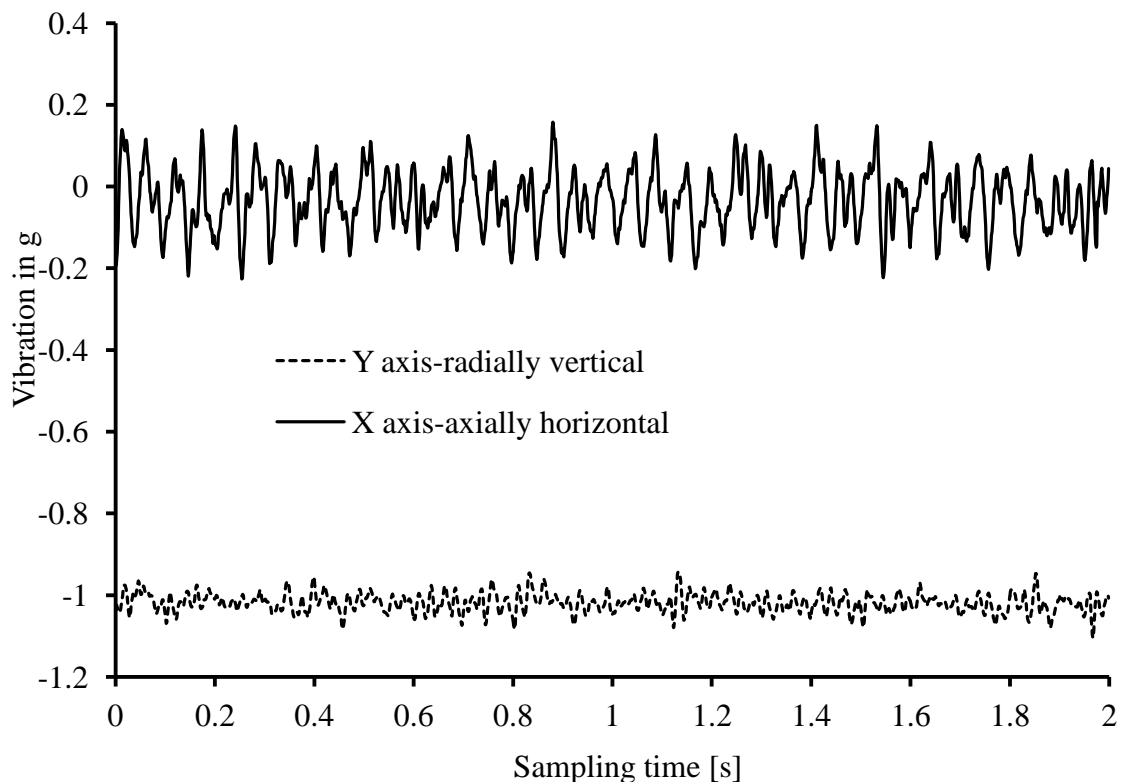


**Figure 7-6** Accelerometer time history (2000 samples)

### 7.3.3 Temperature calibration

A type K thermocouple with a sensitivity of  $41\mu\text{V}/^\circ\text{C}$  and temperature drift of less than  $2^\circ\text{C}$  between  $0^\circ\text{C}$  and  $100^\circ\text{C}$  is interfaced with the K39 PID temperature controller. The three LM35DZ temperature sensors have a sensitivity of  $10\text{mV}/^\circ\text{C}$  and temperature variance of  $\pm 1^\circ\text{C}$ . The  $\pm 1^\circ\text{C}$  resolution can be achieved with the 12-bit resolution of the DSC microcontroller's analog-to-digital converter module, and factory set calibration was used to configure the temperature setting. Temperature monitoring is conducted by viewing the K39 PID temperature controller LCD display and through RS232 serial communication on the GUI, which also implements temperature data storage for the testing chamber, the BLDC DC motor and the lubrication pump.

### 7.4 LVDT Transducer Signal Processing

Two processing modes, in the time and frequency domains, are used to process the acquired LVDT output online and offline, as described in Section 6.8. The online processing shows time domain parameters indicating the general trend of surface contact fatigue, whereas the offline processing gives detailed frequency components and related distributions using data stored in the host computer. Data sample size is based on the FFT lines of resolution and Nyquist frequency ( $F_N$ ). The LVDT data sampling frequency of 100Hz is derived from the control loop frequency. This gives an  $F_N$  of 40Hz when considering the anti-aliasing filter roll-off and a digital transformation factor of 2.56 [Shreve, 1995]. If 800 FFT lines of resolution are chosen to display the data, 2048 samples are required. The bandwidth ( $B_w$ ) of the sample is computed using the following equation.

$$B_w = \frac{F_N}{\text{FFT resolution}} = \frac{40}{800} = 0.05\text{Hz} \quad (7.1)$$

Data capturing time (also known as observation time ( $T_{obs}$ )) is based on the sample bandwidth as follows:

$$T_{obs} = \frac{1}{B_w} = \frac{1}{0.05} = 20\text{s} \quad (7.2)$$

Although a sample of 2048 points for 800 lines resolution is required, an optimum sample data of 2000 is set. Fewer FFT line resolutions could be chosen to reduce sample size and time, but this severely affects display resolution. The beating wave

acquired by the LVDT transducer as shown in the time domain plots (see Figure 3-6) is a complex composite of many frequencies, which thus require finer FFT resolution.

Online processing includes time domain features such as moving average filtering, zero mean crossing, load cycle counting, mean, maxima, minima, peak, crest factor and kurtosis as listed in Figure 6-25 in Chapter 6. Cycle counting is intended to establish the speed ratio of the mandrel and ruby ball to indicate the wear value of the V-groove. Other features indicate the quality of the orbit track and mandrel to establish degradation of the orbital path or mandrel deterioration and change time. Subsequently, the fatigue life of the dental composite can be established. The offline processing of the raw data basically determines the frequency components of the transducer data and relates this to the rolling noise in order to characterize the surface roughness of the orbital track. This eventually discriminates fatigue life moments such as spalling and/or pitting.

## **7.5 Experimental Set-up**

This section describes the design of the experimental layout, the selection of variables to be tested such as contact load and test conditions, and dental composites specimen preparation. The testing was limited to two direct restorations: the Synergy D6 (packable) and Synergy D6 Flow (flowable) dental composites.

### ***7.5.1 Design of Experiments (DoE)***

The design was based on randomized experiments set up and organized into two categories as shown in Table 7-2. Half- and full-factorial designs were used to establish the number of test trials for each category. Category A included 16 trials of randomized experiments devised to examine the effect of testing condition on surface contact fatigue in the two dental composites. The fixed variables were the number of load cycles, compression load and temperature as shown in Table 7-2. The tested variables were dry and wet conditions. Four trials ( $N = 4$ ) were repeated for each tests in each condition.

The output measured was surface fatigue wear with an emphasis on the repeatability and reproducibility of test results. The track depth of  $5\mu\text{m}$  was used as a reference line to indicate the start of the fatigue wear [McCabe et al, 1997]. It was also used to compare the experiment results and fatigue life predictions explained in Section 4.4, in

Chapter 4. Eventually total fatigue of the two dental materials at the end of  $10^6$  load cycles was determined. In total, 16 tests amounting to 272 active test hours were planned in order to achieve a conclusive analysis of category A. The category B experiments aimed to examine the influence of contact load in cyclic rolling contact at  $37^{\circ}\text{C}$  and lubricated (wet) conditions. Similarly, the reference fatigue life was set at a depth of  $5\mu\text{m}$  and the end of  $10^6$  load cycles. Two trials were conducted for each load category, as listed in Table 7-2. A contact load range of 2-4N with 0.5N increments was used. In total 10 test trials amounting to 170 hours were conducted for category B. The entire testing programme involved 26 continuous test trials, amounting to 442 active testing hours (i.e. 30 days). The mechatronic measurement system performed efficiently without failure, showing a high level of reliability and robustness. In order to evaluate the repeatability and reproducibility of results, ANOVA single-factor analysis was used with 0 and 1 indicating dry and wet conditions respectively.

**Table 7-2** Summarized layout of experiments and test variables

| Category | Dental composite     | Variables   |                           |                                    |                |
|----------|----------------------|-------------|---------------------------|------------------------------------|----------------|
|          |                      | Load cycles | Dead weight (Comp. force) | Temperature ( $^{\circ}\text{C}$ ) | Lub. condition |
| A        | SynergyD6, Flow      | $10^6$      | 2.5N (fixed)              | 20                                 | Dry (0)        |
|          |                      |             |                           | 20                                 | Wet (1)        |
|          | Synergy D6, Packable | $10^6$      | 2.5N(fixed)               | 20                                 | Dry (0)        |
|          |                      |             |                           | 20                                 | Wet (1)        |
| B        | Synergy D6, Flow     | $10^6$      | 2.0N                      | 37                                 | Wet (1)        |
|          |                      |             | 2.5N                      | 37                                 | Wet (1)        |
|          |                      |             | 3.0N                      | 37                                 | Wet (1)        |
|          |                      |             | 3.5N                      | 37                                 | Wet (1)        |
|          |                      |             | 4.0N                      | 37                                 | Wet (1)        |

### 7.5.2 Selection of compressive load

The selection was based on the load-based fatigue life approach in which the range of compressive loads applied in the testing was based on preliminary experiments where the dead weight was varied from 1-6 N, from which an S-N curve was obtained as shown in Figure 7-7. The contact stress area for the depth of  $5\mu\text{m}$  was fixed and the

induced stress was assumed to be directly proportional to the applied load, which enabled compressive load to be related directly to the number of load cycles. A similar procedure was used by McCabe et al [1997], in which a fixed weight of 200 g was applied and the stress related to number of load cycles.

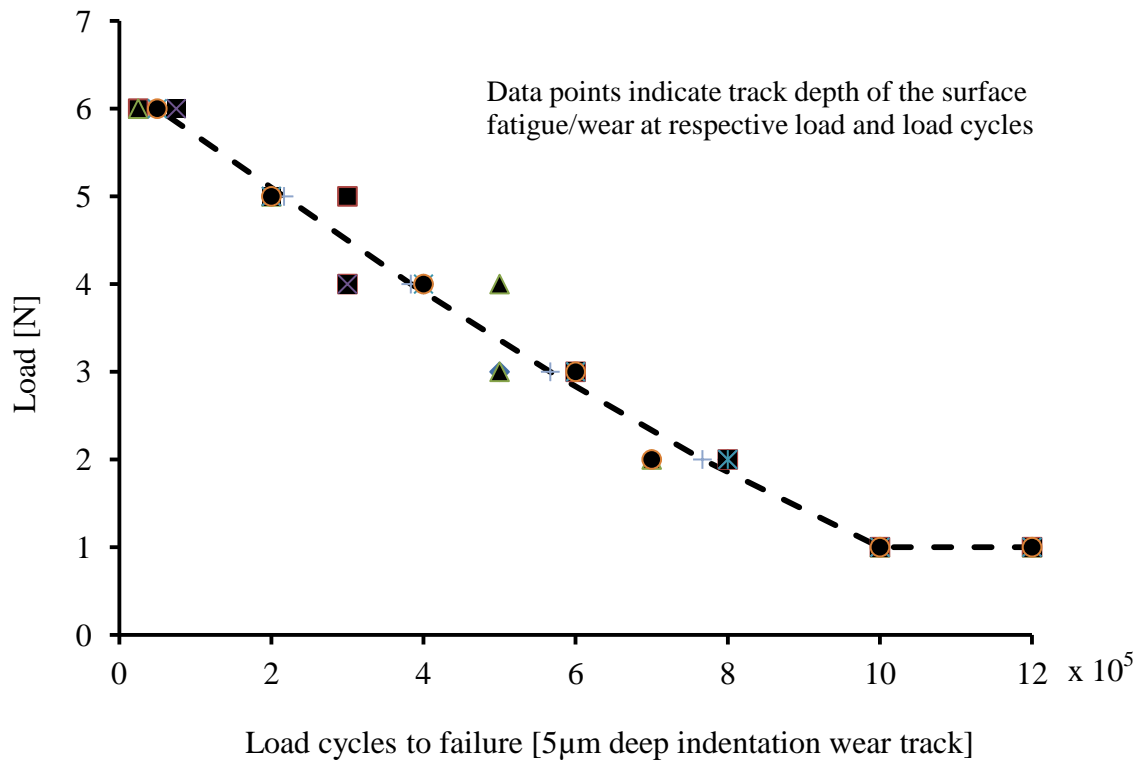


**Figure 7-7** Contact load versus load cycles to failure from experimental data

### 7.5.3 Materials preparation and method

The tests for surface contact fatigue were based on a two-body line contact, in which the ruby ball acted as the antagonist natural tooth and the specimen as a direct restoration. This type of contact is found in the occlusal area [Mair, 1996]. Dental composite specimen was cast in a mould cavity on acrylic PMMA plate with dimensions of  $40 \times 40 \times 6 \text{mm}^3$ , one on each side. The mould cavity size was 18mm in diameter and 1.5mm in depth. The specimen size coupled with versatile carriage settings enabled four tests to be conducted by changing its orientation. The design increased the number of tests per specimen to four and eight per PMMA mould plate, as described in Section 5.2.7 and shown in Figure 5-12. This helps to preserve the homogeneity of specimen material in all the four tests, which is important in ensuring reproducibility. However, it is important that care is exercised in manipulating the blue curing light source in order

to ensure a consistent polymerization of the specimen, as the largest lens is 12 mm in diameter. Profiling of the surface roughness of the prepared specimens indicated that Synergy D6 and SynergyD6 Flow had surface roughness of 15 $\mu$ m and 7 $\mu$ m respectively.

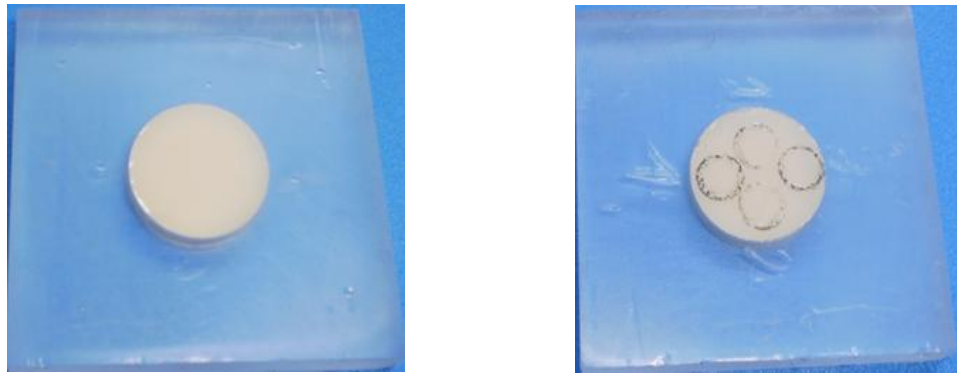
A summary of the main properties of the dental composites selected for the experimental work is given in Table 7-3, whilst their physical and mechanical properties are listed on the manufacturer's data sheet, which included in appendix A5. They are universal nano-filled dental composites used for both posterior and anterior applications. The flowable type is used for *in-situ* application and is made to flow easier than the packable type. They are easily manipulated to shape into the desired form. Their composition in terms of polymer resins, type and size of filler and constituent volume is provided in Table 7-3. Excess material was removed with a polyester strip and pressure applied using another PMMA plate.

**Table 7-3** Description of the dental composite materials used in the test

| <b>Dental composite</b> | <b>Manufacturer</b>        | <b>Curing time(s)</b> | <b>Polymer</b>   | <b>Filler type and size (<math>\mu</math>m)</b>            | <b>Filler content (%vol.)</b> |
|-------------------------|----------------------------|-----------------------|------------------|--|-------------------------------|
| Synergy D6 Packable     | Coltene Whaledent Products | 20                    | BisGMA<br>TEGMA  | Barium glass, silanized silica<br>0.1 $\mu$ m-10 $\mu$ m   | 65                            |
| Synergy D6 Flowable     | Coltene Whaledent Products | 20                    | BisGMA<br>TEGDMA | Barium glass, silanized silica<br>0.04 $\mu$ m-2.5 $\mu$ m | 42                            |

Blue light used to cure the specimens was achieved by applying overlapping exposures of twenty seconds with the specimens covered by polyester strips. The curing torch, (Luxor, Type 4000) had an exposure intensity of 700mW/cm<sup>2</sup>, and exposure was applied to both sides of the PMMA mould to ensure each specimen had an optimum cure while manipulating the curing variables, as per the manufacturer's instructions. A prepared specimen for testing is illustrated in Figure 7.8(a) whereas Figure 7.8(b) shows a tested specimen with four fatigue wear orbital tracks.





(a) PMMA plate with a pre-test specimen (b) PMMA plate with a post- tested specimen

**Figure 7-8** Pre and post test appearances of Synergy D6 dental composite

## **7.6 Experimental Results: Time-domain Analysis**

The results are presented in subsections depending on the type of evaluation and analysis concerned, such as measurement validation and testing category, and is based on the extraction of time-domain features such as mean, peak, crest factor and kurtosis. The results are presented in quantitative form, and a corresponding qualitative analysis is provided in Section 8.5 of Chapter 8.

### **7.6.1 LVDT transducer measurements validation**

In order to determine the accuracy of the LVDT transducer measurements, the profiling of the depth of the fatigue track was carried out in order to correlate LVDT transducer readings with those from the profilometer. Surface fatigue tracks of  $2 \times 10^5$ ,  $4 \times 10^5$ ,  $6 \times 10^5$ ,  $8 \times 10^5$  and  $1 \times 10^6$  load cycles were profiled. The tests were carried out in dry conditions at ambient temperature of  $20^\circ\text{C}$  using a dead weight of 2.5N and Synergy D6 packable dental composite. The profilometer data was acquired and logged into the host PC. The data was processed offline using a bench-type Mitutoyo stylus profilometer (model: SurfTest SV-2000) as shown in Figure 7-9.

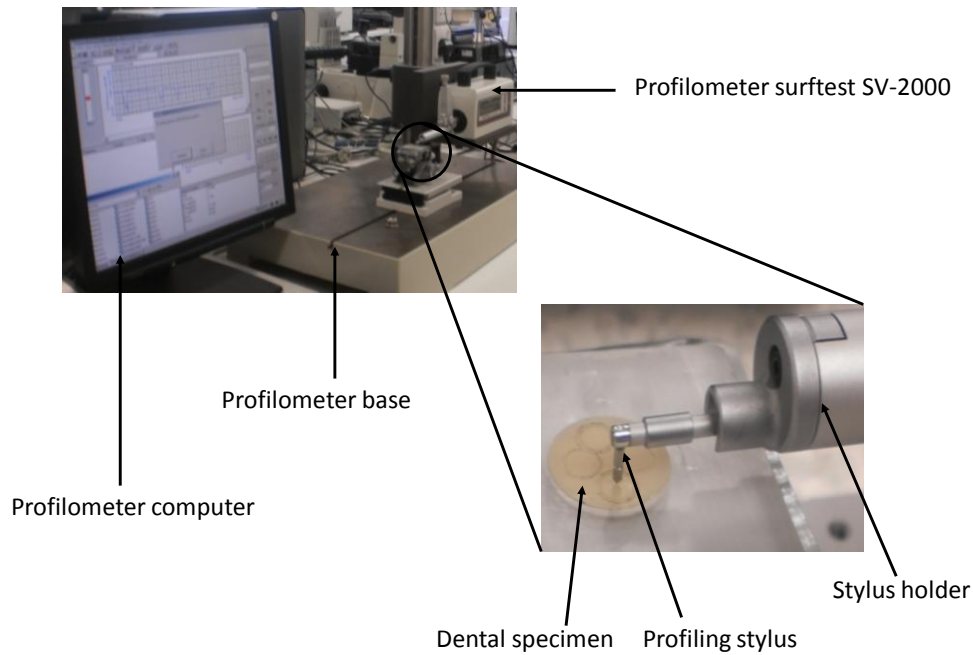
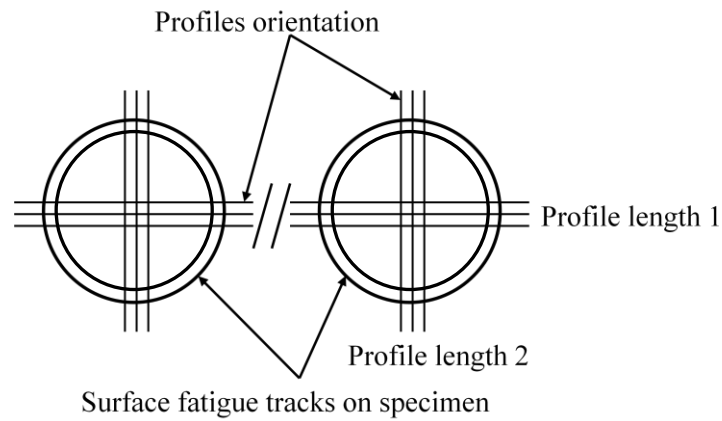
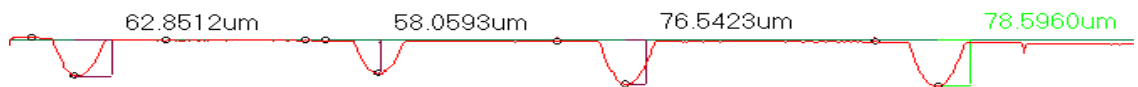


**Figure 7-9** Mitutoyo surface profilometer suite

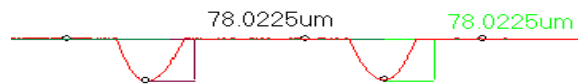
The profilometer has a stylus stroke of 800  $\mu\text{m}$ , traverse length of 50mm and resolution of 0.001mm. It has also, a straightness accuracy of 0.3 $\mu\text{m}$  per 50mm stroke length and a traverse speed of 1mm/s. Two profiling lengths were used. The first was 17.5mm long and a stylus range of 800 $\mu\text{m}$  with a pitch of 1.0 $\mu\text{m}$ , which was used to sample 17500 sample points across two surface fatigue tracks. The second length was 5mm long, with a stylus range of 800 $\mu\text{m}$  and a pitch of 10.0 $\mu\text{m}$  to sample 500 points across one fatigue track, as illustrated in Figure 7-10 (a). In total, six profile measurements were taken for each surface fatigue track, three in each direction, spaced 0.5mm apart and intersecting at 90<sup>0</sup>. The process used a dedicated computer with Surf-pack and Form-pack software for acquiring and analyzing the profile data, as shown in Figure 7-8. The six profile depths were averaged to obtain the measurement value. A comparison of the measurements is summarized in Table 7-4. It can be deduced from the analysis that the LVDT and profilometer measurements are very consistent and that the measurements are within 5% of each other. The track depths towards the centre of the specimen are slightly shorter, and this is attributed to the volumetric shrinkage. (i.e. Synergy D6 Universal has shrinkage of 2.1 %).



a) Surface fatigue profiling schematics



(b) Profile length 1 sample profile across 600,000 and 800,000 load cycle tracks



(c) Profile length 2 sample profile across 800,000 load cycle track

**Figure 7-10** Schematic illustrations of the profilometer measuring method

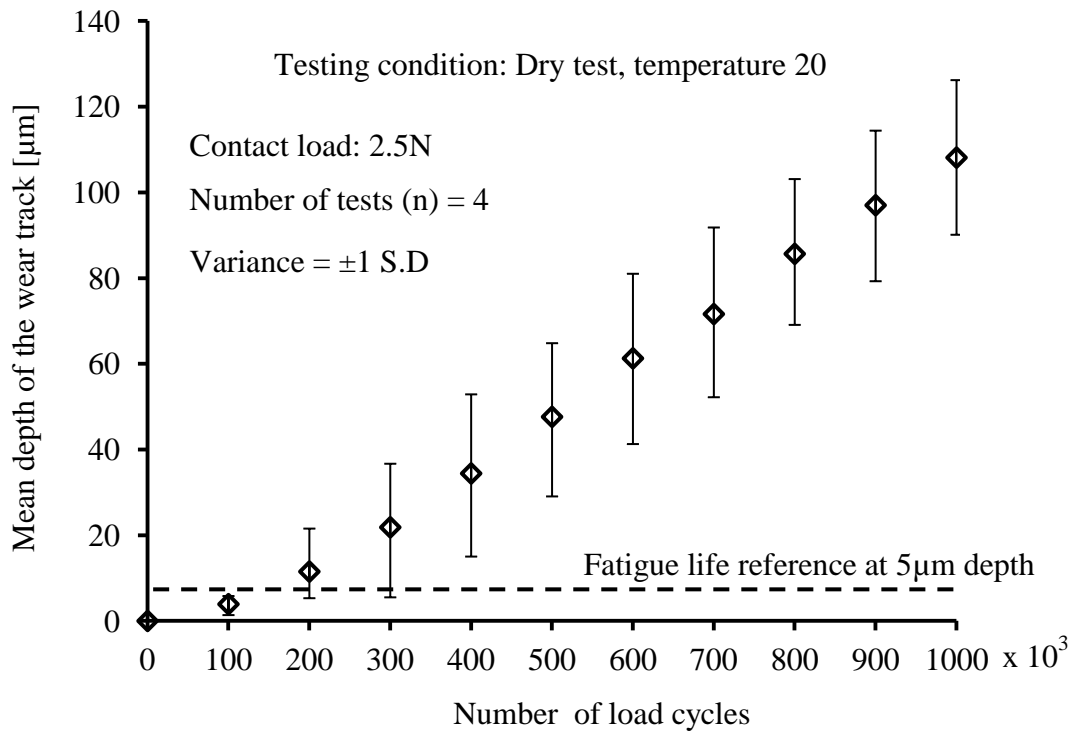
**Table 7-4** Comparison of surface fatigue measurements from the two methods

| No of load cycles | Mean LVDT measurement ( $\mu\text{m}$ ) | Mean profilometer measurement ( $\mu\text{m}$ ) | Measurement deviation (%) |
|-------------------|---|---|---------------------------|
| 200,000           | 22.99                                   | 22.42   | 2.5                       |
| 400,000           | 25.86                                   | 25.03   | 3.3                       |
| 600,000           | 60.90                                   | 60.08   | 1.4                       |
| 800,000           | 80.62                                   | 78.04   | 3.3                       |
| 1,000,000         | 89.77                                   | 87.56   | 2.5                       |

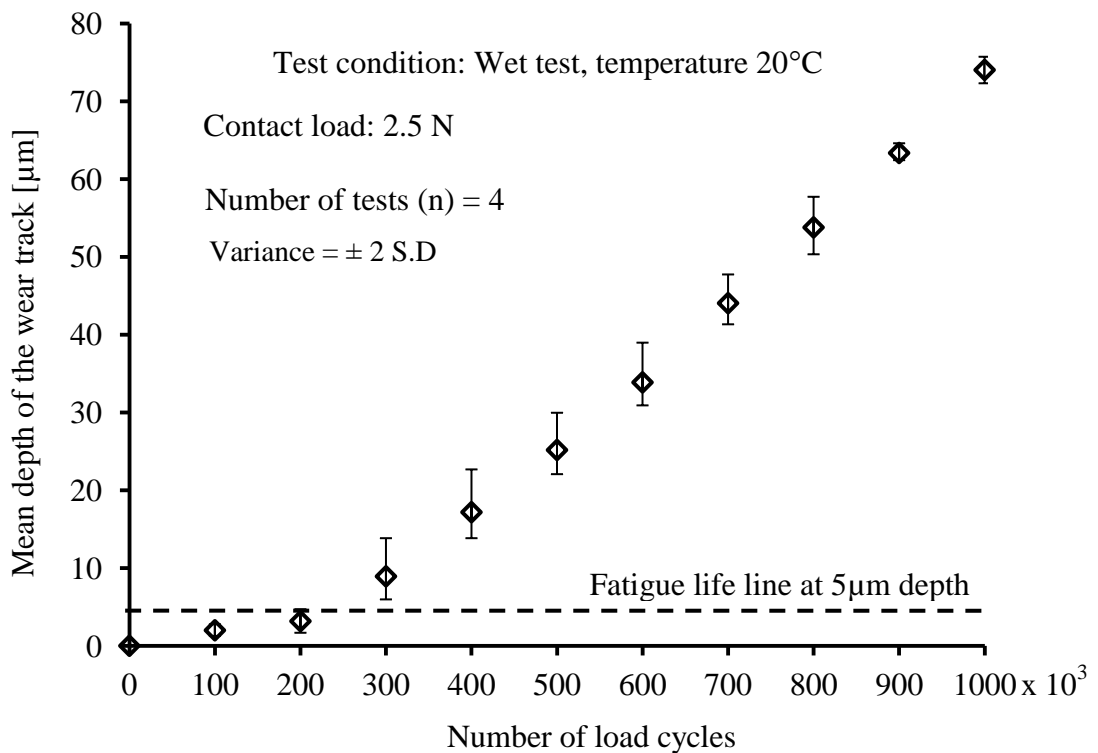
### 7.6.2 Category A: Effects of testing condition on surface contact fatigue

As summarized in Table 7-4, the prime intention of the experiments was to evaluate the pattern of surface wear tracks on specimen of the dental composites against number of fatigue load cycles. In so doing, the reproducibility of the LVDT transducer measurements could be determined. Mean of four trial tests ( $n = 4$ ) were conducted on each specimen of dental composite as described in section 7.3.1. Figure 7.11(a-d) shows

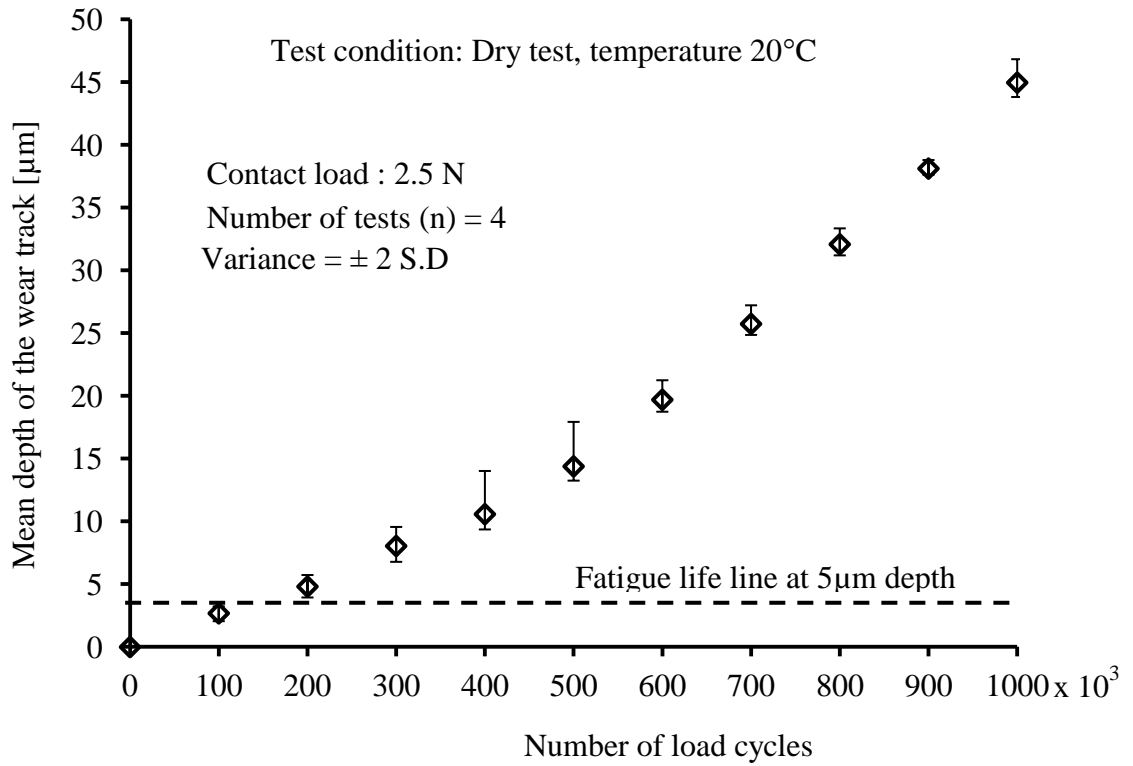
representative plots of the mean fatigue track depth against number of fatigue cycles for the Synergy D6 Universal and Synergy D6 Flow dental composites in dry and wet tests.



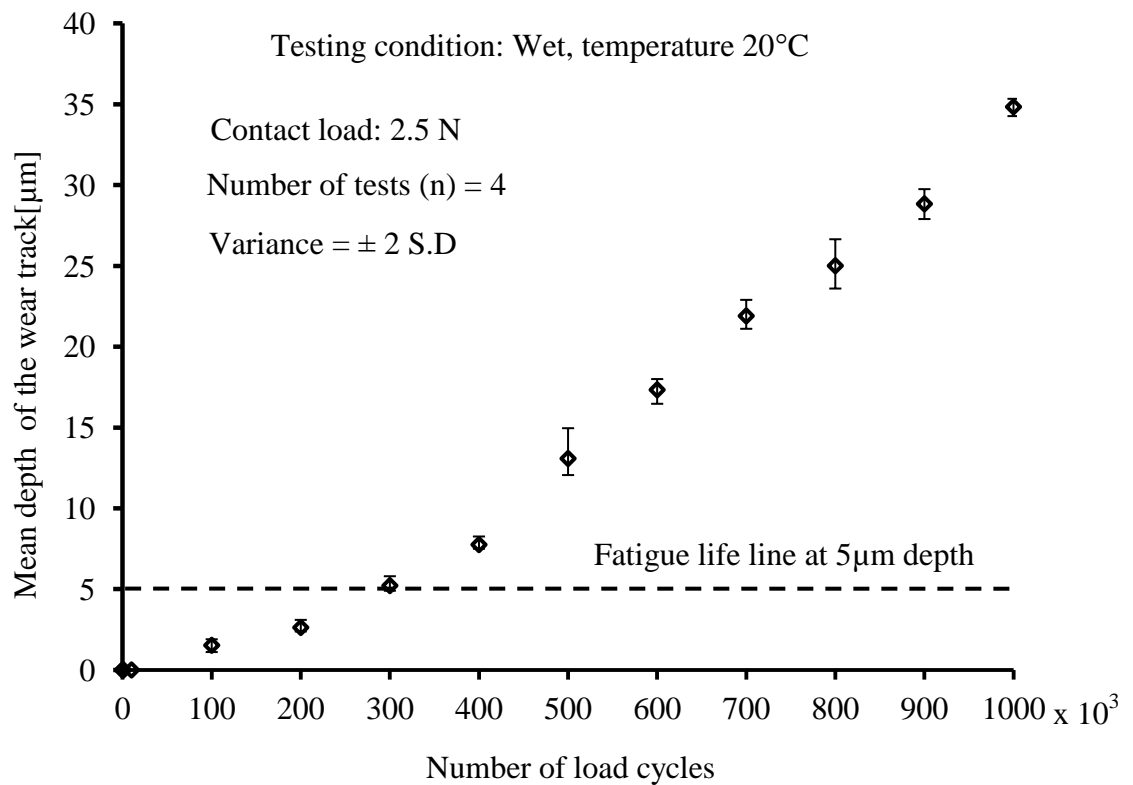
(a) Synergy D6 Universal dry test results



(b) Synergy D6 Universal wet test results



(c) Synergy D6 Flow dry test results



(d) Synergy D6 Flow wet test results

**Figure 7-11** Effects of testing conditions on the surface contact fatigue

It can be observed from the plots that tens of thousands of load cycles are withstood by the specimens of both dental composites before any notable surface degradation occurs, and that the wear rate increases rapidly after the onset of surface degradation. This is noted by the change of the trend of surface track wear (i.e. slope of plots) between  $2 \times 10^5$  and  $5 \times 10^5$  load cycles forming a knee point. The number of load cycles to produce a wear track of  $5\mu\text{m}$  depth lies approximately between  $2 \times 10^5$  and  $5 \times 10^5$  load cycles for a 2.5N contact load in dry and wet testing for both the Synergy D6 Universal and Flow composites. Using ANOVA single factor analysis at the  $p = 0.05$  level of significance, the indicators listed in Table 7-5 were obtained for the Synergy D6 Universal composite while tested in dry and wet conditions.  $F_{3,36}$  indicates the obtained F value of the test statistic, P indicates the obtained probability value,  $F_{\text{crit}}$  indicates the critical value (maximum) that can be obtained at  $p=0.05$  with 4 trials and 10 sampled data. From the ANOVA analysis table it can be deduced that there is no significant difference between the LVDT sampled data with respective number of load cycles for each of the four trials tests. In other words, the variance of data between the trials against different number of load cycles occurs by chance only. The similarity in trends of the fatigue wear between Synergy D6 Universal and the Synergy D6 Flow composites as shown in Figure 7-11(a-d) led to the same conclusion for the reproducibility of the sampled data of fatigue wear for the Synergy D6 Flow.

It can further be deduced from Figure 7-11(a-d) that the fatigue life of Synergy D6 dental composites range between  $3 \times 10^5$  and  $5 \times 10^5$  load cycles in cyclic contact loading. The clinical interpretation is that failure can occur at any time without prior indication, and therefore replacement should be planned.

**Table 7-5** Synergy D6 Universal reproducibility indicators by ANOVA analysis

| <b>ANOVA factor</b> | <b>Dry test at 20<sup>0</sup>C temperature and 2.5N contact load</b> | <b>Wet (lubricated) at 20<sup>0</sup>C temperature and 2.5N contact load</b> |
|---------------------|--|--|
| $F_{3,36}$          | 1.927  | 0.069  |
| P                   | 0.143  | 0.967  |
| $F_{\text{crit}}$   | 2.87   | 2.87   |

The testing continued until  $10^6$  load cycles, as recommended for stress-based fatigue testing for tolerant polymeric materials [Baran, et al. 2001], in order to appreciate the full magnitude of degradation. Nevertheless, Synergy D6 Universal dental composite

induced more fatigue wear than Synergy D6 Flow in both dry and wet conditions, despite having the same Vickers hardness value of 222 HV (73 kg/mm<sup>2</sup>). Figure 7-11(a-b) shows that the value of total surface fatigue for Synergy D6 Universal were on average 108 μm and 75 μm in dry and wet tests, whereas Figure 7-10(c-d) shows that for Synergy D6 Flow the values of surface fatigue were 48 μm and 35 μm only. The difference in surface quality is attributed to the observation and a detailed discussion is in Section 8.5 of Chapter 8. Cured specimen of Synergy D6 Universal had a surface roughness of 15μm whereas that of Synergy D6 Flow had surface roughness of 7μm measured using the Mitutoyo surface profilometer suite, attributed to filler size and composition of each dental composite.

Furthermore, a notable variance of approximately 20 μm occurred on the total fatigue wear during the dry test of Synergy D6 Universal at the end of 1x10<sup>6</sup> load cycles as indicated by the variance in Figure 7.11 (a). The huge variance was specific to location and investigations attributed it to the variation in surface hardness at the respective testing locations due to inconsistent manipulation of the curing torch. This led to non-uniform polymerization resulting in low curing strength and hardness at these locations. The problem was resolved by using an overlapping curing method, as shown in Figure 7.12, which reduced the variation as revealed in the subsequent plots of Figure 7.11 (b-d), where the mean variances are smaller and consistent than Figure 7.11 (a).

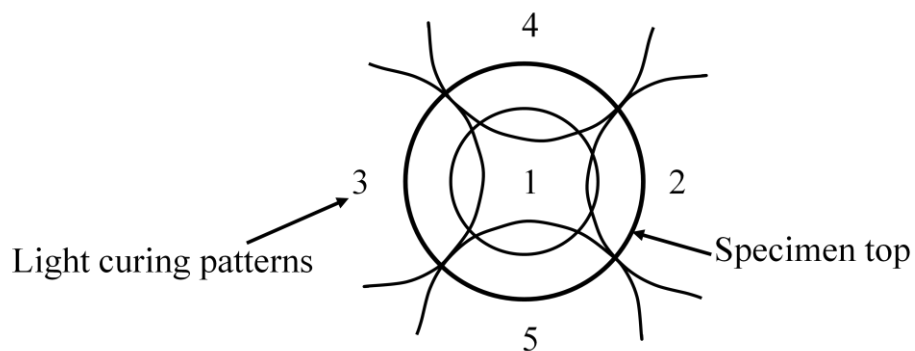


**Figure 7-12** Illustration of the overlapping curing method

To summarize, an apparent reproducibility of the test results exists in all four plots in as shown in Figure 7.11(a-d). Using ANOVA single factor analysis, average reproducibility across all four tests is 70%, which is considered to be fairly good.

### 7.6.3 Category B: Effects of loading on surface contact fatigue

Figure 7-13 shows the mean wear depth against number of load cycles for the Synergy D6 Flow composite caused by the rolling effects of contact loads with magnitudes between 2N to 4N. The test was conducted in lubricated conditions at a temperature of 37°C in order to partially simulate the oral environment. It can be deduced from the plots in Figure 7-13 that a good correlation exists between the different contact load tests and the measurement data which has a high degree of reproducibility. The variation of the track depth with number of load cycles increases with the increased magnitude of the applied contact load ( $p < 0.05$  using ANOVA analysis).

Similarly, the dental composite withstood tens of thousands of load cycles before any notable surface degradation occurred, followed by a rapid rate of material removal after the onset of surface degradation. The number of load cycles required to produce a wear track of 5µm depth lies between  $3 \times 10^5$  and  $5 \times 10^5$  load cycles for all of the contact loads.

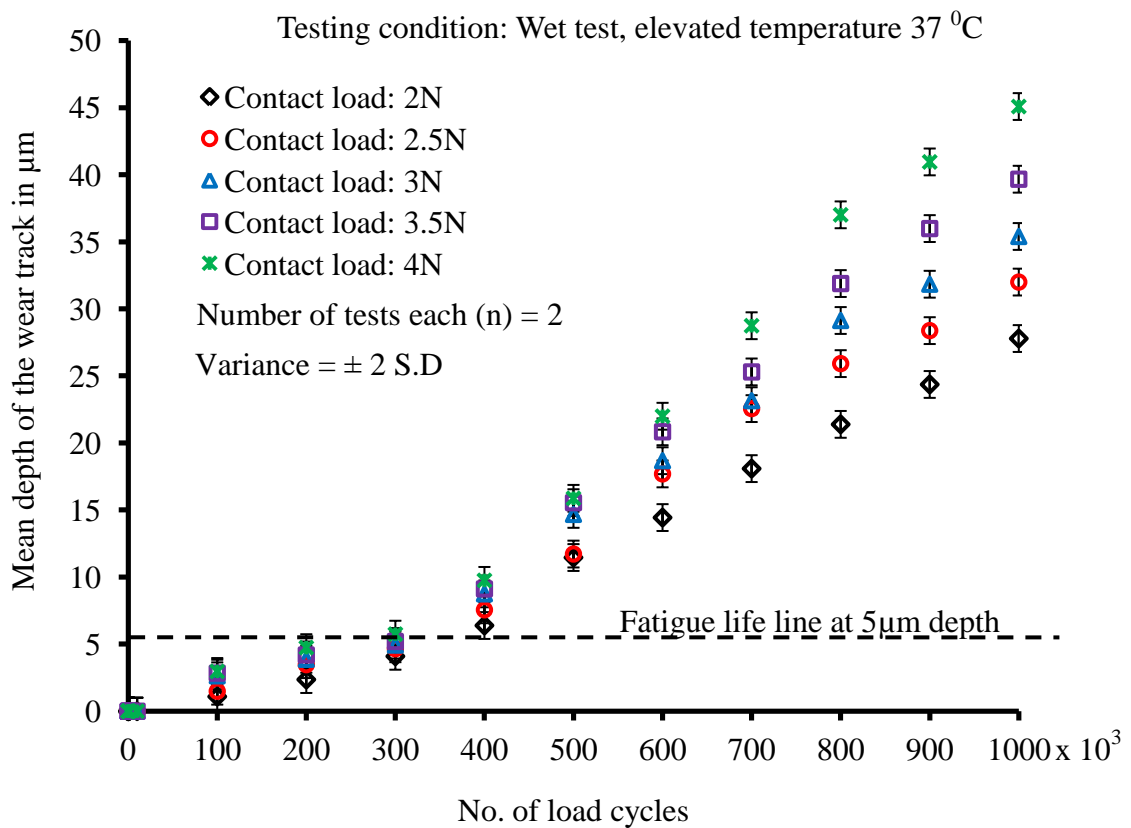


**Figure 7-13** Effects of contact load on surface fatigue



The tests were terminated after  $10^6$  load cycles, and the depth of the surface fatigue track for the 4 N contact load was approximately 50  $\mu\text{m}$  (0.05 mm), followed by the 3.5 N contact load with a depth just over 40  $\mu\text{m}$  (0.04 mm). The 3 N contact load gave a depth of approximately 35  $\mu\text{m}$  (0.035mm), the 2.5 N load had a depth with approximately 32  $\mu\text{m}$  (0.032 mm) and finally the 2 N contact load gave a depth just less than 30  $\mu\text{m}$  (0.03 mm). It can be concluded that the larger the contact load, the higher the rate of surface contact fatigue and the greater the fatigue damage occurring on the dental composite. The findings are consistent with the surface contact fatigue measurements conducted using the profilometry method [Fujii et al, 2004].

On the other hand, it is clear that lubrication has a significant influence on the rate of surface fatigue wear of the dental composite. Referring to the Synergy D6 Flow composite which has shown statistically ( $p < 0.05$ ) more resistance to surface fatigue wear in both dry and wet testing, it can further be deduced that surface fatigue wear was reduced significantly at 2.5N contact load (32 $\mu\text{m}$ ), compared to that obtained under the same contact load in dry testing (i.e. 48 $\mu\text{m}$ ). Despite increasing the contact load by a factor of 1.6 in the lubricated testing, much the same surface fatigue wear could be obtained (i.e. 47 $\mu\text{m}$ ). It can further be suggested that testing at 37 $^{\circ}\text{C}$  (as recommended by ISO/TS 14569-2:2001 for a human oral temperature), increased the visco-elastic properties of the dental composite and subsequently enhanced the lubricity of the contact area, thus leading to reduced surface wear compared to that found in the dry and wet testing at 20 $^{\circ}\text{C}$ .

#### ***7.6.4 Peak, RMS, Crest Factor and Kurtosis surface fatigue indicators***

The initiation and propagation of surface contact fatigue can be studied using various time- domain features, such as peak, root-mean-square (RMS), crest factor, skewness, and kurtosis which are all time-domain statistical measures. These indicate the surface quality of the parts in rolling contact. The features were extracted from the time domain array of sampled data and which was also used to obtain the means used in the surface fatigue plots in sections 7.4.2 and 7.4.3. Primarily, these time-domain features differentiate between the impulsive rolling noises due to surface damage from one sample of data to the next acquired after  $100 \times 10^3$  load cycles have been completed. The close similarities found in the trends of the features in the tests conducted prompted the elaboration of one test only. The Synergy D6 Universal dry test features are explained

based on the sampling of 2000 data array. The analysis of other time-domain features can be inferred from these conclusions.

**Peak:** this is a simple time-domain feature indicating an increase in rolling noise due surface degradation, and its trend is shown in Figure 7-14. An unsteady peak of  $50\mu\text{m}$  is noted with an increasing number of load cycles until  $5 \times 10^5$  cycles, and then this is followed by a jump to  $58\mu\text{m}$  at  $6 \times 10^5$  load cycles with increased standard deviation indicating that there was a sudden increase of peak, possible due to spalling. A subsequent decline from  $7 \times 10^5$  load cycles back to just below  $50\mu\text{m}$  is also observed, indicating that  $6 \times 10^5$  load cycles is the moment when significant rolling noise occurs due to severe surface degradation on the orbital track. This trend agrees well with that shown in Figure 7-11(a), indicating that the material withstood several hundred thousands of rolling load cycles before noticeable damage appeared which was then followed by a steady rate of surface contact fatigue.

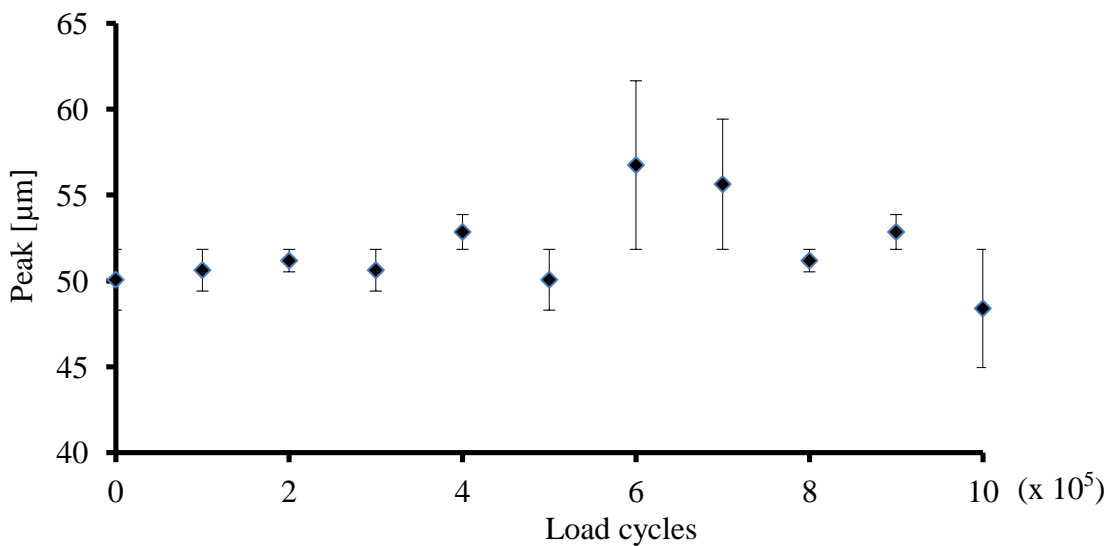


**Figure 7-14** Peak amplitude as function of load cycles

**RMS:** this indicates the power content of the rolling noise against the number of load cycles, and signifies the progress of the surface degradation. Figure 7-15 shows no significant changes in the energy content during the  $1 \times 10^6$  load cycles; except for small fluctuations due to surface damage, leading to micro-pitting cracks between  $2 \times 10^5$  and  $7 \times 10^5$  load cycles. The decrease is partly due to surface fatigue wear which changes the contact geometry from line contact to surface contact, thus dampening the rolling noise energy.

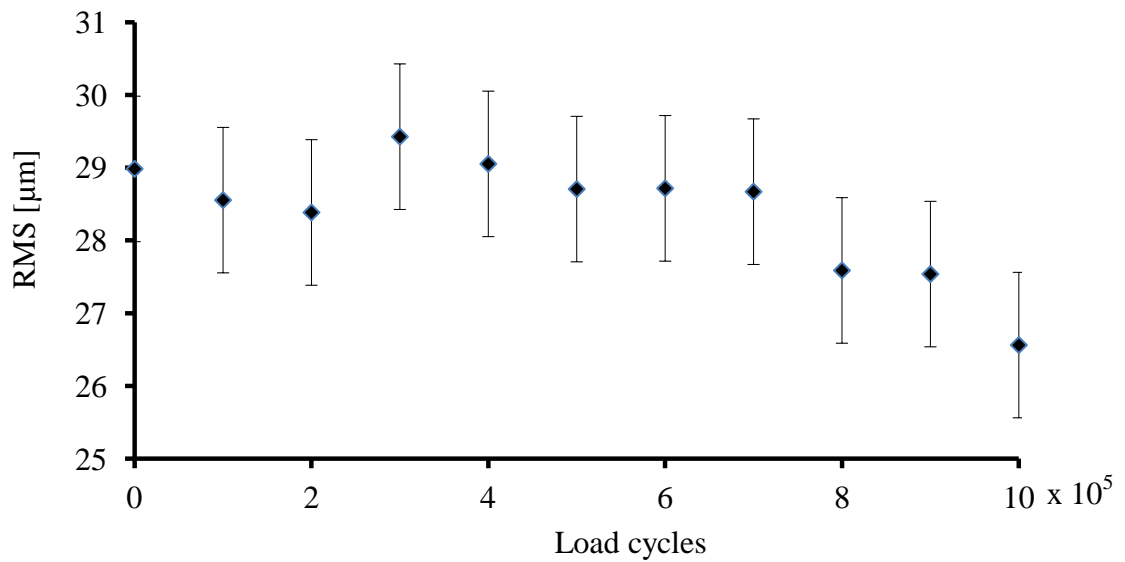


**Figure 7-15** Root mean square (RMS) as function of load cycles

**Crest Factor:** in order to give a conclusive analysis of the peak and RMS values, the crest factor (CF) was analyzed. This is the ratio of the peak to RMS and shows how much impacting exists in the rolling noise wave due to a sudden breaking force, such as in micro-pitting and spalling. The CF plot in Figure 7-16 shows progressive but neither steady nor significant impulsive forces due to the rolling track degradation. Increased impacting noise is noted to occur at  $4 \times 10^5$  and  $6 \times 10^5$  load cycles, indicating that the surface quality was severely deteriorating during this interval due to accumulated surface and sub-surface stresses and strains.

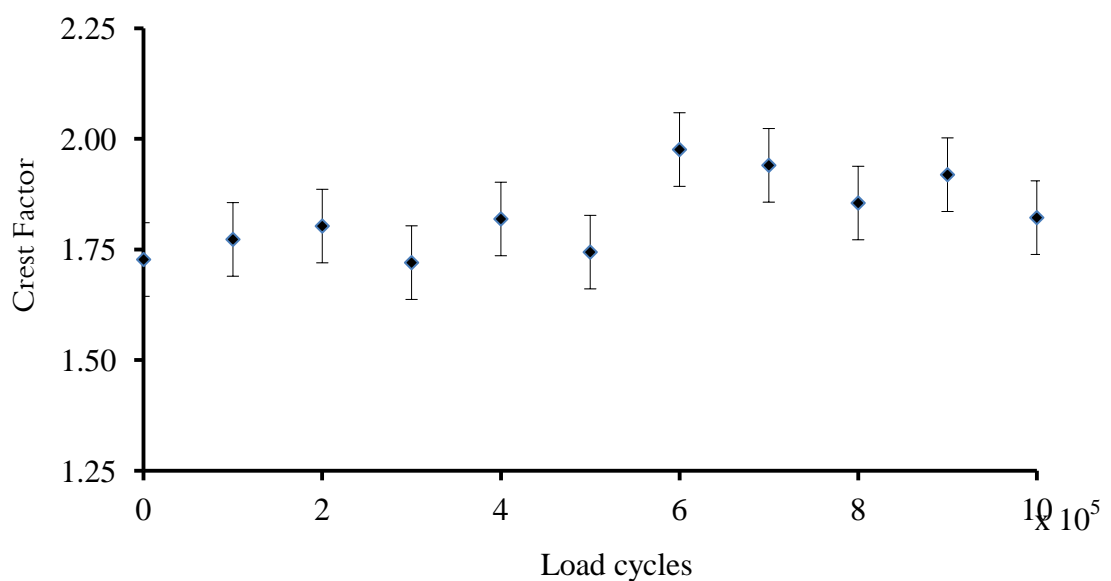


**Figure 7-16** Crest factor as function of load cycles

**Kurtosis:** this indicates the peakedness or flatness of the rolling noise amplitudes, signalling an increase in surface deterioration. Kurtosis as a function of load cycles in the test is shown in Figure 7-17, indicating that the peaks increased from a constant flattening trend from 1.26 to 1.32 between  $4 \times 10^5$  and  $6 \times 10^5$  load cycles. The value of kurtosis is below 1.5, which indicates a pure sine wave and thus signifies the beating characteristics. Overall, the distribution of the rolling noise is scattered with no significant peaks except for the fundamental amplitude of the rolling frequencies. In other words, the surface fatigue damage was influenced by random surface and sub-surface cracks without defined a growth pattern.

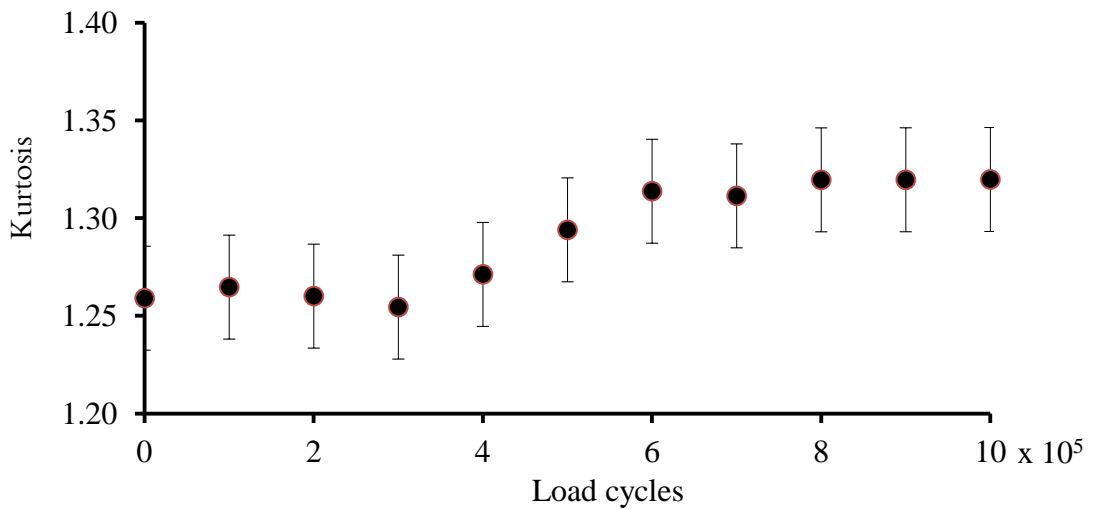


**Figure 7-17** Kurtosis as function of load cycles

**Cycle counting:** online cycle counting is an important time-domain feature which indicates the speed ratio between the mandrel and orbit rotations and ultimately the quality of the V-shaped groove on the mandrel. Load cycles are counted online for a defined sampling time of 28 seconds. Next, the speed (i.e. 240 rpm) of the mandrel is established during the sampling time in order to determine the speed ratio between the mandrel and orbit rotations. Before counting, the raw digitized data shown in Figure 7-18 is filtered using the moving average filter shown in Figure 7-19 in order to remove spikes and noise which could lead to incorrect cycle counting. The data is then normalized to a range of  $\pm 5$ , and, using the orientation of the data from positive to negative (+/-), the software counts the zero crossing rates to establish the number of cycles within the sampled data as indicated in a table of extracts from the processed data

displayed on the GUI as shown in Appendix A6.1. Two crossings count as one cycle.

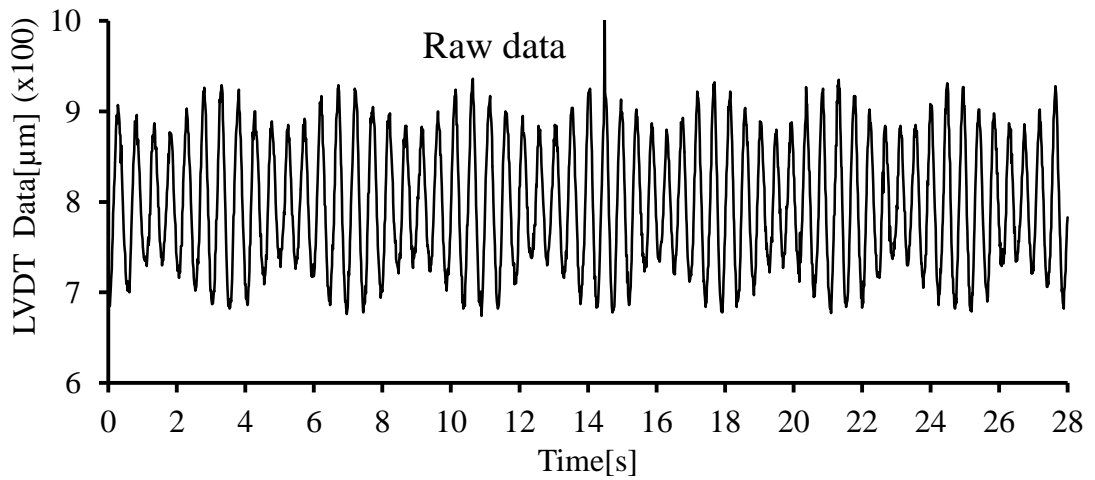


**Figure 7-18** LVDT transducer raw digitized data

Alternatively, the technique can be regarded as the online monitoring of the quality of the mandrel groove. For a perfect  $120^{\circ}$  groove mandrel, a speed ratio of 1.87 was established, where 1.9 was considered to be sufficient, between the mandrel to orbital rotation. However, it is noted that the time needed to sample and digitize 2000 data has increased from 20s to 28s. This increase is attributed to the speed of uploading and storing digitized data to the processor RAM pending online feature extraction upon reaching the speed of 2040 rpm. Feature extraction and transmission to the host PC through the RS 232 serial communication takes 1.5 minutes (90 seconds).

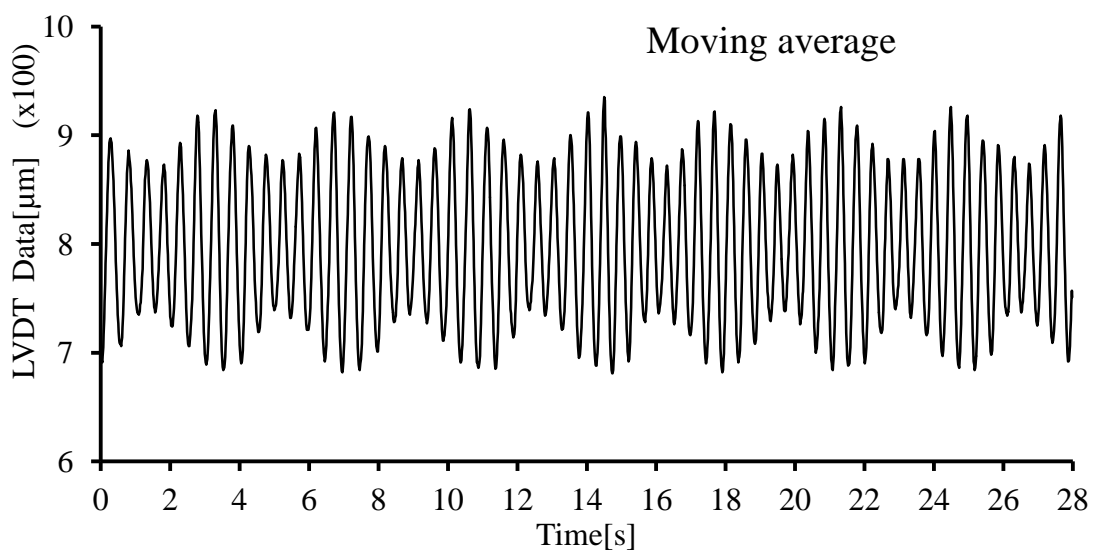


**Figure 7-19** LVDT transducer moving average filter data

## 7.7 Experimental Results: Frequency-domain Analysis

The frequency-domain analysis was conducted offline due to the processing limitations of the chip with floating-point integer in a multi-tasks environment. Frequency domain analysis included time-domain data for the LVDT at 240 rpm and accelerometer at 2040 rpm as described in sub section 7.4.2. The LVDT data analysis intended to determine spectra variation due to degraded surface quality of the dental specimen along the orbital path at the initial (0 k), intermediate (600 k) and final (1000 k) load cycles. The accelerometer data analysis aimed to characterize the onset and progressive growth of the surface fatigue on the orbital path.

### 7.7.1 Low speed-LVDT frequency domain analysis

The two features processed offline were the fast Fourier transform (FFT) and frequency distribution skewness. FFT was used to identify changes in fundamental frequencies and any new frequencies due to surface deterioration. This was carried out for the raw data in time-domain for the initial (0), intermediate ( $6 \times 10^5$ ) and final ( $1 \times 10^6$ ) load cycles. This is because of the change of trends observed in the time domain plots, as depicted in the peak plot in Figure 7.14, which indicate three scenarios of the surface fatigue. The FFT plots are shown in Figures 7-20 to 7-22. It can be deduced from the plots that the fundamental orbital rolling and mandrel frequencies are 2.151 Hz and 1.851 Hz respectively.

The speed ratio of the mandrel frequency to the ball orbital frequency with a  $120^\circ$  symmetrical V-groove was approximately 1.85 Hz as compared to the theoretical value of 1.87 Hz, (i.e. which might be superimposed in the frequency band), giving an orbital rolling frequency of 2.15 Hz when the mandrel is rotating at 4 Hz, as shown in Figure 7-20. It can further be deduced from Figure 7-21 that the amplitudes of the fundamental frequencies decline slightly with growing erratic side band frequencies, suggesting that changes have occurred in the contact geometry and surface roughness after  $6 \times 10^5$  load cycles. It can be stated that the increase in rolling noise with the deterioration of surface integrity is due to the stress induced in the subsurface areas, which develops micro-cracking in the weak boundary of the polymer matrix and fillers and eventually spalls overtime. The surface fatigue grows as a function of the number of load cycles until  $1 \times 10^6$  cycles as shown in Figure 7-22. Despite growing in magnitude, the components of the emerging rolling noise frequencies appear to shift location with increasing

numbers of load cycles as can be seen in Figure 7-21 and 7-22. The shift can also be attributed to the increase in orbital contact geometry and damage to surface integrity as the surface contact fatigue advances. Nevertheless, the FFT of the LVDT transducer data only indicates the progressive deterioration of the contact area rather than the actual moment of spalling. The actual trends of surface degradation as a function of load cycles is monitored using the accelerometer data in the frequency-domain at high sampling frequency of 1 kHz during strong rolling noise at the speed of 2040 rpm and is presented in sub section 7.7.2.

In summary, the LVDT transducer signal is a composite of several frequency components ranging from the fundamental rolling frequencies, surface quality noise, pitting and spalling noise. Another interesting observation is the positively-skewed (left-aligned) frequency distribution, which indicates that the cumulative surface damage obeys the fatigue lifetime model of failure [Birnbaum and Saunder, 1969]. The skewness coefficient increases from 0.02 at 0 load cycles to 0.062 at  $6 \times 10^5$  load cycles and finally to 0.11 at  $10^6$  load cycles. The progressive increase indicates that the extremes of high rolling noise were increasing due to the growing surface deterioration.

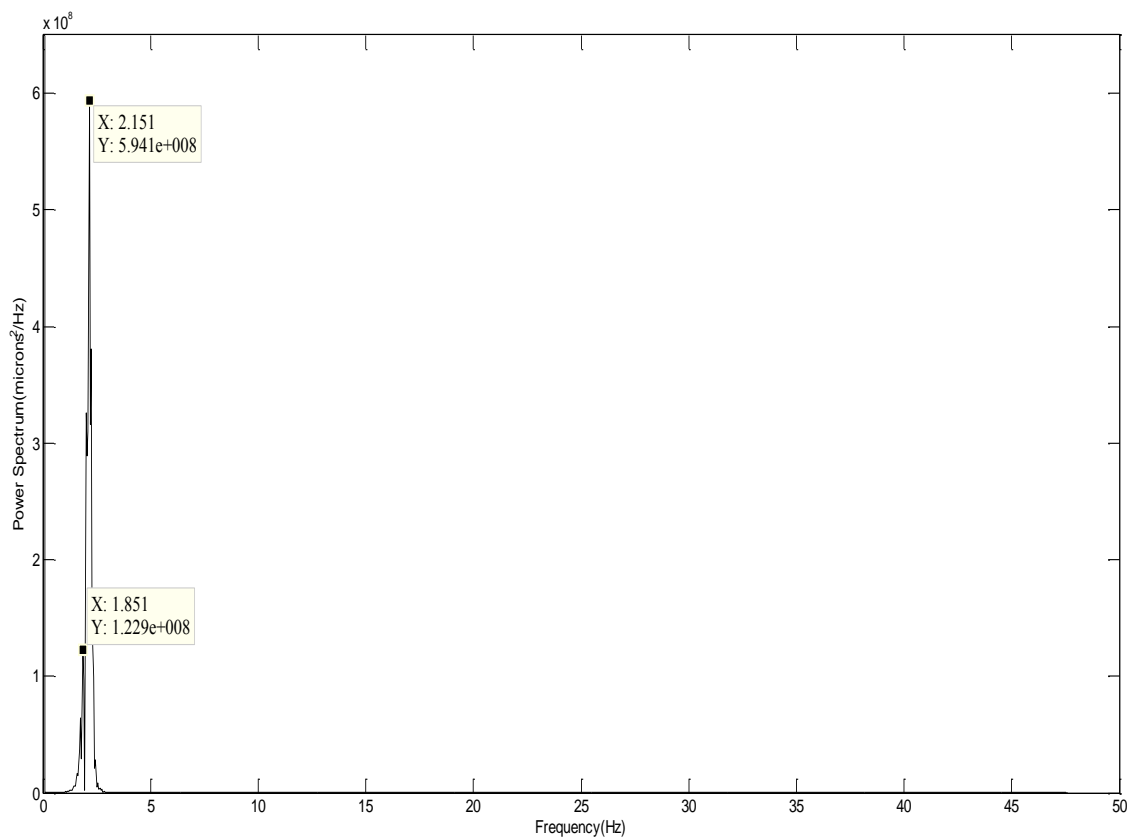


**Figure 7-20** Frequency domain plot at 0 load cycles

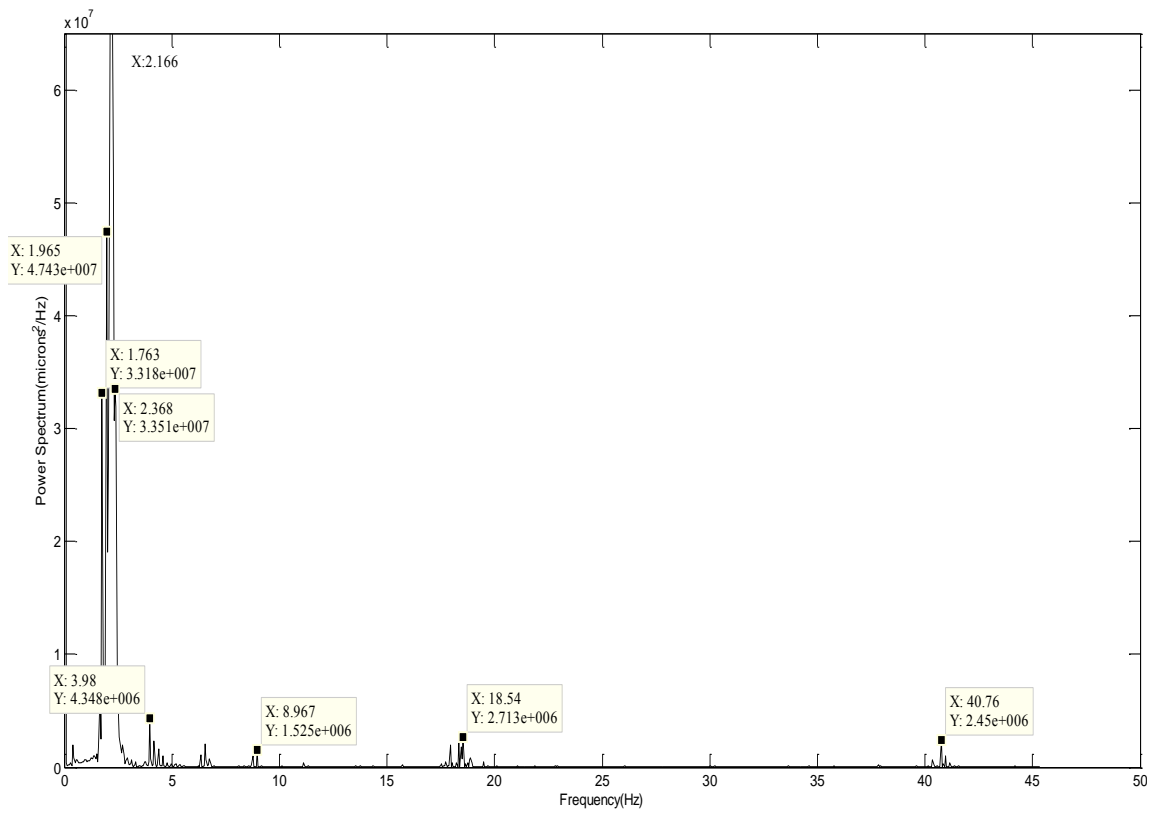


**Figure 7-21** Frequency domain plot at end of 600,000 load cycles

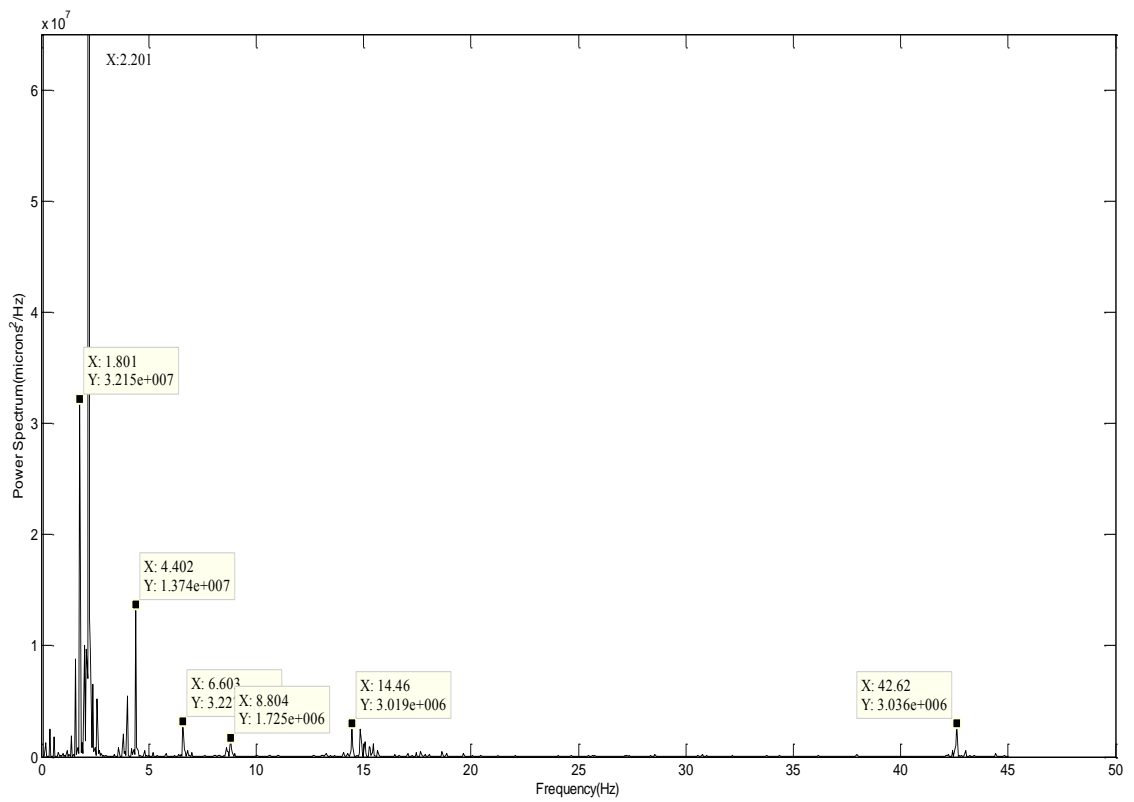


**Figure 7-22** Frequency domain plot at end of 1,000,000 load cycles



Furthermore, there are other sources of imperfection which could contribute to the complexity of LVDT transducer signal wave components, leading to the sidebands noted in Figures 7-20 to 7-22. Sources such as manufacturing imperfections and tolerances in machine elements such as the mandrel, spindle and bearings have been found to contribute about 16 $\mu$ m of oscillation due to misalignments. Moreover, the spin rolling effect keeps changing the contact geometry of the mandrel and ball with the specimen surface, due to the sphericity and diametrical tolerances of the ruby balls. According to manufacturer's data sheet, ruby balls with grade ABFMA 25 have a diameter tolerance of  $\pm 2.5 \mu\text{m}$  and a sphericity of 0.625  $\mu\text{m}$  [[www.goodfellow.com](http://www.goodfellow.com)-accessed on 05.03.2012]. Spinning rolling keeps changing the contact positions of the ball with respect to the mandrel and specimen, thus leading to oscillation waves of about 5  $\mu\text{m}$ .

### ***7.7.2 Running-speed accelerometer frequency domain analysis***

Three dimensional waterfall plots of the rolling contact noise at 2040 rpm from the initial (0 k) load cycle to the final (1000k) load cycles are shown in Figure 7-23 (a-c). The X-axis indicates number of load cycles, the Y-axis indicates frequency in Hertz, and the Z-axis indicates their spectra distributions for the three testing conditions: (a) dry at temperature of 20°C (b) lubricated (wet) at 20°C and (c) lubricated (wet) at 37°C.

Figure 7-23 (a) shows the rolling noise pattern for the dry testing of Synergy D6 flow at 20°C. Evidence of increased rolling friction and damage on the contact interface compared to the lubricated testing is implied by the wide-band noise. The ball-specimen contact rolling speed spectra are the highest and random at 18 rev/s and with the mandrel-ball speed at 34 rev/s. The first and second harmonics of the rolling speed of the ball-specimen contact are present at 36 rev/s and 54 rev/s respectively. The spectra of the ball-specimen contact fluctuate between 6000-14000g<sup>2</sup>/Hz depending on the surface quality along the orbital rolling path. Only the rolling speed noise is noted on the frequency domain of the first FFT plot at zero (0) load cycles. Additional spectra of the rolling noises emerge at 100 load cycles onwards, with a pronounced pattern between 300k and 800k load cycles. The pattern of the emerging spectra is indicative of an increase in surface degradation. Additional details of the waterfall plot in Figure 7-23 (a) can be found in the corresponding two-dimensional FFT plots in Appendix A7.1.

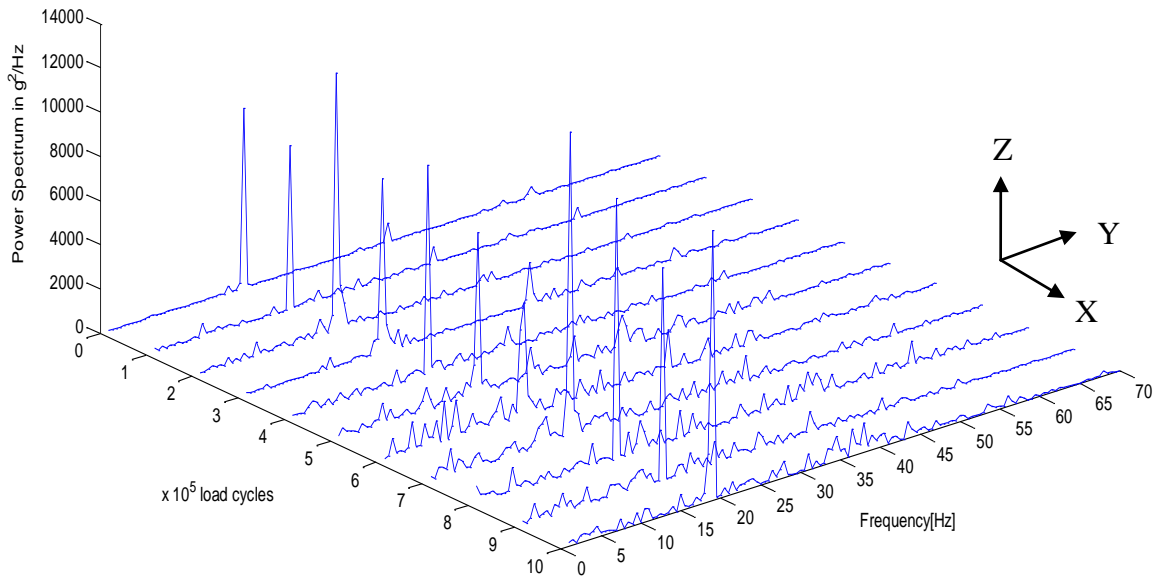


**Figure 7-23 (a)** Waterfall plots for Synergy D6 flow dry testing at 20°C

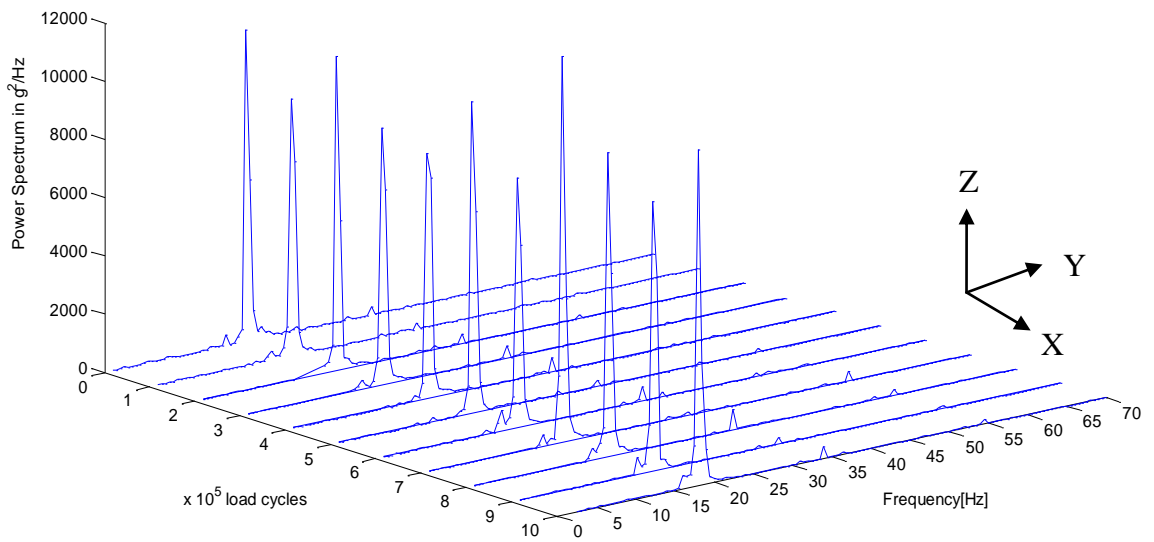


**Figure 7-23 (b)** Waterfall plots for Synergy D6 flow lubricated testing at 20°C

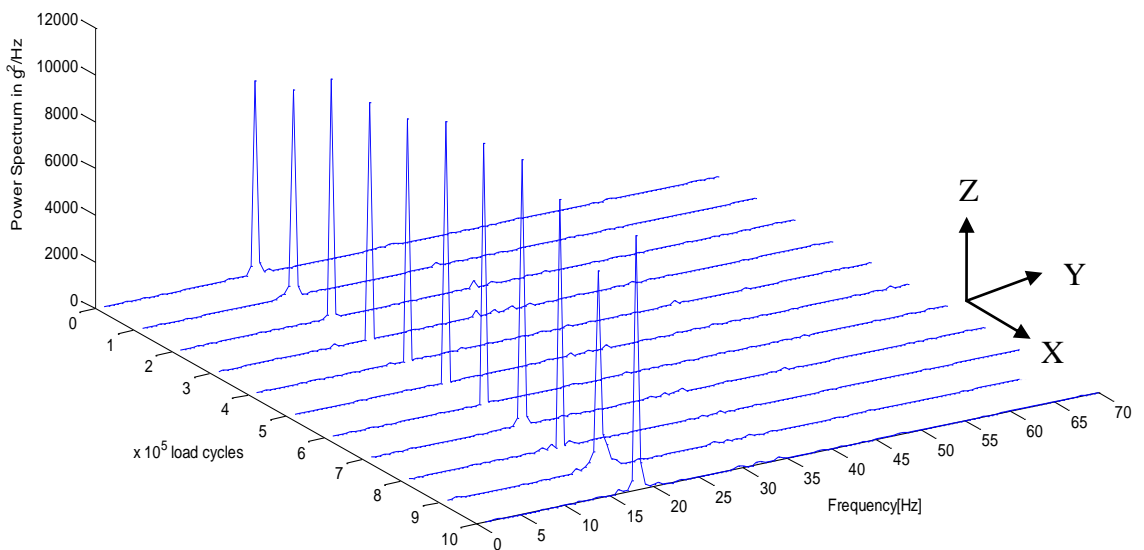


**Figure 7-23 (c)** Waterfall plots for Synergy D6 flow lubricated testing at 37°C

The random spectra are attributed to the trapped broken debris (spalls) between the ball and the dental specimen, which amplifies the deformation mechanisms and surface roughness of the rolling path. Consequently, the rolling path of the dental specimen is subjected to multi-surface wear scenario which includes adhesion, abrasion and surface contact fatigue leading to accelerated surface wear compared to that in lubricated testing as demonstrated in Figure 7-11 (a-d).

Figure 7-24 (b) shows the waterfall plot for a lubricated testing condition of Synergy D6 flow at temperature of 20°C. In this test, distilled water constantly flowed and lubricated the test area, thus washing away any broken debris and reducing friction. The ball-specimen and mandrel-ball rolling speeds have spectra at 18rev/s and 34 rev/s respectively. The first and second harmonics of the 18 rev/s are as shown in Appendix A7.2. Although the ball-specimen rolling noise spectra are still random, their magnitudes have slightly reduced and are oriented better between 9000 g<sup>2</sup>/Hz and 12000g<sup>2</sup>/Hz. The deformation noise is not clearly visible on the three dimensional waterfall plots, but can be better appreciated in the two-dimensional FFT plots in Appendix A6.3.

The growing rolling noise trend from 100k as depicted in the FFT plot is due to the orbital surface and subsurface deteriorations as the surface contact fatigue is slowly growing with load cycles before becoming severe between 400k and 800k load cycles. The significantly reduced rolling noise is due to the absence of debris adhering to rolling path because it is immediately washed away by the flowing lubricant. This leaves only cyclic loading as a mechanism for the surface fatigue. The cyclic stress accumulates with load cycles causing micro-cracks failure in the subsurface at the weak boundary interface of polymer matrix and particulate fillers. The micro-cracks grow with load cycles and eventually emerge to the surface and coalesce to spall. Ultimately, the entire rolling path surface fails by contact fatigue.

The waterfall plot in Figure 7-24(c) represents lubricated testing at an elevated temperature of 37°C, which is considered to be the clinical oral condition for a healthy person [ISO/TS14569-2:2001]. Generally, the trend is similar to that observed in Figure 7-4(b) involving the lubricated (wet) condition at 20°C. Nevertheless, here the ball-specimen rolling speed spectra at 18 rev/s are uniform starting at 10000g<sup>2</sup>/Hz and growing systematically to 12000g<sup>2</sup>/Hz at between 300k and 700k load cycles before

declining again to a  $10000\text{g}^2/\text{Hz}$  spectra at 1000k load cycles. Very low amplitude spectra can be discerned in the two-dimensional FFT plots in Appendix A7.3. The significant smoothness observed in the waterfall and FFT plots is attributed to the dampening effect of the polymeric matrix at elevated temperature due to the softening of the visco-elasticity of the dental composite [Fujii et al, 2004]. This conclusion is supported further by the fact that Synergy D6 Flow has a polymer matrix (max is 35% by volume) than glass filler particulate (42%) as specified by the manufacturer's data sheet [[www.coltene.com](http://www.coltene.com) accessed on 15.05.2014].

## **7.8 Summary**

The findings revealed that an excellent control of speed and position using a closed PI loop in pulse timing and pulse counting methods has been demonstrated at 240 rpm and 2040 rpm. Sensor data acquisition and processing have been successfully implemented. The LVDT and accelerometer measurements have quantified and qualified in detail the surface contact fatigue of the dental composites tested, establishing the onset to lie between 300k and 400k load cycles, depending on composition of the dental composites and testing conditions. Online temperature control and monitoring has also been successfully implemented. Analysis of the test results has indicated that the failure of the dental composites is mainly due to surface contact fatigue. This is revealed by the waterfall and FFT plots of the rolling contact signal acquired using the accelerometer, except in the dry testing conditions, where a combination of surface wear mechanisms exist. Nevertheless, the effects of the other mechanisms of the surface wear under cyclic rolling are minimal compared to that of the fatigue wear. The online processing of the LVDT transducer data is a milestone achievement towards developing a fully intelligent mechatronic measurement system to provide instant interpretations of surface fatigue data during testing.

## CHAPTER 8 DISCUSSION

This chapter discusses the achievements and challenges in the design, development and testing of the mechatronic fatigue measurement system, with reference to the hypothesis *“It is feasible to develop an intelligent mechatronic rolling-ball device to measure real time surface contact fatigue in dental composites”* Considering that the quantitative evaluation and analyses have been dealt with in the respective chapters, this chapter mainly focus on the qualitative comparison of the present research findings with those obtained from other relevant research. The discussion is grouped in sections with reference to the present research work flow, and therefore starts with the modelling of the rolling ball kinematics and LVDT sensor validation, followed by the FEA of the surface contact fatigue and fatigue life prediction. In a similar way, discussion of the achievements and challenges in the design and development of the mechatronic hardware and software systems is presented, followed by the discussion of the system implementation, operations and experimental results.

### 8.1 Rolling Ball Kinematic Modelling and LVDT Sensor Validation

An important aspect of a mechatronic system is a good degree of automation of the variables in the process. To achieve the desired automation of the mechatronic rolling ball device, a systematic study was conducted to establish the relationship between the mandrel’s rotations and the orbital rolling of the ball on the specimen in order to determine precise number of load cycles. Moreover, the study needed to establish the causes of the beating pattern in the signal from the LVDT transducer, and to devise a methodology to count online the number of load cycles. Equally importantly, the study should validate the suitability of the LVDT transducer for sampling meaningful data for online and offline surface contact fatigue measurement.

The study has found that the LVDT transducer output has a complex sinusoidal pattern with many frequency components primarily arising from rolling contact noise. Moreover, there exists a relationship between the mandrel’s rotation and the ball’s orbital rolling, which is a function of the mandrel groove angle as established in Chapter 3. The mandrel has to have a symmetrical V-groove in order to ensure three-point contact between the mandrel-ball and ball-specimen and to prevent the ball from slipping during rolling and surface contact fatigue can only be guaranteed if the ball is rolling without slip [McCabe et al 1997, 2000; Yap et al, 2002]. The study has further

established that the speed relationship depends on neither the ball diameter nor the orbital contact radius, as initially expected. Many other ball-on-plate tribometers have related the mandrel and ball rolling speeds on the basis of the ball's diameter and the rolling orbit radius [Stachowiak et al, 2004; DeSouza et al, 2012].

In addition, the kinematic modelling established that the beating signal is due to opposing misalignments of the mandrel and the specimen's mould axes, coupled with the constructive and destructive addition of the sinusoids from the mandrel speed and the ball-specimen orbital rolling speeds. With reference to this research, the ratio of the mandrel to orbital speed was found to vary from 1, when the ball is freely moving on the specimen with no constrained motion relative to any other surface, to 2 when the mandrel groove is hemispherical and the point of contact is at the apex and moving relative to and in phase with the specimen-ball contact. Therefore, a mandrel symmetrical V-groove of  $120^{\circ}$  leading to a speed ratio of 1.886 between the mandrel and ball-specimen contact orbit was selected by virtue of a simplified and distinctive beating phenomenon. Notwithstanding, this it was further established that the specimen needed to be held at a horizontal inclination of  $1.5^{\circ}$  in order to obtain more points pronounced wave form. Preference was not given to the speed ratio of 2 which produced an in-phase and somewhat beat-free signal. This was because the two-point contact would increase the chance of the ball slipping. Besides this, the ball's contact wear would be accelerated by having only one contact path, as compared to three in the V-grooved mandrel. These insights have been very useful in deciding the optimum size of the V-groove. Previous prototypes had used a symmetrical V-groove of  $90^{\circ}$  but led to very complex beating phenomena and made it difficult to analyze.

The kinematic modelling of the LVDT sensor signal was also verified by Matlab simulation using both theoretical and actual experimental data, as described in Chapter 3. The results obtained from the theoretical simulation correlated to a good degree with those obtained from experimental simulation. The experiments were used to validate the suitability of the sensor in acquiring the surface fatigue wear measurements online. It was established that the LVDT transducer could measure surface fatigue to within a 5% correlation with the measurements obtained from a profilometer. The surface fatigue data exhibited a good degree of reproducibility corresponding to those reported by McCabe et al [1997; 2000] and Fujii et al [2004]. On the basis of these findings, the LVDT transducer was adopted as the online sensor for measuring the surface contact

fatigue wear of dental composites. However, a signal conditioning circuit was incorporated to amplify and filter its output before the main processor's ADC module acquires, digitizes and processes the data online.

## **8.2 FEA of Surface Contact Fatigue and Fatigue Life Prediction**

Another important aspect of the pre-design evaluation was to validate the mechanisms of the evolution of surface contact fatigue on the dental composite based on deformation stresses. Ultimately, the nature of surface fatigue failure could be established and subsequently used to predict the fatigue life of the dental composites. The analysis aimed to establish an alternative method to predict the fatigue life of the dental composites. The method would complement the empirical line method which was obtained by interpolation of experimental data and has been in use currently [McCabe et al, 1997]. Various applications of FEA in predicting fatigue life of structured materials were reviewed in order to devise the new method as discussed in section 2.10. Based on this, FEA was used to model and simulate the rolling contact of the ball on the specimen to determine the deformation stresses and establish the equivalent fatigue stress. The fatigue stress was applied using the Basquin relation to predict the fatigue life of the dental composite under surface contact loading.

The FEA results showed that the dental composite suffered multi-axial deformation stresses in all directions. The hydrostatic stresses were mainly compressive, whereas the deviatoric stresses were tensile. However, their magnitudes varied significantly, being the highest in the rolling direction as detailed in Chapter 4. In addition, the stresses were mostly compressive, particularly at the pile-up region just ahead of the rolling ball. Severe stresses were also noted under the contact point in the applied load direction. The region was dominated by compressive stresses with noticeable tensile and shear stresses. The same observation was realized in the lateral third axis, with lower magnitudes than in the rolling and loading axes. Preliminary simulation of indentation showed that the shear and von Mises stresses were equal and occurred at a subsurface region. The same observation was noted with the dental composite in rolling contact, where the stresses were at maxima 0.1mm below the surface. Severe subsurface stress is an important tribological aspect of rolling contact fatigue failure and is characterized by spalling failure after cyclic contact loading or prolonged rolling contact [Johnson, 1985; Weinzapfel, 2010; Xiao-feng, 2013]. As detailed in Chapter 4, the depth of the sub-

surface stresses is determined by many factors, such as the surface quality of the materials in contact, the geometry of the contacting bodies and load size. The observations provided a strong justification for the notion that dental composites under cyclic rolling contact fail due to surface contact fatigue. The justification is based on the number of load cycles elapsed before the on-set of surface fatigue confirming that failure commenced in the subsurface region. The modelling results correlated well with findings from the current and previous surface contact loading tests.

Furthermore, it was established that the rolling contact loading was complex, combining compressive, tensile and shear stresses. Von Mises failure criterion was used to evaluate equivalent fatigue stress for the dental composite in surface contact rolling under HCF mode as explained in section 4.4. Using Basquin equation, fatigue life ranged between 200,000 and 360,000 load cycles based on the  $b$  exponent between -0.048 and -0.05 [Anastasios and Keller 2011] for the Synergy D6 composites. The fatigue life predicted was in close correlation with experimental findings published by McCabe et al [1997; 2000] and Fujii et al. [2004] using similar dental composites. Hence it can be concluded that deformation stress and Basquin equation can be used to predict fatigue life and provide first-hand knowledge of a planned testing. The knowledge is a vital tool in the planning and managing a physical laboratory testing. However, further research is needed to characterize the empirical database for the fatigue exponent ( $b$ ) for dental composites based on their S-N curve.

FEA modelling has not only enhanced the understanding of the deformation mechanisms of the dental composites, but also shed light on the evolution of surface contact fatigue. Previous studies by McCabe et al [1997; 2000] and Fujii et al [2004] focused on experimental testing and results coupled with high order microscopic scanning in order to interpret surface contact fatigue. In the present research, focus has been to compare surface fatigue life using analytical and experimental methods. Predicted surface fatigue life based on FEA and HCF failure mode has correlated that obtained experimentally using the empirical line method at  $5\mu\text{m}$ . However, a comprehensive and dedicated research is needed to develop typical empirical constants for the analytical evaluation due to broad types of dental composite with vast characteristics and compositions.



### **8.3 Designing the Mechatronic System Hardware**

The mechatronic system hardware was synergistically designed to combine mechanical and electrical parts with electronic interfaces, including sensors and drives, in an integrated and portable rolling-ball device. The detailed design processes based on the product design methodology and models by Pahl and Beitz, [1988], Pugh, [1991] and Tseng and Jiao, [1997] as explained in Chapter 5. The mechatronic design not only optimized the previous prototypes, but also incorporated new features, such as the closed loop PI speed and position control of the motor, online data acquisition and processing, automated lubricating and heating systems to mimic the human oral cavity in terms of moisture and temperature, and a versatile carriage enabling eight tests per one PMMA mould. The ISO/TS 14569-2:2001 standard for testing the wear of dental materials using two-or three-body contact was adhered to in selecting and optimizing the design variables. On the other hand, increasing the number of tests per PPMA mould from one in the previous prototypes, to eight in the current design provides significant savings in terms of consumables, preparation and energy thus reducing carbon emissions and increase homogeneity of the specimen.

The materials used for the rolling ball device (i.e. Kastal 300 aluminium alloy and Stainless steel Type 304) offer unique corrosion resistance, which was desired due to elevated temperature and moist environment in the test chamber. The horizontal layout of the rolling ball device allows the free-falling of worn debris thus avoiding it sticking to the wear groove to cause adhesive wear or becoming an abrasive agent leading to abrasive wear. It also facilitates lubricant flow and washing of the test area. Notwithstanding the advantages of a horizontal layout, it has proved to be more difficult to insert and retain the ball between the mandrel and the specimen. The cable and dead weight loading sub-system ensures that contact is maintained between the ball and test specimen regardless of wear. Importantly, the loading method was proved the most efficient and economical when compared to other loading methods such as those using a spring and pneumatic. The vibration mounts isolate the rolling ball from surrounding vibrations to ensure that the LVDT displacement is wholly due to the ball's rolling movements.

A synchronous toothed belt drive was use in order to ensure the speed ratio between the BLDC motor and spindle is 1:1. The strategic use of the belt drive aimed to eliminate

direct coupling of the mandrel to the motor shaft as used in the previous versions of the rolling ball device [McCabe, 1997, Fujii et al, 2004]. Therefore, the belt drive eliminates the change of the LVDT due to the rise of motor temperature which impacts on its shaft length. Moreover, the belt drive design eliminates direct motor vibrations and axial play due to bearing clearance. Additionally, the mechatronic measurement system incorporates an encoder for measuring speed and providing a feedback to the speed control loop. In doing so, the precise speed and position move of the motor can be determined, thus providing an accurate cycle counting compared to the prototype. By using the BLDC DC motor, the mechatronic measurement system increases operation reliability, and reduces maintenance downtime and costs.

Unavoidably, the power supplies had to be separated due to EMI noise. Switching mode power supplies had to be used due to unavailability of the linear mode power supplies with the size and characteristics desired. Nevertheless, efforts were made to assemble them into one unit, leading to a three-piece mechatronic measurement system, which are integrated rolling ball device, power supply unit and host PC. The range of the electrical and electronic components necessitated two power supplies and voltage regulator with different DC voltage outputs such as 24V,  $\pm 12V$ , 9V, 5V and 3.3V. The host PC provides the GUI, permanent data storage and post-processing including offline processing. The lubricant is discharged rather than recycled water to eliminate any other agent of wear such as impurities and bacteria. The lubrication system was designed to deliver 1ml drip every 15seconds, thus avoiding flooding the testing surrounding and tedious refilling.

Overall, the mechatronic rolling ball device has eliminated inaccuracy of measurements caused by the spring resonance in the previous design and ensure the constant normal loading of the specimen against the rolling ball as desired. It has also eliminated inaccuracies caused by frequent mounting and dismounting of the specimen due to profiling after every  $100 \times 10^3$  load cycles. It has also reduced the tedious manning operations required in the previous devices for monitoring testing processes. Figure 8-1 shows a photo image with different views of the mechatronic measurement system for surface fatigue of dental composites with labelling of the important parts. Detailed description of the parts, including design, selection and functionalities are available in their respective sections in Chapters 5 and 6.

## 8.4 Designing the Embedded System Hardware and Software

The embedded hardware consists of the main controller and peripheral controllers and drivers for dedicated tasks. The main controller, the DsPIC33FJ256GP710A (DSC microcontroller) was chosen based on its multi-tasking capabilities and interfaces such as for timing, serial communications, analog to digital conversion, input capture and output compare modules, as well as extended interrupt service routines, flash and data memories. Although DSCs with higher performance do exist and could be used to enhance system capabilities and versatility, the focus here was on low-cost embedded hardware which would ultimately lead to a low-cost mechatronic measurement system. In addition, the DSC combines the deterministic characteristics of a microcontroller chip with the computational ability of a DSP chip in one processor, thus serving two purposes at the same time. The design philosophy was to have the DSC controlling and driving peripheral controllers and drivers for the BLDC motor, the LVDT transducer, the accelerometer and temperature sensors and the drives and control of the lubrication and heating system through their dedicated sub-controllers.

The automation software is comprised of two parts: the real-time embedded algorithm for controlling and processing tasks for the main controller and sub-controllers using the pseudo code programming; and the graphical user interface (GUI) based on the flow code programming. The CCS C platform was used to write and compile program codes for the various designed algorithms, such as closed loop PI control, LVDT transducer data sampling and online processing and storage, accelerometer sampling and processing, heating and lubricating, and RS232 serial communications.

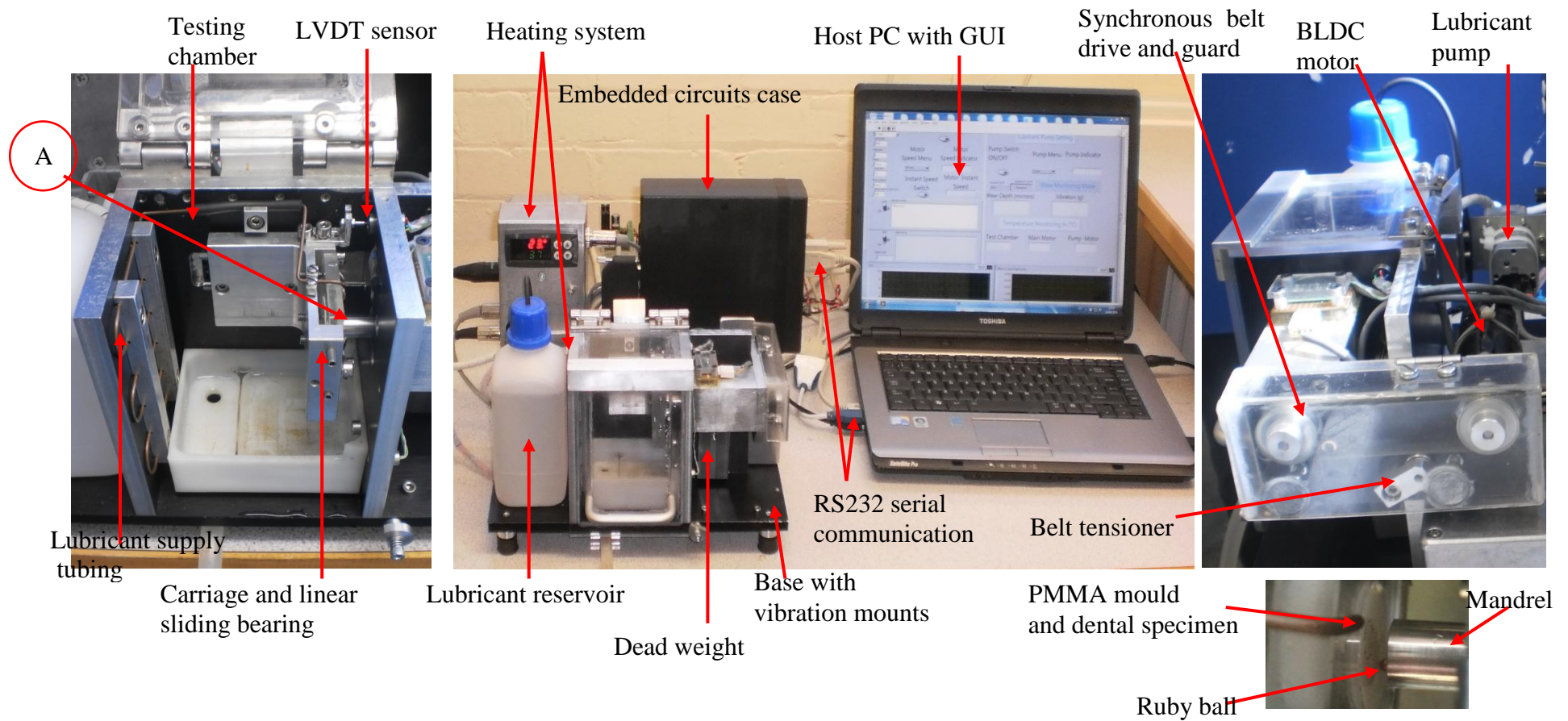


**Figure 8-1** New mechatronic surface fatigue measurement system

On the other hand, LabVIEW was used to develop the GUI to provide users with access to the real-time software by sending commands and receiving data. With the exception of ball insertion, systematic automation has been implemented for the mechatronic system to allow simultaneous and sequential multi-task operations, such as BLDC motor control, LVDT data sampling and online processing, heating and lubrication.

Therefore, the integration of the automation software in the mechatronic measurement system eliminates the limitations of the previous prototype designs which included inability to precisely count the load cycles, automatic data sampling and online processing and condition monitoring of the testing environments and tedious manual operations.

## **8.5 Testing and Evaluation of the Mechatronic Measurement System**

Several experiments categorized into two groups were conducted to evaluate and qualify the performance of the mechatronic measurement system, of which details and results have been described in Chapter 7. Generally, all the test results correlate well with results obtained using profilometry measurements in previous studies [McCabe et al, 1994, 1997, 2000; Fujii et al, 2004] in which the previous versions of the rolling ball device were used to conduct surface contact fatigue tests. In other words, there is a statistically significant correlation ( $p=0.05$ ) between the LVDT transducer measurements with the profilometry measurements, thus confirming that the online measurement method has been successful. Therefore the need to profile the fatigue track after every  $100 \times 10^3$  load cycles is eliminated, thus increasing the accuracy of measurements by reducing human error.

With reference to section 2.5, it is important that *in vitro* test conditions simulate as closely as possible those in *in vivo* tests (i.e. in the human oral cavity). Although dry testing may be thought not to have clinical relevance and should only be used for the study of tribology, there exist pathological and medical conditions which subject about 20% of the general population to so-called dry mouth syndrome [Rehme, 2014]. This is a health disorder leading to acidic saliva or reduced salivary flow (i.e. hypo-salivation) in the mouth. According to Dr. M. Rehme, the associated disorders range from sleeping disorders such as snoring to physical disorders like dehydration and mouth breathing. Medications for hypertension, depression and allergies, for example, have also been found to cause hypo-salivation. Hence, scenarios associating with dry testing conditions could exist in the oral cavity, particularly when a person with hypo-salivation eats dry

food. This provides a justification for the dry testing of dental composites, despite the relevant scenarios not being so well known. This is because dry food particles are likely to adhere to the antagonist teeth during chewing due to presence of insufficient saliva to wash them away. Essentially, this leads to a three-body cyclic contact loading in the OCA, resulting into multi-wear mechanisms.

Therefore, considering the influence of testing conditions, it has been shown that the Synergy D6 Universal composite experiences more surface fatigue wear than the Synergy D6 Flow in dry and wet conditions at 20°C, despite the two having similar mechanical properties. The difference is attributed mainly to the composition of these dental composites. With reference to McCabe et al [1997] and Baran et al [2001] on the effective composition of dental composites, Synergy D6 Universal has a higher filler-volume fraction in which the composition of fillers is 65%. Consequently, it is more brittle and susceptible to brittle fracture upon the onset of fatigue damage. The fracture propagates rapidly along the weak area of the polymer matrix and the filler-boundary interface in the form of micro-cracks which combine and emerge to the surface and eventually detach as spalls. Thus, significant surface wear is noted on the cyclic rolling path of the Synergy D6 Universal specimen. On the other hand, Synergy D6 Flow has less filler composition (42% by volume) and consists of less viscous polymers, making it more ductile and resistant to cyclic loading. The ductility tends to absorb some of the stresses induced on the specimen, and thus large cyclic loads and cycles are needed before fatigue damage is suffered. Basically, this phenomenon was observed during the testing, as evidenced by the mean wear plots in Figure 7.11 (a-d). This is regarded as the main cause of the difference in surface fatigue damage. Presumably, another factor is associated with the difference in surface roughness (i.e. the surface quality) of the two composite specimens, which may lead to on-surface or subsurface failure initiation mechanisms [Alfredsson, 2000; Slack and Sadeghi, 2010; Sanctus et al, 2012]. The surface roughness of the specimen made from Synergy D6 Universal was 15 µm and that of the specimen made from Synergy D6 Flow was 7 µm. Therefore, fatigue failure starts on or just below the surface for materials with rougher surfaces as compared to finely polished material in which the surface fatigue starts deeper in the subsurface region [Anastasios and Keller, 2011].

Furthermore, these observations can be satisfactorily explained by referring to the FEA analysis, which established that finely polished surfaces are likely to suffer less sub-

surface damage than rough contact bodies. According to McCabe et al [2000], finely polished dental composite have maximum multi-axial stresses, with damage further away inside the sub-surface region thus taking much longer to emerge on the surface and propagate. The authors further argued that there exist compressive and shear stresses underneath the contact region of dental restorations, which cause the composite to suffer subsurface micro-cracks at critical areas. When these micro-cracks reach the surface, they are propagated and/or filled with lubricating medium which causes high hydrodynamic pressure which becomes a medium for accelerated fractures and surface fatigue failure. To conclude, surface quality significantly influences the difference in onset and amount of surface fatigue experienced by Synergy D6 Universal and Synergy D6 Flow composite.

On the other hand, the reason for less reduced surface fatigue wear experienced by the Synergy D6 Flow compared to the Synergy D6 Universal can be attributed to the difference in lubricity of the two dental composites due to the type of filler used. It can be argued that the amorphous silica in Synergy D6 Flow composite lowers the coefficient of friction and enhances lubricating characteristics, thus leading to reduced surface fatigue compared to Synergy D6 Universal which contains glass silica with no such characteristics. A study by Alsem et al [2008], found that amorphous silica has better friction and lubrication characteristics than glass silica. Moreover, dry testing causes increased surface fatigue damage on dental composites than wet testing. This agrees well with theory, on the basis that the rolling friction force is much higher in a dry environment than in a lubricated environment, thus subjecting the contact region to increased surface fatigue or wear.

The effect of contact load on the induced surface fatigue wear in the Synergy D6 Flow dental composite was tested at a temperature of 37<sup>0</sup>C and lubricated conditions. It was found that the number of load cycles to cause the onset of surface contact fatigue was reduced by increasing the contact load, and higher contact loads led to increased depths of the surface fatigue wear on the specimen. The increase in contact load causes an increase in contact stresses, which increases the rate of propagation of the micro-cracks in the sub-surface region and thus accelerates the onset of surface degradation. The observation is justifiable and has also been reported by other researchers [Fujii et al, 2004; DeSouza et al, 2012; Lawson et al, 2013] that the fatigue wear of dental composite is a function of the applied load, boundary conditions and geometry of the

specimen. Nevertheless, in this specific test, the amount of surface fatigue wear is somewhat reduced compared with another lubricated test on the same material at a temperature of 20<sup>0</sup>C. This is attributed to the increased visco-elasticity characteristics at 37<sup>0</sup>C, which may result in an element of compressive creep over the course of time which thus reduces the effect of contact rolling as compared to tests conducted at a temperature of 20<sup>0</sup>C [Fujii et al, 2004].

In addition to the conclusions which can be drawn from the above discussion, it has been established that the type of lubricant used contributes to reduced fatigue wear. A study by Turssi et al [2006] found that deionised water reduced the amount of wear in in-vitro testing when compared to dry testing for two-body wear simulation, due to its inherited lubricity conditions. However, the authors cautioned that, due to the difference in surface coating properties, the use of water may lead to an overestimate of the amount of wear experienced due to the absence of the properties of human saliva. It has also been established that acidic lubricants are likely to cause more wear in dental materials than alkaline lubricants due to chemical and/or erosion wear [Lambrechts et al, 2006; Del Vigna de Almeida et al, 2008]. From the present findings, distilled water is a better preference due to its neutrality with a pH between 5-8 rather than deionised water which may still contain bacteria and alkaline minerals and tends to re-attract metal ions when in contact with metallic surroundings (such as metallic tubing) Yamamoto et al [2002] found that water decreases the coefficient of friction and the wear rate in polymeric composites involved in plastic deformation mechanisms. The rolling ball induces elastic-plastic deformation to the dental composites which contain synthetic polymers as one of their constituents. Therefore, it is sufficient to argue that the use of distilled water as a lubricant contributes to a good degree to the reduction in surface fatigue wear.

On average, a healthy human being has intermittent cyclic chewing cycles of 1x10<sup>6</sup> per year based on 1Hz masticating frequency in the OCA and 15 minutes of three episodes of chewing per day [McCabe et al, 1994, 1997; Gratton et al, 2001; Verplancke et al, 2011]. According to Lambrechts et al [1989], the wear rate of enamel in the OCA is 41µm per year. McCabe and Ogden [1986] suggested that, over a period of three years, an annual wear rate of 30µm to 150µm is expected in respect of the best-worst case scenarios for dental composite restorations. Based on these findings, the surface fatigue wear induced by the mechatronic rolling ball device for 1x10<sup>6</sup> load cycles and averaging



between 30 $\mu$ m and 100 $\mu$ m is deemed to lie within the acceptable range of dental restoration wear. On account of the experimental results, it can further be argued that the performance of the rolling ball device is within acceptable limits. However, a more rigorous evaluation based on a wider range of dental restoration composites is suggested in order to quantify and qualify the device for the ISO/TS 14569-2:2001 standards.

On the other hand, the mechatronic rolling ball measurement system has the ability to determine instantly the quality of the fatigue wear track without the need to profile the specimen. This is achieved by observing the display of the time-domain statistical features such as mean, peak, crest factor and kurtosis during sampling after every 100x10<sup>3</sup> load cycles. Referring to Section 7.4, time-domain indicators such as peak, RMS, crest factor and kurtosis have been used successfully to graphically interpret the progress of surface contact fatigue. Although the display does not rule out the need for the scanning electronic microscopy (SEM) scanning when deemed suitable, it does provide the user with first-hand information about the progress of the test process and what should be expected from the SEM scanning.

The online feature processing enables the user to monitor the testing process, as reported in fatigue life prediction studies for rolling contact bearings [Lie et al, 2006; Bhende et al, 2011]. Depending on the user's discretion, a graphical plot of these time-domain features can be plotted in order to provide an intuitive interpretation and understanding of the progress of surface contact fatigue. Furthermore, the new system provides online monitoring of the status of the V-groove by indicating the number of load cycles sampled, which can easily be compared against actual motor revolutions in order to give the speed ratio between the mandrel and orbital contact. Additionally, offline data processing, which includes frequency-domain components such as amplitude, FFT and distribution (as shown in Section 7.5), can be conducted on the host PC to provide an in-depth analysis of the surface degradation of the fatigue wear track with respect to the number of load cycles. The offline processing discriminates the time-domain data into frequency components and amplitudes. In doing so, fundamental frequencies and surface degradation frequency components, including their distribution, are identified and analyzed. The main advantage of the online and offline LVDT transducer data processing is that the number of specimens requiring profiling and SEM scanning is reduced, thus saving time and resources.

However, the online and offline feature interpretation requires the user to have a basic knowledge of data analysis in order to meaningful interpret the vibration data every  $100 \times 10^3$  load cycles. Also, the processing is conducted after every  $100 \times 10^3$  load cycles and can only show the quality of the wear track at the end of the fatigue load cycle. Notwithstanding, the sampling is also conducted at low speed, when there is minimal vibration. Therefore, an instantaneous data display during the fracture moment can be achieved by installing an accelerometer, thus indicating the respective number of cycles of which the spalling or pitting occurred.

Overall, the mechatronic rolling ball measurement system has been integrated with features which did not exist in the conventional prototype devices and which are expected to reduce human error in measurements, thus require less manned operation, and provide a better control of the process variables as well as increasing measurement efficiency and reliability. Nevertheless, there still exists a need to profile the surface fatigue track in order to study its surface morphology and enhance surface fatigue testing and analysis.

## **8.6 Summary**

This chapter has provided a qualitative description of the performance improvements made by the mechatronic measurement system in comparison with the two previous prototypes. In addition, the new integrated features and functionalities have increased its robustness, reliability and efficiency in acquiring and processing measurements, including online processing thus making it more versatile and user-friendly. It is worth mentioning that the design is unique in the sense that other ball tribometers use abrasion or a combination of fatigue and abrasion mechanisms to induce surface wear on the specimen. The fact that the ball rolls without slip assumes that failure is by surface /rolling contact loading only and that the failure results from surface/rolling contact fatigue due to plastic deformation and spalling mechanisms.

## CHAPTER 9 CONCLUSION AND FUTURE WORK

The design and the development of an intelligent mechatronic measurement system for the online measurement of the surface fatigue of dental composites has been complex. Challenges encountered previously in acquiring and characterizing online sensor data in terms of meaningful surface wear measurements had hindered the progress of the design. This research has studied the complex cyclic rolling motion of a ball constrained in a V-groove and developed techniques to acquire and interpret surface fatigue measurements using an LVDT transducer both online and offline. In addition, the study has designed testing conditions which mimic the human oral environment in terms of temperature and lubrication. This chapter presents a summary of the contributions and achievements of the study while discussing potential areas for further work which could not be accomplished within the timescale of this research.

### 9.1 Conclusions

An innovative design of a rolling ball device has been developed and experimentally tested. The new design has adhered to the ISO/TS 14569-2:2001 specifications for the *in-vitro* wear testing of dental materials. The research motivation was to develop an affordable and intelligent technology for testing dental composites in order to cater for medium-sized research laboratories. A review of the only two existing prototypes, which also included preliminary tests, was conducted in order to establish what improvements were needed in the new design. The objectives of the research were systematically executed to design and develop the mechatronic rolling ball device.

An extensive literature review was conducted of dental materials with an emphasis on dental composites, formulation methods and types, and existing testing methods and devices, including their merits and demerits, in order to establish the basis for this research. This was finally narrowed down to surface contact fatigue, its mechanism, manifestation and relevant previous research on the development of the rolling ball device. The review concluded by considering how FEA could be used to model and establishes theoretically the mechanisms of evolution of surface contact fatigue and the fatigue life of dental composite in order to optimize surface contact fatigue testing.

The rolling ball motion was modelled and studied using motion kinematics to establish the speed relationship between the mandrel–ball and ball-specimen contact points based

on a V-grooved mandrel in order to provide three-point contact. The study provided insights into the composition of the LVDT transducer signal, which is a beating composite sinusoidal wave. Subsequently, the number of load cycles to subject the specimen to would be established.

FEA modelling has been conducted to study the deformation of the dental material due to stresses induced by the cyclic rolling motion. The conclusion was drawn that the material deformed elastically and plastically, thus making it susceptible to fatigue failure. Cyclic compression-tension was also noted just ahead of and behind the rolling ball, whereas compression and shear loading were seen underneath the rolling ball. In addition, the stress tensors revealed a combination of compression and tensile deformation. Therefore, the mean compressive stress was used to predict the fatigue life of the dental composites based on HCF. Then, based on the theoretical analysis, an innovative mechatronic rolling ball measurement system was designed and developed.

Pugh concept selection and decision matrices were used to evaluate the suitability of the selection of mechanical and electronic components. Qualitative evaluation of the mechatronic hardware layout and components was conducted based on the design specifications and observing the requirements of the ISO/TS 14569-2:2001 standards. The same technique was extended to the selection of the main embedded processor and the dedicated drivers and controller modules for the sub-systems. The ultimate goal was to obtain an integrated and portable bench-top mechatronic measurement system. However, to eliminate interference by electromagnetic noise during measurement, the power supply unit had to be separated, leading to two portable units. The mechatronic measurement system design details are presented in Chapters 5 and 6 with supplementary technical information included in respective appendices.

## **9.2 Summary of Achievements**

The following achievements were made in this research:

- An extensive literature review of dental materials, their composition, physical
- and mechanical properties, and testing methods and technologies, with a focus on the in-vitro testing of the surface fatigue of dental composites.

- A new mechatronic rolling ball device was designed and developed with the capability to simulate the temperature and moisture conditions of the human oral cavity in addition to the capability to use different contact loadings.
- An embedded control system was designed and developed incorporating dedicated sub-systems for the closed loop PI speed control/drive of the BLDC motor actuator, and also to control and operate the sensors and drive the lubricating pump.
- A real time control algorithm was designed and developed with a dedicated algorithm for the closed loop PI speed control combining pulse timing and pulse counting speed measurement modes. It also incorporates LVDT sensor and temperature sensor data acquisition and processing, and lubricant pump control.
- The performance of the mechatronic rolling ball device was evaluated using a comprehensive testing programme at temperatures of 20<sup>0</sup>C and 37<sup>0</sup>C and in dry and lubricated conditions. Test results indicated 70% reproducibility was achieved, including 5% consistence with the profilometer measurements.
- A FEA of the surface contact fatigue on the dental composite specimen was conducted, to establish the mechanisms of the evolution of contact fatigue, fatigue stresses on the contact region and predicted fatigue life (initiation load cycles) based on the HCF mode (stress-based life) approach and it was established that Synergy D6 dental composite had a fatigue life ranging between 209 x10<sup>3</sup> to 359 x10<sup>3</sup> load cycles depending on testing conditions.
- Kinematic modelling of the constrained rolling ball was established to evaluate the contact points in the rolling relationship and the composition of the LVDT signal. An optimum symmetrical V-groove of 120 degrees was established, which gave a speed ratio of 1.87. Ultimately, a speed ratio of 1.9 was chosen based on a one-digit decimal format.
- A Graphical User Interface (GUI) was designed and developed based on LabVIEW flow code programming software to facilitate the user interaction with the control software, data storage and post-processing.

### **9.3 Recommendations for Future Work**

The research hypothesis was: *“It is feasible to develop an intelligent mechatronic rolling-ball device to measure in real time the surface contact fatigue of dental composites”* In this respect, the aims and objectives of the research have been met,

helping to fulfill the hypothesis with regards to meeting ISO/TS 14569-2:2001 specifications for testing wear of dental materials. Although the research has largely proven the hypothesis, a number of potential challenges were encountered, thus limiting the total success of the research. The following recommendations should be considered for future improvements in this design:

- **Embedded control and data acquisition system:** the speed and RAM of the processor play a crucial role in the performance of the embedded systems. However this goes hand in hand with cost implications. The research was based on using a low-cost processor of the DSC family (dsPIC33FJ256GP710A) which combines the computational capability of the DSP and the deterministic control of a PIC processor to perform both motor control and data acquisition and processing tasks. Although the envisaged tasks have been achieved, a number of limitations were noted in executing various multitasking operations. Typical challenges have been synchronizing data acquisition and processing time with the servo control loop timing, including power limitations in processing the floating point format. Therefore, two low-cost microcontroller processors (a master and slave) should be used in the future, and interfaced using serial peripheral interface (SPI) or intra-integrated circuit (I<sup>2</sup>C) communication. The master processor should control the servo speed control loop and communications with GUI and the slave processor would be dedicated to data acquisition and processing only before sending them to GUI through the master processor.
- **Embedded real time software:** the ready availability of library resources coupled with a user-friendly programming platform for the sharing and exchange of information are vital tools in any software development. It has been noted that the CCS PCD platform for the dsPIC30F, dsPIC33F and PIC24 families of microcontrollers is still in development and much information, including libraries, are based on the lower-levels platforms, especially PCM and PCH for programming the PIC16 and PIC18 microcontroller families. A lot of challenges were encountered during software development and no immediate solution was available, particularly for emerging programmers. In future, the C30 compiler from the Microchip should be used due to its variety of open source documentation and library resources.

- **Online data processing:** one aspect of the condition monitoring was to establish the number of fatigue load cycles online based on the mandrel-orbital speed ratio and groove geometry, including overall data processing. This has been achieved by normalizing the mean to zero and establishing the change in the crossing sign to derive the cycle counts. However, fast online data processing can be achieved with a separate dedicated processor. Thus, future designs should incorporate a dedicated processor for online data processing, including cycle counts achieved by counting ball passes.
- **Fatigue life prediction of dental composites:** a need for a comprehensive testing programme exists in order to establish empirical data for the fatigue exponents ( $b$ ) of dental composite materials in order to use them in predicting fatigue life, as is available for metallic materials. It is difficult to predict the fatigue life of dental composites with confidence relying only on the general range of the S-N curve which is between -0.040 and -0.125 for polymer composites [Anastasios and Keller, 2011]. In this research a comparison between the empirical line method and fatigue life prediction was used to determine the onset of surface contact fatigue.
- **Graphical User Interface software:** the mechatronic measurement system GUI was developed using LabVIEW graphical programming. LabVIEW GUI is easy to develop and is user-intuitive, thus saving a lot of development time. However, LabVIEW software is expensive and a licence is required. Therefore, in the future the GUI should be developed using Visual Basic programming, which is free and readily compatible with Microsoft Windows programs.
- **LVDT displacement sensor:** the surface fatigue data acquisition uses an LVDT displacement transducer. Although fatigue wear measurements are correct to  $\pm 10$  micrometres, the signal output comprises many types of noise from electrical sources. Therefore, a fibre-optic displacement sensor should be used in the future to avoid such interference noise.
- **Mechanical hardware system:** although the mechanical hardware design has met the necessary design requirements, some improvements will greatly improve its versatility in specimen setting and user interfacing. Envisaged improvements areas include:

- **Versatile specimen carriage:** the current carriage uses ball-point screws to locate the specimen into position against a strategically located metal lever and pre located ball-point screws. Future design should used ball-point screws and machined-slots to reduce specimen misalignment.
- **Device base height:** the vibration mount should be replaced with one with a diameter of 60mm and a height of 100mm to improve user-machine interaction and give a ground clearance height with better access to the lubricant drainage system and dead weight mounting.
- **Cable and dead weight loading system:** the system performs excellently and is proposed for future designs. One special aspect is the constant loading of the specimen against the rotating ball thus ensuring effective contact load. The current design uses a grub screw to mount the load on the steel rope. To ease mounting and dismounting, a slotted disk weight should be used instead in the future and a clearance hole included on the base plate to allow the rope extending to the clearance ground for the easy mounting and dismounting of the dead weight.

#### 9.4 Publications

- Marandu, S.I., and Bicker, R., (2012), Design of a Mechatronic Surface Contact Fatigue Tester for Dental Resin Composites, 2nd International Conference in Mechanical and Industrial Engineering, Arusha, Tanzania
- Marandu, S.I., and Gumno, Gu., Bicker, R. and German., G., (2014), Experimental Study of Dental composite using Mechatronic Fatigue Measurement System, Manuscript for the Review of Scientific Instruments Journal (Submission: September, 2014).



## REFERENCES

- Alfredsson, B. (2000) A Study on Contact Fatigue Mechanism. *Doctoral thesis*, Royal Institute of Technology (KTH); Stockholm, Sweden.
- Alsem, D. H, Dugger M.T, Stach, D.A and Ritchie R.O. (2008) Micro-scale friction and sliding wear of Polycrystalline Silicon Thin structure films in ambient air, *Journal of Microelectromechanical Systems*, 17:5:1144-1154.
- Anastasios P.V and Keller, T.,( 2011) Fatigue of Fiber–reinforced composites, *Springer*, 2011, Technology and Engineering
- Anusavice, K.J. (1996) *Phillip's Science of Dental Materials* 10<sup>th</sup> edition. W.B. Saunders, London.
- ASTM (1993) ASTM E-647-93: Standard method for measurement of fatigue crack growth rates *The American Society for Testing and Materials*, Philadelphia, ASTM.
- Bapna, M.S., Gadia, C.M. and Drummond, J.L. (2002) Effect of aging and cyclic loading on the mechanical properties of glass ionomer cements. *European, Journal of Oral Science*. 110:330-334.
- Baran, G., Boberick, K. and McCool, J. (2001) Fatigue of restorative materials. *Critical Review of Oral Biology and Medicine*. 12:350-359.
- Baran, G., Sadeghipour, K., Jayaraman, S., Silage, D.; Paul, D. and Boberick, K. (1998). Crack propagation directions in un-filled resins. *Journal of Dental Research*. 77(11):1864-1873
- Barden, M., Clarke, R.L., Nicholson, J.W. and Parkers, S.(1997) *Polymeric Dental Materials*. Springer-Verlag, Berlin.
- Berkovitz, B.K.B., Holland, G.R and Moxham, B.J. (1977) *A Colour Atlas and Textbook of Oral Anatomy*. (London: Wolfe Medical Publications Ltd)
- Birnbaum Z. W., and Saunder, S.C. 1969b) Estimation for a family of life distributions with applications to fatigue, *Journal of Applied probability*, 6, pp 328-347.
- Bolotin, V.V (1999). Mechanics of fatigue. *Boca Raton, FL: CRC Press*.
- Braem, M.J. A., Davidson, C.L., Lambrechts, P. and Vanherle, G. (1994a) In-vitro flexural fatigue limits of dental composites, *Journal of Biomedical Material Research*. 28:1397-1402
- Cantwell, W.J. and Roulin-Moloney, A.C.(1988) Fractography of un-filled and particulate-filled epoxy resins, *Journal of Material Science*. 23:1615-1631

- Chimello, D.T., Dibb, R.G.P., Corona, S.A.M. and Lara, E.H.G. (2001) Assessing wear and surface roughness of different composite resins after tooth brushing. *Material Research*, 4:4.
- Chuang, T.J., Jahanmir, S. and Tang, H.C. (2003) Finite element simulation of straight plunge grinding for advanced ceramics, *Journal of European Ceramic*. 23:1723-1733.
- Craig, R.G. (2002) Optical, thermal, and electrical properties, *Restorative Dental Materials*, 10 (Ed). St. Louis: Mosby; 1997: 30-55.
- Crossbank Dentalcare, “Tooth coloured and cosmetic fillings: Online Materials” [Available at: [www.crossbankdental.co.uk](http://www.crossbankdental.co.uk), Accessed in February, 2014]
- Czichos H (1986) Introduction to friction and wear. In: *Friction and wear of polymer composites*, K Friedrich editor. Amsterdam: Elsevier, pp. 1-22.
- Davidson, D.L. and Lankford, J. (1992) Fatigue crack growth in metals and alloys: mechanisms and micromechanics. *International Journal of Material Review*. 37:45-76.
- De Souza, J. A, Dolavale, L. C and Carmargo, S.D. (2012) Wear mechanisms of dental composite restorative materials by two different in-vitro methods, *Material Research*, ISSN 1516-1439
- De-Almeida, P.D.V., Gregio A.M.T., Machado, M.A.N, de Lima, A.A.S; Azevedo, L.R,(2008) .*Saliva Composition and Functions:A Comprehensive Review*. the Journal of Contemporary Dental Practice, Vol.9 No3. pp 1-11. Available: [www.thejcdp.com](http://www.thejcdp.com).
- Deb, S. (1998) Polymers in dentistry, *Proceedings of Institution of Mechanical Engineers*. 212(H): 453-464.
- DeLong, R. (2006) Inter-oral restorative material: rethinking the current approaches: how to measure wear *Dental Materials*. 22 :702-711
- DeLong, R. and Douglas, W. H. (1991) Development of an artificial oral environment for testing of dental of dental restoratives: biaxial force and movement control. *Journal of Dental Research*. 62:92-113.
- Den Hartog, J. P., (1956) *Mechanical vibrations*, Dover Edition (1985), Dover Publications, Inc. New York, 1. ISBN 0-486-64785-4
- Drummond, J.L., Botsis, J., Zhao, D and Samyn, J. (1998) Fracture properties of aged and post-processed dental composite. *Eurpean Journal of Oral Science*. 106:661-666.
- Dyer, K.P. and Isaac, D.H. (1998) Fatigue behaviour of continuous glass fibre reinforced composites. *Journal of Composites, Part B*. 29:725-733

- Eschenauer H., Koski,J., Osyczka, A., (1990) Multicriteria Design Optimization:Procedures and Applications ISBN: 978-3-642-48699-9 Springer-Verlag,Berlin.
- Fatemi, A.; Yang, L., (1998) Cumulative fatigue damage and life prediction theories: a survey of the state of the art for homogeneous materials *Int. J. Fatigue* Vol.1, pp 934
- Ferracane, J.L., (1995) Current trends in dental composites. *Critical Review of Oral Biology and Medicine*. 6:302-308.
- Ferracane, J.L., Condon, J.R., Mitchem, J.C. (1992) Evaluation of sub-surface defects created during the finishing of composites. *Journal of Dental Research*. 71:1628-1632.
- Fischer-Cripps, A.C. (1999) The Hertzian contact surfaces. *Journal of Materials Science* 34: 129– 137.
- Frunza, M.C, Frunza, G. and Luca, R. (2011) Experimental model for dynamic friction analysis in dental contacts, *Proceedings of the 3<sup>rd</sup> International Conference on E-Health and Bioengineering-EHB 2011*, Iasi, Romania.
- Fujihara, K., Teb, K., Gopal, R., Loh, P. L., Ganesh, V. K., Ramakrishna, S., Foong, K. W. C. and Chew, C. L. (2004) Fibrous composite materials in dentistry and orthopaedics: review and applications, *Composite Science Technology*. 64:775-788
- Fujii, K., Carrick E. T., Bicker, R. and McCabe J. F. (2004) Effect of the applied load on surface contact fatigue of dental filling materials; *Journal of Dental Materials*, 20:931-938
- Gratton, D.G., Aquillino S.A and Stanford, C. M. (2001) Micromotion and dynamic fatigue properties of the dental implant-abutment interface, *The Journal of Prosthodontic Dentistry* pp47-52.
- Gwinnet, A.J (1992) Structure and composition of enamel *Operative Dentistry* 17(5):10-17
- Han, P., Dia, K. and Jia, H. (2000) 3-D finite element analysis of stress distributions in supporting tissue of clasp-type partial dentures of transferring occlusion force, *Hua Xi Kou Qiang Yi Xue Za Zhi*. 18(4):262-265
- [Available at [www.ncbi.nlm.nih.gov/pubmed/12539539](http://www.ncbi.nlm.nih.gov/pubmed/12539539). [Accessed on 5<sup>th</sup> July, 2010].
- Harass, M; Friedrich, K and Almajid, A.A., (2010) Tribological behaviour of selected engineering polymers under rolling contact, *Tribology International* 43:635-646
- Harrass, M., Friedrich, K. and Almajid, A.A. (2010) Tribological behaviour of selected engineering polymers under rolling contact, *Journal of Tribology International*, 43:635-645.

- Hefferren, J.H. (1976) A laboratory method for assessment of dentifrice abrasivity *Journal of Dental Research*. 55:563-573.
- Heintze, S. D. (2010) Predictability of clinical wear by laboratory wear methods for evaluation of dental restorative materials, *PhD Thesis, (2010)*, University of Groningen.
- Herbert, E.G., Pharr, G.M., Oliver, W.C., Lucas, B.N. and Hay, J.L. (2001) On the measurement of stress-strain curves by spherical indentation, *Thin Solid Films*. 398-399:331-335
- Hibbeler, R.C. (2007) *Engineering Mechanics: Statics and Dynamics (Eleventh ed.)*, Pearson, Prentice Hall: 441–442.
- Hu, X., Marquis, P.M and Shortfall, C.(2003) Influence of the filler loading on two-body wear of dental composite, *Journal of rehabilitation*, 30:729-737
- Hu, X.; Harrington, E.; Marquis, P.M. and Shortall, A.C.(1999) The influence of cyclic loading on the wear of a dental composite, *Journal of Biomaterials*. 20:907-912.
- Hughes, J.A., Weat, N. X., Parker, D. M., van den Braak M. H. and Addy. M. (2000) Effects of pH and concentration of citric, malic and lactic acids on enamel, *in-vitro*, *Journal of Dentistry*. 28:147–52
- Husain, A.R. (2003) Development of dental material testing equipment *MPhil. Eng Mechatronic Eng*. Final year project.
- Industrial Technologies, (2008) *Precision balls for industrial and optical applications catalogue*. <http://industrialtechnologies.net> [Accessed in 10.10.2010]
- ISO/TS 14569-2:2001, Dental materials -Guidance on testing of wear, Part 2: Wear by two and/or three body contact, *ISO Standard on Dental Materials Testing Catalogue, 2001*; <http://www.iso.org> [Accessed in 2010/2011]
- Jakus, K., Ritter, J.E. and Sullivan, J.M.(1981) Dependence of fatigue predictions on the form of the crack velocity equation, *Journal of America Ceramics Society*. 64:372-374
- Johnson K, L (1958) The Effect of Spin upon the Rolling Motion of Elastic Sphere on a Plate. *Journal of Applied Mechanics*, Trans ASME, pp 332-338.
- Johnson, K. L.,(1985) *Contact Mechanics*, Cambridge University Press, Cambridge
- Kalachandra, S., Taylor, D.F., Deporter, C.D. Grubbs, H.J. and McGrath, J.E. (1993) Polymeric materials for composite matrice in biological environments, *Polymers*. 34:778-785
- Karger-Kocsic, J., Felhos, D., Xu, D. and Schlarb, A.K. (2008) Unlubricated sliding and rolling wear of thermoplastic dynamic vulcanizates (Santoprene<sup>®</sup>) against steel *Wear*,

- 265: 292-300. Available online at [www.sciencedirect.com](http://www.sciencedirect.com) [Accessed on 26<sup>th</sup> February, 2010].
- Kelly, J. R. (1997) Ceramics in restorative and prosthetic dentistry. *Annual Review of Materials Science*. 27:443-468.
- Kemp-Scholte, C.M. and Davidson, C.L. (1998) Marginal sealing of curing contraction gaps in class V composite resin restorations, *Journal of Dental Restoratives*. 67:841-845.
- Kim, T.W, Cho, Y. J, An, D.M and Lee, H.W. (2003) The Fatigue Crack Initiation Life Prediction Based on Several High Cycle Fatigue Criteria under Spherical Rolling contact , *Tribology Transactions*, 46 (1):76-82,
- Lambrechts, P., Debels, E., Landuyt, K.V., Pneumans, M. and Meerbeek, B.V. (2006) How to simulate wear? Overview of existing methods, *Dental Materials*. 22:693-701
- Lawson,N.C, Janyavula,S., Ckir, D. And Burgess, J.O.(2013) An analysis of the physiologic parameters of intraoralwear: a review *Journal of physics D:Applied Physics*
- Lee, S., Chiang, H., Lin, C.; Huang, H. and Dong, D. (2000) Finite element analysis of thermo-debonding mechanism in dental composites, *Biomaterials*, 21:1315-1326.
- Lewis, R. and Dwyer-Joyce, R.S. (2005) Wear of human teeth: a tribological perspective, *Proceedings of Institution of Mechanical Engineers J: Journal of Engineering Tribology*. 219: 1-18.
- Mackerle, J. (2003) Finite element analysis and simulation of machining: An addendum bibliography (1996-2002) *International Journal of Machine Tool Manufacturing*. 43:103-114
- Mair, L. H.; Strlaski T. A., Vowels R. W. and Loyd, C. H. (1996) Wear: mechanisms, manifestations and measurement report of a workshop, *Journal of Dentistry*, 24:141-148.
- Mayoof, F.N,(2009) *Beating phenomenon of multi-harmonic defect frequencies in a rolling element bearing: Case study from water pumping station*, Proceedings of the World Academy of Science, Engineering and Technology, Vol.57, 2009; pp.327-331.
- McCabe, J. F.; Abu Kasim, N. H. and Clearly, S. (1997) A rolling-ball device for producing surface fatigue and its application to dental materials, *Journal of Materials Science*, 32:283-287.
- McCabe, J. F., Wang, Y. and Braem M.J.A. (2000) Surface contact fatigue and flexural fatigue of dental restorative materials, *Journal of Biomedical Material Research*, 50:375-380

- McCabe, J.F., and A.R. Ogden (1987) The relationship between porosity, compressive fatigue limit and wear in composite resin restorative materials. *Journal of Dental Materials*: 3:9-12.
- McCabe, J. F., Walls, A.W.G (2008) Applied Dental Materials, 9<sup>th</sup> Edition, *Blackwell Publishing Ltd*, 22:195-202
- McKinney, J.E. and Wu, W. (1982) Relationship between subsurface damage and wear of dental restorative composites *Journal of Dental Restoratives*. 61:1083-1088.
- Mesarovic, S.D.J and Fleck, N.A.(1999) Spherical indentation of elastic-plastic solids, *Proceedings of the Royal Society of London*, 455 (A):2707-2728.
- Mizayaki, H., Kanematsu, W., Hyunga, H., Yoshizawa, Y., Hirao, K. and Ohji, T. (2009) Rolling contact fatigue properties and fracture resistance of silicon nitride ceramics with various microstructures, *Corrosion, Wear, Fatigue and Reliability of Ceramics Publication*, Wiley-American Ceramic Society, Hoboken, ISBN: 9780470456330:91-99.
- Monasky, G.E. and Taylor, D.F. (1971) Studies in the wear of porcelain, enamel and gold, *Journal of Prosthetic Dentistry*. 25:299-306.
- Moszner, N., and Salz, U. (2001) New development of polymeric dental composites, *Proceedings of Polymeric Science*. 26:565-569.
- Nankali A, (2002) *Investigation of strength properties of the hard materials of the tooth roots*, Ministry of Public Health of Ukraine / Ukrainian Scientific Medical Youth Journal, Quarterly Scientific Journal No. 33, pp74-76
- National Instruments, (2012) *How to choose the right sensor for your measurement*, NI Tutorial 13654-en [1] LVDT and vibration. Available: [www.ni.com](http://www.ni.com)
- Nicholson, J.W. (2000) Adhesive dental materials and their durability, *International Journal of Adhesives*. 20:11-16.
- Nicholson, J.W. (2007) Polyacid-modified composite resins ('compomers') and their use in clinical dentistry, *Dental Materials*. 23:615-622.
- Oh, W.; DeLong, R. and Anusavice, K.J. (2002) Factors affecting enamel and ceramic wear: a literature review, *Journal of Prosthetic Dentistry*. 87:451-459.
- Paris, P.C.; Gomez, M.P. and Anderson, W.P. (1961) A rational analytic theory of fatigue, *Trends Engineering*. 13:9-14
- Park, Y.J. and Pharr, G.M. (2004) Nanoindentation with spherical indenter: finite element studies of deformation in the elastic-plastic transition regime, *Thin Solids Films*. 447-448:246-250.

Potocnik, R. Goncz, P, Flasker, J and Glodez, S., (2010) Fatigue life of double slewing ball bearing with irregular geometry, *Fatigue*, 2010, *Procedia Engineering*, 2:1877-1886.

Powers, J. and Bayne, S.C. (1988) Friction and wear of dental materials, *ASM Handbook, vol 18, Friction, Lubrication and Wear Technology* (Metal Park, OH: ASTM): 666-681.

Prakki, A.; Cilli, R.; Mondelli, R.F.L.; Kalachandra, S. and Pereira, J. C. (2005) Influence of pH environment on polymer based dental material properties, *Journal of Dentistry*. 33:91-98.

Qualtrough, A. J. E. and Piddock, V. (1997), Ceramics updates, *Journal of Dentistry* 25:91-95.

Raabe, D.; Alemzadeh, A.J.L.; Harrison, A.L. and Ireland, A.J. (2009) The chewing robot: a new biologically-inspired way to evaluate dental restorative materials *Conference Proceedings of IEEE: Engineering in Medicine and Biology Society*. IEEE EMBS 2009, Minneapolis, MN. 978-1-4244-3296-7/09. : 6050-6053

Randall, R.C.; and Wilson, N.H.F.; (1999), Clinical testing of restorative materials: some historical landmarks, *Journal of Dentistry*. 27:543-550.

Rao, S.S. (2011) *Mechanical Vibrations*, 5<sup>th</sup> Edition, Pearson Education, Inc., publishing as Prentice Hall, 1 Lake Street, Upper Saddle River, NJ 07458, 3:267-275

Rehme, M. (2014) A New solution for Dry Mouth Syndrome: Discover Biological Dentistry and the Tooth Body Connection, *Dental Health, Diet & Nutrition, Oral Health, Oral Hygiene* [www.toothbody .com accessed on 15.07. 2014]

Ratlidge, D.K.; Smith, B.G.N. and Wilson, R.F. (1994) The effect of restorative materials on the wear of human enamel, *Journal of Prosthetic Dentistry*. 72:194-203.

Rees, J.S. and Jacobsen, D.C. (2000) The effect of interfacial failure around a class V composite restoration analyzed the finite by the finite element method,, *Journal of Oral Rehabilitation*. 27:111-116 (s).

Reifsnider, K. (1980) Fatigue behaviour of composite materials, *International Journal of Fracture*. 16:563-583.

Rodrigues, S.A. J.R., Ferracane, J.L. and Della Bona, A. (2007) Flexural strength and Weibull analysis of a microhybrid and a nanofill composite evaluated by 3- and 4-point bending tests, *Dental Materials*. 24 :426-431.

Rosenblum, M. A. and Schulman, A. (1997) A review of all-ceramics restorations, *Journal of America Dental Association*, 127:297-307.

- Sraml, M., Flaker J., Potrc , I. (2003) Numerical procedure for predicting the rolling contact fatigue crack initiation, *Int. J. Fatigue*, Vol. 23: 585-595.
- Sadeghipour, K.; Chen, W. and Barant, G. (1994) Spherical micro-indentation process of polymer-based materials: a finite element study, *Journal of Physics. D: Applied Physics*. 27:1300-1310.
- Sadeghipour, K., Baran G., Zhang, H., and Wu, W (2003) Modelling of Fatigue Crack Propagation During Sliding Wear of Polymers, *Journal of Engineering Materials and Technology*, Transactions of the ASME, 125:pp97-106.
- Sanctus,C., Beghini, M., Bartilotta, I., and Facchini, M., (2012) Surface and Subsurface Rolling Contact Fatigue Characteristic Depths and Proposal of Stress Index, *International Journal of Fatigue*, 45:71-81.
- Shreve, D.H, (1995) Signal processing for effective vibration analysis, *IRD Mechanalysis, Inc.* Columbus, Ohio.
- Singh, V., Misra1, A., Marangos, O., Park, J., Ye, Q., Kieweg, S. L., and Spencer, P.( 2011) Fatigue life prediction of dentin-adhesive interface using micromechanical stress analysis, *Journal of Dental Materials*, Elsevier, 27(9): e187–e195.
- Slack, T and Sadeghi, F., (2010) Explicit Finite Element Modelling of Subsurface Initiated Spalling in Rolling Contacts, *Tribology International*, 43: 1693-1702.
- Song, X.; Yin. L. ; Han, Y. and Jia, L. (2007) Finite element analysis of subsurface damage of ceramic prostheses in simulated intraoral dental resurfacing, *Wiley InterScience*. [www.interscience.wiley.com](http://www.interscience.wiley.com) [Accessed on 2<sup>nd</sup> July 2010]
- Spahl, W.; Budzikiewicz, H. and Geurtsen, W. (1994) Extractable residual monomers from various resin materials: a qualitative study (abstract), *Journal of dental Research*. 73: 295.
- Stephens, R. I. and Fuchs, H.O. (2001) Metal Fatigue in Engineering, (*Second edition Ed.*). John Wiley and Sons, Inc. 69, ISBN 0-471-51059-9.
- Suresh, S. (1998) Fatigue of materials, *Cambridge, UK*: Cambridge University Press.
- Taljat, B. and Pharr, G.M. (2004) Development of pile-up during spherical indentation of elastic-plastic solids, *International Journal of solids and structures*. 41:3891-3904.
- Taylor, D.F., Bayne, S.C., Leinfelder, K.F., Davis, S. and Koch, G.G. (1994) Pooling of long term clinical wear data for posterior composites, *American Journal of Dentistry*. 7:167-174.
- Taylor; G.I. (1934) The mechanism of plastic deformation of crystals, *Proceedings of Royal Society. (A)* 145:362–415.



Turssi, C.P, Faraoni, J.J. De Menezes, M. And Serra, M.C(2006) Analysis of Potential lubricants for in vitro wear testing, *Journal of Dental Materials, Elsevier* 22:77-83.

Upadhyay, D.; Panchal, M. A.; Dusbey R. S. and Srivastava V. K. (2006) Corrosion of alloys used in dentistry: a review, *Material Science Engineering (A)* 432:1-11.

Vasudeva, G. (2009) Finite element analysis: a boon to dental research, *The Internet Journal of Dental Science*. 6:2, 1-5. ISSN: 1937-8238. [www.ispub.com](http://www.ispub.com) [accessed 5<sup>th</sup> July 2010]

Venz, S. and Dickens, B. (1991) NIR-spectroscopic studies of water sorption characteristics of dental resins and composite, *Journal of Biomedical Material Research*. 25: 1231-1248.

Verplanckle, K, De Waele, W. And De Bruyn, H.(2011) Dental implants, what should be known before an *in-vitro* study. *Journal of sustainable construction and design*, Ghent University, Belgium.

Wang, L.; D' Allpino; P.H.P. Gonzaga and Perreira, L.J.C. (2003). Mechanical properties of dental restorative material: Relative contribution of laboratory tests, *Journal of Applied Oral Science*, 11:162-167.

Wang, L., D'Allpino, P.H.P., Gonzaga L.C., and Perreira, J. (2003) Mechanical properties of dental restorative material: Relative contribution of laboratory tests *Journal of Applied Oral Science*. 11:162-167.

Watts, D.C.; McAndrew, R. and lloyd, C.H. (1987), Thermal diffusivity of composite restorative materials, *Journal of Dental Research*. 67:1576-1578.

West, N.X.; Maxwell, A.; Hughes, J.A.; Parker, D.M.; Newcombe, R.G. and Addy, M. (1998). A method to measure clinical erosion. The effect of orange juice consumption on erosion of enamel, *Journal of Dentistry*. 26:329-336.

Wilson, N.H.F. (1990), The evaluation of materials: relationships between laboratory investigations and clinical studies, *Journal of Operative Dentist*. 15:149-155.

[www.smiledesign.org.uk](http://www.smiledesign.org.uk) The complete guide to a beautiful smile, *Online Guide from Smile Design Organization-UK*. [Accessed on 15<sup>th</sup> May 2010].

Xu, D (2009) *Dry rolling friction and wear of elastomeric systems and their finite element modelling*, PhD Dissertation, Technical University Kaiserslautern.

Xu, D. and Karger-Kocsis, J. (2010) Rolling and sliding properties of hybrid systems composed of uncured/cured HNBR and partly polymerized cyclic butylenes terephthalate *Journal of Tribology International*, 43:289-298.

- Yap, A.U.J.; Chew, C.L.; Ong, L.F.K.L. and Teoh, S.H. (2002) Environmental damage and occlusal contact area wear of composite restoratives, *Journal of Dental Research*. 63:914-920.
- Yuan, L. and Järvenpää, V.M., (2006) *On paper machine roll contact with beating vibrations*, Proceedings in Applied Mathematics and Mechanics, Vol. 6, pp.343-344.
- Zang, B. and Peng, X.H. (2000) Grinding damage prediction for ceramics via CDM model, *Journal of manufacturing science and engineering*. 122:51-58.
- Zheng, J. and Zhou Z.R. (2007), Study of in-vitro wear of human tooth enamel *Tribology Letter*, 26:181-189.
- Zhong-yu P.; Bin-shi X.; Hai-dou.; W. and Chun-Huan P. (2010) Investigation of rolling contact fatigue lives of Fe–Cr alloy coatings under different loading conditions *Surface Coating and Technology*. 204: 1405–141.
- Zhou, Z.R. and Zheng, J. (2008) Tribology of dental materials: a review, *Journal of Physics. D: Applied Physics*. 41 113001:1-22.
- Zhou, J. and Wu, G. (2009) Experimental study of cyclic rolling-contact fatigue of silicon nitride balls, *Tribology Transactions* 52(5): 663 – 670.

## APPENDICES

### Appendix 1: Rolling ball Kinematic Modelling Matlab Codes

#### *A1.1 Time-domain to frequency-domain (FFT) codes.*

```
Data = xlsread('mysimon.xls');
time = M(:,1);
dev = M(:,2);
Size=length(dev);
Y = fft(dev);
N = length(Y);
Y(2) = [];
power = abs(Y(1:N/2)).^2;
nyquist =500;
freq = (1:N/2)/(N/2)*nyquist;
plot(freq,power);
xlabel('Frequency(Hz)')
ylabel('Power Spectrum(microns^2/Hz)')
title('Frequency Domain Analysis Plot of Dry test')
```

#### *A1.2 Beating phenomenon modelling codes*

```
function Beat_Frequency
close all
clc
D = 2.50;%Mandrel groove diameter [mm]
W = 12.57; % Omega is Mandrel speed [rpm]
w = 11.56; % Omega is balls speed [rpm]
Y= 0.01;% gamma is small dental specimen misalignment [radians]
B =0.01; % Betta is small mandrel misalignment [radians]
alpha=125;%Mandrel groove angle
t=0:0.001:18
h= 0.5*D*(Y*sin(W*t)+ B*sin(w*t));
plot(t,h);
xlabel('Time [sec]')
ylabel('Amplitude [mm]')
```

#### *A1.3 3D plotting to depict surface fatigue wear codes*

```
% Reads data from Excel and creates and image
% Set window style to 'docked'
set(0,'DefaultFigureWindowStyle','docked');
```

```

'Scan4I.xls' % Enter file name and Matlab will read the file. Note
that the file must be
% saved in the same folder as this program
file = 'Scan2.xls'%('Please enter filename (in inverted commas. Eg
'Sample.xls')\n');
Data = xlsread(file);
%Sorts the data into 3 scalars (representing the X, Y, and Z co-
ordinates)
V1 = Data(:,1);
V2 = Data(:,2);
V3 = Data(:,3);
Size=length(V3);
% 'n' is the number of lines scanned. In the case of 'Dental Scan 2'
this
% was 111. If this changes in future you will need to change n
n = 111;
% 'm' is the number of points taken per line. It is calculated
% automatically from 'n'
m=round(Size/n);
% Total number of points
NumObs=n*m;
% Convert the three vectors into matrices to represent the 3-D surface
for i=1:n
    X=m*i-(m-1);
    for j=1:m
        if X <= numel(V1);
            SurfX(i,j)=V1(X);
            SurfY(i,j)=V2(X);
            SurfZ(i,j)=V3(X);
            X=X+1;
        end
    end
end
% In many cases, scans will not be perfect and sometimes points will
be
% dropped. The below 'for' loop attempts to compensate for this.
B2 = 0;

for i = 1:n
    for j = 1:m
        if SurfX(i,j) ~= SurfX(1,j);

```

```

    B2 = B2+1;
    SurfX(i,j) = SurfX(1,j);
    SurfY(i,j) = SurfY(i,1);
    end
    end
end
% Create the image
figure()
surf(SurfX,SurfY,SurfZ)
axis equal
xlabel('X')
ylabel('Y')
zlabel('Z')
shading interp
colorbar

```

#### ***A1.4 3D Waterfalls plotting to depict surface fatigue trends with load cycles***

```

clear all
clc
close all
M=xlsread('simon_WT_a.xlsx','A1:C1969');
X=M(:,1);
Y=M(:,2);
V=M(:,3);
K=find(X==0)
plot3(X(K),Y(K),V(K))
hold on
for i=1:10
K=find(X==i)
plot3(X(K),Y(K),V(K),'b')
end
xlabel('x 10^5 load cycles'),
ylabel('Frequency[Hz]'),
zlabel('Power Spectrum in microns^2/Hz '),

```

## Appendix 2: Embodiment Design Evaluation and Estimation

### A2.1 BLDC Servomotor torques estimation

Equation A2.1 was used to estimate the peak torque requirements of the servo motor.

$$T_P = (T_L + T_J + T_F) * 1.2 \quad (A2.1)$$

$$T_L = \frac{N * R}{\eta} = \frac{\mu * F_{max} * R}{\eta} \quad (A2.2)$$

Where  $N$  is normal force,  $F_{max}$  is the maximum force exerted by the dead weight (design dead weight is 1 kg),  $\mu$  is the coefficient approximated at 0.2 and  $\eta$  is the mechanical

$$\frac{T_L = 0.2 * 1 * 9.81 * 0.00225}{0.8}$$

Hence  $T_L = 5.63\text{mNm}$ . For sealed ball bearing and angular contact bearings, a friction factor ( $C_f$ ) of 0.125 is preferred [NMB Minebea, 2009]. Therefore, the torque required to overcome friction ( $T_F$ ) is estimated by equation A2.3

$$T_F = C_f * T_L = 0.125 * 5.63 = 0.7\text{mNm} \quad (A2.3)$$

Inertia torque ( $T_J$ ) is the torque to accelerate and decelerate the load. It also includes the inertia of the motor. If  $J_L$  is load inertia,  $J_M$  is motor shaft inertia,  $J_P$  is pulleys inertia,  $J_B$  is belt inertia,  $J_S$  spindle and mandrel inertia and  $\alpha$  is the required acceleration, and then total torque required to overcome combined inertia ( $T_J$ ) can estimated using equation A2.4. In addition, mass of a specific element being considered is abbreviated ( $m$ ), its diameter ( $d$ ), its density ( $\rho$ ) and its length is denoted by ( $l$ ).

$$T_J = (J_L + J_M + J_P + J_B + J_S) * \alpha \quad (A2.4)$$

$$J_L = \frac{1}{8} m d^2 = \frac{\pi}{32} \rho l d^4 = \frac{\pi}{32} * 7990 * 0.018 * (0.010)^4 = 1.41 * 10^{-7} \text{kgm}^2$$

$$J_M = 21.9 \text{gmcm}^2 = 2.19 * 10^{-6} \text{kgm}^2 \quad [\text{Maxon, model 272765}]$$

$$\begin{aligned} J_P &= \frac{1}{8} m d^2 = \frac{\pi}{32} \rho l (d_o^4 - d_i^4) = \frac{\pi}{32} * 2700 * 0.016 * (0.022^4 - 0.004^4) * 2 \\ &= 1.985 * 10^{-06} \text{kgm}^2 \end{aligned}$$

$$J_B = \frac{1}{4}md^2 = \frac{1}{4} * 0.02 * 0.23^2 = 2.645 * 10^{-6}kgm^2$$

$$J_s = \left(\frac{\pi}{32}\rho ld^4\right)_{spindle} = \frac{\pi}{32} * 7860 * 0.115 * 0.004^4 = 2.272 * 10^{-8} kgm^2$$

Total inertia load ( $J_T$ ) is the summation of individual elements inertia and equals to  $6.96 * 10^{-6} kgm^2$ . Expected motor high speed to actuate surface fatigue is 2000 rpm.

Considering a “*safety margin of 10% as a rule of thumb to account for miscellaneous factors which are beyond calculations if trapezoidal speed curve is assumed*” [AN 885-Microchip, 2003]. Considering 10% safety margins, design motor speed is estimated at 2400 rpm. If the acceleration time from standstill speed ( $\Omega_0=0$  rpm) to actuating speed ( $\Omega_f=2400$  rpm) is estimated to be 0.2 s, then required acceleration is given by equation A2.5.

$$\alpha = \frac{(\Omega_f - \Omega_0)}{t_a} = \frac{2 * \pi}{60 * 0.2} (2400 - 0) = 1256.64 \text{ rad/s}^2 \quad (\text{A2.5})$$

Inertia torque is a product of inertia load and rate of acceleration from standstill to working speed and is estimated by equation A2.4:

$$T_j = 6.96 * 10^{-6}kgm^2 * 1256.64 \frac{rad}{s^2} = 8.75 * 10^{-3}Nm = 8.75 \text{ mNm}.$$

Peak torque requirements is the sum of the individual torques multiplied a safety factor. Therefore peak torque is estimated by equation A2.1:

$$T_p = (5.63 \text{ mNm} + 0.7 \text{ mNm} + 8.75 \text{ mNm}) * 1.2 = 25.382 \text{ mNm}.$$

From the analysis, Maxon EC-max 30 (model 272766) brushless dc motor with  $\phi 30$  mm, driving power rating of 40W, nominal torque of 34.3mNm, voltage and 12V, maximum nominal speed of 6660 rpm and a rated current of 2.83A ( Figure 4.9) was selected and tested for the desired peak current and supply voltage. From Maxon EC-max data sheet, torque constant ( $K_t$ ) for the 12Vdc supply motor is 12.9mNm/A and its back EMF constant ( $K_e$ ) is  $1.355 * 10^{-3}$  V/rpm. Equations A2.6 and A2.7 were used to check peak current and supply voltage requirements.

$$I = \frac{T_p}{K_t} = 25.382 / 12.9 = 1.97A \quad (\text{A2.6})$$

$$V = RI + K_e \omega_m = 1.01 * 1.97 + 1.355 * 10^{-3} * 2400 = 5.242V \quad (A2.7)$$

## A2.2 Linear bearing estimation

Previous prototypes have been used IKO precision bearing model BSR 20 40 SL which has a maximum stroke length of 12mm. In the current design, the stroke has been extended to 22mm to improve access to maintenance, quick mounting and dismounting using IKO precision bearing model BSR 20 50 SL. Loading analysis for the bearing was checked using IKO catalogue, page 13 and 15. The basic dynamic load rating (C) is 790N; therefore the basic rating life was estimated using equation A2.8. The volume of the specimen carriage in Figure 4.8 was estimated to be  $1.755 \times 10^{-4} \text{ m}^3$  and the density of KASTAL 300 was  $2660 \text{ kg/m}^3$ . This gave an estimated weight of 0.5kg. The specimen carriage induced a load (P) of 5N on the BSR precision sliding bearing is.

$$L = 50 * \left(\frac{C}{P}\right)^3 \quad (A2.8)$$

Where L is rating life in  $10^3$ metres, C is basic dynamic load rating (N) and P is the applied load (N).

$$L = 50 * \left(\frac{790}{5}\right)^3 = 197.2 * 10^3 \text{ metres}$$

Rating life in hours can be obtained from equation A2.9 if stroke length and number of strokes per minutes are known.

$$L_h = \frac{10^6 * L}{2 * 60 * S * n_1} \quad (A2.9)$$

$L_h$  is the rating life (hours), S is the stroke length (mm) and  $n_1$  is the number of strokes per minute (m/min). Maximum stroke length is 22mm. Since it is not possible to estimate the actual number of stroke per minute, the maximum recommended stroke per minute (30m/min) is used for analysis purpose (actual strokes per minute are relatively lower; mainly during settings). Using equation 4.9, the value of  $L_h$  are estimated as:

$$L_h = \frac{10^6 * 197.2 * 10^3}{2 * 60 * 0.022 * 30} = 2.49 * 10^9 \text{ hours}$$

The IKO specifications for smooth and quiet operation require the loading to be not more than one half (1.5) of the static capacities. However, it was established that the



loading was far below the static load rating. It was important to check its suitability against recommended application safety factors because actual loading could exceed theoretical loading due vibration shocks and manufacturing factors. The static safety factor ( $f_s$ ) is expressed by equation A2.10

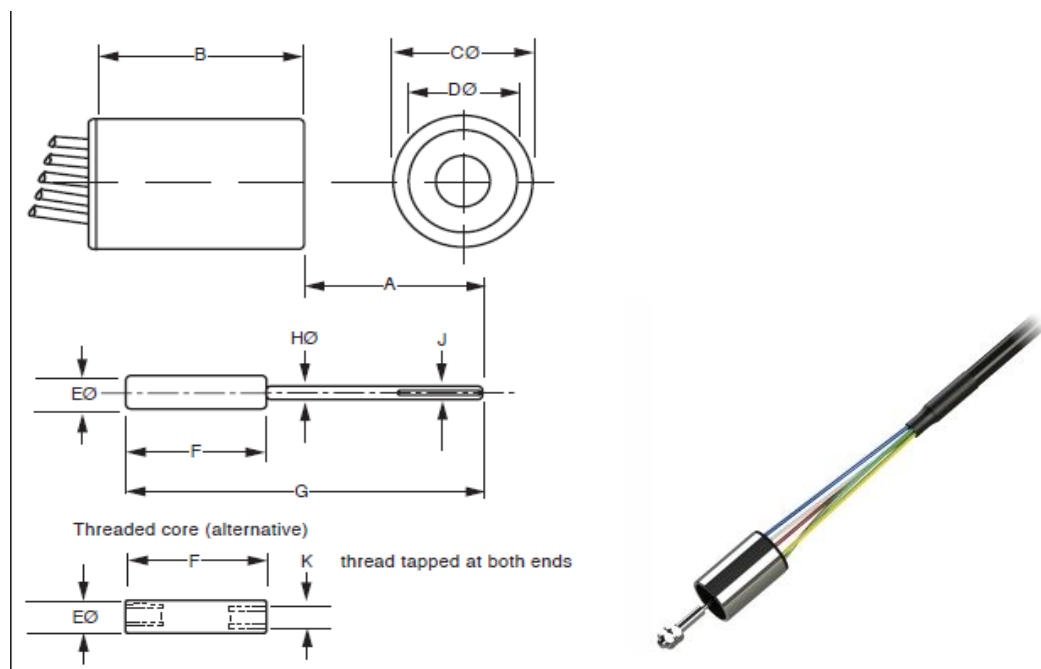
$$f_s = \frac{C_o}{P_o} \quad (\text{A2.10})$$

$C_o$  is the basic load rating in N;  $P_o$  is the maximum static load in N, and the safety factor ( $f_s$ ) for operation with vibration and shocks ranges from 3 to 5. Worst case scenario was considered in which by choosing a minimum safety factor ( $f_s$ ) of 3 and  $C_o$  of 548N from IKO data sheet.

$$P_o = \frac{548N}{3} = 182.7N$$

Applied load ( $P$ ) =5N, which is far lower than  $P_o$ , hence the static loading is safe. Checking for shocking load against its recommended factor of safety ( $f_w$ ); from 1.5 to 3 for application with shocks,  $f_w = \frac{P_o}{P}$ , it was concluded that  $P_o \gg \gg 3xP$ . The selection of the bearing satisfied all the loading condition imposed on the precision linear bearing in this application. The maximum working temperature of the precision linear bearing is 100<sup>0</sup> in continuous operation, and the current application temperature is 37<sup>0</sup>C, thus the there is no risk of failure due to elevated temperature. Further specifications and mounting instructions are available in IKO bearing website [IKO, 2002].

### A2.3 LVDT's sensor specifications



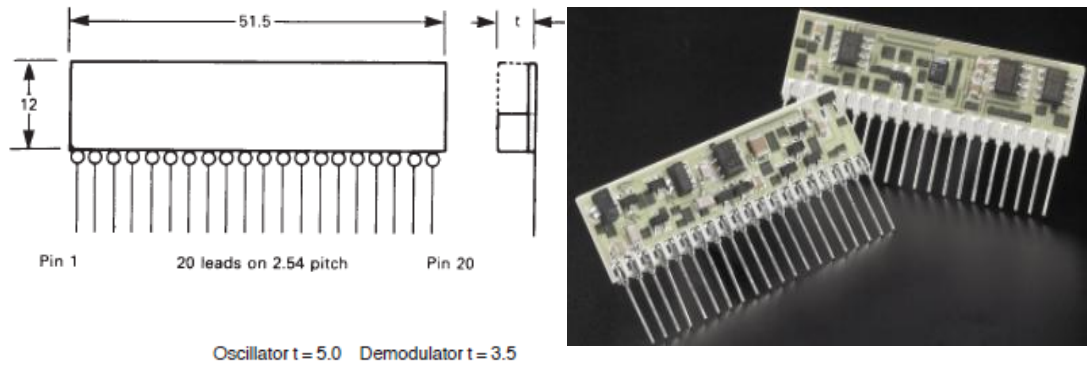
(a) LVDT transducer components view      (b) LVDT transducer photo image

**Figure A1-2** LVDT transducer schematic views and photo image [Solatron, 1997]

**Table A2-1** SM1 LVDT transducer mechanical specifications

|   | SM1                                  | SM3       |
|---|--------------------------------------|-----------|
| <b>Stroke, ±mm</b>                      |                                      |           |
| Nominal calibrated                      | 1                                    | 3         |
| Increase in output                      | 2                                    | 4         |
| <b>Dimensions, mm</b>                   |                                      |           |
| A, at electrical zero                   | 12.5                                 | 15        |
| B                                       | 15                                   | 35        |
| C                                       | 9.52                                 | 9.52      |
| D                                       | 3.5                                  | 3.5       |
| E                                       | 2.5                                  | 2.5       |
| F                                       | 9.9                                  | 20.6      |
| G                                       | 25                                   | 42.5      |
| H                                       | 1                                    | 1         |
| J                                       | M2 x 6-6g                            | M2 x 6-6g |
| K, unif thread                          | 1-72 x 4                             | 1-72 x 5  |
| <b>Weight, g</b>                        |                                      |           |
| Body, including leads                   | 6                                    | 8         |
| Armature assembly                       | 0.5                                  | 1.5       |
| Threaded core                           | 0.2                                  | 0.7       |
| <b>Non-linearity, % of total stroke</b> |                                      |           |
| Silver grade                            | 0.3                                  | 0.3       |
| Standard grade                          | 0.5                                  | 0.5       |
| <b>Materials</b>                        |                                      |           |
|   | Case: 400 series stainless steel     |           |
|   | Push rod: 300 series stainless steel |           |

Detailed specifications are provided in the hybrid oscillator and demodulator data sheet [Solatron technology, 1997].



(a) LVDT hybrid module schematic view (b) LVDT hybrid module photo image

**Figure A2-3** Hybrid oscillator and demodulator solid states modules [Solatron, 1997]

#### A2.4 Heating wattage estimation

The correct heating wattage for the heating mat needed be computed. Ambient temperature was fixed at 15°C to simplify calculation and the test chamber temperature needed to rise to 37°C averagely after half an hour upon switching on. The test chamber dimensions are 100 x 80 x 135 mm and have all four sides made using aluminium alloy. The guard that covers the top and front faces have been made using Perspex glass. The test chamber layout is depicted in Figure A4.1.

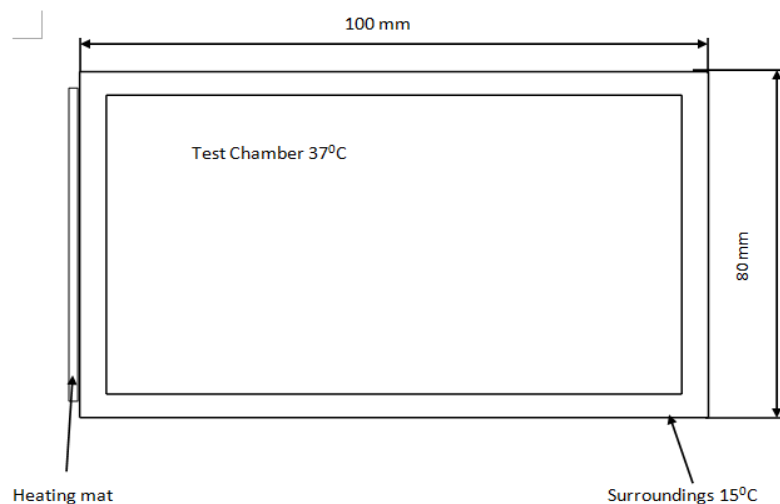


**Figure A2-4** *In-vitro* test chamber layout (not to scale)

Wattage to raise test chamber temperature from 15<sup>0</sup>C to 37<sup>0</sup>C and maintain at this point throughout the test time is estimated using equation A4.1.

$$Total\ wattage\ (W_t) = (Sensible\ heat\ up\ wattage\ (W_s) + Heat\ loss\ wattage\ (W_l)) * 1.25 \quad (A2.11)$$

Where sensible heat-up wattage included wattage to raise the temperature of the air inside test chamber, all materials inside the test chamber and its inner walls from 15<sup>0</sup>C to 37<sup>0</sup>C. To simplify presentation, sensible heat-up wattages are summarized in Table 4.6; computed using equation A2.12.

$$W_s = \frac{\zeta V C_{sp} (T_{37} - T_{15})}{t} \quad (A2.12)$$

$\zeta$  is the density of the material,  $V$  is volume,  $C_{sp}$  is the specific heat capacity,  $T$  is temperature in Kelvin for the part and  $t$  is time to raise the temperature from 15<sup>0</sup>C to 37<sup>0</sup>C, which has been approximated to 30 minutes (1800 seconds). Dimensions of the parts are available on their respective working drawings.

**Table A2-2** Heat up wattage for *in-vitro* test chamber

| Material                       | $\zeta$ (kg/m <sup>3</sup> ) | $C_{sp}$ (J/kgK) | $W_s$ (Watts) |
|--------------------------------|------------------------------|------------------|---------------|
| Air                            | 1.2                          | 1006             | 0.02          |
| Aluminium alloy                | 2660                         | 938              | 26.96         |
| PMMA(Perspex) guard            | 1400                         | 1466             | 2.70          |
| Precision linear bearing (S/S) | 8060                         | 503              | 0.72          |
| Teflon container               | 2200                         | 1050             | 4.50          |
| Total                          |                              |                  | 34.90         |

The specific heat loss per area for an aluminium material is 25W/m<sup>2</sup>K. Heat transfer coefficient for PMMA is 0.19 W/m-K; hence a 5mm thick PMMA has a specific heat loss of 38 W/m<sup>2</sup>K. Overall heat loss is estimated by using equation A2.13:

$$Heat\ loss\ wattage\ ((W_l) = U_A * A * \Delta T \quad (A2.13)$$

$U_A$  is specific heat loss per area;  $A$  is the area of material losing heat and  $\Delta T$  change in temperature in Kelvin. Wattage loss for aluminium is 18.76W and for PMMA 1 is 17.97 W Total heat loss wattage is 36.73W.

### Appendix 3: Mechatronic Rolling-ball Device Hardware Documents

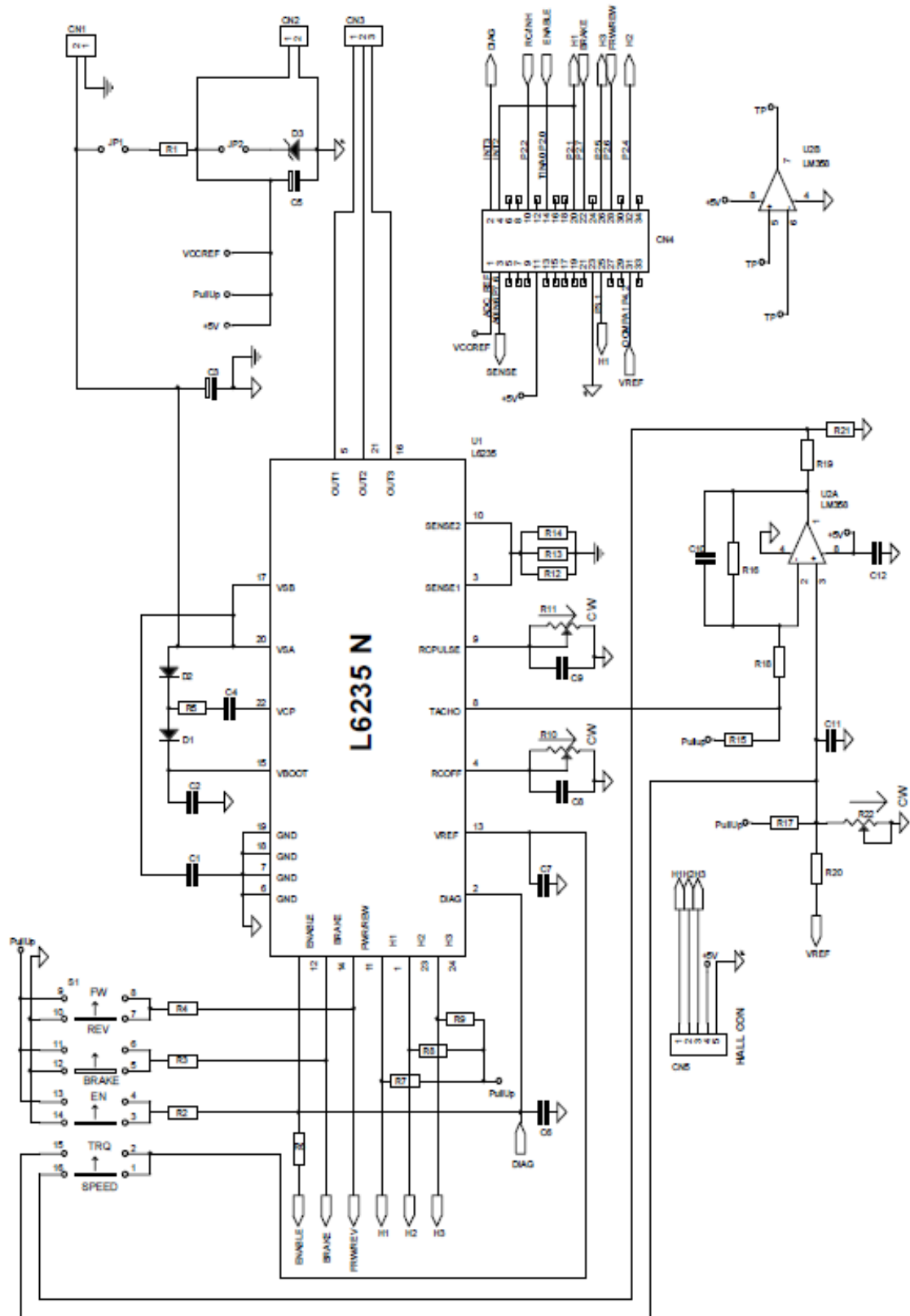
*A3.1 Assembled layout of the mechatronic rolling-ball device (attached A3\_sheet)*

*A3.2 Part list of the mechatronic rolling-ball device (with reference to A3.1)*

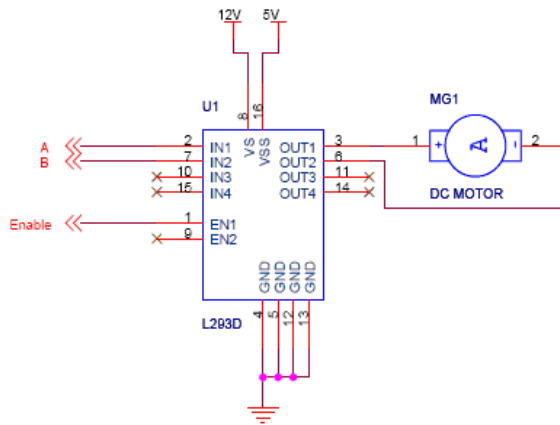
| ITEM | QTY | PART NUMBER                 | DESCRIPTION  |
|------|-----|-----------------------------|--|
| 1    | 1   | BASE PLATE                  | ALUMINIUM PLATE<br>180MMX280MMX10MM                |
| 2    | 6   | ISO 4762 - M4 X 16          | HEXAGON SOCKET HEAD CAP SCREW<br>ALUMINIUM PLATE   |
| 3    | 1   | INTERMEDIATE BRACKET        | 185MMX135MMX10MM                                   |
| 4    | 15  | ISO 4762 - M4 X 10          | HEXAGON SOCKET HEAD CAP SCREW                      |
| 5    | 1   | LEFT CROSS BRACKET          | ALUMINIUM PLATE 80MMX135X10MM                      |
| 6    | 1   | RIGHT CROSS BRACKET         | ALUMINIUM PLATE<br>80MMX135MMX10MM                 |
| 7    | 13  | ISO 4762 - M4 X 12          | HEXAGON SOCKET HEAD CAP SCREW                      |
| 8    | 1   | SPINDLE MOUNTING BLOCK      | ALUMINIUM BLOCK<br>40MMX40MMX74MM                  |
| 9    | 1   | SPINDLE                     | COLD ROLLED ALLOYED STEEL                          |
| 10   | 8   | ISO 4762 - M3 X 5           | HEXAGON SOCKET HEAD CAP SCREW                      |
| 11   | 2   | ISO 104 - 0 10 - 4 X 12 X 6 | HEXAGON SOCKET HEAD CAP SCREW                      |
| 12   | 2   | GRIP RING                   | CARBORIZED STEEL                                   |
| 13   | 1   | MANDREL /ROTOR              | STAINLESS STEEL 317                                |
| 14   | 1   | ISO 4026 - M2.5 X 3         | HEXAGON SOCKET SET SCREWS WITH<br>FLAT POINT       |
| 15   | 1   | SLIDE BEARING               | SLIDING BEARING BSR 20 50 SL                       |
| 16   | 1   | SPECIMEN CARRIAGE           | ALUMINIUM ALLOY                                    |
| 17   | 1   | UNIVERSAL L BRACKET         | ALUMINIUM ALLOY                                    |
| 18   | 1   | PERISTALTIC PUMP            | OFF SHELF ASSEMBELED MODULE                        |
| 19   | 1   | BEARING SPACER              | ALUMINIUM ALLOY                                    |
| 20   | 1   | CABLE PULLEY                | ALLOYED STEEL                                      |
| 21   | 1   | ISO 104 - 2 72 - 4 X 16 X 6 | HEXAGON SOCKET HEAD CAP SCREW                      |
| 22   | 1   | ISO 7089 - 4 - 140 HV       | PLAIN WASHERS - NORMAL SERIES<br>- PRODUCT GRADE A |
| 23   | 3   | ISO 4762 - M4 X 20          | HEXAGON SOCKET HEAD CAP SCREW                      |
| 24   | 1   | MOTOR MOUNTING BRACKET      | ALUMINIUM ALLOY                                    |
| 25   | 1   | 3PHASE BLDC MOTOR           | OFF SHELF ASSEMBELED MODULE                        |
| 26   | 1   | ENCODER                     | OFF SHELF ASSEMBELED MODULE                        |
| 27   | 3   | ISO 4762 - M1.6 X 5         | HEXAGON SOCKET HEAD CAP SCREW                      |
| 28   | 2   | BELT PULLEY ASSEMBLY        | ALUMINIUM ALLOY                                    |
| 29   | 2   | ISO 4026 - M3 X 5           | HEXAGON SOCKET SET SCREWS WITH<br>FLAT POINT       |
| 30   | 1   | PERSPEX GUARD ASSEMBLY      | PERSPEX 3mm  |
| 31   | 4   | SPRINGED STRIP CLAMP        | STAINLESS STEEL 317L                               |
| 32   | 1   | LVDT SENSOR                 | OFF SHELF ASSEMBELED MODULE                        |
| 33   | 2   | ISO 4032 - M2               | HEXAGON NUTS, STYLE 1 - PRODUCT<br>GRADES A AND B  |
| 34   | 1   | LVDT BRACKET                | ALUMINIUM ALLOY                                    |
| 35   | 1   | ISO 4028 - M3 X 5           | HEXAGON SOCKET SET SCREWS WITH<br>DOG POINT        |

| ITEM | QTY | PART NUMBER               | DESCRIPTION                                  |
|------|-----|---------------------------|--|
| 36   | 1   | DEAD WEIGHT               | MILD STEELS                                  |
| 37   | 1   | CABLE                     | ALLOYED STEEL                                |
| 40   | 1   | TENSIONING BRACKET        | ALUMINIUM ALLOY                              |
| 41   | 1   | LUBRICANT PIPE A          | BRONZE                                       |
| 42   | 1   | LUBRICANT PUMP B          | BRONZE                                       |
| 43   | 1   | ADHESIVE HEATING MAT      | OFF SHELF ASSEMBLED MODULE                   |
| 44   | 4   | ISO 10642 - M4 X 10       | OFF SHELF BOLTS                              |
| 45   | 2   | ACCELEROMETER             | OFF SHELF ASSEMBLED MODULE                   |
| 46   | 1   | LUBRICANT PIPE C          | BRONZE                                       |
| 47   | 1   | LUBRICANT RESERVOIR       | OFFSHELF HDPE BOTTLE                         |
| 48   | 2   | LUBRICANT PIPE SUPPORT    | ALUMINIUM ALLOY                              |
| 49   | 5   | ISO 4762 - M4 X 6         | HEXAGON SOCKET HEAD CAP SCREW                |
| 50   | 7   | ISO 4027 - M4 X 10        | HEXAGON SOCKET SET SCREW WITH CONE POINT     |
| 51   | 1   | ISO 4026 - M8 X 8         | HEXAGON SOCKET SET SCREWS WITH FLAT POINT    |
| 52   | 1   | ISO 1207 - M4 X 8         | SLOTTED CHEESE HEAD SCREWS - PRODUCT GRADE A |
| 53   | 4   | RUBBER MOUNT              | NATURAL RUBBER                               |
| 54   | 2   | ISO 4026 - M4 X 10        | HEXAGON SOCKET SET SCREWS WITH FLAT POINT    |
| 55   | 1   | SYNCHRONOUS TIMING BELT   | OFFSHELF REINFORCED POLYMER                  |
| 56   | 1   | LUBRICANT COLLECTING TANK | MACHINED HDPE                                |
| 57   | 1   | PIPE PART 1               | BRONZE                                       |
| 58   | 3   | 10 MM BSP NUT             | BRONZE                                       |
| 59   | 1   | 10MM MALE FEMALE ADAPTOR  | BRONZE                                       |
| 60   | 1   | PIPE PART 2               | BRONZE                                       |
| 61   | 4   | MOUNT SPACER              | ALUMINIUM ALLOY                              |
| 62   | 1   | PIPE SUPPORT              | ALUMINIUM ALLOY                              |
| 63   | 1   | PMMA MOULD & SPECIMEN     | PMMA/SYNERGY D6                              |
| 64   | 1   | PIPE SUPPORT 2            | ALUMINIUM ALLOY                              |
| 65   | 1   | ISO 4762 - M4 X 8         | HEXAGON SOCKET HEAD CAP SCREW                |
| 66   | 1   | GUARD SUPPORT             | ALUMINIUM ALLOY                              |

### A3.3 BLDC motor control and driver circuit schematic



### A3.4 Peristaltic pump driver circuit schematic




**Truth Table**

| A | B | Description               |
|---|---|---------------------------|
| 0 | 0 | Motor stops or Breaks     |
| 0 | 1 | Motor Runs Anti-Clockwise |
| 1 | 0 | Motor Runs Clockwise      |
| 1 | 1 | Motor Stops or Breaks     |


For above truth table, the Enable has to be Set (1). Motor Power is mentioned 12V, but you can connect power according to your motors.

### A3.5 Solid state relay (SSR) for powering the heater



**MOSFET BASED  
DC SOLID-STATE RELAY**

**SOM02060**

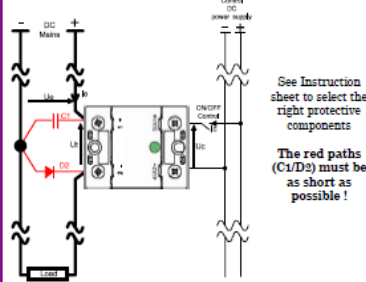


- ▶ Latest MOSFET technology generation.
- ▶ Ultra low on-state resistance.
- ▶ Low output leakage current.
- ▶ Low control current consumption.
- ▶ Built-in overvoltage protection
- ▶ Reverse protected triggered control input to avoid linear control risks
- ▶ No radiated or conducted disturbances
- ▶ Touch protected housing IP20

|                                 |           |
|---------------------------------|-----------|
| Control voltage range           | 3.5-32VDC |
| Max. permanent output voltage   | 40VDC     |
| Max. load current with heatsink | 20ADC     |

| Load voltage range | Load current range        | Control input voltage range | In & case / Out insulation | Connections     | Dimensions (WxHxD) | Weight |
|--------------------|---------------------------|-----------------------------|----------------------------|-----------------|--------------------|--------|
| 5-40VDC            | Up to 20A (with heatsink) | 3.5-32VDC                   | 2.5kV                      | Screw terminals | 45 x 58.5 x 30     | 80g    |

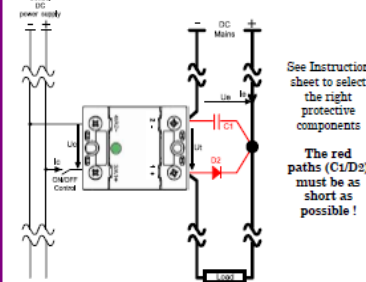
**Fig. 1 HIGH SIDE WIRING DIAGRAM**  
(Load connected to "-")



See Instruction sheet to select the right protective components

The red paths (C1/D2) must be as short as possible!

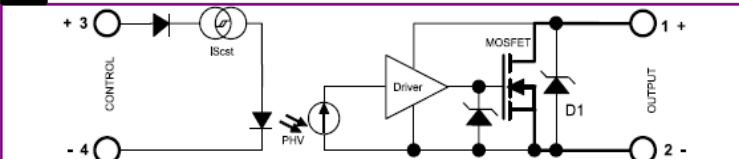
**Fig. 2 LOW SIDE WIRING DIAGRAM**  
(Load connected to "+")



See Instruction sheet to select the right protective components

The red paths (C1/D2) must be as short as possible!

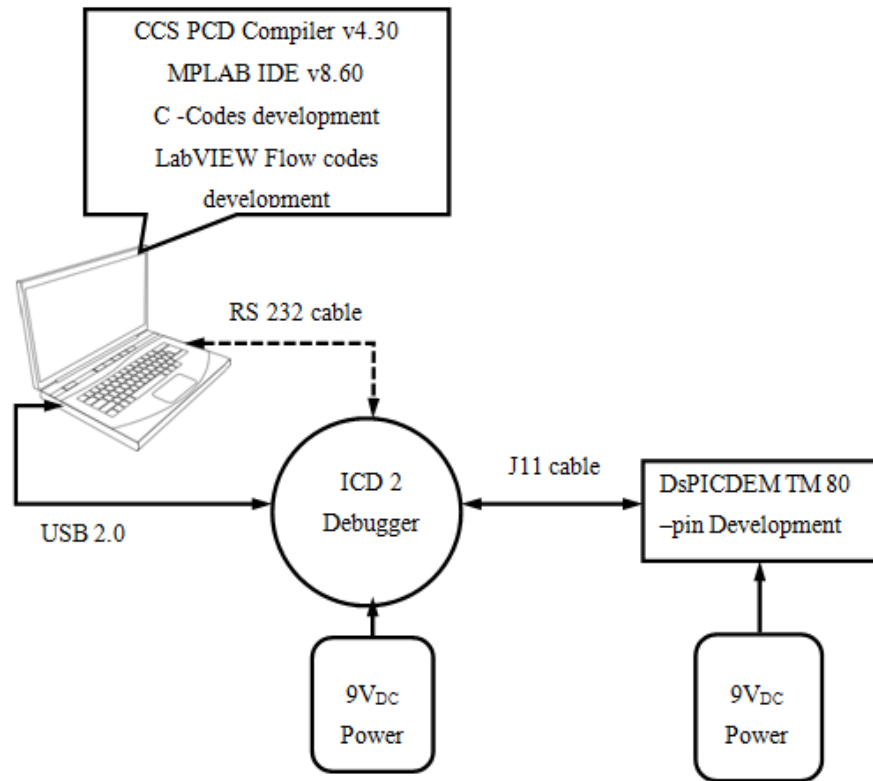
**Fig. 3 INTERNAL DIAGRAM**



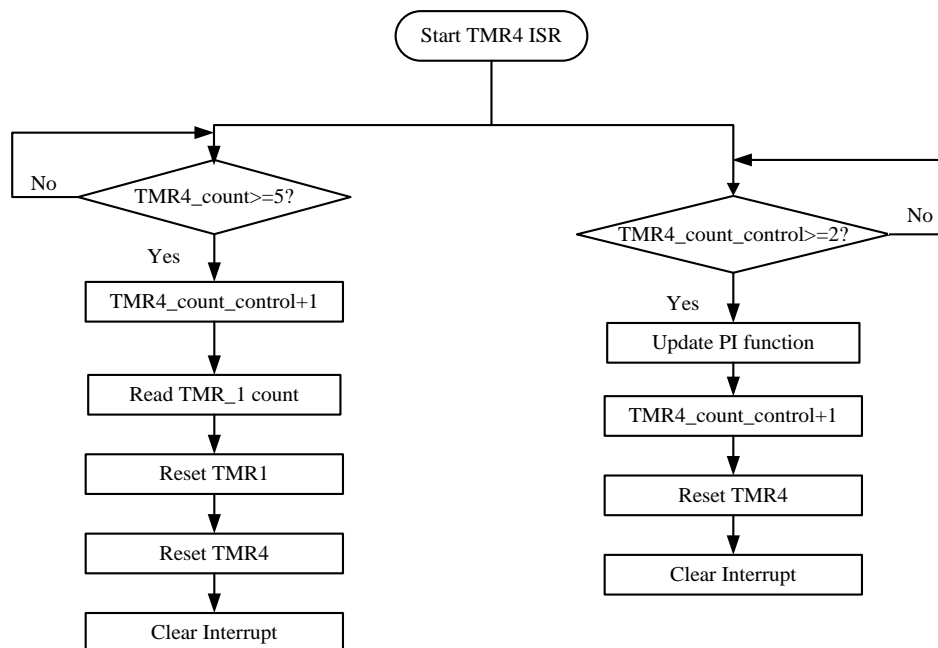


## Appendix 4: Supplementary Embedded Hardware and Software Documents

### A4.1 Configuration set-up of the CCS\_PCD/MPLAB IDE C-Programming



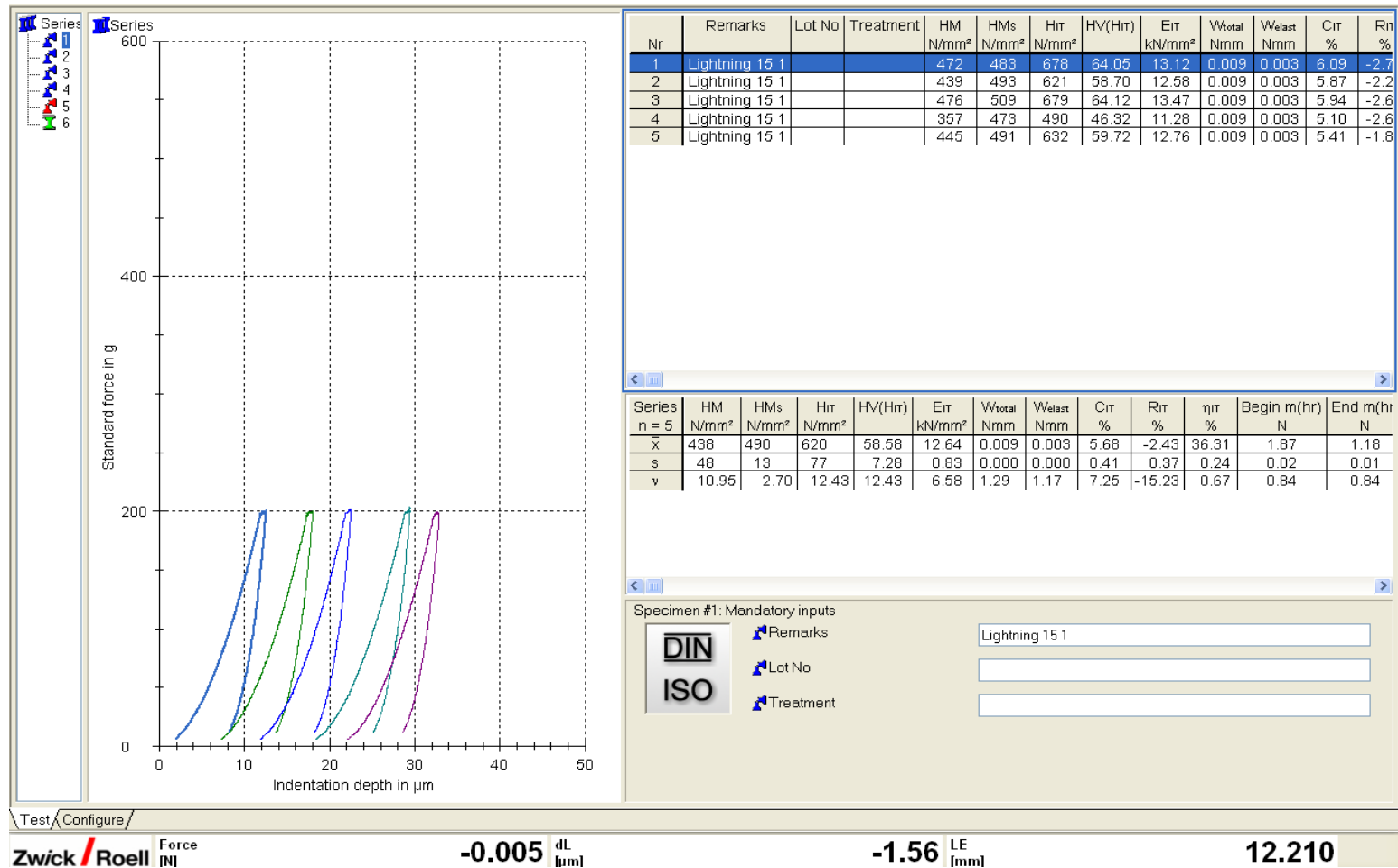
### A4.2 Interrupt Service Routine for speed control Flowchart



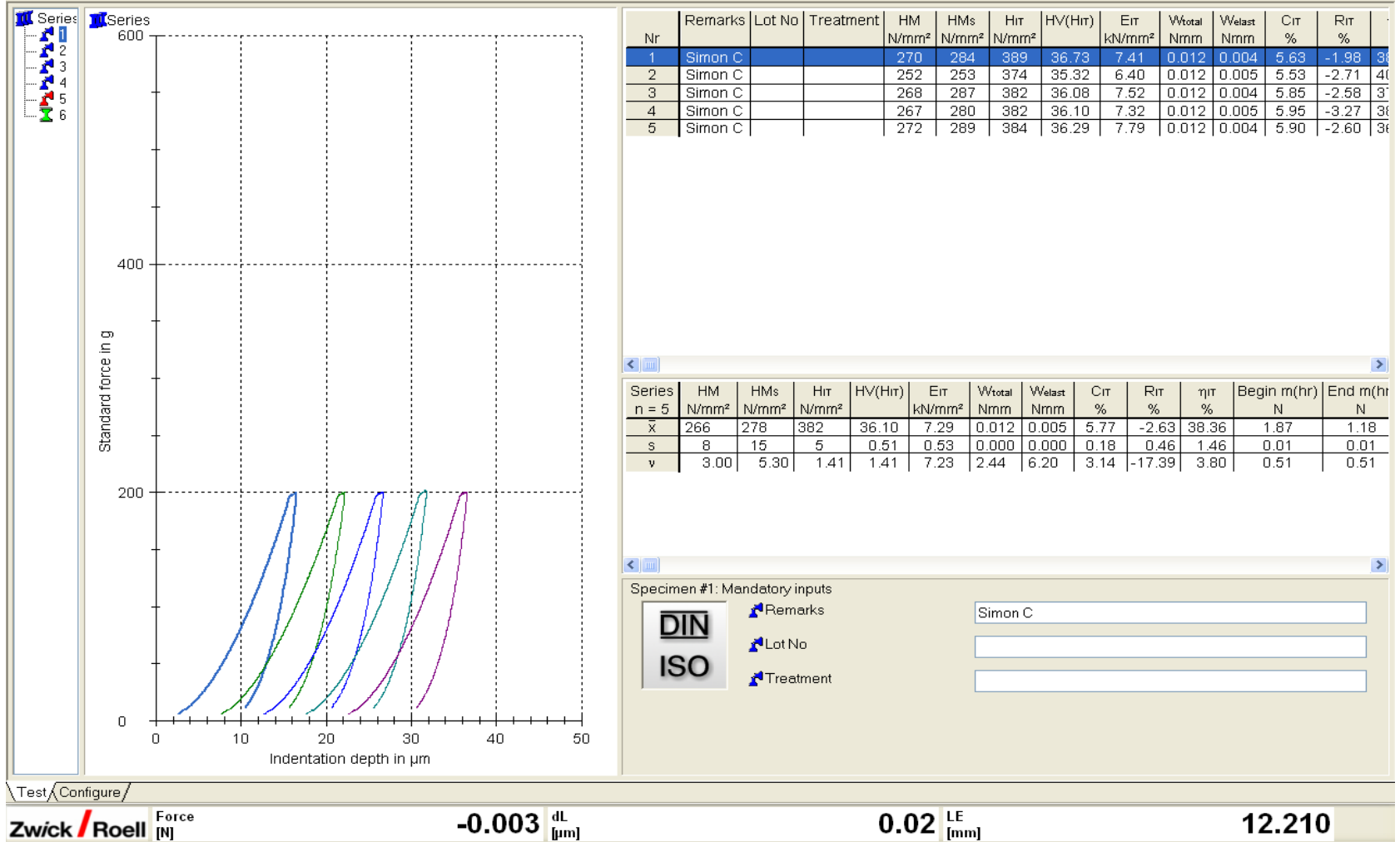
### A4.3 Overall Embedded System Program Flowchart (attached A3 sheet)

## Appendix 5: Synergy D6 Martens Hardness Tests Results for Dental Specimens

### A5.1 Synergy D6 Packable Composite



## A5.2 Synergy D6 Flowable Composite



Zwick / Roell Force [N]

-0.003 dL [μm]

0.02 LE [mm]

12.210

## Appendix 6: Encoder, LVDT and Accelerometer Signal Measurements

### *A6.1 Extract table from the LVDT data on GUI display showing online cycle counting method*

| nth value | time | ADC buffer value | MAV | Mean | Max | Min | Max MAV | Min MAV | N_MAV | Cycle count |
|-----------|------|------------------|-----|------|-----|-----|---------|---------|-------|-------------|
| 0         | 0.01 | 686              | 695 | 686  | 686 | 686 | 695     | 695     | -5    | 0           |
| 1         | 0.03 | 689              | 693 | 687  | 689 | 686 | 695     | 693     | -5    | 0           |
| 2         | 0.04 | 685              | 691 | 686  | 689 | 685 | 695     | 691     | -5    | 0           |
| 3         | 0.06 | 693              | 697 | 688  | 693 | 685 | 697     | 691     | 5     | 1           |
| 4         | 0.07 | 706              | 705 | 691  | 706 | 685 | 705     | 691     | 5     | 1           |
| 5         | 0.08 | 715              | 717 | 695  | 715 | 685 | 717     | 691     | 5     | 1           |
| 6         | 0.10 | 726              | 731 | 700  | 726 | 685 | 731     | 691     | 5     | 1           |
| 7         | 0.11 | 746              | 747 | 705  | 746 | 685 | 747     | 691     | 5     | 1           |
| 47        | 0.67 | 770              | 770 | 782  | 907 | 685 | 897     | 691     | -2    | 1           |
| 48        | 0.69 | 792              | 788 | 782  | 907 | 685 | 897     | 691     | -1    | 1           |
| 49        | 0.70 | 804              | 805 | 783  | 907 | 685 | 897     | 691     | 0     | 2           |
| 50        | 0.71 | 821              | 821 | 783  | 907 | 685 | 897     | 691     | 1     | 2           |
| 51        | 0.73 | 841              | 834 | 785  | 907 | 685 | 897     | 691     | 1     | 2           |
| 52        | 0.74 | 851              | 851 | 786  | 907 | 685 | 897     | 691     | 2     | 2           |
| 53        | 0.76 | 856              | 865 | 787  | 907 | 685 | 897     | 691     | 3     | 2           |
| 84        | 1.19 | 760              | 769 | 790  | 907 | 685 | 897     | 691     | -2    | 2           |
| 85        | 1.20 | 786              | 777 | 790  | 907 | 685 | 897     | 691     | -1    | 2           |
| 86        | 1.22 | 786              | 795 | 790  | 907 | 685 | 897     | 691     | 0     | 3           |
| 87        | 1.23 | 803              | 814 | 790  | 907 | 685 | 897     | 691     | 0     | 3           |
| 88        | 1.25 | 842              | 828 | 791  | 907 | 685 | 897     | 691     | 1     | 3           |
| 89        | 1.26 | 855              | 845 | 791  | 907 | 685 | 897     | 691     | 2     | 3           |
| 90        | 1.27 | 856              | 859 | 792  | 907 | 685 | 897     | 691     | 3     | 3           |
| 117       | 1.65 | 767              | 768 | 794  | 907 | 685 | 897     | 691     | -2    | 3           |
| 118       | 1.67 | 776              | 776 | 794  | 907 | 685 | 897     | 691     | -1    | 3           |
| 119       | 1.68 | 787              | 787 | 794  | 907 | 685 | 897     | 691     | -1    | 3           |
| 120       | 1.69 | 795              | 797 | 794  | 907 | 685 | 897     | 691     | 0     | 4           |
| 121       | 1.71 | 810              | 807 | 794  | 907 | 685 | 897     | 691     | 0     | 4           |
| 122       | 1.72 | 818              | 821 | 794  | 907 | 685 | 897     | 691     | 1     | 4           |
| 123       | 1.74 | 829              | 830 | 795  | 907 | 685 | 897     | 691     | 1     | 4           |
| 124       | 1.75 | 853              | 841 | 795  | 907 | 685 | 897     | 691     | 2     | 4           |
| 150       | 2.11 | 751              | 741 | 795  | 907 | 685 | 897     | 691     | -3    | 4           |
| 151       | 2.13 | 751              | 754 | 794  | 907 | 685 | 897     | 691     | -2    | 4           |
| 152       | 2.14 | 752              | 767 | 794  | 907 | 685 | 897     | 691     | -2    | 4           |
| 153       | 2.16 | 788              | 781 | 794  | 907 | 685 | 897     | 691     | -1    | 4           |
| 154       | 2.17 | 795              | 799 | 794  | 907 | 685 | 897     | 691     | 0     | 5           |

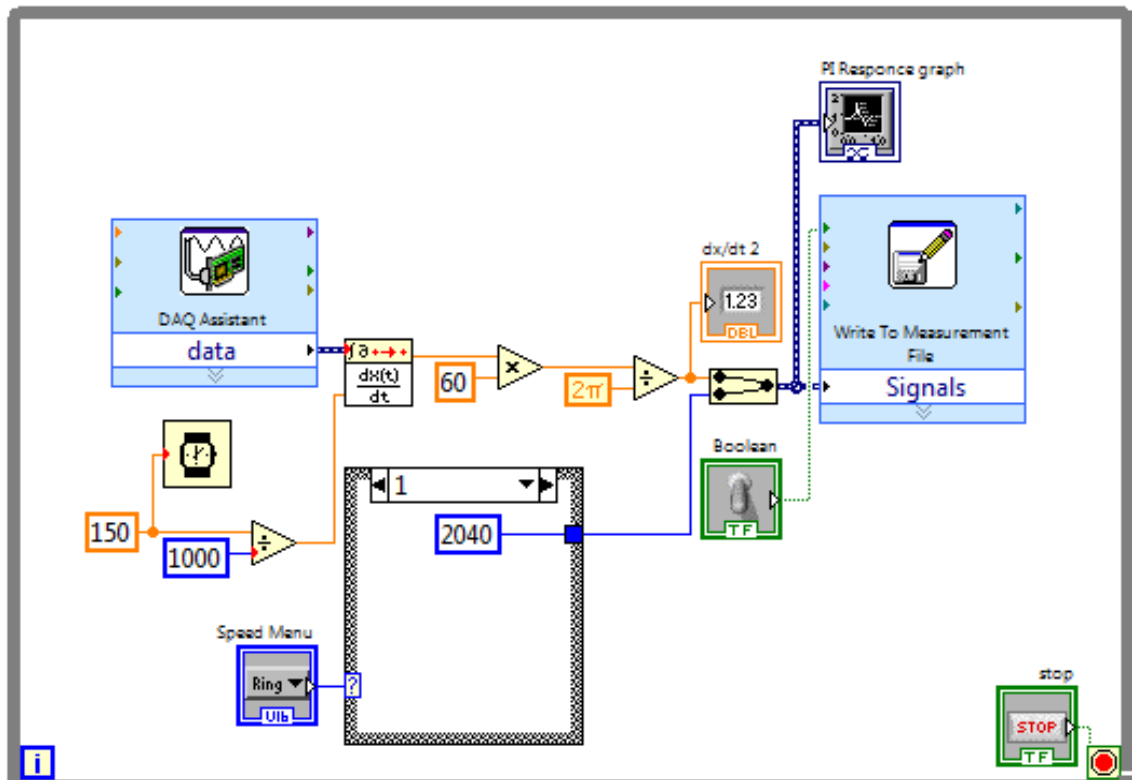
| nth value | time | ADC buffer value | MAV | Mean | Max | Min | Max MAV | Min MAV | N_MAV | Cycle count |
|-----------|------|------------------|-----|------|-----|-----|---------|---------|-------|-------------|
| 155       | 2.18 | 821              | 816 | 794  | 907 | 685 | 897     | 691     | 1     | 5           |
| 157       | 2.21 | 841              | 846 | 795  | 907 | 685 | 897     | 691     | 2     | 5           |
| 158       | 2.23 | 859              | 858 | 795  | 907 | 685 | 897     | 691     | 3     | 5           |
| 364       | 5.11 | 772              | 775 | 796  | 929 | 682 | 923     | 684     | -2    | 10          |
| 365       | 5.12 | 789              | 783 | 796  | 929 | 682 | 923     | 684     | -1    | 10          |
| 366       | 5.14 | 786              | 795 | 796  | 929 | 682 | 923     | 684     | -1    | 10          |
| 367       | 5.15 | 801              | 809 | 796  | 929 | 682 | 923     | 684     | 0     | 11          |
| 368       | 5.17 | 828              | 821 | 796  | 929 | 682 | 923     | 684     | 0     | 11          |
| 369       | 5.18 | 844              | 840 | 796  | 929 | 682 | 923     | 684     | 1     | 11          |
| 390       | 5.47 | 732              | 732 | 797  | 929 | 682 | 923     | 684     | -3    | 11          |
| 391       | 5.49 | 732              | 733 | 797  | 929 | 682 | 923     | 684     | -3    | 11          |
| 396       | 5.56 | 766              | 768 | 796  | 929 | 682 | 923     | 684     | -2    | 11          |
| 397       | 5.57 | 787              | 780 | 796  | 929 | 682 | 923     | 684     | -1    | 11          |
| 398       | 5.59 | 793              | 792 | 796  | 929 | 682 | 923     | 684     | -1    | 11          |
| 399       | 5.60 | 804              | 806 | 796  | 929 | 682 | 923     | 684     | 0     | 12          |
| 400       | 5.61 | 814              | 816 | 796  | 929 | 682 | 923     | 684     | 0     | 12          |
| 401       | 5.63 | 833              | 827 | 796  | 929 | 682 | 923     | 684     | 0     | 12          |
| 429       | 6.02 | 728              | 732 | 796  | 929 | 682 | 923     | 684     | -3    | 12          |
| 430       | 6.03 | 743              | 741 | 796  | 929 | 682 | 923     | 684     | -3    | 12          |
| 431       | 6.05 | 751              | 754 | 796  | 929 | 682 | 923     | 684     | -3    | 12          |
| 432       | 6.06 | 764              | 769 | 796  | 929 | 682 | 923     | 684     | -2    | 12          |
| 433       | 6.08 | 786              | 785 | 796  | 929 | 682 | 923     | 684     | -1    | 12          |
| 434       | 6.09 | 804              | 802 | 796  | 929 | 682 | 923     | 684     | -1    | 12          |
| 435       | 6.10 | 823              | 821 | 796  | 929 | 682 | 923     | 684     | 0     | 13          |
| 436       | 6.12 | 836              | 838 | 796  | 929 | 682 | 923     | 684     | 1     | 13          |
| 437       | 6.13 | 860              | 855 | 796  | 929 | 682 | 923     | 684     | 2     | 13          |
| 438       | 6.15 | 869              | 873 | 797  | 929 | 682 | 923     | 684     | 2     | 13          |
| 439       | 6.16 | 891              | 887 | 797  | 929 | 682 | 923     | 684     | 3     | 13          |
| 440       | 6.17 | 910              | 896 | 797  | 929 | 682 | 923     | 684     | 3     | 13          |
| 441       | 6.19 | 907              | 906 | 797  | 929 | 682 | 923     | 684     | 4     | 13          |
| 537       | 7.53 | 715              | 723 | 796  | 929 | 676 | 923     | 682     | -4    | 15          |
| 538       | 7.55 | 733              | 738 | 796  | 929 | 676 | 923     | 682     | -3    | 15          |
| 539       | 7.56 | 762              | 760 | 796  | 929 | 676 | 923     | 682     | -2    | 15          |
| 540       | 7.57 | 783              | 779 | 796  | 929 | 676 | 923     | 682     | -1    | 15          |
| 541       | 7.59 | 809              | 799 | 796  | 929 | 676 | 923     | 682     | -1    | 15          |
| 542       | 7.60 | 810              | 818 | 796  | 929 | 676 | 923     | 682     | 0     | 16          |
| 543       | 7.62 | 831              | 836 | 796  | 929 | 676 | 923     | 682     | 1     | 16          |
| 544       | 7.63 | 859              | 853 | 796  | 929 | 676 | 923     | 682     | 2     | 16          |
| 545       | 7.64 | 872              | 868 | 796  | 929 | 676 | 923     | 682     | 2     | 16          |
| 546       | 7.66 | 893              | 882 | 796  | 929 | 676 | 923     | 682     | 3     | 16          |

| nth value | time  | ADC buffer value | MAV | Mean | Max  | Min | Max MAV | Min MAV | N_MAV | Cycle count |
|-----------|-------|------------------|-----|------|------|-----|---------|---------|-------|-------------|
| 674       | 9.45  | 740              | 748 | 797  | 929  | 676 | 923     | 682     | -3    | 19          |
| 675       | 9.46  | 760              | 758 | 797  | 929  | 676 | 923     | 682     | -2    | 19          |
| 676       | 9.48  | 773              | 772 | 797  | 929  | 676 | 923     | 682     | -2    | 19          |
| 677       | 9.49  | 782              | 787 | 797  | 929  | 676 | 923     | 682     | -1    | 19          |
| 678       | 9.51  | 807              | 801 | 797  | 929  | 676 | 923     | 682     | -1    | 19          |
| 679       | 9.52  | 817              | 817 | 797  | 929  | 676 | 923     | 682     | 0     | 20          |
| 680       | 9.53  | 830              | 832 | 797  | 929  | 676 | 923     | 682     | 1     | 20          |
| 681       | 9.55  | 850              | 844 | 797  | 929  | 676 | 923     | 682     | 1     | 20          |
| 682       | 9.56  | 860              | 858 | 797  | 929  | 676 | 923     | 682     | 2     | 20          |
| 683       | 9.58  | 867              | 869 | 797  | 929  | 676 | 923     | 682     | 2     | 20          |
| 1024      | 14.35 | 746              | 745 | 797  | 936  | 674 | 924     | 682     | -3    | 29          |
| 1025      | 14.36 | 763              | 763 | 797  | 936  | 674 | 924     | 682     | -2    | 29          |
| 1026      | 14.38 | 786              | 782 | 797  | 936  | 674 | 924     | 682     | -1    | 29          |
| 1027      | 14.39 | 800              | 800 | 797  | 936  | 674 | 924     | 682     | -1    | 29          |
| 1028      | 14.41 | 819              | 821 | 797  | 936  | 674 | 924     | 682     | 0     | 30          |
| 1029      | 14.42 | 836              | 839 | 797  | 936  | 674 | 924     | 682     | 1     | 30          |
| 1030      | 14.43 | 865              | 856 | 797  | 936  | 674 | 924     | 682     | 2     | 30          |
| 1031      | 14.45 | 877              | 876 | 797  | 936  | 674 | 924     | 682     | 3     | 30          |
| 1349      | 18.90 | 729              | 735 | 797  | 1010 | 674 | 935     | 681     | -3    | 39          |
| 1350      | 18.91 | 757              | 753 | 797  | 1010 | 674 | 935     | 681     | -3    | 39          |
| 1351      | 18.93 | 765              | 770 | 797  | 1010 | 674 | 935     | 681     | -2    | 39          |
| 1352      | 18.94 | 795              | 789 | 797  | 1010 | 674 | 935     | 681     | -1    | 39          |
| 1353      | 18.96 | 806              | 807 | 797  | 1010 | 674 | 935     | 681     | -1    | 39          |
| 1354      | 18.97 | 826              | 827 | 797  | 1010 | 674 | 935     | 681     | 0     | 40          |
| 1355      | 18.98 | 844              | 842 | 797  | 1010 | 674 | 935     | 681     | 1     | 40          |
| 1356      | 19.00 | 867              | 859 | 797  | 1010 | 674 | 935     | 681     | 2     | 40          |
| 1357      | 19.01 | 871              | 871 | 797  | 1010 | 674 | 935     | 681     | 2     | 40          |
| 1358      | 19.03 | 889              | 880 | 797  | 1010 | 674 | 935     | 681     | 2     | 40          |
| 1511      | 21.17 | 760              | 758 | 797  | 1010 | 674 | 935     | 681     | -2    | 44          |
| 1512      | 21.18 | 784              | 777 | 797  | 1010 | 674 | 935     | 681     | -2    | 44          |
| 1513      | 21.20 | 786              | 795 | 797  | 1010 | 674 | 935     | 681     | -1    | 44          |
| 1514      | 21.21 | 819              | 815 | 797  | 1010 | 674 | 935     | 681     | 0     | 45          |
| 1515      | 21.22 | 828              | 831 | 797  | 1010 | 674 | 935     | 681     | 0     | 45          |
| 1516      | 21.24 | 862              | 856 | 797  | 1010 | 674 | 935     | 681     | 1     | 45          |
| 1517      | 21.25 | 862              | 874 | 797  | 1010 | 674 | 935     | 681     | 2     | 45          |
| 1518      | 21.27 | 911              | 894 | 797  | 1010 | 674 | 935     | 681     | 3     | 45          |
| 1519      | 21.28 | 909              | 907 | 797  | 1010 | 674 | 935     | 681     | 3     | 45          |
| 1520      | 21.29 | 929              | 921 | 797  | 1010 | 674 | 935     | 681     | 4     | 45          |
| 1670      | 23.39 | 752              | 756 | 797  | 1010 | 674 | 935     | 681     | -3    | 49          |

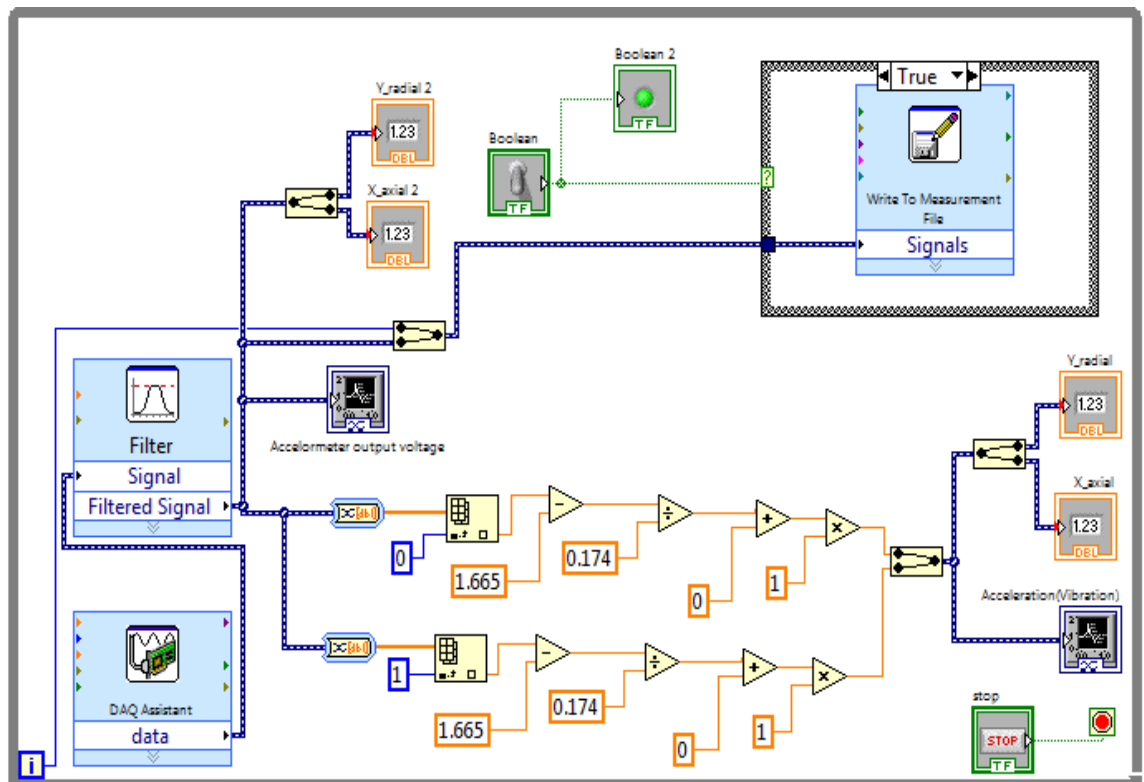
| nth   |       | ADC    |     |      |      |     | Max | Min |       | Cycle |
|-------|-------|--------|-----|------|------|-----|-----|-----|-------|-------|
| value | time  | buffer | MAV | Mean | Max  | Min | MAV | MAV | N_MAV | count |
| 1671  | 23.41 | 766    | 765 | 797  | 1010 | 674 | 935 | 681 | -2    | 49    |
| 1672  | 23.42 | 773    | 775 | 797  | 1010 | 674 | 935 | 681 | -2    | 49    |
| 1673  | 23.44 | 787    | 788 | 797  | 1010 | 674 | 935 | 681 | -1    | 49    |
| 1674  | 23.45 | 798    | 801 | 797  | 1010 | 674 | 935 | 681 | -1    | 49    |
| 1675  | 23.46 | 817    | 812 | 797  | 1010 | 674 | 935 | 681 | 0     | 50    |
| 1676  | 23.48 | 830    | 824 | 797  | 1010 | 674 | 935 | 681 | 0     | 50    |
| 1677  | 23.49 | 831    | 839 | 797  | 1010 | 674 | 935 | 681 | 1     | 50    |
| 1678  | 23.51 | 848    | 852 | 797  | 1010 | 674 | 935 | 681 | 1     | 50    |
| 1837  | 25.73 | 745    | 756 | 797  | 1010 | 674 | 935 | 681 | -3    | 54    |
| 1838  | 25.75 | 774    | 777 | 797  | 1010 | 674 | 935 | 681 | -2    | 54    |
| 1839  | 25.76 | 805    | 797 | 797  | 1010 | 674 | 935 | 681 | -1    | 54    |
| 1840  | 25.77 | 825    | 819 | 797  | 1010 | 674 | 935 | 681 | 0     | 55    |
| 1841  | 25.79 | 839    | 842 | 797  | 1010 | 674 | 935 | 681 | 1     | 55    |
| 1842  | 25.80 | 856    | 859 | 797  | 1010 | 674 | 935 | 681 | 2     | 55    |
| 1845  | 25.84 | 892    | 891 | 797  | 1010 | 674 | 935 | 681 | 3     | 55    |
| 1846  | 25.86 | 898    | 890 | 797  | 1010 | 674 | 935 | 681 | 3     | 55    |
| 1930  | 27.03 | 752    | 751 | 797  | 1010 | 674 | 935 | 681 | -3    | 57    |
| 1931  | 27.05 | 763    | 766 | 797  | 1010 | 674 | 935 | 681 | -2    | 57    |
| 1932  | 27.06 | 773    | 779 | 797  | 1010 | 674 | 935 | 681 | -2    | 57    |
| 1933  | 27.08 | 799    | 795 | 797  | 1010 | 674 | 935 | 681 | -1    | 57    |
| 1937  | 27.13 | 866    | 858 | 797  | 1010 | 674 | 935 | 681 | 1     | 58    |
| 1938  | 27.15 | 869    | 871 | 797  | 1010 | 674 | 935 | 681 | 2     | 58    |
| 1986  | 27.82 | 721    | 723 | 797  | 1010 | 674 | 935 | 681 | -4    | 59    |
| 1987  | 27.83 | 701    | 709 | 797  | 1010 | 674 | 935 | 681 | -4    | 59    |
| 1988  | 27.85 | 704    | 700 | 797  | 1010 | 674 | 935 | 681 | -5    | 59    |
| 1989  | 27.86 | 689    | 692 | 797  | 1010 | 674 | 935 | 681 | -5    | 59    |
| 1990  | 27.87 | 687    | 692 | 797  | 1010 | 674 | 935 | 681 | -5    | 59    |
| 1991  | 27.89 | 682    | 693 | 797  | 1010 | 674 | 935 | 681 | -5    | 59    |
| 1992  | 27.90 | 701    | 698 | 797  | 1010 | 674 | 935 | 681 | -5    | 59    |
| 1993  | 27.92 | 706    | 706 | 797  | 1010 | 674 | 935 | 681 | -5    | 59    |
| 1994  | 27.93 | 717    | 718 | 797  | 1010 | 674 | 935 | 681 | -4    | 59    |
| 1995  | 27.94 | 724    | 730 | 797  | 1010 | 674 | 935 | 681 | -4    | 59    |
| 1996  | 27.96 | 744    | 744 | 797  | 1010 | 674 | 935 | 681 | -3    | 59    |
| 1997  | 27.97 | 761    | 757 | 797  | 1010 | 674 | 935 | 681 | -3    | 59    |
| 1998  | 27.99 | 774    | 751 | 797  | 1010 | 674 | 935 | 681 | -3    | 59    |
| 1999  | 28.00 | 757    | 797 | 797  | 1010 | 674 | 935 | 681 | 0     | 59    |

n=2000  
PEAK=168  
RMS=70  
CF= 2.4  
KURT=1.80

**A6.2 Lab VIEW flow-codes for the PI speed data acquisition and GUI display**

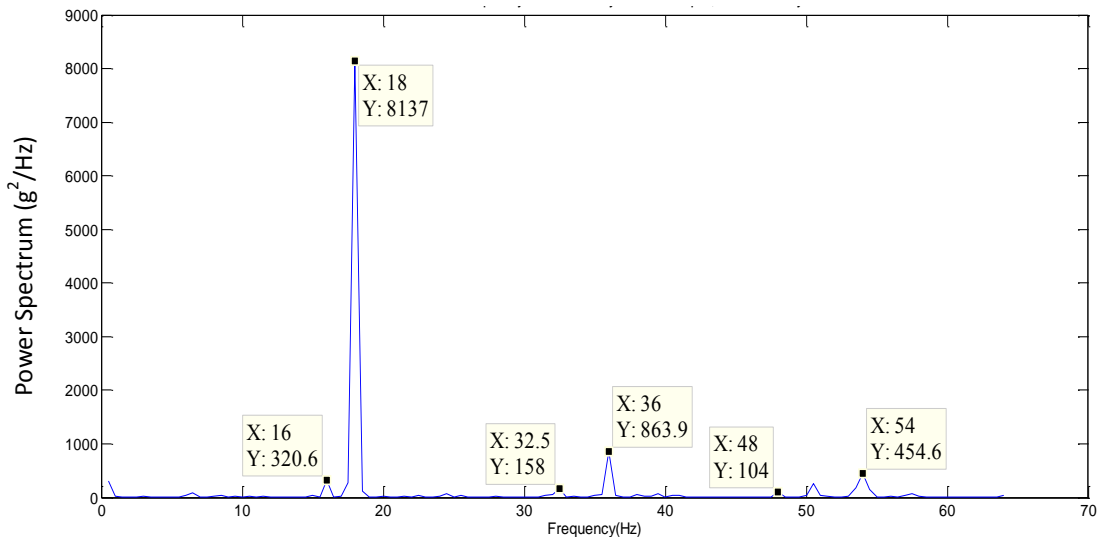


**A6.3 Lab VIEW code for the Accelerometer data acquisition and GUI display**

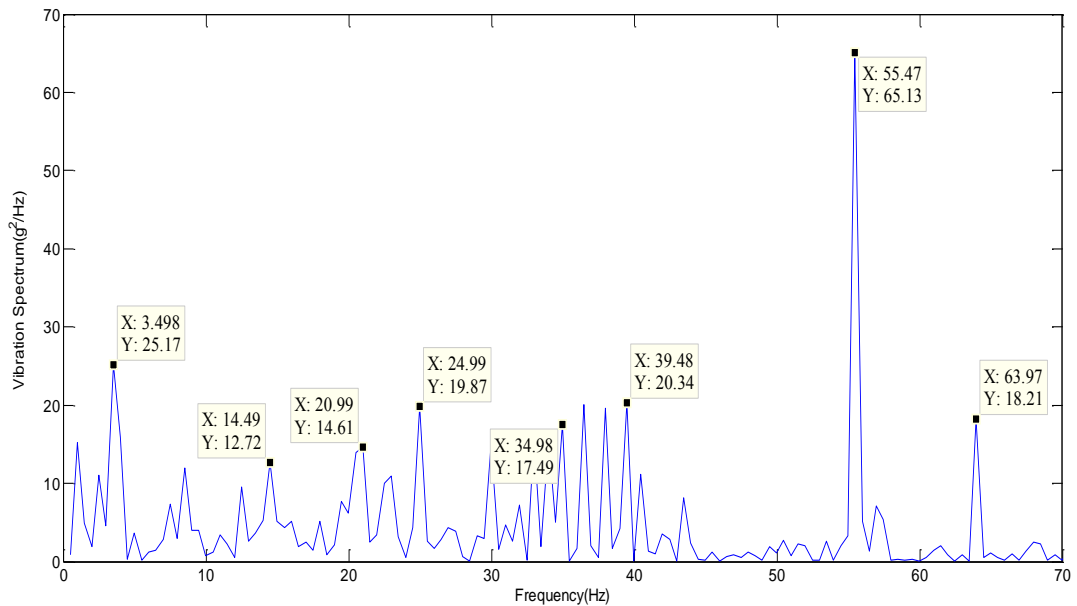




**A6.4 Accelerometer FFT plot for the axial horizontal (X-axis) \_**



**A6.5 Accelerometer FFT plot for the radial vertical (Y-axis) \_**



**Appendix 7: Supplementary Frequency Domain Results for Synergy D6 Flow**

**A7.1 2D plots for Synergy D6 flow dry testing at 20°C (see attached A3 sheet)**

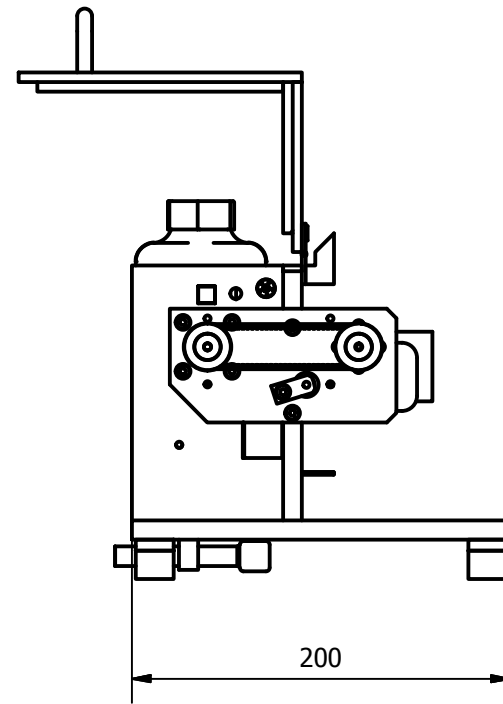
**A7.2 2D plots for Synergy D6 flow lubricated testing at 20°C (see attached A3 sheet)**

**A7.3 2D plots for Synergy D6 flow lubricated testing at 37°C (see attached A3 sheet)**

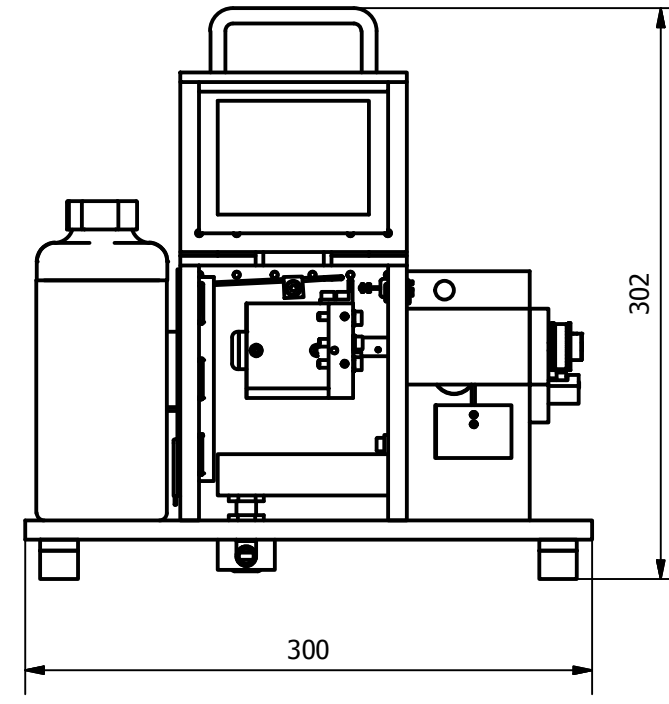
# Appendix A3.1: Mechatronic rolling ball device hardware

NB: Scale 1:4  
Dimensions are mm

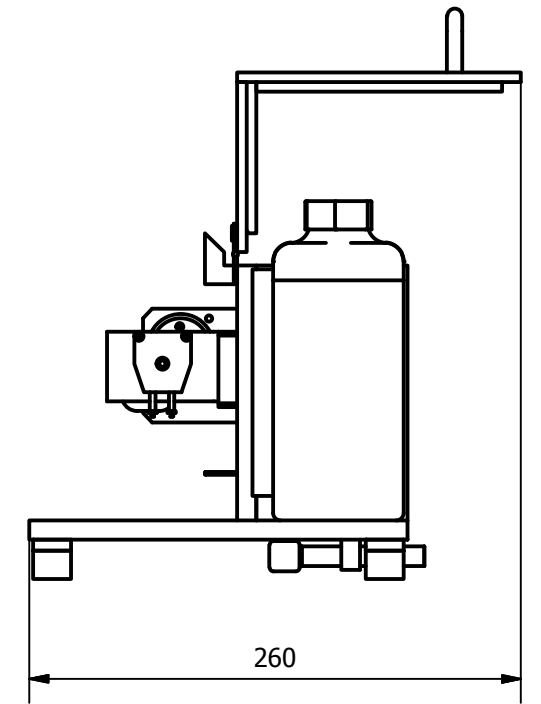
Only visible parts are ballooned for clarity, please refer items on the Part list to Fig 5-16 and Fig. 8-1 for identification



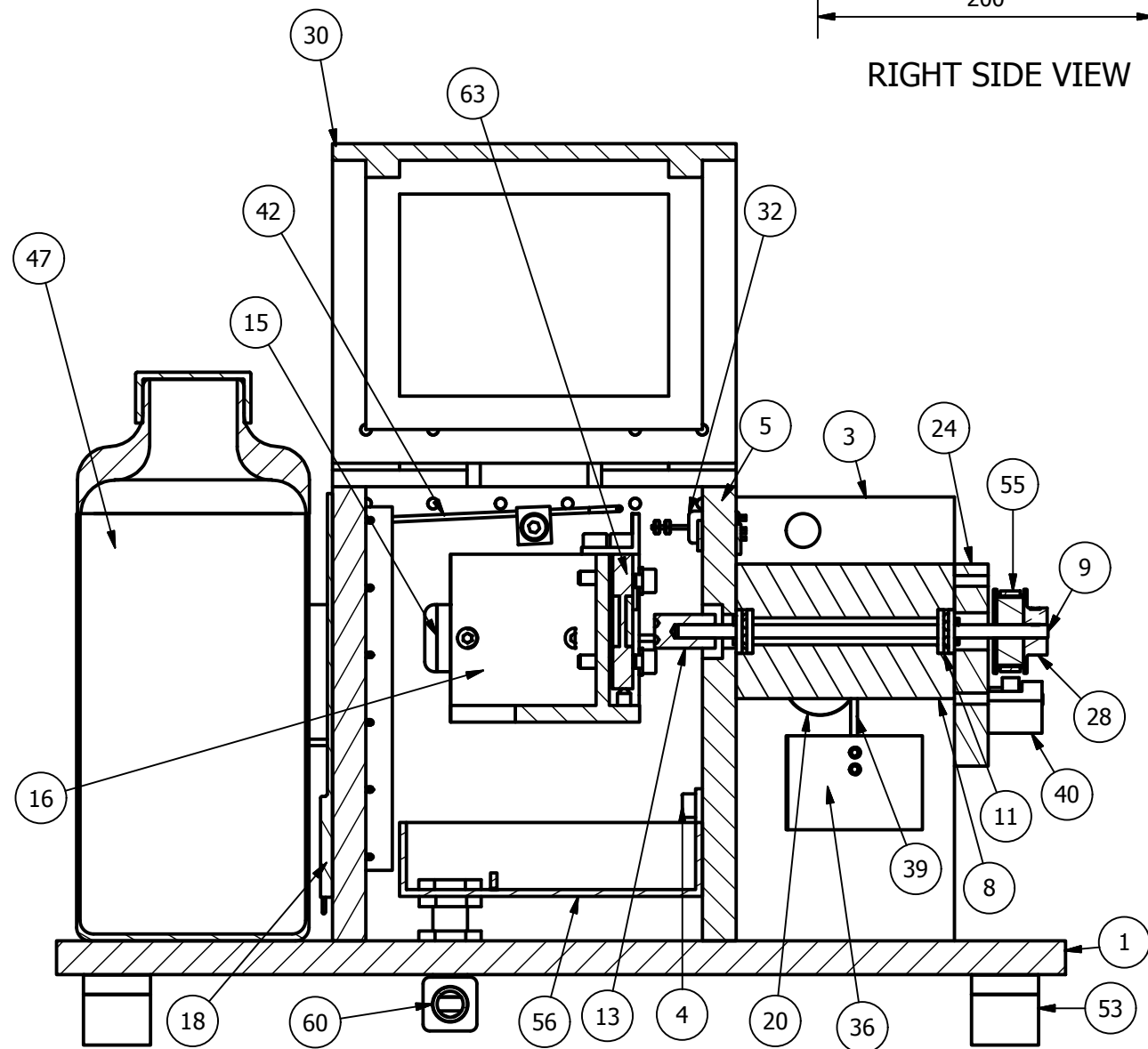
RIGHT SIDE VIEW



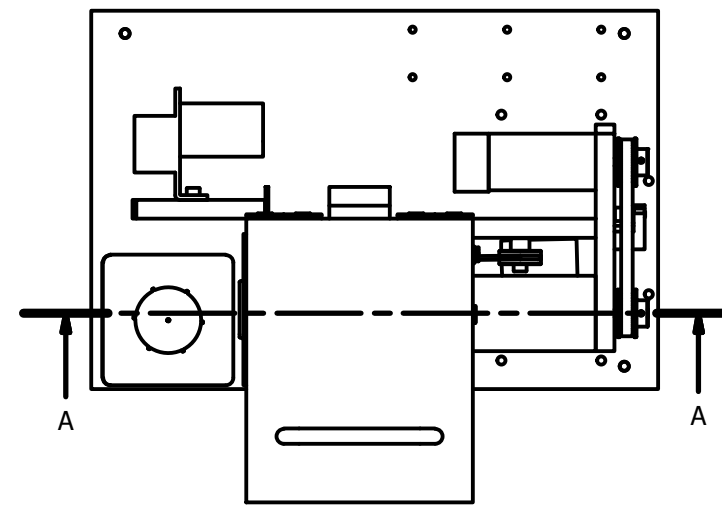
FRONT VIEW



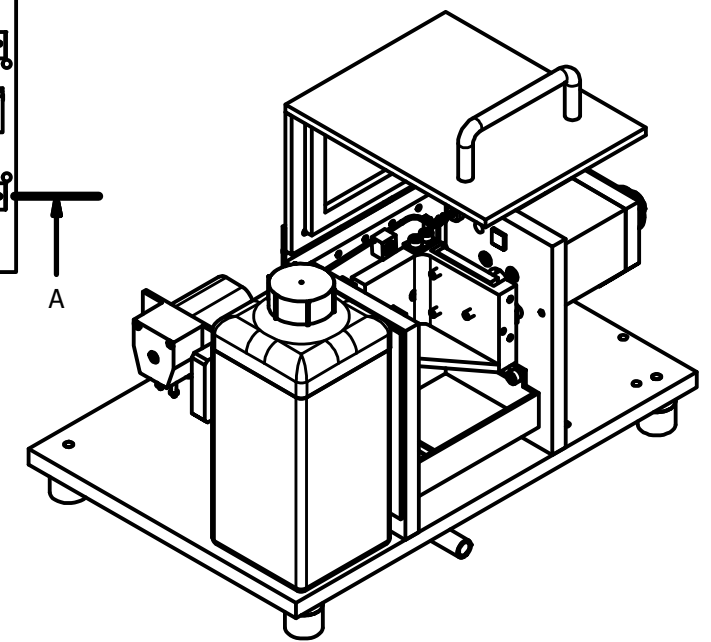
LEFT SIDE VIEW



FRONT VIEW SECTION A-A

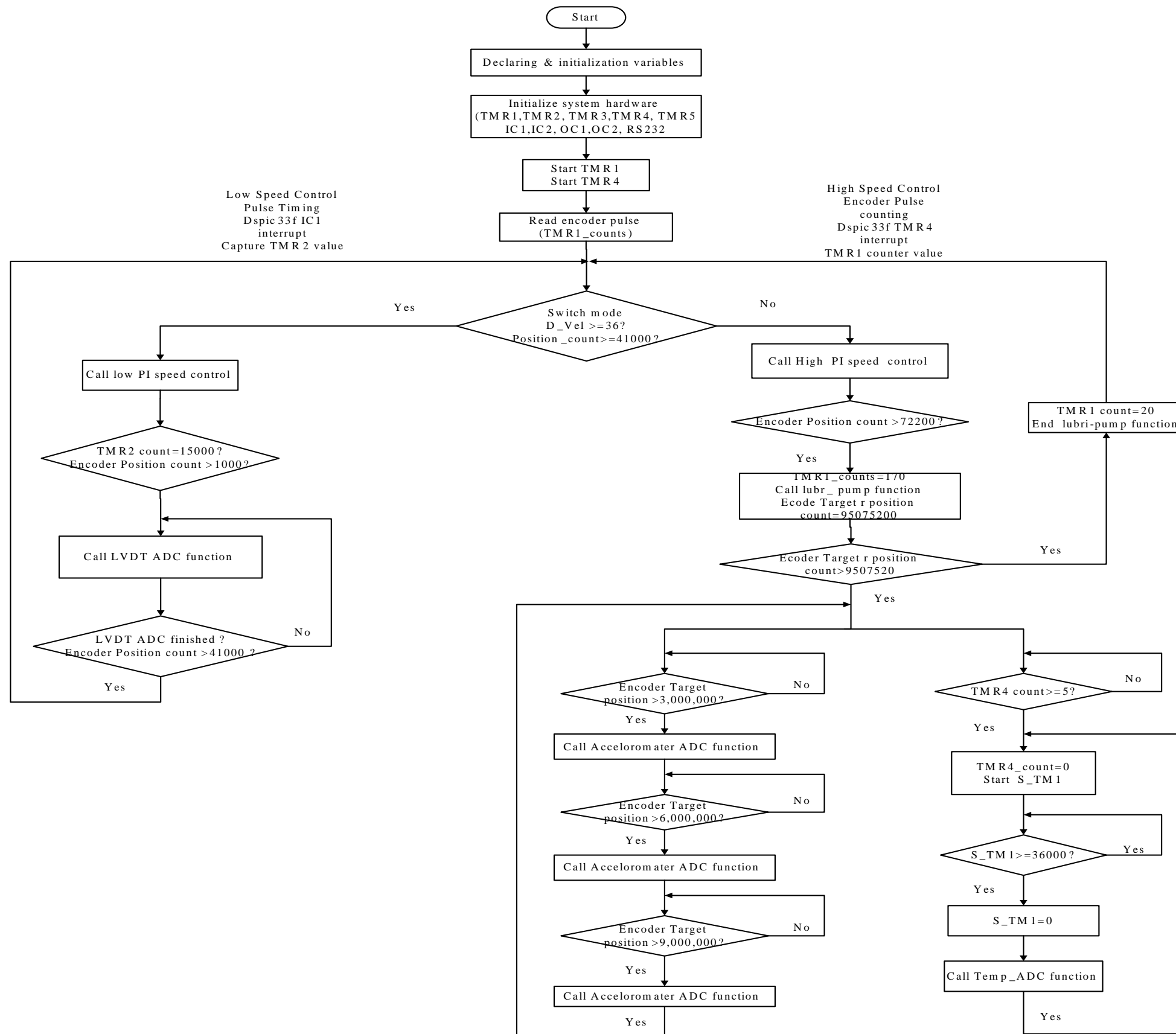


TOP VIEW

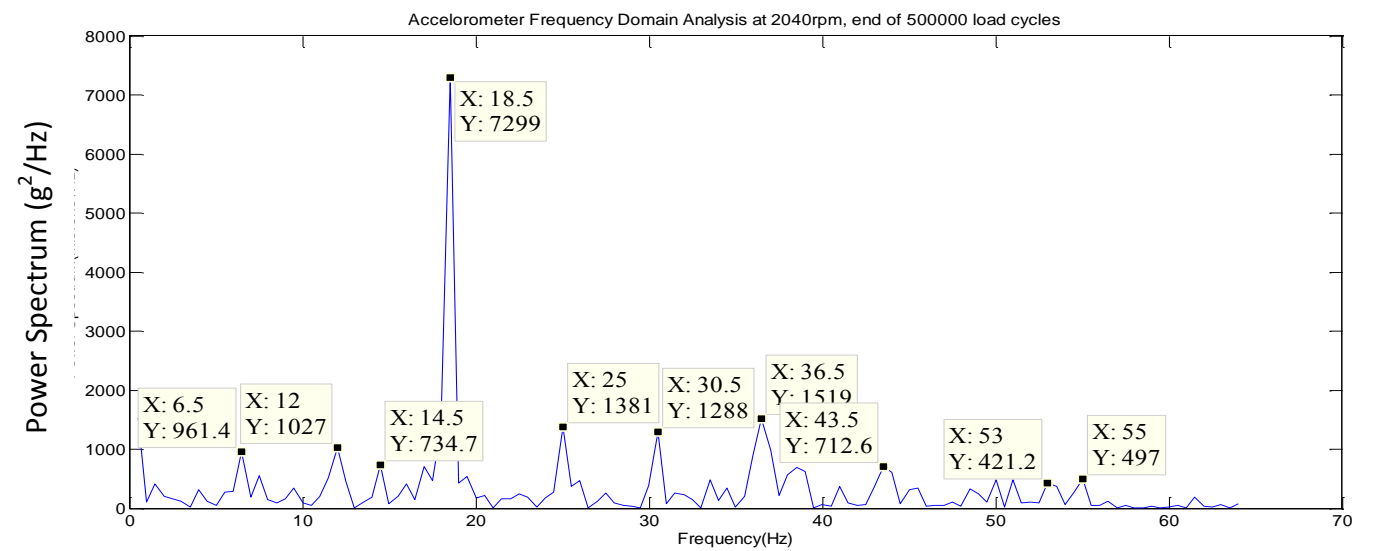
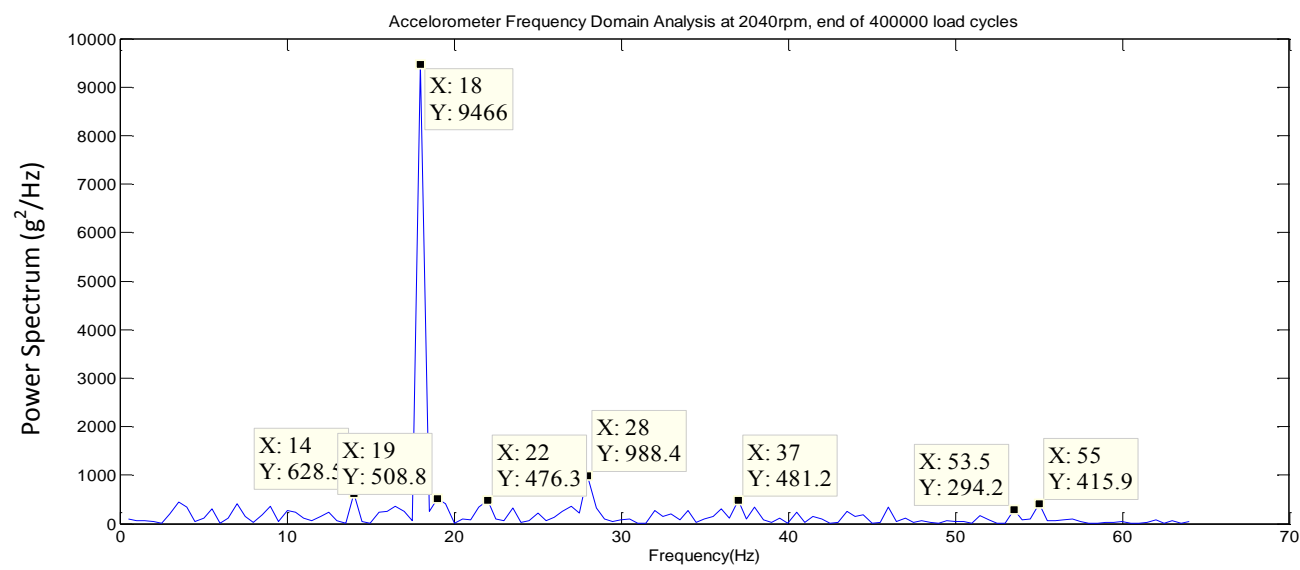
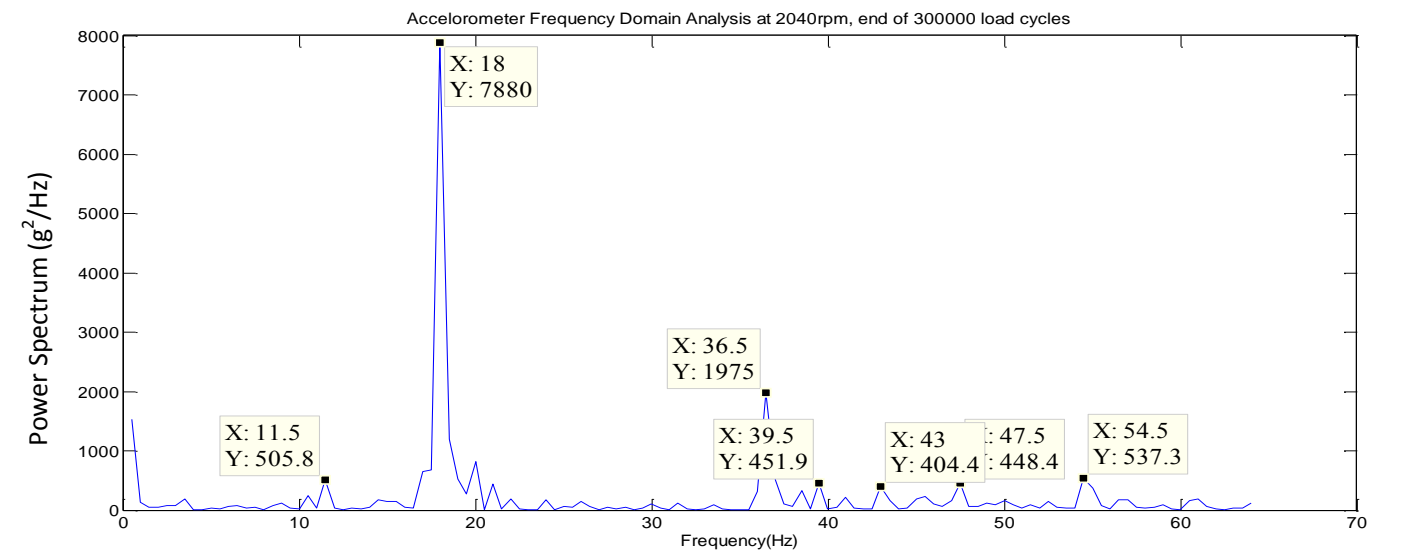
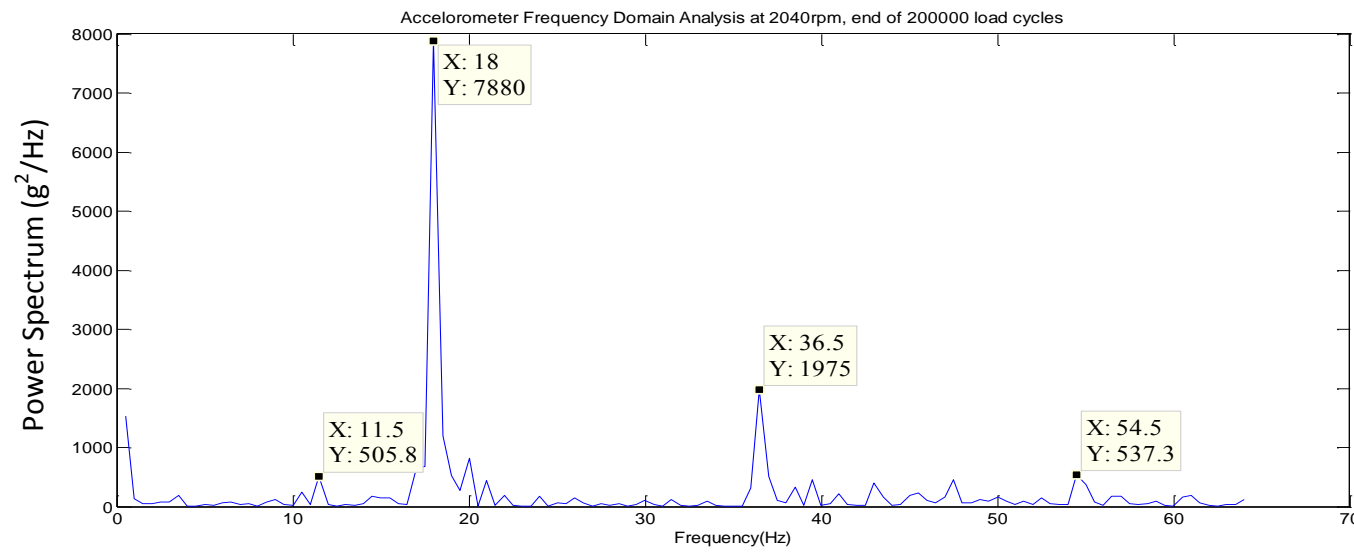
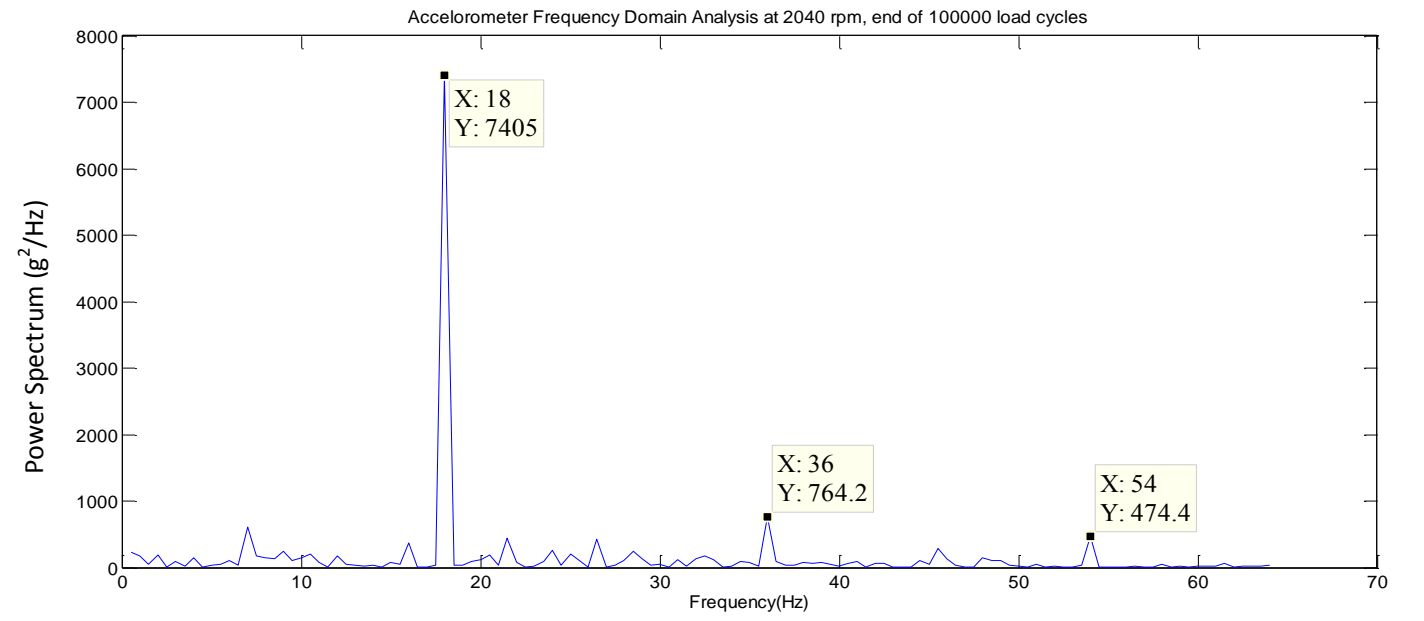
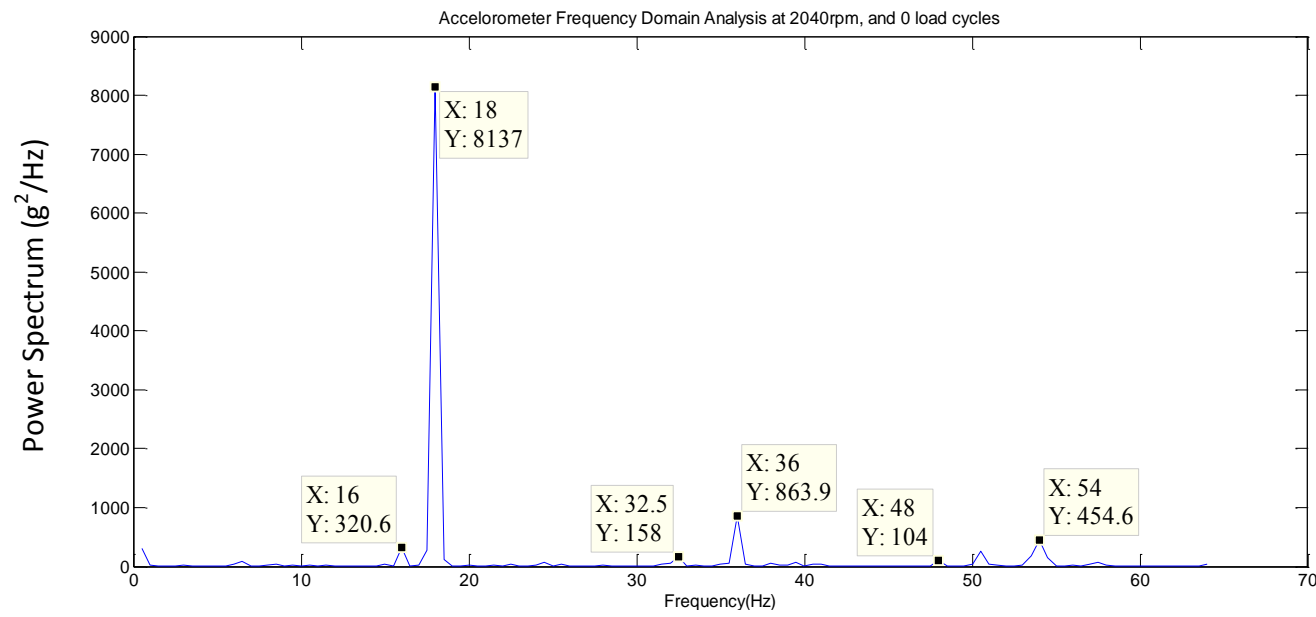


ISOMETRIC VIEW

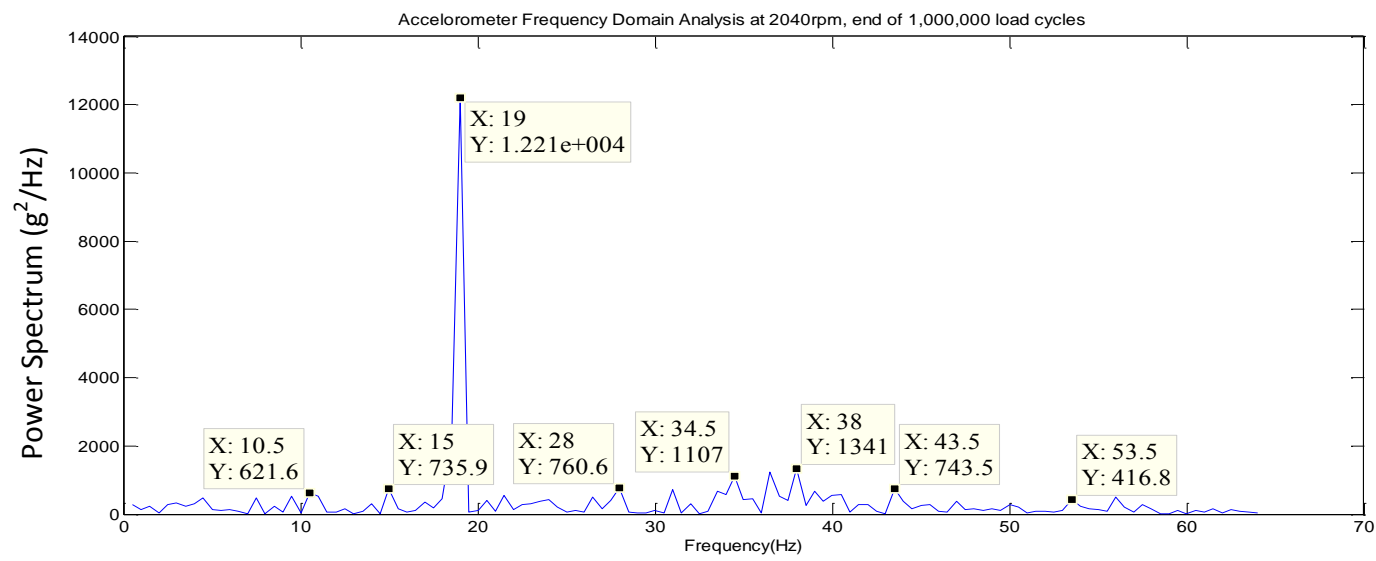
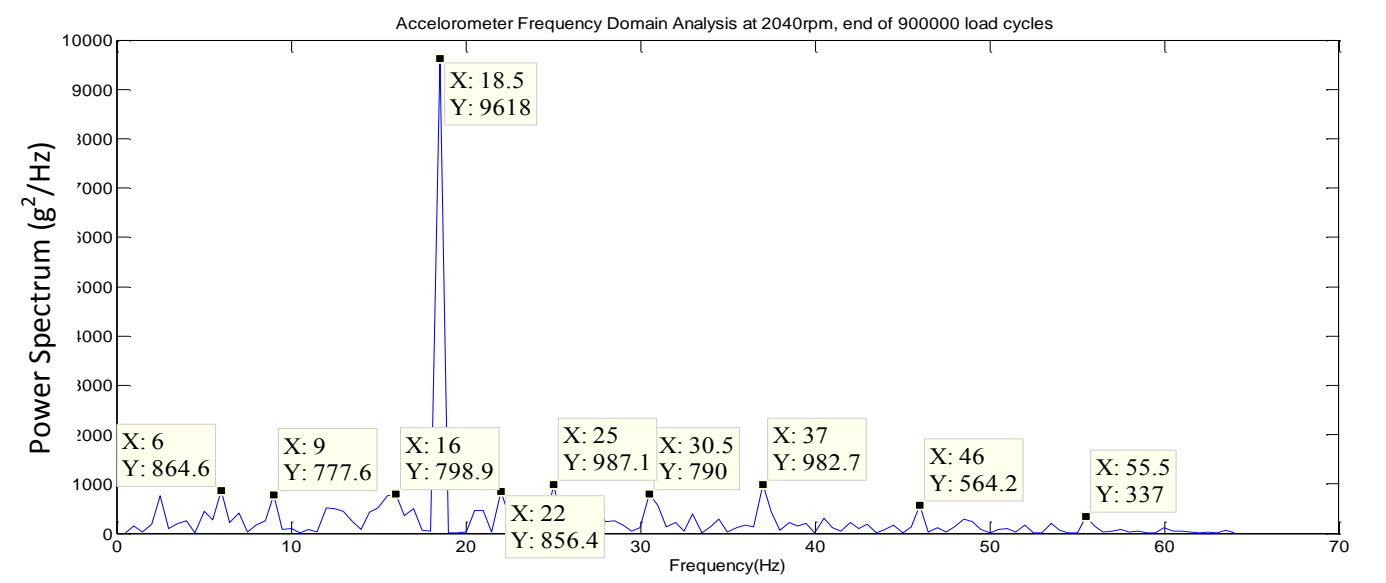
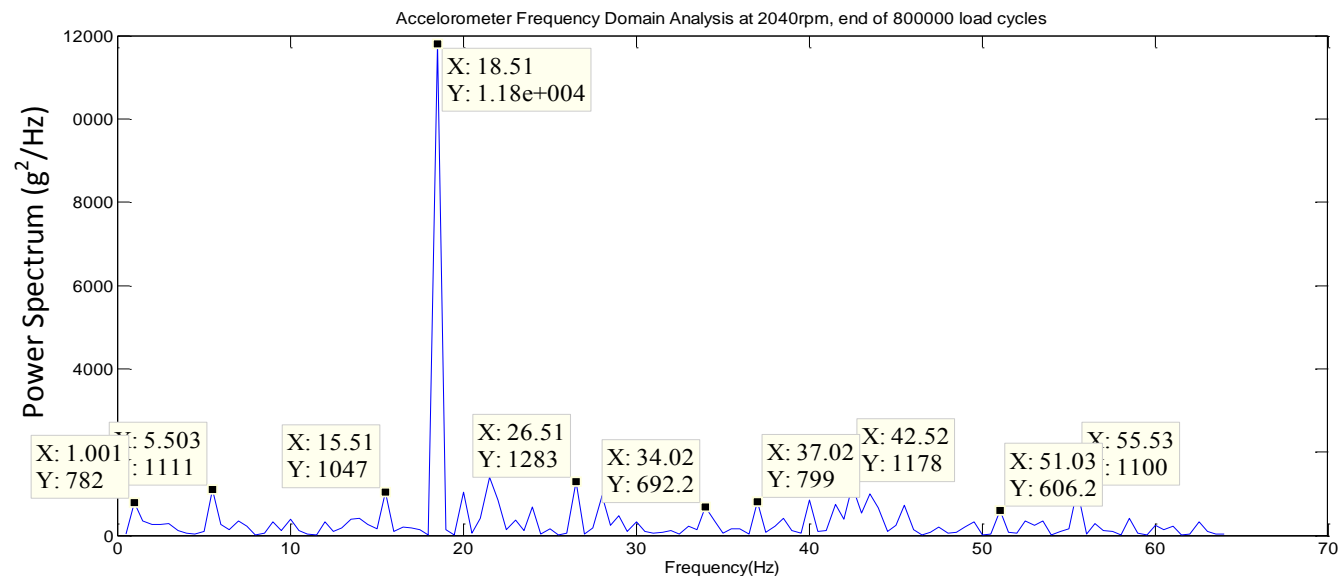
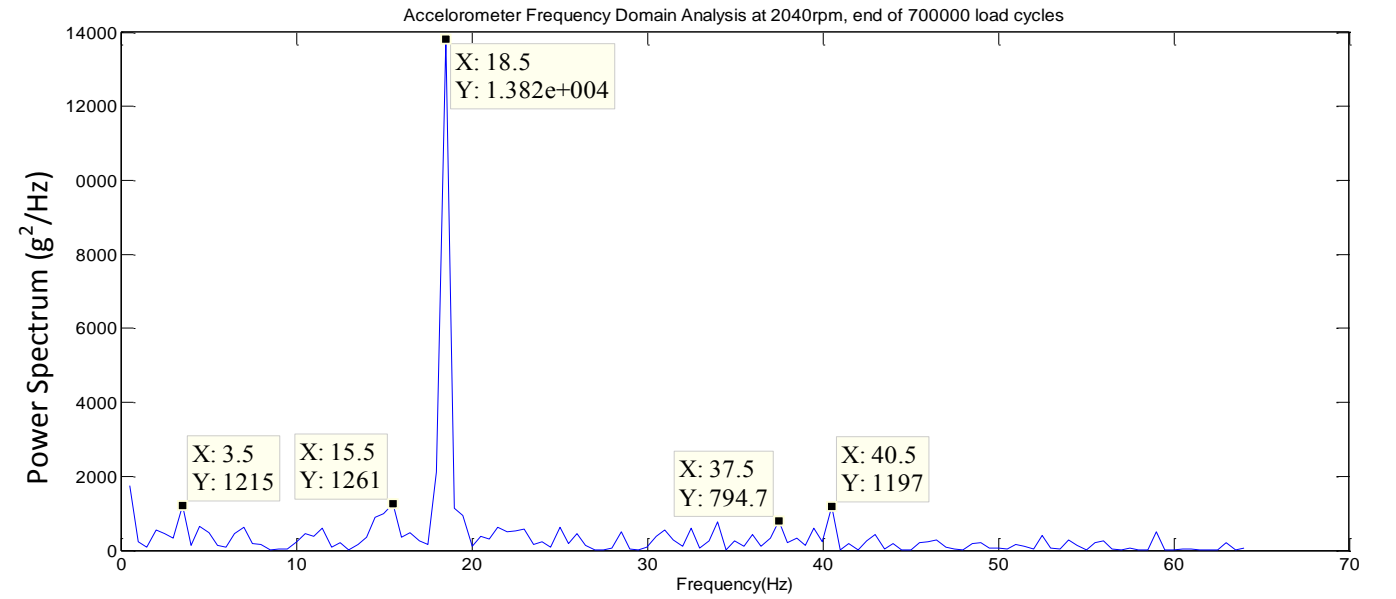
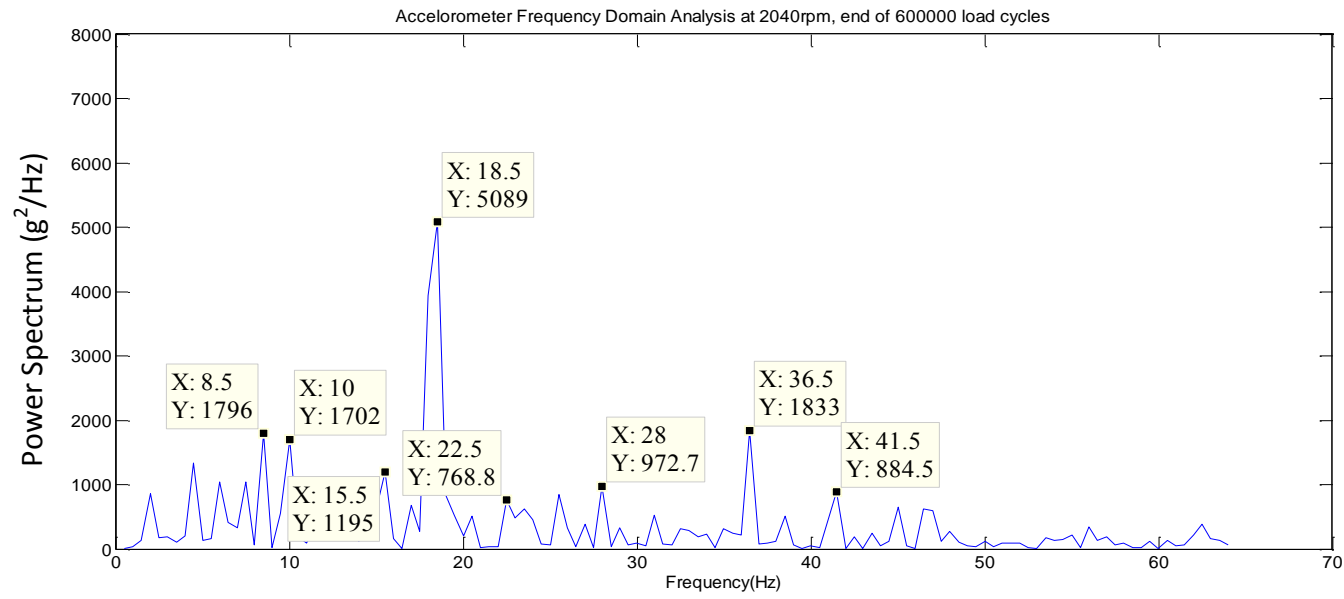
|                                |                        |                         |                                 |                    |                |
|--------------------------------|------------------------|-------------------------|---------------------------------|--------------------|----------------|
| Designed by<br>Simon I.Marandu | Checked by<br>R.Bicker | Approved by<br>R.Bicker | Date<br>3.10.2011               | Date<br>03.09.2012 |                |
| MSE Newcastle University       |                        |                         | Mechatronic Rolling Ball Device |                    |                |
|                                |                        |                         | Simon.I.Marandu                 | Edition<br>0       | Sheet<br>1/ 50 |



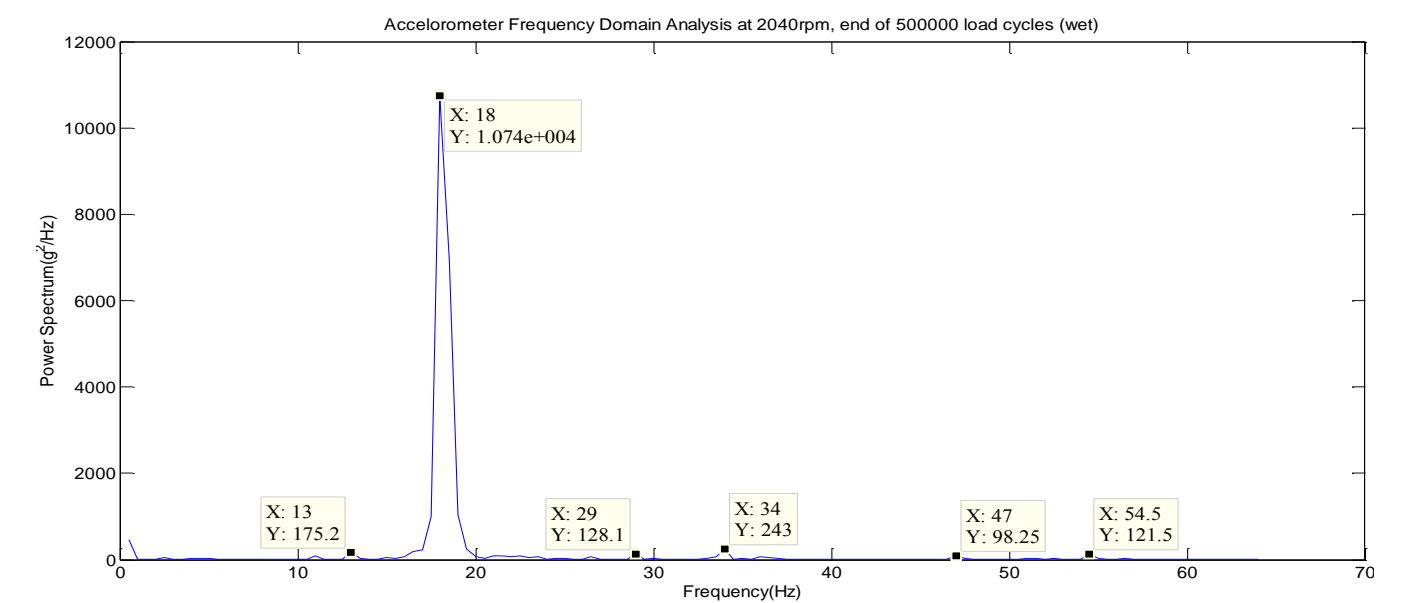
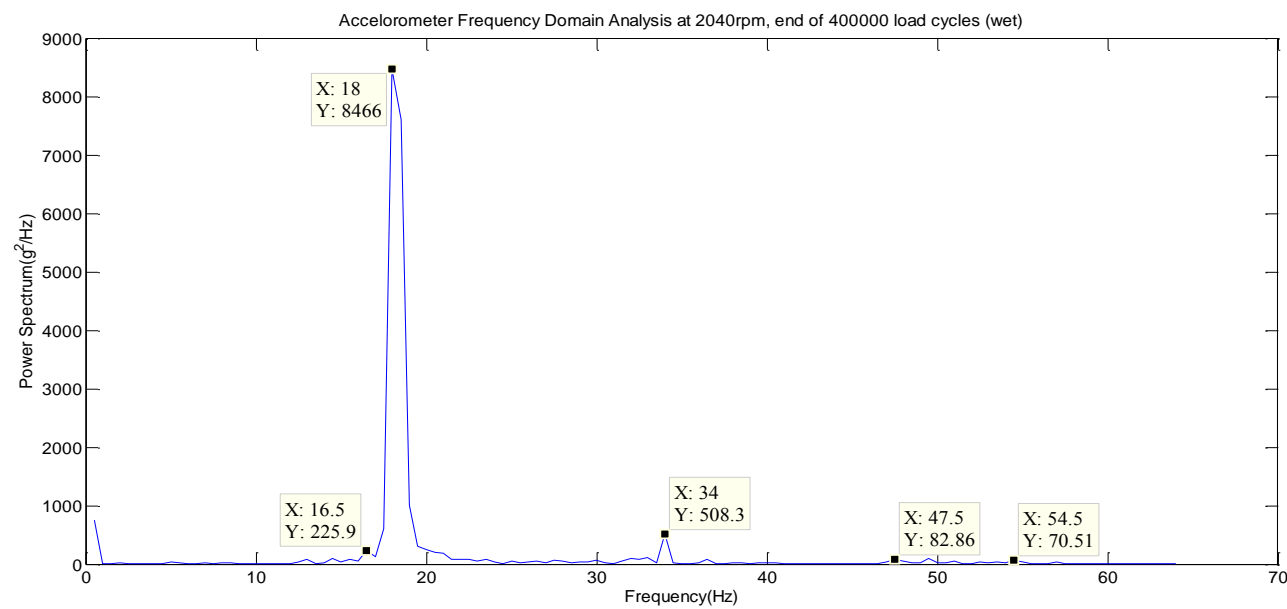
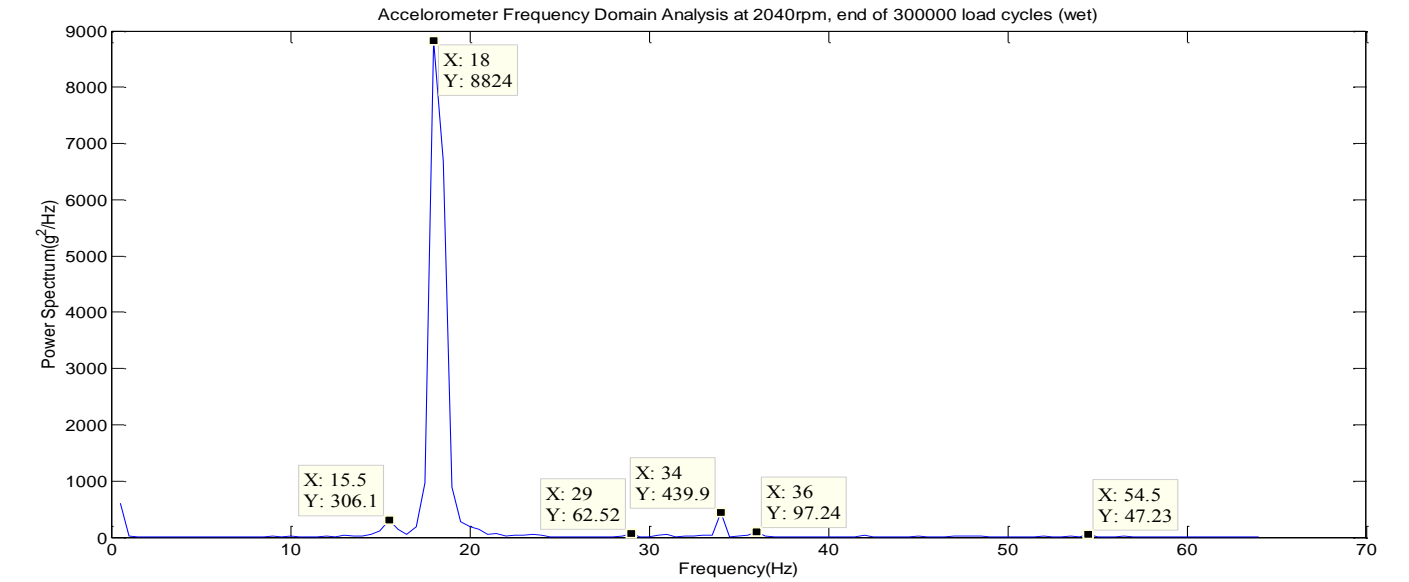
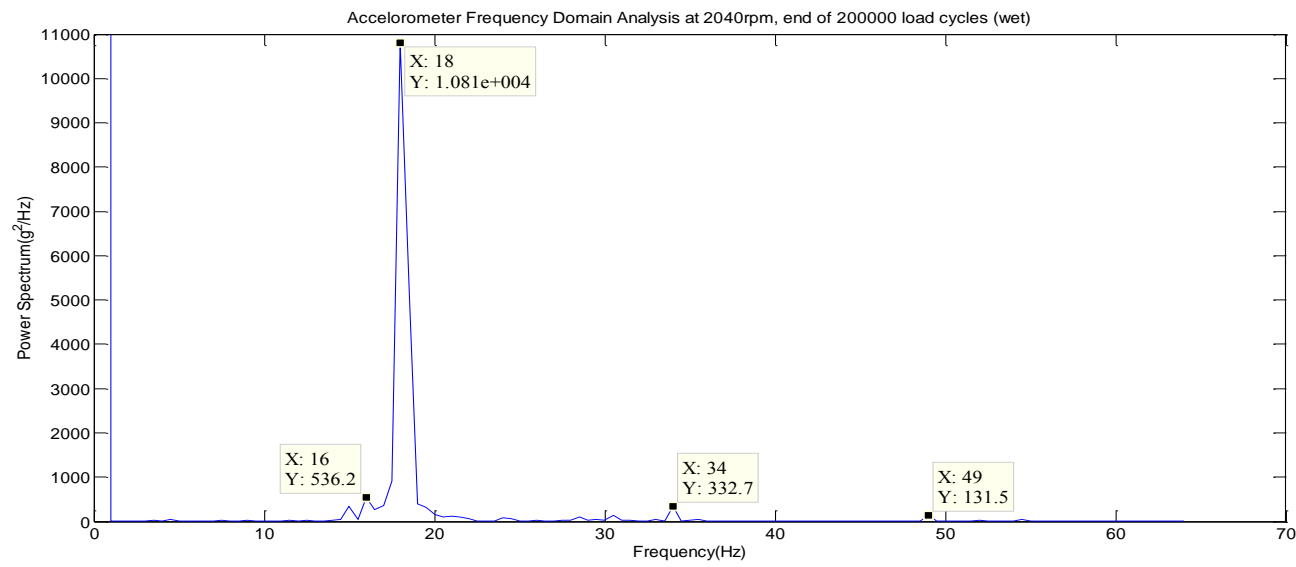
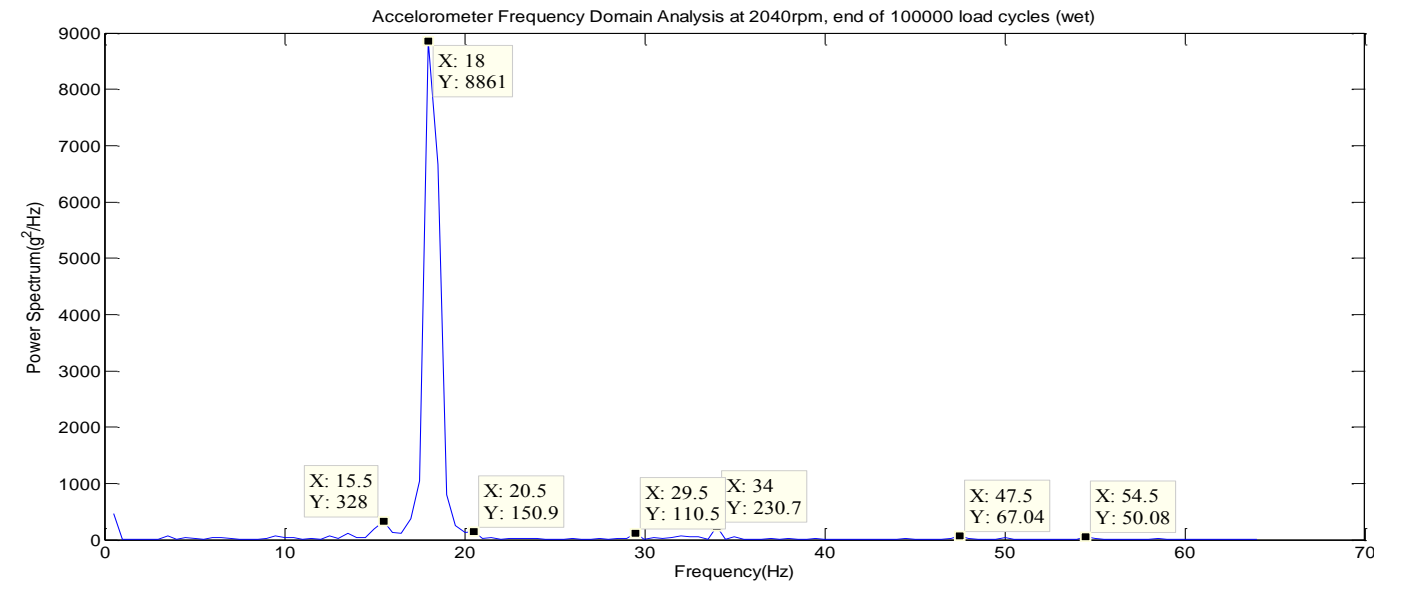
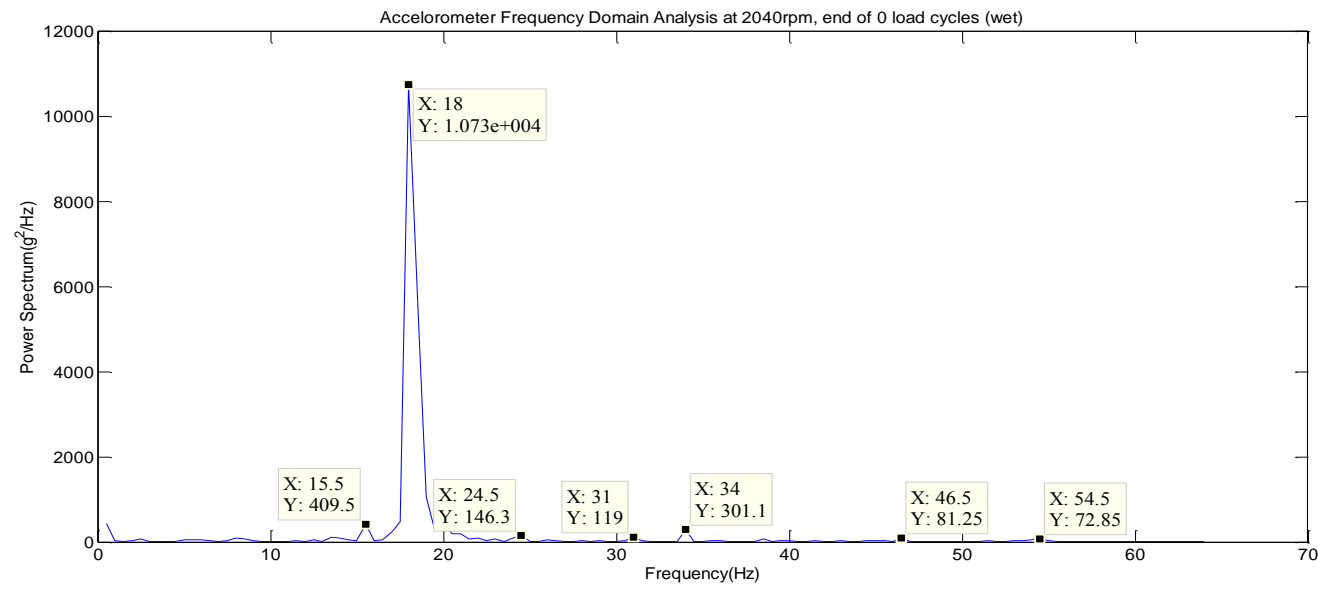
## 2D FFT plots for Synergy D6 Flow Dry Testing at Room Temperature of 20°C



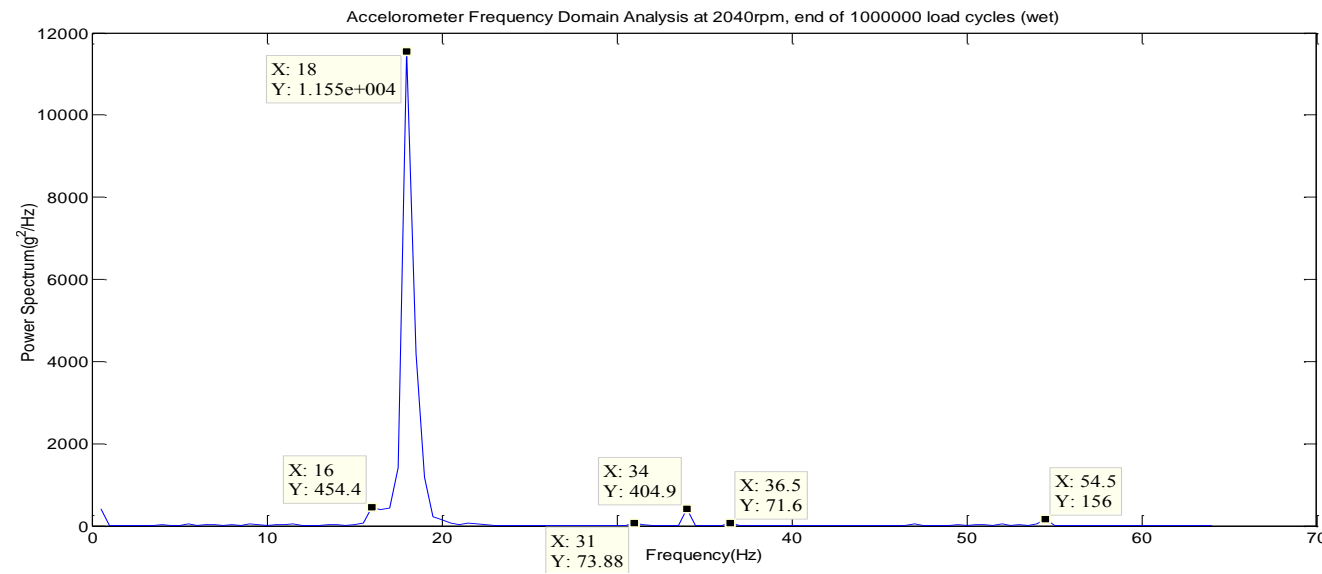
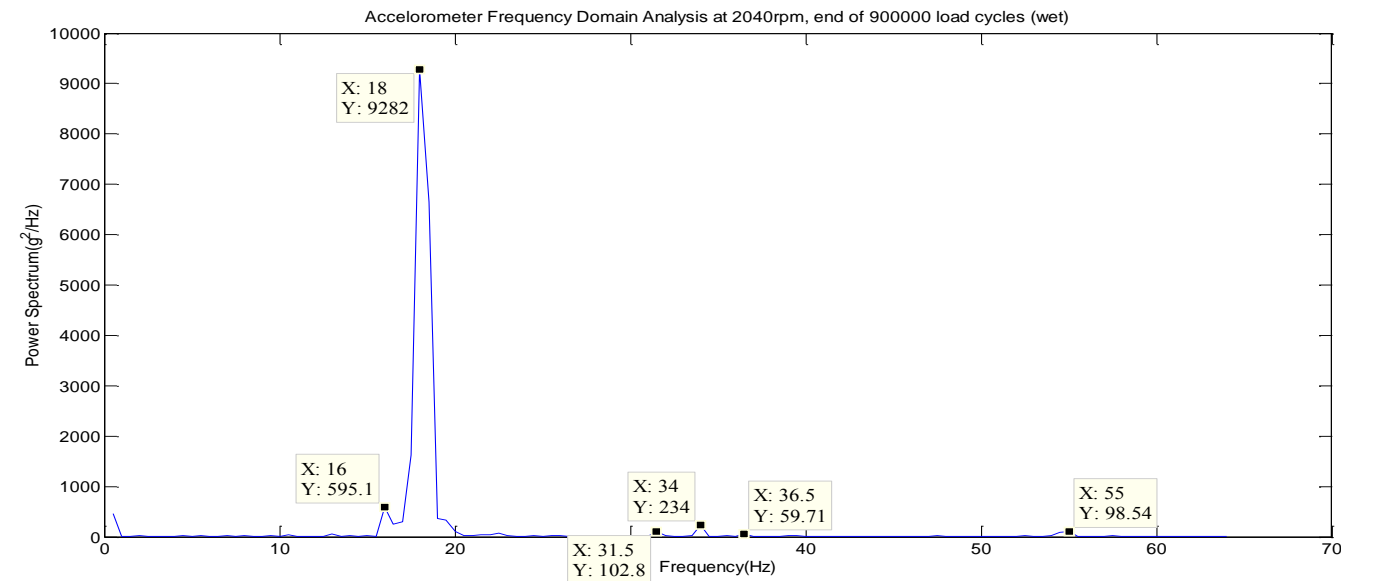
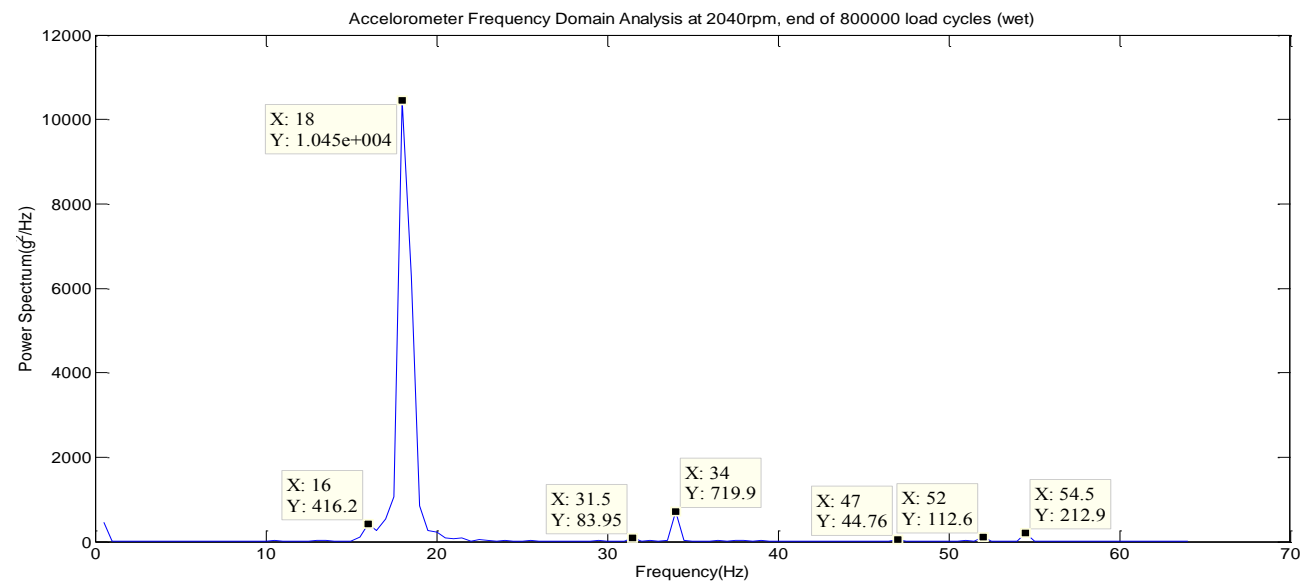
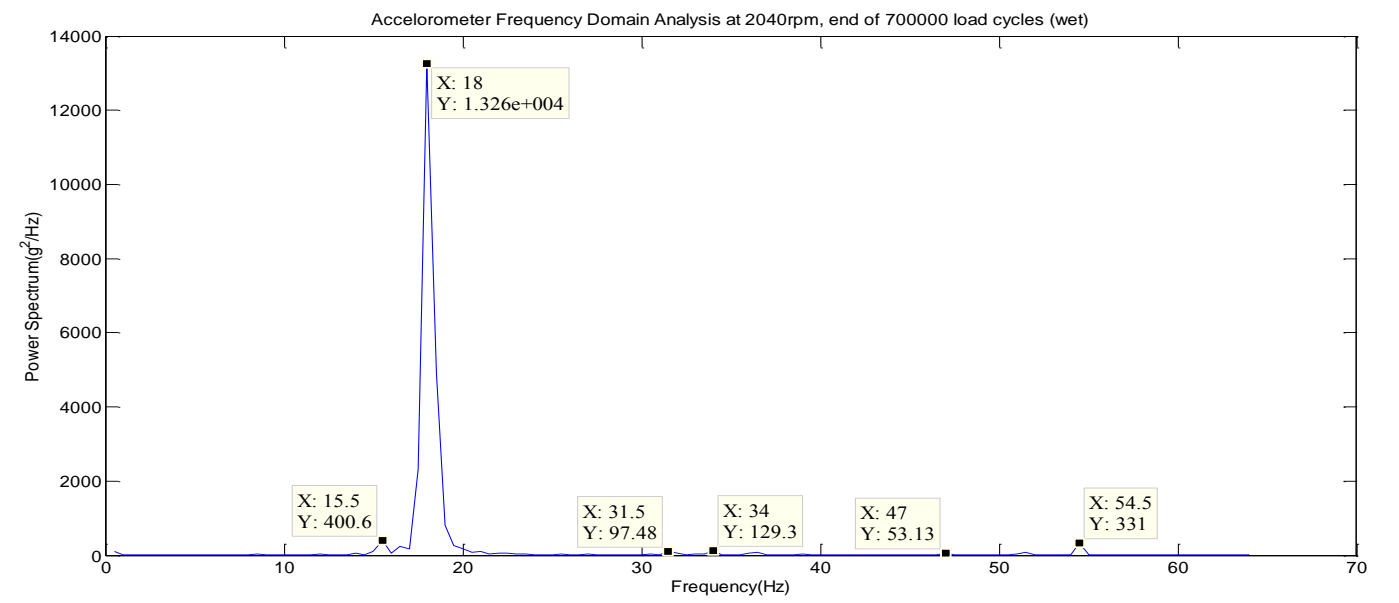
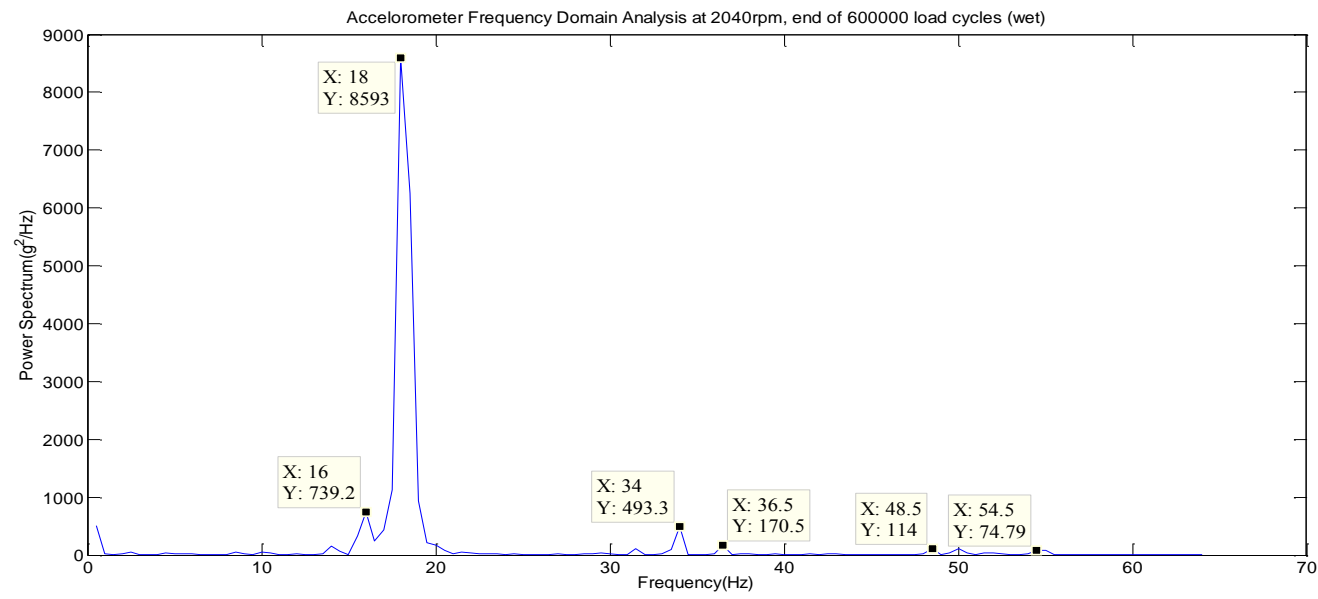
## 2D FFT plots for Synergy D6 Flow Dry Testing at Room Temperature of 20°C



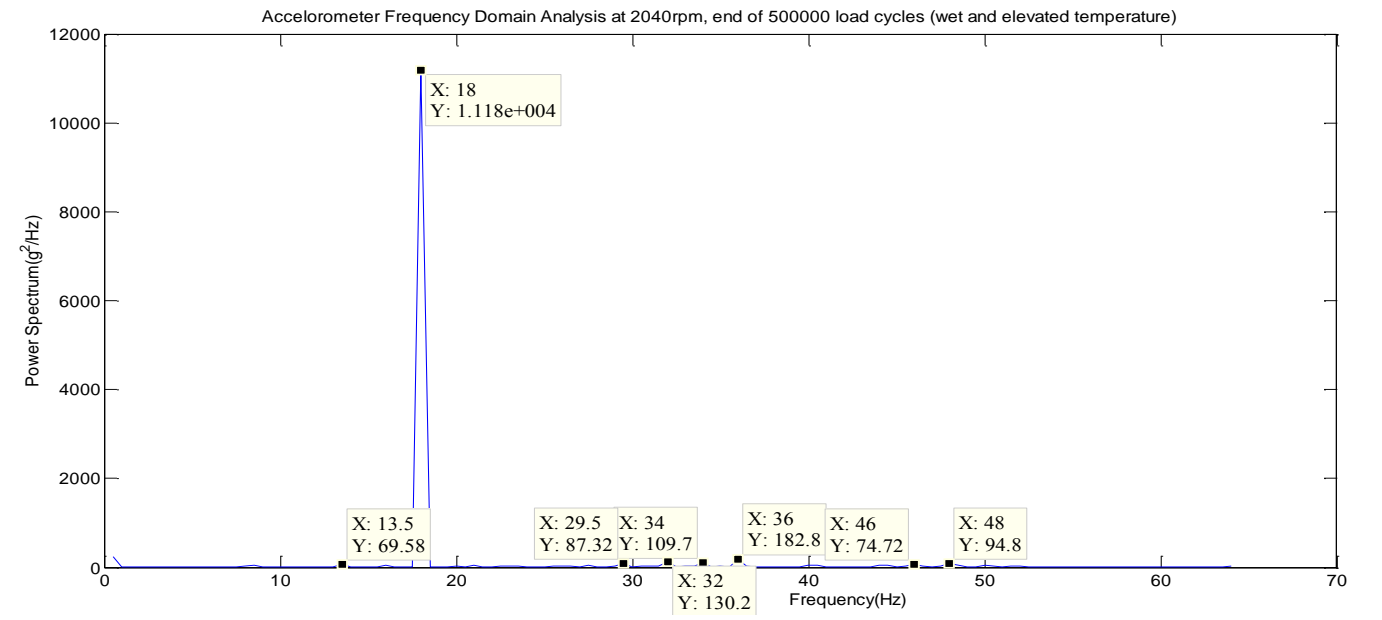
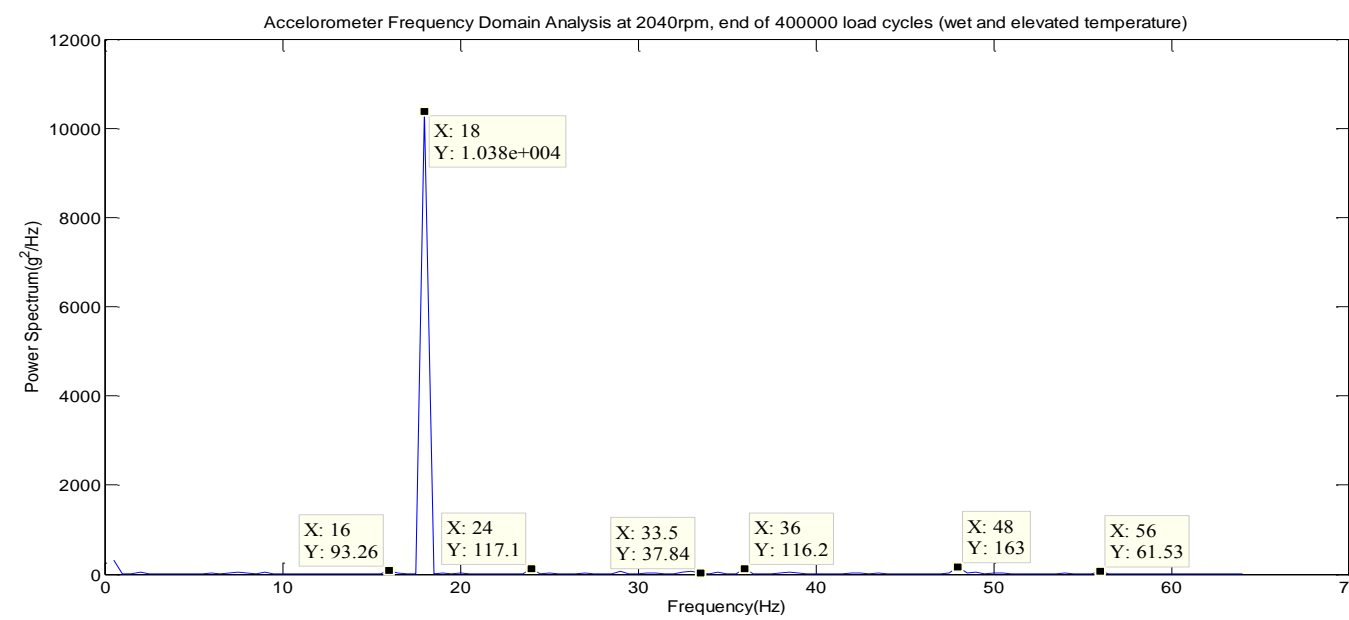
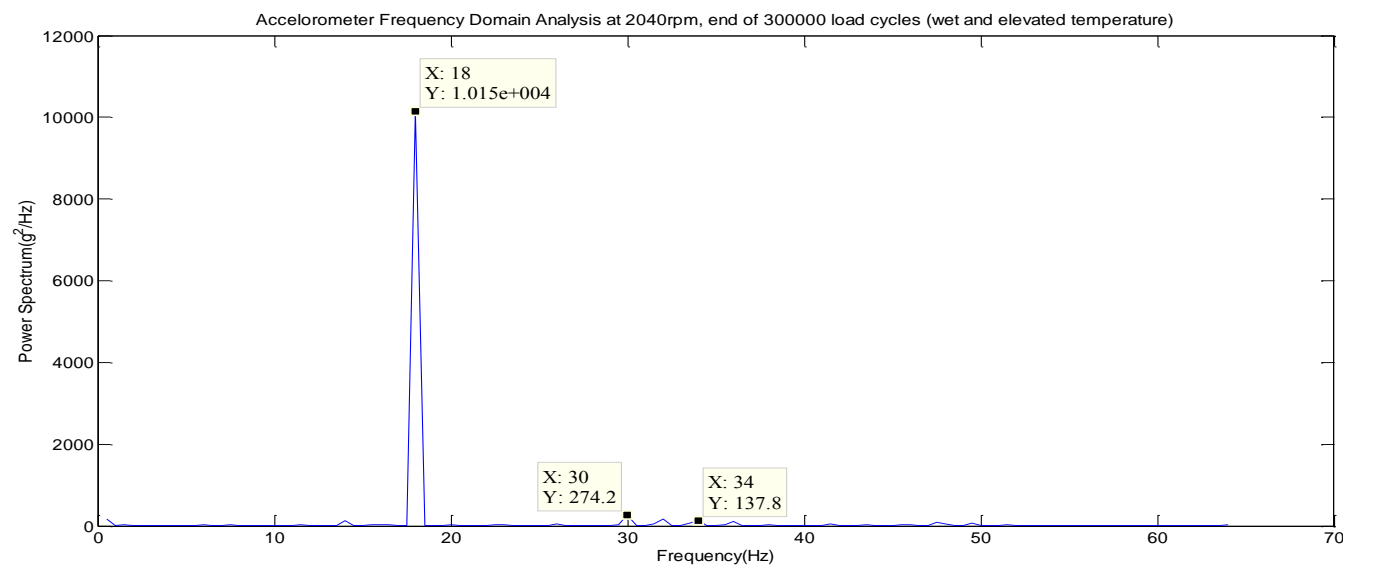
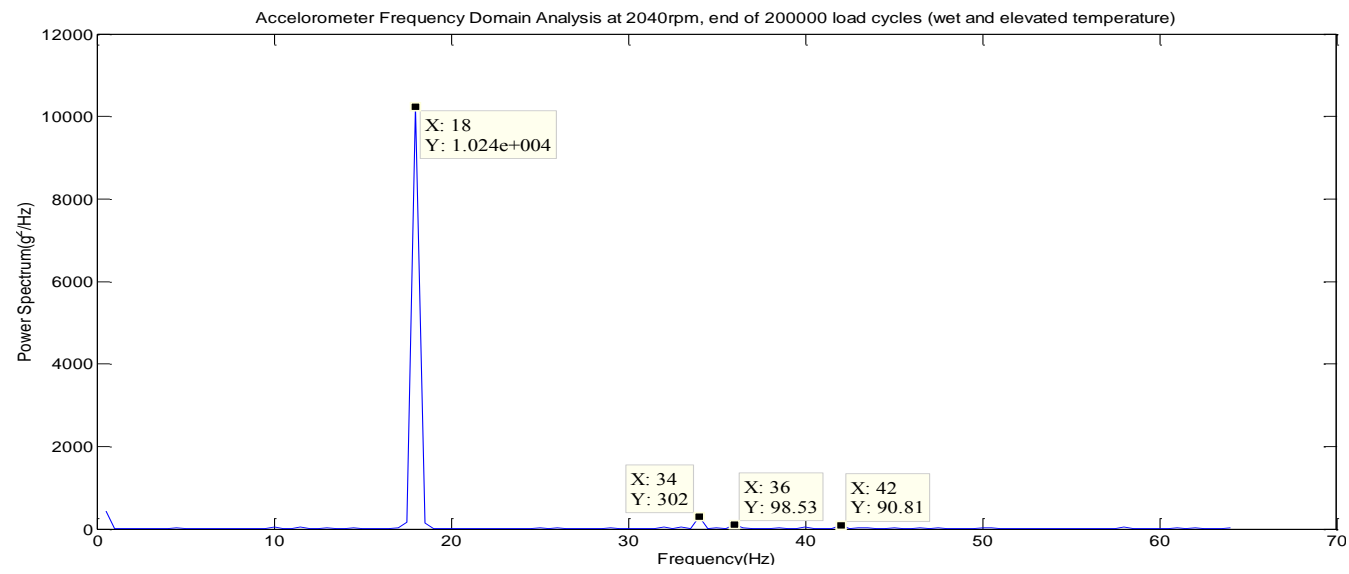
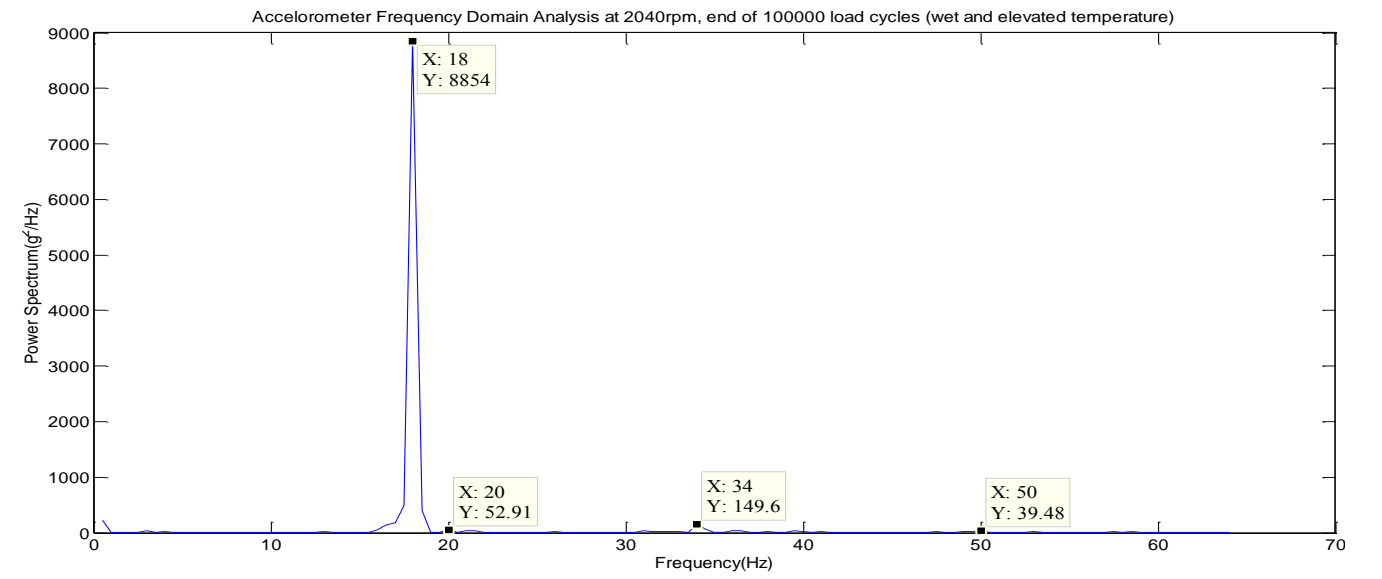
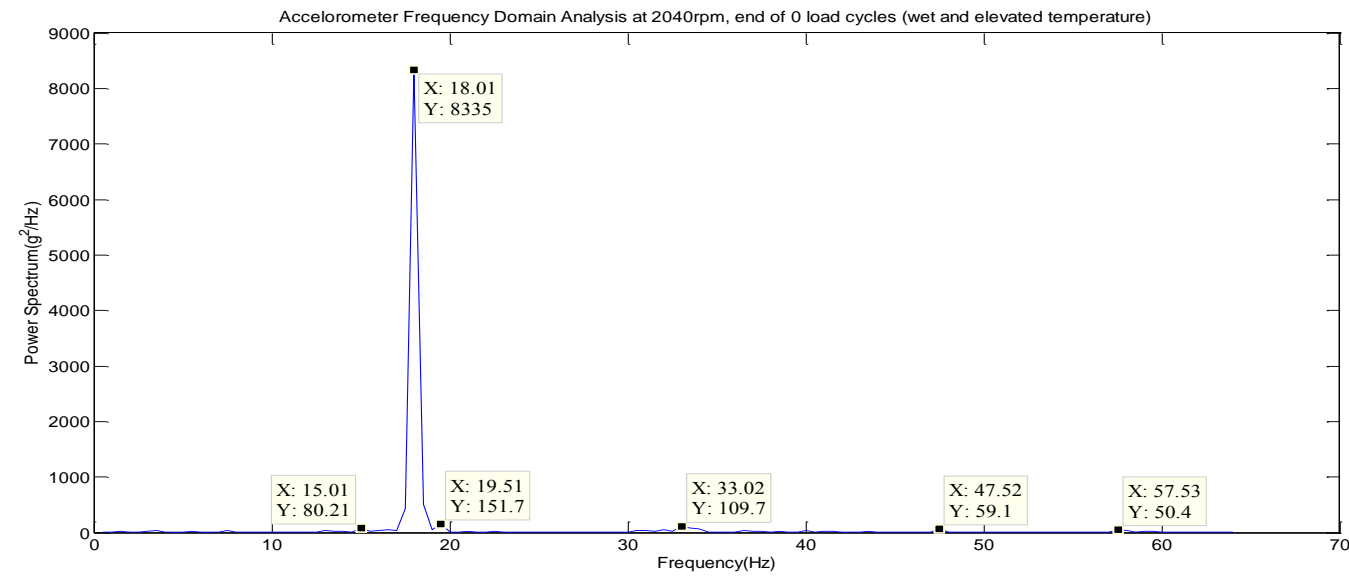
## 2D FFT plots for Synergy D6 Flow Lubricated (Wet) Testing at Room Temperature of 20°C



### 2D FFT plots for Synergy D6 Flow Lubricated (Wet) Testing at Room Temperature of 20°C



## 2D FFT plots for Synergy D6 Flow Lubricated (Wet) Testing at Elevated Temperature of 37°C





## 2D FFT plots for Synergy D6 Flow Lubricated (Wet) Testing at Elevated Temperature of 37°C

